# Unveiling the Versatility of Titanium and Iron Nanostructures: Applications Across Medicine, Environmental Remediation and Organic Reactions

**Daliane Regis Correa da Silva**

Thesis submitted to the University of Ottawa
in partial Fulfillment of the requirements for the degree of Doctorate in Philosophy
in Chemistry

Department of Chemistry and Biomolecular Sciences
Faculty of Science
University of Ottawa

Supervisor: Juan (Tito) Scaiano

# In dedication to

My parents, Ari Eustaquio and Edva for prioritizing my education, and providing unconditional support and encouragement in every step of my journey.

"The great tragedy of science – the slaying of
a beautiful hypothesis by an ugly fact"

-Thomas Henry Huxley

# Abstract

With the rise of material science comes the increasing demand for multiple elements for essential applications. The overexploitation of certain minerals has raised concerns about the sustainability of these practices. Materials such as noble metals have not only limited availability but also impose environmental and social risks upon extraction and processing. Thus, it becomes imperative to search for more sustainable alternatives and explore their potential uses across various fields. This dissertation will focus on iron and titanium-based nanomaterials, employing them in diverse systems and evaluating their uses in the medical, environmental, and catalysis fields.

First, iron oxide will be studied through the fabrication of magnetic nanoparticles (MNPs) coated with lignin. The capping material was chosen as a sustainable and biocompatible alternative. The relatively low toxicity of iron makes these nanoparticles a great option for therapeutic materials, particularly for antibacterial uses. The four fabricated nanoparticles—Lignin@Fe (LFe), Lignin@FeAg (LFeAg), Lignin@Co (LCo) and Lignin@FeCo (LFeCo) —exhibit mild antibacterial properties in the absence of light. However, when illuminated with a near-infrared (NIR) wavelength, 810 nm, they become powerful antibacterial agents, achieving bactericidal levels with a 6-log reduction within 5 to 30 minutes of irradiation. NIR light is advantageous as it falls within the biological window, allowing deep tissue penetration during *in vivo* applications. Combining the photothermal effect generated upon light irradiation with the chemical production of hydroxyl radicals (•OH) via Fenton reactions resulted in even greater bactericidal activity, achieving complete eradication (≥ 6 log units) within 1-5 minutes of incubation.

Ti-based materials were also studied, specifically focusing on the semiconductor $TiO_2$. This is a powerful photocatalyst, but its applications are limited due to its powder form. Interested in the potential environmental uses of these materials, which benefit from fixed-bed reactions and supported catalysts, we produced three fibrous $TiO_2$ materials. These included $TiO_2$ nanofibres

($TiO_2$NF) and two types of $TiO_2$ supported on glass fibres. We observed that the range of catalytic activity towards crocin bleaching varied according to the material properties, particularly surface area. Interestingly, their behaviour in flow systems differed from that in batch ones. We found that $TiO_2$ deposited on glass wool (TGW) not only exhibited higher catalytic activity in flow systems but also presented itself as a more viable alternative for application in various flow systems.

Further interested in this new material and its potential as an alternative for fixed bed reactors, we tested it for antibacterial activity. To our surprise, the initial experiments revealed that while TGW exhibited excellent catalytic activity in the degradation of an organic dye, its bactericidal activity was limited. This unexpected discovery prompted the development of several testing conditions, which ultimately resulted in little to no improvement in bacterial inactivation. Based on these findings, we discussed the limitations of supported catalysts and explored strategies to overcome these challenged in developing optimal candidates for water remediation under realistic conditions.

Finally, the two elements, Ti and Fe, were combined to form a new magnetic $TiO_2$ catalyst, produced via a simple one-pot method. This catalyst leverages the excellent photocatalytic properties of $TiO_2$ under UVA irradiation and the magnetic behaviour of iron, which also acts as an electron acceptor, reducing electron-hole recombination. This role is typically fulfilled by noble metals, which are expensive and have limited availability. The combination of these two features produces an effective catalyst for organic reactions. The model reaction chosen was the oxidative coupling of benzyl alcohol and nitrobenzene to synthesize Schiff bases. This reaction produces industrially relevant molecules, especially in the synthesis of pharmaceuticals. Our catalyst demonstrated impressive Schiff base formation rates of about 6.8 mmol/h, approximately ten times higher than those reported in the literature. Additionally, the catalyst can be magnetically removed, facilitating its removal after the reaction.

# Acknowledgements

First and foremost, I want to thank God for making this possible and providing me with the protection and guidance needed to complete this research successfully. I would like to express my deep gratitude to my supervisor, Prof. Juan C. Scaiano, for allowing me to be part of your group and for your patience, understanding, and encouragement. Your passion for science and dedication to teaching and mentoring have been truly inspiring. I am forever grateful for the opportunity you have given me, not only to learn chemistry but also to become a better professional. Your kind heart and exemplary leadership are reflected in your incredibly successful group and have influenced me to aspire to be a supportive co-worker and mentor.

I also want to extend my heartfelt thanks to all the members of the Scaiano group. It is incredible how people from so many backgrounds come together to create a welcoming and supportive environment. I am truly grateful to work with individuals who encourage me to express myself and cheer for my success. A personal thank you to Drs. Anabel Lanterna, Bowen Wang, and Ayda Elhage, were fundamental in my first years by teaching me, a young biologist, how to navigate chemistry research. Their expertise and dedication continue to inspire me. A special thank you to Dr. Rodolfo Texeira, who visited our group during my first year of graduate school. His patience and passion for chemistry were indispensable to my understanding of photochemistry. Rodolfo also became a cherished friend whose company and conversations I greatly miss. I would also like to thank Dr. Neeraj Joshi, a great scientist who is always willing and available to help and teach us. His constant smile and great humour make even the hardest days enjoyable. Lastly, a special thank you to Dr. Yun Liu, who not only dedicated herself to helping me run and understand the electron microscope but also became a trusted advisor and confidant.

I would like to extend a very special thank you to Mahzad, Melissa, and Saba, who have become more than colleagues—they are dear friends who were instrumental in my PhD journey. Their expertise and patience helped me overcome numerous challenges. Their support and friendship were fundamental for my endurance through these years. I am profoundly grateful to

have had such incredible people by my side, cheering for me and always willing to drop everything to help.

I would also like to thank all my friends and family for their constant understanding and support. I am fortunate to be surrounded by people who embrace life with a light-hearted spirit, making every moment enjoyable. A special thank you to the friends Canada has given me, Louise, Gustavo, Lais, Nathalia, Hugo and Nayara. Together, we created a supportive network, celebrating together, consoling each other, and never leaving me alone during the toughest times of my adaptation to Canada. I am deeply grateful to my family in Canada, Luana and Raphael who welcomed me into their lives and their home. They were my pillars, ensuring I never gave up. Luana and Raphael, always cared for me, even cooking meals to ensure I was okay.

My biggest thanks go to my family. None of this would be possible without your unconditional support. I am deeply grateful to my loving and understanding parents, who have always accepted and encouraged me in all my dreams. Your efforts to prioritize my education, even at the expense of your own needs, have allowed me to reach the places I wanted to be. Growing up in such a nurturing environment has profoundly shaped me both personally and professionally, and I will always carry this with me. I would also like to thank my brothers, Lucas and Andre, who are my best friends. Despite the physical distance between us, I know I can always count on you to listen, help, and cheer me up.

Lastly, a huge thank you to my love and partner, Raynald, who has embraced and shared every moment of this journey with me. Your support has been invaluable, navigating through all the challenges, pushing me forward, listening to me and celebrating the great moments together. I do not think I could have done it without you. Thank you for being my official proofreader and the toughest reviewer.

# Contribution Statement

This dissertation is based on three peer-reviewed publications, and one publication currently being prepared for submission. I am the leading author or one of the leading authors in all of the publications that will be presented. Additionally, I was directly involved in other research that led to publications where I was not the first author. These are listed in the List of Publications section. Although those works will not be discussed in detail in this thesis, the technical and theoretical knowledge I gained from the experiments conducted and the discussions with my collaborators were crucial to the execution of the research presented here. In this section, I will clarify my direct contributions to the works presented in each chapter of this dissertation and highlight the intellectual and physical contributions made by each of my collaborators.

All the research presented in this thesis was conducted under the supervision of Dr. Scaiano. His mentorship, creativity, and support were fundamental to the execution of this work. Dr. Scaiano directly assisted me with research ideas, experimental design, and data interpretation. Dr. Anabel Lanterna, a former research associate in our group, was also directly involved in helping me, special during my first years. She assisted me with the adaption to the chemistry laboratory, teaching me techniques assisting with data analysis, and visualization, and giving valuable feedback.

In the second chapter, I discuss the synthesis of magnetic NPs, Dr. Scaiano and I were the two authors of this work. I conducted the experimental research and discussed the results with Dr. Scaiano who via our regular meetings gave valuable feedback for the development of the project.

Chapter 3 will describe the fabrication of three fibrous $TiO_2$ materials. The first material, $TiO_2$ nanofibres were fabricated during my time at Rhodes University, South Africa. There, I was welcomed into Dr. Nyokong's group and had the opportunity to learn about electrospinning. I was mentored by Dr. Nyokong and Dr. Mapukata, who assisted me with training and adjusting the methodology. Dr. Mapukata also worked on optimizing the fabrication process and the material characterization. The techniques used for nanofibres' synthesis helped me develop a new material, $TiO_2$@Glass filters, which were fabricated with the support of Sara Curie. Utilizing similar

precursors and calcination methods, Sara developed the glass-filter-supported $TiO_2$, a material that is also being tested as black $TiO_2$ in other projects within our group. By exploring similar synthetic routes, I was able to fabricate the $TiO_2$@GW and conduct the characterization of all materials. Additionally, I also performed all the degradation experiments and developed the bench-scale flow system, described in this chapter.

Chapter 4 expands on the work with fibrous $TiO_2$, which I conceptualized based on the results observed in the antibacterial studies. During the final term of my Ph.D. studies, I was fortunate to receive the help and guidance of Dr. Silvero, a post-doctorate fellow in our group. Dr. Silvero helped me understand the microbiological interactions with the catalyst and developed and executed experiments. This work was also made possible due to the support of Dr. Joshi, whose expertise with the fluorescence lifetime microscope was essential for setting up the instrument, training me, and assisting with the data analysis.

Lastly, chapter 5 describes work done in collaboration with Melissa J. Cely, a Ph.D. candidate in our group. For this work, I synthesized and characterized the magnetic $TiO_2$ ($Fe_3O_4$@$TiO_2$), based on the techniques developed in the previous chapters. Meanwhile, Melissa synthesized the other metal-based catalysts, Pd@$TiO_2$ and Cu@$TiO_2$. Melissa had been actively involved in photocatalysis for organic reactions, and her expertise on the topic was essential to developing the protocols, executing experiments and analyzing the data. Together, we conducted the chemical reactions, analyzed the results and wrote the manuscript, thus so, that we shared the first authorship of this work

# List of Publications

### Publications Presented in this Thesis

da Silva, D. R. C. & Scaiano, J. C. Exploring the Antibacterial Properties of Lignin-coated Magnetic Nanoparticles Synthesized in a One-pot Process. Photochem. and Photobiol. 2023, 99(2), 706-715.

da Silva, D. R. C., Mapukata, S., Currie, S., Kitos, A. A., Lanterna, A. E., Nyokong, T. & Scaiano, J.C. Fibrous $TiO_2$ alternatives for semiconductor-based catalysts for photocatalytic water remediation involving organic contaminants. ACS omega. 2023 8(24), 21585-21593.

da Silva, D. R. C., Cely-Pinto, M. & Scaiano, J. C. Color-Coordinated Photocatalysis of the One-Pot Synthesis of Schiff Bases from Benzyl Alcohol and Nitro Compounds Using a Hybrid Magnetic Catalyst. Catalysts. 2024, 14(9), 612.

### Co-Authored Publications Not Discussed in this Thesis

Bourgonje, C. R., da Silva, D. R., McIlroy, E., Calvert, N. D., Shuhendler, A. J., & Scaiano, J. C. Silver nanoparticles with exceptional near-infrared absorbance for photoenhanced antimicrobial applications. Journal of Materials Chemistry B. 2023, 11(26), 6114-6122.

Yaghmaei, M., da Silva, D. R. C., Rutajoga, N., Currie, S., Li, Y., Vallieres, M., Silvero, M. J., Joshi, N., Wang, B. & Scaiano, J. C. Innovative Black $TiO_2$ Photocatalyst for Effective Water Remediation Under Visible Light Illumination Using Flow Systems. Catalysts. 2024 14(11), 775.

# Table of Contents

**Abstract** ..... **iii**
**Acknowledgements** ..... **v**
**Contribution Statement** ..... **vii**
**List of Publications** ..... **ix**
**Table of Contents** ..... **x**
**List of Figures** ..... **xii**
**List of Schemes** ..... **xxii**
**List of Tables** ..... **xxiii**
**List of Abbreviations** ..... **xxvii**

**1. Introduction** ..... **1**
1.1 Open remarks ..... 1
1.2 Nanomaterials ..... 1
1.3 Synthesis of Nanomaterials ..... 5
1.4 Applications of Nanomaterials ..... 9
1.5 Choice of elements ..... 15
1.6 Objectives ..... 25
1.7 References ..... 26

**2. Exploring The Antibacterial Properties of Lignin-Coated Magnetic Nanoparticles Synthesized in a One-Pot Process** ..... **36**
2.1 Preamble to Chapter 2 ..... 36
2.2 Post-print version of Manuscript ..... 37
2.3 Post-print Version of Supporting Information ..... 65
2.4 Accompaniment to Chapter 2 ..... 73

**3. Fibrous $TiO_2$ Alternatives for Semiconductor-Based Catalysts for Photocatalytic Water Remediation Involving Organic Contaminants** ..... **74**
3.1 Preamble to Chapter 3 ..... 74
3.2 Post-print version of Manuscript ..... 75

3.3 Post-print Version of Supporting Information ..... 99
3.4 Accompaniment to Chapter 3 ..... 116

**4. Investigating the Antibacterial Performance of Supported $TiO_2$ on Glass Wool Fibres: Challenges and Optimization Strategies ..... 117**
4.1 Preamble to Chapter 4 ..... 117
4.2 Pre-submission Version of Manuscript ..... 118
4.3 Pre-submission Version of Supporting Information ..... 147
4.4 Accompanied Chapter 4 ..... 157

**5. Magnetic catalyst for efficient One-Pot Synthesis of Schiff Bases from Benzyl Alcohol and Nitro Compounds under UV irradiation ..... 158**
5.1 Preamble to Chapter 5 ..... 158
5.2 Submitted Manuscript ..... 159
5.3 Submitted Version of Supporting Information ..... 185
5.4 Accompanied Chapter 5 ..... 197

**6. Conclusions and Future Directions ..... 198**
6.1 Further analysis and Future directions ..... 198
6.2 Conclusions ..... 205
6.3 References ..... 208

**A: Appendix ..... 209**
A.1 -Statistical Analysis of data presented in Chapter 2 ..... 209
A.2 -Statistical Analysis of data presented in Chapter 4 ..... 220
A.2.2 References ..... 222
A.3 -Journal Permissions ..... 222
A.3 Journal permissions ..... 223

# List of Figures

**Figure 1.2.1.** Illustration of the electronic structure of a semiconductor, showing the valance band (VB) and the conduction band (CB), separated by the band gap (Bg). Recombination events are shown as dashed lines. When in the surface the electrons ($e^-$) can be transferred to electron acceptors (A), which are reduced. Holes ($h^+$) receive electrons from electron donors (D), which become oxidized. ..... **3**

**Figure 1.2.2.** Illustration of the electronic structure of a semiconductor, showing the valance band (VB) and the conduction band (CB), separated by the band gap (Bg). Recombination events are shown as dashed lines. When in the surface the electrons ($e^-$) can be transferred to electron acceptors (A), which are reduced. Holes ($h^+$) receive electrons from electron donors (D), which become oxidized. ..... **4**

**Figure 1.3.1.** Representations of nanoparticle formation via chemical reduction. On top, a plot of the La Mer model for the generation of atoms (A), nucleation (B) and growth (C). On the bottom is an illustrative diagram of particle formation according to the steps described by the La Mer model. M0 atoms are represented by the orange circles ..... **6**

**Figure 1.3.2.** Schematic illustration of the electrospinning setup. A syringe is loaded with a polymer solution and attached to a syringe pump. An electric field is generated between the needle and the metallic collector, by an external power supply. Under the electric current, the polymer is ejected forming the Taylor cone, which is elongated, forming long fibres. The produced nanofibres are accumulated in the collector ..... **8**

**Figure 1.4.1.** Diagram demonstrating the potential bactericidal effects of metallic NPs. Once in contact with the cells, NPs can directly interact with bacterial membranes increasing permeability and causing membrane dysfunction. Inside the cell, they can trigger oxidative stress *via* ROS production, disrupting cellular functions and damaging DNA and RNA, culminating in cell death. Image adapted from reference,[79] under the Creative Commons license (CC-BY 4.0) ..... **12**

**Figure 1.4.2** Diagram of the potential photocatalytic degradation routes of pollutants using semiconductors nanomaterials. Upon light excitation, excited electrons are generated, and they can be transferred to adsorbed pollutants producing reduced compounds. Electrons can also be transferred to other electron donors, in this example, $O_2$ is reduced producing superoxide anion ($O^{-\bullet}$). The excited $e^-$ leaves behind a positively charged hole that oxidizes adsorbed molecules, such as pollutants or other electron donors, like water, producing hydroxyl radicals ($^\bullet OH$) and a proton. The produced radicals $O^{-\bullet}$ and $^\bullet OH$, can also react with the pollutants. Bg: Bandgap; $e^-$: electron; $h^+$: hole; VB: valence band; CB: conduction band. ..... **15**

**Figure 1.5.1.** Periodic table representing the critically of 62 metals according to (A) supply risk, (B) environmental implications, and (C) vulnerability to supply restriction. Adapted from reference[101] with permission from Proceedings of the National Academy of Sciences (PNAS) ..... **17**

**Figure 1.5.2.** Crystal structure of (A) magnetite ($Fe_3O_4$), and (B) maghemite ($\gamma$-$Fe_2O_3$). In magnetite, $Fe^{2+}$ ions (green spheres) occupy the tetrahedral interstices, each bound to four $O^{2-}$ ions (orange spheres). $Fe^{3+}$ ions (blue spheres) occupy the octahedral positions, each bound to six $O^{2-}$ ions. In maghemite, $Fe^{3+}$ ions (blue spheres) can be surrounded by either six or four $O^{2-}$ ions. Crystal structures were drawn with the VESTA software,[101] using data from the Materials Project for $Fe_2O_3$ (mp-565814) and for $Fe_3O_4$ (mp-19306) from database version v2023.11.1.[119] ..... **19**

**Figure 1.5.3.** Diagram illustrating the transition of the magnetic states with changes in particle diameter. Bulk ferromagnetic materials consist of a multi-domains structure, which transition to single domain and eventually to a superparamagnetic as the particle diameter decreases. From top to bottom, the behaviour of particles under an external magnetic field (with strength H) is shown. Ferromagnetic materials retain their magnetization even after the magnetic field is removed (H=0, bottom), while superparamagnetic materials lose magnetization. Green arrows represent particles with mass and electronic charges. ..... **20**

**Figure 1.5.4.** Representation of the crystal structure of anatase (A), brookite (B) and rutile (C) $TiO_2$. $TiO_6$ octahedra are represented by purple and yellow octahedra. Red spheres represent $O2^-$ ions. The highlighted yellow octahedra show 4 edge sharing forming zig-zag chains in anatase (A), the edge and corner sharing in brookite (B) and the edge sharing along the c-axis, interlinked by corner sharing in rutile (B). Image reproduced with permission from reference[112] Copyright 2010, Elsevier..... **23**

**Figure 1.5.5.** Representative TEM image of commercial P25 nanoparticles. Scale Bar = 50 nm. ..... **24**

**Figure 2.2.1** XRD patterns for the MNPs LFe (A), LFeAg (B), LFeCo (C) and LCo (D). Crystalline structures were analyzed from the XRD diffractograms and compared with the existing profiles on the ICDD database. LFe: $Fe_3O_4$ (PDF 04-013-9808 - red), LFeAg: Ag (PDF 04-014-0266 - blue) and $Fe_3O_4$ (PDF04-008-8145 - red), LCo: $Co_3O_4$ (PDF 04-015-4721 - red) and CoOH (PDF 04-005-7243 - blue), and LFeCo: $Fe_2O_3$ (PDF 01-072-6226 - blue) and $CoFe_2O_4$ (PDF 04-022-3956 - blue). ..... **45**

**Figure 2.2.2** Representative TEM images for the synthesized magnetic nanoparticles: (A) LFe, (B) LFeAg, (C) LFeCo and (D) LCo. Scale bars: 50 nm. (E) Photographs showing the magnetic behaviour of the MNPs in the presence of an external magnetic field..... **47**

**Figure 2.2.3** Diffuse Reflectance spectra (arbitrary but comparable units) of the MNP measured at room temperature between 300-1200 nm: LFe (red), LFeAg (blue), LCo (black) and LFeCo (green). ..... **49**

**Figure 2.2.4** $Log_{10}$ reduction of (A) *E. coli* (B) *S. aureus*, after treatment with MNPs or lignin A alone (31.5-1000 mg/L) for 16 h in 50 % LB at 37°C and 140 rpm, under dark. Cell growth was determined by the plate counting method and log reduction was obtained by comparing bacterial growth in presence of nanoparticles to a control incubated without the NPs. Error bars represent standard deviations of the log reduction, n=5. (*$p < 0.05$, **$p < 0.01$, ***$p < 0.001$). ..... **50**

**Figure 2.2.5** Temperature changes over time of aqueous solutions of MNPs (125 mg/mL) after irradiation with 810 nm LED (0.99 W/cm$^2$). Temperature was measured with an IR thermometer every 5 min. The control sample (green) was pure water. ..... **52**

**Figure 2.2.6** Bactericidal activity against *E.coli* (A) and *S. aureus* (B) after treatment with MNPs (125 mg/L) alone ( LFe, LFeAg, LCo, and LFeCo) and with MNP and NIR (810 nm - 0.99 W/cm$^2$) irradiation (LFe + NIR, LFeAg + NIR, LCo + NIR, and LFeCo + NIR). Treatment was done 1, 5, 15 and 30 min, and cell growth was determined by the plate counting method. And log reduction was compared to the initial bacterial inoculum. Error bars represent standard deviations of the log reduction, n=3. (*p < 0.05, **p < 0.01, ***p < 0.001)..... **53**

**Figure 2.2.7** (A) Oxidation of TMB (1 mM) in the presence of the MNPs (125 mg/L) or Lignin A and 0.1 mM of $H_2O_2$, after 20 min of reaction in PBS. In the inset, images of TMB solutions before and after reaction with MNPs. Bactericidal activity against *E. coli* (A) and *S. aureus* (B) after treatment with MNPs (125 mg/L) and 0.1 mM of $H_2O_2$ (LFe, LFeAg, LCo, and LFeCo). And in the presence of the MNP, $H_2O_2$ and NIR irradiation (810 nm) (LFe + NIR, LFeAg + NIR, LCo + NIR, and LFeCo + NIR). Treatments were done for up to 30 min. Bacterial viability was determined by the plate counting method and log reduction was determined by comparing the cell viability to initial bacterial inoculum. Error bars represent standard deviations of the log reduction, n=3. (*p < 0.05, **p < 0.01, ***p < 0.001). ..... **56**

**Figure 2.2.8** Cell viability of human fibroblasts (HT1080) measurements was carried out using the MTT colorimetric assay. Cells were treated with 125 mg/L of the nanocomposites, and 0.1 mM of $H_2O_2$ in the presence (red) and absence (black) of NIR (810 nm - 0.99 W/cm$^2$) irradiation for 5 min. Nanocomposites were removed with an external magnet and cells were incubated for 24 h before viability tests. Error bars represent standard deviations, n=3. (*p < 0.05) ..... **58**

**Figure 2.3.1** Representative TEM images comparing LFeAg NPs synthesized using different initial concentrations of lignin A: 10 mg/L (left) and 1 mg/L (right). Prior to the imaging, the NPs were dispersed on EtOH and sonicated for 30 min. 20 µL of the ethanolic MNPs solution was dropped on the copper side of TEM grids and air dried overnight before being inserted on a JEM2100F FETEM (JEOL) instrument. Scale bars: 50 nm. ..... **65**

**Figure 2.3.2** Size distribution of the MNPs: LFe (a), LFeAg (b), LCo (c), and LFeCo (d). Particle sizes were obtained using their TEM images. The measurements were estimated from the largest diameter of a minimum of 300 individual particles. ..... **66**

**Figure 2.3.3** Thermogravimetric analysis (TGA) graphs of the MNPs, evaluating the lignin content of LFe (a), LFeAg (b), LCo (c), and LFeCo (d). 10 mg of each sample was loaded into a Q5000 IR instrument under $N_2$ or airflow (120 mL/min) and the weight changed as the function of temperature was measured between 25-850°C with a heating rate of 10 °C/min. ..... **67**

**Figure 2.3.4** Log reduction of *E. coli* incubated at higher temperatures. The Initial bacterial solution at 0.1$OD_{600\ was}$ incubated at 45°C for 1, 5, 15, 30, and 60 min. Log reduction was calculated relative to the number of viable cells before the experiment (CFU/mL). Error bars indicate means ± standard deviations (n=3). ..... **68**

**Figure 2.3.5** Hydroxyl radicals detection using coumarin as a standard probe. Presence of the hydroxylated product, 7-hydroxycoumarin was detected by following the fluorescence at 454 nm (ex 340 nm). On the left, the fluorescence of 7HC, at 454 nm, after incubation with 125 mg/L of MNP and 0.1 mM of $H_2O_2$, in dark and under NIR irradiation (810 nm) for 1, 5, 15 and 30 min. On the right, fluorescence at 454 nm after incubation with 125 mg/L of MNP with and without $H_2O_2$ (0.1 mM) for 30 min in dark and under NIR irradiation (light) (810 nm) .....**69**

**Figure 2.3.6** The cumulative released amount of ions (iron, silver and cobalt) from the MNP solutions (125 mg/L) after 30 min irradiation with 810 nm LEDi (0.99 W/cm$^2$) (light) or after incubation in the dark for 30 min (dark). Ions in solution were measured using ICP-OES following the Fe, Ag and Co emissions line at 238.20 nm, 338.29 nm, and 238.89 nm respectively. Amounts of released ions are expressed in parts per million (ppm). .....**71**

**Figure 2.3.7** Cell viability of human fibroblasts (HT1080) treated with 125 mg/L of Lignin@FeCo (LFeCo) and uncapped FeCo nanocomposites in the presence (red) and absence (black) of NIR (810 nm - 0.99 W/cm$^2$) irradiation for 5 min. Nanocomposites were removed with an external magnet and cells were incubated for 24 h prior to viability tests. For cell viability, MTT (0.5 mg/mL) reagent was added to the treated cells. After 2h incubation, the produced formazan crystals were dissolved in DMSO, and the absorbance was measured at 590 nm. The viability percentage was calculated by comparing absorbances of treated cells to untreated controls incubated in the dark. Error bars represent standard deviation. .....**72**

**Figure 3.2.1.** Representative SEM images of fibrous $TiO_2$: (A) $TiO_2$ nanofibres (TNF), (B) $TiO_2$ Deposited on a glass wool fibre (TGW), and (C) $TiO_2$ deposited on glass filter fibre (TGF). All the SEM images were taken after materials calcination at 500 °C. Scalebar: 10µm .....**84**

**Figure 3.2.2.** (A) XRD diffractogram of the produced fibrous materials: $TiO_2$ NF (red) $TiO_2$@GF (blue) and $TiO_2$@GW (black) and the PDF card 01-073-1764 pattern for anatase $TiO_2$. (B) Normalized diffuse reflectance of the fibrous $TiO_2$ materials (solid line) and emission of the black light used in the experiments (dashed line). Tauc plots are shown in Figure 3.3.8. .....**85**

**Figure 3.2.3.** A) Crocin bleaching rates, in the dark (black) and un-der irradiation using a black light (red), in the presence of the fibrous $TiO_2$-rich materials. Crocin remaining based on the absorbance at 440 nm over time. B) Decay of crocin absorption as a function of time in the presence of the fibrous $TiO_2$-rich mate-rials. Insert: slope ratio and the difference between dark and light treatment for the three fibrous catalysts. Slopes (rates) are based on the last 3 points (black heavy line) before turning on the 400 nm light and the three points immediately after the lights are turned on (red heavy line). All rates in units of $10^{-6}$ min$^{-1}$. .....**87**

**Figure 3.2.4.** Reusability test results of the 5 cycles of crocin bleaching, followed at 440 nm. Experiments run in batch with an initial dye concentration of 8.1 µM, and under UVA irradiation (18 W/m$^2$). .....**90**

**Figure 3.2.5.** Crocin bleaching (%) using TGW (black), TGF (blue) or TNF (red) in a continuous flow system. The initial dye concentration was 8.1 µM in water and under Blacklight irradiation (λ=400 nm) (18 W/m$^2$). Bleaching is calculated based on the absorbance on the decrease at the absorbance at 440 nm .....**91**

**Figure 3.2.6.** Radar plot of the fibrous catalysts for a relative comparison according to their physical features and chemical activity. The $TiO_2$-rich catalysts were ranked from 1 to 3 in the five categories, based on the results from this contribution. ..... **93**

**Figure 3.3.1**. Photographs of the fibrous $TiO_2$ materials. (a) $TiO_2$ nanofibres (TNF), (b) $TiO_2$@Glass wool (TGW), and (c) $TiO_2$@Glass filter (TGF). ..... **100**

**Figure 3.3.2.** Close-up photographs of Glass wool alone, before the deposition of $TiO_2$ (left) and Glass wool after the deposition of $TiO_2$ (right)..... **101**

**Figure 3.3.3.** Representative SEM images of (a) the electrospun $TiO_2$/PVP nanofibres before calcination, (b) commercial glass wool fibres and (c) commercial glass fibres filter before pre-treatment and addition of $TiO_2$ precursors..... **102**

**Figure 3.3.4.** EDS mapping of TGW. SEM image used for the analysis (a) and elemental mapping showing Ti (b) and Si (c) distribution on TGW. EDS mapping overlap of Ti and Si components (d). ..... **103**

**Figure 3.3.5** EDS mapping of TGF. SEM image used for the analysis (a) and elemental mapping showing Ti (b) and Si (c) distribution on TGF. EDS mapping overlap of Ti and Si components (d). ..... **104**

**Figure 3.3.6.** EDS mapping of TNF. SEM image used for the analysis (a) and elemental mapping showing Titanium (b) and Silica (c) and Oxygen (d)..... **105**

**Figure 3.3.7.** ATR FTIR spectra of the three fibrous materials (TNF, TGF and TGW) and their supports, glass filter (GF) and glass wool (GW). Solid samples were dried under vacuum before the measurements. Notice the presence of the Ti-O and Si-O signals, with the latter missing for TNF as expected. ..... **106**

**Figure 3.3.8.** Tauc plots showing the determination of the band gaps for the three materials studied. The plots are based on the diffuse reflectance data shown in Figure 3.2.2B. ..... **107**

**Figure 3.3.9.** Decay of crocin absorbance as a function of time when irradiated with black light ($\lambda \sim 400$ nm, 18 W/m$^2$ for the single LED used) for 180 min (red). The dark control experiment is shown in black. Error bars show the estimated error of 2%. Crocin concentration used was 8.1 μM in water and the change in absorbance was measured using absorption maxima at 440 nm. ..... **108**

**Figure 3.3.10.** Decay of crocin absorbance as a function of time when incubated with the glass support catalyst used in this work: glass wool (GW) and glass filter (GF), under irradiation with black light (L) for 180 min or under dark for the same time (D). Crocin concentration used was 8.1 μM in water and the change in absorbance was measured using absorption maxima at 440 nm. Light source used had maximum emission at 400 nm, 18 W/m$^2$ for the single LED used. ..... **109**

**Figure 3.3.11**. Photographs of TGF after 3 h dark incubation inside an aqueous crocin solution (8.1 μM) (left), and the same TGF piece after exposure to black light (UVA/Visible) illumination for 3 h (right). ..... **110**

**Figure 3.3.12.** Hydroxyl radical production was evaluated using coumarin probe. Coumarin is oxidized to 7-hydroxyl coumarin in the presence of •OH, the product has strong fluorescence at 454 nm when excited at 332 nm. Graphs

show the fluorescence spectra of aqueous solutions of coumarin irradiated in the presence of TNF (a), TGW (b) or TGF (c) for 1, 2 and 3 hours. ..... **111**

**Figure 3.3.13.** Crocin bleaching using the three fibrous $TiO_2$ catalysts, TNF, TGW and TGF under an inert atmosphere, $N_2$ (black) and under air (red). Samples were irradiated for 3 hours with a black light ($\lambda \sim 400$ nm, 18 W/m$^2$ for the single LED). Crocin concentration used was 8.1 μM in water and the change in absorbance was measured using maximum absorbance at 440 nm. ..... **112**

**Figure 3.3.14** Photoluminescence spectroscopy of the photocatalysts and supports excited at 300 nm. Analysis was carried out using a Perkin-Elmer LS-50 luminescence spectrometer, and fluorescence spectra were recorded between 320 and 580 nm using a front-face attachment. APTES- Glass wool (black), Glass wool (purple), Glass filter (blue), $TiO_2$@ Glass wool (green), $TiO_2$ P25 nanoparticles (orange) and $TiO_2$ nanofibres (red) ..... **113**

**Figure 3.3.15** Diffuse reflectance of the three fibrous materials after crocin adsorption under dark for three hours (solid lines). Dashed line: UV-vis spectra of an aqueous solution of crocin (8.1 μM). ..... **114**

**Figure 3.3.16** HPLC-DAD analysis of an aqueous s solution of crocin 1 mM at 440 nm of the initial solution (black) and after degradation with TGW (red), The conjugated structure of crocin allows for several isomers that can be seen in peaks 1-5. The UV-vis spectra of those peaks are present in the insert, showing the similarity of the peaks. HPLC was done using a C18 column, and a mixture of acetonitrile and water as the mobile phase. .... **115**

**Figure 4.2.1** Log reduction of *E.coli* bacterial count after incubation with 10 mg/mL APTES-Glass wool (GW) and $TiO_2$ deposited on glass wool (TGW), in the absence of light (dark) and irradiated with four UVA bulbs (8 W each) (Light) for 24 hours. Control light was measured in a bacterial solution exposed to the same light source but without a catalyst. Log reduction was calculated based on the bacterial count of a control incubated protected from the light. Error bars represent standard deviation. (*$p < 0.05$, **$p < 0.001$, ***$p = 0.00$). ..... **124**

**Figure 4.2.2** (A) Hydroxyl radical detection using coumarin as a standard probe. The presence of the hydroxylated product, 7-hydroxycoumarin was detected by measuring the fluorescence at 454 nm (ex: 340 nm). Coumarin solution (0.25 mmol in 5 % LB) was irradiated with UVA light for 1, 3, 6 and 24 hours, without catalyst (Control+Light), with 10 mg/mL APTES Treated Glass wool (GW+Light), and with 10 mg/mL of $TiO_2$+GW in presence and absence of light (TGW+Light) and TGW Dark. (B) Fluorescence emission spectra of coumarin solution in LB 5% (pH 3.0) (red) and in dH2O (grey), both samples were irradiated with UVA light irradiation for three hours with 10 mg/mL of TGW ..... **129**

**Figure 4.2.3** Log reduction of *E. coli* bacterial count after incubation with 10 mg/mL APTES-Glass Wool (GW) (red) and $TiO_2$-deposited Glass Wool (TGW) (grey) under UVA irradiation for 3 hours. Agitation samples were mixed using a circular rotator for the full duration of irradiation. Sonicating samples were irradiated under static conditions and sonicated for three minutes before plating. Log reduction was calculated based on the bacterial count of a control incubated in the absence of light for the same duration. Error bars represent the standard deviation. * $p<0.05$ ..... **131**

**Figure 4.2.4.** Characteristic Fluorescence lifetime images (FLIM) of *E. coli* cells stained with SYTO9 after 3 hours incubation. The images depict E. coli cells in 5 % LB in PBS, either untreated or treated, after three hours in the dark or irradiated with UVA light. Treated samples were incubated with either 10 mg/mL of APTES glass wool or $TiO_2$@glass wool (TGW). Different colours represent various lifetimes of the dye, excited at 485 nm. The colour bar scale ranges from 0.8 to 3 ns. The brightness of the images was enhanced by 20% to ensure all FLIM data is clearly visible. ..... **134**

**Figure 4.2.5** Characteristic Fluorescence lifetime images (FLIM) of *E. coli* cells stained with SYTO9 after 24 hours of incubation. The images depict *E. coli* cells in 5 % LB in PBS, either untreated or treated, after 24 hours in the dark or irradiated with UVA light. Treated samples were incubated with either 10 mg/mL of APTES glass wool or $TiO_2$@glass wool (TGW). Different colours represent various lifetimes of the dye, excited at 485 nm. The colour bar scale ranges from 0.8 to 3 ns. The brightness of the images was enhanced by 20% to ensure all FLIM data is clearly visible. ..... **135**

**Figure 4.2.6.** Histograms of fluorescence lifetime distribution on control samples (A) and on samples treated with 10 mg/mL of TGW. In grey are samples incubated and protected from light and in red samples irradiated with UVA light (370 nm). Bacteria concentration was set to $OD_{600}$=0.1 in 5% LB. ..... **136**

**Figure 4.3.1** Viable *E. coli* cells count for the control sample (dark control) incubated under the same conditions of the treatments but without catalyst and protected from light. The initial bacterial inoculum was $1x10^6$ CFU/mL in 5 % LB in PBS. Viables were incubated without agitation at room temperature, but due to the light exposure, the ambient temperature close to the light source was 34 °C after 24 hours. Viable cells were determined by plate counting colony forming units (CFU) and results were expressed as CFU/mL. Those viable bacterial counts were utilized to calculate log reduction for the treatment samples ..... **147**

**Figure 4.3.2.** Emission spectra of the UVA bulb used in this work. Irradiance was measured after light was passed through the glass vial containing LB 5 % without glass wool (grey) and with 10 mg/mL of GW (red). ..... **148**

**Figure 4.3.3** Fluorescence emission spectra of a 025 mmol solution of coumarin in LB 5% (pH 3.0) before (grey) and after UVA irradiation for 24 hours with 10 mg/mL of $TiO_2$@glasswool (Red) and APTES-Treated glass wool (purple). The peak at 454 nm (ex: 340 nm) is indicative of the formation of 7-hydroxycoumarin (7-HC). .... **149**

**Figure 4.3.4** Histograms of fluorescence lifetime distribution on samples containing Live *E. coli* (Green) and dead bacteria (red). Bacteria concentration was set to $OD_{600}$=0.1 in 5% LB. Dead cells were obtained by heating the bacterial solution, and the absence of viable bacteria was confirmed via plate counting. ..... **150**

**Figure 4.3.5** Average TSCPC curves for samples containing live E. coli (green) and dead bacteria (red), and the Instrument response function (IRF) (black). Bacteria concentration was set to $OD_{600}$=0.1 in 5% LB. Dead cells were obtained by heating the bacterial solution, and the absence of viable bacteria was confirmed via plate counting. ..... **151**

**Figure 4.3.6** Example of FLIM images of samples containing live (A) and dead (B) E. coli cells. Bacteria concentration was set to $OD_{600}$=0.1 in 5% LB. Dead cells were obtained by heating the bacterial solution, and

the absence of viable bacteria confirmed via plate counting. Different colours represent various lifetimes of the dye, excited at 485 nm. The colour bar scale ranges from 0.8 to 3 ns. The brightness of the images was enhanced by 20% to ensure all FLIM data is clearly visible.....**152**

**Figure 4.3.7** Representative images of $TiO_2$@GW in 5% LB without SYTO9. (A) White light microscope and (B) Fluorescence lifetime image (ex: 485 nm). Different colours represent various lifetimes of the dye, excited at 485 nm. The colour bar scale ranges from 0.8 to 3 ns. The brightness of the images was enhanced by 20% to ensure all FLIM data is clearly visible. .....**155**

**Figure 4.3.8** Representative FLIM image of $TiO_2$@GW sample irradiated with UVA light for 24 hours. Yellow arrows show lifetimes shorter than the ones for live cells on the catalyst surface. Initial *E.coli* concentration was set at $10^6$ CFU/mL in 5% LB in PBS. Different colours represent various lifetimes of the dye, excited at 485 nm. The colour bar scale ranges from 0.8 to 3 ns. The brightness of the images was enhanced by 20% to ensure all FLIM data is clearly visible.....**156**

**Figure 5.2.1.** Representative TEM images of $TiO_2$ (A), Pd@TiO2 (B), $Fe_3O_4$@$TiO_2$ (C) and Cu@$TiO_2$ (D). Red arrows indicate representative Pd and Cu nanoparticles on P25. Scale bar: 20 nm .....**166**

**Figure 5.2.2.** XRD patterns of the catalysts used: $TiO_2$ (P25) (black), Pd@$TiO_2$ (green), Fe@$TiO_2$ (red) and Cu@$TiO_2$ (blue). Numbers in parenthesis correspond to the characteristic (h k l) interplanar planes for each crystalline phase. A: anatase $TiO_2$ and R: rutile $TiO_2$ .....**168**

**Figure 5.2.3.** Chromatograms showing the peaks obtained after performing the reaction with nitrobenzene 0.1 M in benzyl alcohol and 10 mg of $Fe_3O_4$@$TiO_2$. 5 mL of solution was irradiated for 3h under UVA irradiation and continuous stirring. Samples were taken every hour and filtered using a PTFE syringe filter. 3,5-Di-tert-butyltoluene was used as an external standard (peak at 10.84 min) The products have the following retention times: BenzA (5.17 min), 3-Benzylaniline (3-BA) (12.21 min), Schiff Base (15.10 min). The timed events feature of the local user interface was used (Turned off at 6.20 minutes and activated at 8.70 minutes) to prevent the risk of a high concentration of Benzyl Alcohol reaching the detector. .....**170**

**Figure 5.2.4.** Chromatograms showing the peaks obtained after performing the reaction with 3-nitroanisole 0.1 M in benzyl alcohol and 10 mg of $Fe_3O_4$@$TiO_2$. 5 mL of solution was irradiated for 3h under UVA irradiation and continuous stirring. Samples were taken every hour and filtered using a PTFE syringe filter. 3,5-Di-tert-butyltoluene was used as an external standard (peak at 10.84 min) The products have the following retention times: BenzA (5.17 min), *m*-anisidine (9.63 min), Schiff Base N-(4-Methoxybenzylidene)aniline (17.94 min). The timed events feature of the local user interface was used (Turned off at 6.20 minutes and activated at 8.70 minutes) to prevent the risk of a high concentration of Benzyl Alcohol reaching the detector. .....**172**

**Figure 5.2.5.** Photocatalytic performance for the selectively generated Schiff Base N-Benzylideneaniline in the coupled system of benzyl alcohol and nitrobenzene using different catalysts under UVA light irradiation for 1-3 h. Reaction conditions: benzyl alcohol (as the solvent, 5 mL), nitrobenzene (0.1 mmoles/L), M@$TiO_2$ (10 mg), under Argon, UVA light irradiation (λ= 370 nm). Schiff-base production was quantified using GC-MS. .....**173**

**Figure 5.2.6.** Plausible scenario to understand the activity shown by $Fe_3O_4$@$TiO_2$. Figure inspired by similar concepts in the literature.[15] .....**178**

**Figure 5.3.1.** Emission spectra of light sources used in this work. In Blue 1x450 nm LED, in red 1x370 nm LED (UVA at higher intensity) and in black 1x370 nm LED (UVA at Lower intensity). ND: neutral density filter. .....**185**

**Figure 5.3.2.** $Fe_3O_4$@$TiO_2$ after its synthesis next to a magnet to demonstrate its response to an external magnetic field. .....**186**

**Figure 5.3.3**. Diffuse Reflectance of the catalysts used in this study. .....**187**

**Figure 5.3.4**. Mass spectra of the products. Each spectrum shows (●) the molecular ion of the molecules. .....**188**

**Figure 5.3.5.** Chromatograms showing the peaks obtained after performing the reaction with nitrobenzene 0.1 M in benzyl alcohol and 10 mg of $TiO_2$. 3,5-Di-tert-butyltoluene was used as an external standard (peak at 10.84 min) The major products have the following retention times: BenzA (5.17 min), Schiff Base (15.10 min). The timed events feature of the local user interface was used (Turned off at 6.20 minutes and activated at 8.70 minutes) to prevent the risk of a high concentration of Benzyl Alcohol reaching the detector. .....**189**

**Figure 5.3.6.** Chromatograms showing the peaks obtained after performing the reaction with nitrobenzene 0.1 M in benzyl alcohol and 10 mg of Pd@$TiO_2$. 3,5-Di-tert-butyltoluene was used as an external standard (peak at 10.84 min) The major products have the following retention times: BenzA (5.17 min), Schiff Base (15.10 min). The timed events feature of the local user interface was used (Turned off at 6.20 minutes and activated at 8.70 minutes) to prevent the risk of a high concentration of Benzyl Alcohol reaching the detector. .....**190**

**Figure 5.3.7.** Chromatograms showing the peaks obtained after performing the reaction with nitrobenzene 0.1 M in benzyl alcohol and 10 mg of Cu@$TiO_2$. 3,5-Di-tert-butyltoluene was used as an external standard (peak at 10.84 min) The major products have the following retention times: BenzA (5.17 min), Schiff Base (15.10 min). The timed events feature of the local user interface was used (Turned off at 6.20 minutes and activated at 8.70 minutes) to prevent the risk of a high concentration of Benzyl Alcohol reaching the detector. .....**191**

**Figure 5.3.8.** Chromatogram showing the peaks obtained after 3 hours at 450 nm light irradiation. No peak for the Schiff base (15.10 min) was obtained after reacting with nitrobenzene 0.1 M in benzyl alcohol and 10 mg of $Fe_3O_4$@$TiO_2$. 3,5-Di-tert-butyltoluene was used as an external standard (peak at 10.84 min). The timed events feature of the local user interface was used (Turned off at 6.20 minutes and activated at 8.70 minutes) to prevent the risk of a high concentration of Benzyl Alcohol reaching the detector. .....**193**

**Figure 5.3.9**. A control Experiment without light irradiation Chromatogram showing no peak for the Schiff base (15.10 min) was obtained after reacting with nitrobenzene 0.1 M in benzyl alcohol and 10 mg of $Fe_3O_4$@$TiO_2$. 3,5-Di-tert-butyltoluene was used as an external standard (peak at 10.84 min). The timed events feature of the local user interface was used (Turned off at 6.20 minutes and activated at 8.70 minutes) to prevent the risk of a high concentration of Benzyl Alcohol reaching the detector. .....**194**

**Figure 6.1.1** Diffuse reflectance comparing the optical properties of white $TiO_2$ on glass filter ($wTiO_2$@GF) (red line) and black $TiO_2$ on glass filter ($bTiO_2$@GF) (black line) (A). Photographs illustrating the visual difference between white and black Titanium dioxide (B). .....**201**

**Figure 6.1.2** Log reduction units for a bacterial solution ($10^6$ CFU/mL) treated in a continuous flow system containing 3.37 g of $TiO_2$@Glasswool (TGW). The total system volume was 36.7 mL, with a residence time of 20 minutes, including a irradiation time of 13 minutes. Each time point represents the time necessary for a solution to passthrough the entire system (residence time), in the dark (black line) and irradiated with a UVA light (red line). .....**203**

# List of Schemes

**Scheme 1.4.1**. Main equations for iron-catalysed Fenton reaction.....14

**Scheme 1.5.1**. General chemical balanced equation for the co-precipitation method using $Fe^{2+}$ and $Fe^{3+}$ in alkaline environment. .....21

**Scheme 3.3.1**. Crocin chemical structure.....100

**Scheme 5.2.1.** Thermal Schiff Base synthesis.....161

# List of Tables

**Table 2.2.1** Summary of the characterizations for MNP. Particle size was obtained from the TEM images of the nanomaterials. Crystalline structures were analyzed from the XRD diffractograms and compared with the existingprofiles on the ICDD database. LFe: $Fe_3O_4$ [PDF 04-013-9808], LFeAg: Ag [PDF 04-014-0266] and Fe3O4 [PDF04-008-8145], LCo: $Co_3O_4$ [PDF 04-015-4721] and CoOH [PDF 04-005-7243] and LFeCo: $Fe_2O_3$ [PDF 01-076-4579] and $CoFe_2O_4$ [PDF 04-022-3956]. Crystallite size was calculated using the Scherrer equation using data from the XRD diffractograms. Lignin content was obtained using Thermogravimetric analysis (TGA), measured between 25-300°C under $N_2$. Metal quantification was done using ICP-OES following Fe, Ag and Co emission line. ..... 48

**Table 2.2.2** Summary of the bactericidal activity against *E. coli and S. aureus* after treatment with MNPs (125 mg/L) and NIR (0.99 W/cm$^2$) for 1 and 5 min, determined by the plate counting method. Bactericidal activity was measured as $\log_{10}$ reduction, by comparing cell viability after treatment with the initial bacterial inoculum. PTT treatment was done with solely NIR irradiation in the presence of the MNPs. CDT treatment was a combination of NIR irradiation presence of 0.1 mM $H_2O_2$. ..... 57

**Table 2.3.1** The cumulative released amount of ions (iron, silver and cobalt) from the MNP solutions (125 mg/L) after 30 min irradiation with 810 nm LEDi (0.99 W/cm$^2$) (light) or after incubation in the dark for 30 min (dark). Ions in solution were measured using ICP-OES following the Fe, Ag and Co emissions line at 238.20 nm, 338.29 nm, and 238.89 nm respectively. Percentages were calculated based on the total amount of NPs added to the solution. ..... 70

**Table 3.2.1** Energy distribution of a single LED measured with a spectroradiometer. ..... 80

**Table 3.2.2** Specific surface area (m$^2$/g) of the fibrous catalysts and their support materials (if applicable)[a]. ..... 86

**Table 4.2.1** Log reduction of *E. coli* bacterial count after incubation with $TiO_2$@Glass wool (TGW) with different concentrations of catalyst (0-20 mg/mL) or different initial bacterial concentrations. Samples were irradiated with UVA light for 3 hours. Log reduction was calculated based on the bacterial count of a control incubated protected from the light. Standard deviation values are presented in parentheses. ..... 127

**Table 4.3.1** Average lifetime ($\tau_{average}$) calculated from the ROI from the treatment images shown in the main text. The total lifetime for each treatment was calculated as an average of 15 ROIs. Different lifetimes were calculated for cells found in solution from the ones found in close contact with the glass wool (Or TGW). ..... 153

**Table 5.2.1.** Metal loading of the three bimetallic catalysts evaluated in this work. Metal quantification was done using ICP-OES following Fe, Pd, and Cu emission lines. ..... 167

**Table 5.2.2.** Optimizing Schiff-base yield produced $Fe_3O_4$@$TiO_2$ as a catalyst.[a] Reusing the catalyst and the Benzyl alcohol solution after 3 hours irradiation. .....175

**Table 5.3.1.** Comparison table illustrating the findings of this study alongside previous research on the one-pot Schiff Base synthesis using nitrobenzene and benzyl alcohol as reagents. The table shows the production rates in mmol h-1 achieved with various catalytic materials under different conditions. Production rates were estimated using the highest published yields for each reference, multiplying the initial nitrobenzene concentration, divided by the reaction times. .....192

**Table A.1.1.1** Output of the ANOVA test. Tests were done using the $Log_{10}$ reduction for each sample, done in triplicates. Degrees of freedom were calculated by the subtraction of the sample size number (24), by the number of parameters (1). Sum Sq was calculated from the squared $Log_{10}$ values. Mean Sq by dividing the Sum Sq by the degree of freedom. F value is the ratio between the variance between the groups (how much the means of different groups vary from each other) over the variance within a group (how much the individual data points within each group vary from their group mean). Pr > F is the p-value associated with the F value calculated. 0 '***', 0.001 '**', 0.01 '*' , 0.05 '.', 0.1 '' .....210

**Table A.1.1.2** Compact Letter Display (CDL) from the Tukey HSD test performed on the data from the MIC assay against E.coli. From ANOVA results we concluded that the average between groups is statistically different assuming $p<0.05$. To learn where the differences are, we performed a post hoc test, Tukey, which did a multiple comparison between the log10 reduction values. To facilitate visualization, we employed CLD analysis which groups similar treatments in letter groups. Lignin@Fe (LFe), Lignin@FeAg (LFeAg), Lignin@Co (LCo) and Lignin@FeCo (LFeCo). MNPs in solution are expressed in mg/L. .....211

**Table A.1.2.1** Output of the ANOVA test. Tests were done using the $Log_{10}$ reduction for each sample, done in triplicates. Degrees of freedom were calculated by the subtraction of the sample size number (40), by the number of parameters (1). Sum Sq was calculated from the squared $Log_{10}$ values. Mean Sq by dividing the Sum Sq by the degree of freedom. F value is the ratio between the variance between the groups (how much the means of different groups vary from each other) over the variance within a group (how much the individual data points within each group vary from their group mean). Pr > F is the p-value associated with the F value calculated. 0 '***', 0.001 '**', 0.01 '*' , 0.05 '.', 0.1 '' .....212

**Table A.1.2.2** Compact Letter Display (CDL) from the Tukey HSD test performed on the data from the Photodynamic therapy test against *E.coli*. From the ANOVA results we concluded that the average between groups is statistically different assuming $p<0.05$. To learn where are the differences, we performed a post-hoc test, Tukey, which did a multiple comparison between the $log_{10}$ reduction values. To facilitate visualization, we employed CLD analysis which groups similar treatments in letter groups. Lignin@Fe (LFe), Lignin@FeAg (LFeAg), Lignin@Co (LCo) and Lignin@FeCo (LFeCo). Controls dark and light were the NPs incubated in 50% LB only. .....213

**Table A.1.2.3** Compact Letter Display (CDL) from the Tukey HSD test performed on the data from the chemodynamic therapy assay against *E.coli*. From the ANOVA results we concluded that the average between groups is statistically different assuming $p<0.05$. To learn where are the differences, we performed a post-hoc test, Tukey, which did a multiple comparison between the $\log_{10}$ reduction values. To facilitate visualization, we employed CLD analysis which groups similar treatments into letter groups. Lignin@Fe (LFe), Lignin@FeAg (LFeAg), Lignin@Co (LCo) and Lignin@FeCo (LFeCo). Controls dark and light were the NPs incubated in 50% LB only. ....214

**Table A.1.3.1** Output of the ANOVA test. Tests were done using the $\text{Log}_{10}$ reduction for each sample, done in triplicates. Degrees of freedom were calculated by the subtraction of the sample size number (24), by the number of parameters (1). Sum Sq was calculated from the squared $\text{Log}_{10}$ values Mean Sq by dividing the Sum Sq by the degree of freedom. F value is the ratio between the variance between the groups (how much the means of different groups vary from each other) over the variance within a group (how much the individual data points within each group vary from their group mean). Pr > F is the p-value associated with the F value calculated. 0 '***', 0.001 '**', 0.01 '*' , 0.05 '.', 0.1 '' ....215

**Table A.1.3.2** Compact Letter Display (CDL) from the Tukey HSD test performed on the data from the MIC assay performed against *S. aureus*. From the ANOVA results, we concluded that the average between groups is statistically different assuming $p<0.05$. To learn where the differences are, we performed a ***post-hoc*** test, Tukey, which did a multiple comparisons between the $\log_{10}$ reduction values. To facilitate visualization, we employed CLD analysis which group similar treatments into letter groups. Lignin@Fe (LFe), Lignin@FeAg (LFeAg), Lignin@Co (LCo) and Lignin@FeCo (LFeCo). MNPs in solution are expressed in mg/L ....215

**Table A.1.4.1** Output of the ANOVA test. Tests were done using the $\text{Log}_{10}$ reduction for each sample, done in triplicates. Degrees of freedom were calculated by the subtraction of the sample size number (40), by the number of parameters (1). Sum Sq was calculated from the squared $\text{Log}_{10}$ values. Mean Sq by dividing the Sum Sq by the degree of freedom. F value is the ratio between the variance between the groups (how much the means of different groups vary from each other) over the variance within a group (how much the individual data points within each group vary from their group mean). Pr > F is the p-value associated with the F value calculated. 0 '***', 0.001 '**', 0.01 '*' , 0.05 '.', 0.1 '' ....216

**Table A.1.4.2** Compact Letter Display (CDL) from the Tukey HSD test performed on the data from the Photodynamic therapy test against *S. aureus*. From the ANOVA results we concluded that the average between groups is statistically different assuming $p<0.05$. To learn where are the differences, we performed a post-hoc test, Tukey, which did a multiple comparison between the $\log_{10}$ reduction. To facilitate visualization, we employed CLD analysis which groups similar treatments into letter groups. Lignin@Fe (LFe), Lignin@FeAg (LFeAg), Lignin@Co (LCo) and Lignin@FeCo (LFeCo). Controls dark and light were the NPs incubated in 50% LB only. ....217

**Table A.1.4.3** Compact Letter Display (CDL) from the Tukey HSD test performed on the data from the Chemodynamic therapy test against S. aureus. From the ANOVA results we concluded that the average between groups is statistically different assuming $p<0.05$. To learn where are the differences, we performed a post hoc test, Tukey, which did a multiple comparison between the $\log_{10}$ reduction. To facilitate visualization, we employed CLD analysis which groups similar treatments in letter groups. Lignin@Fe (LFe), Lignin@FeAg (LFeAg), Lignin@Co (LCo) and Lignin@FeCo (LFeCo). Controls dark and light were the NPs incubated in 50% LB only. ..... 218

**Table A.1.5.1** Output of the ANOVA test. Tests were done using the percentage viability for each sample, done in triplicates. Degrees of freedom were calculated by the subtraction of the sample size number (10), by the number of parameters (1). Sum Sq was calculated from the squared % viability values. Mean Sq by dividing the Sum Sq by the degree of freedom. F value is the ratio between the variance between the groups (how much the means of different groups vary from each other) over the variance within a group (how much the individual data points within each group vary from their group mean). Pr > F is the p-value associated with the F value calculated. 0 '***', 0.001 '**', 0.01 '*' , 0.05 '.', 0.1 '' ..... 219

**Table A.1.5.2** Compact Letter Display (CDL) from the Tukey HSD test performed on the data from the MTT assay test on HT1080 cells. From the ANOVA results we concluded that the average between groups is statistically different assuming $p<0.05$. To learn where are the differences, we performed a post hoc test, Tukey, which did a multiple comparison between the % viability values. To facilitate visualization, we employed CLD analysis which groups similar treatments into letter groups. Lignin@Fe (LFe), Lignin@FeAg (LFeAg), Lignin@Co (LCo) and Lignin@FeCo (LFeCo). Controls dark and light were the NPs incubated in DMEM in absence of NPs. ..... 219

**Table A.2.1** Output of the ANOVA test. Tests were done using the $\text{Log}_{10}$ reduction for each sample, done in triplicates. Degrees of freedom were calculated by the subtraction of the sample size number (40), by the number of parameters (1). Sum Sq was calculated from the squared $\text{Log}_{10}$ values Mean Sq by dividing the Sum Sq by the degree of freedom. F value is the ratio between the variance between the groups (how much the means of different groups vary from each other) over the variance within a group (how much the individual data points within each group vary from their group mean). Pr > F is the p-value associated with the F value calculated. 0 '***', 0.001 '**', 0.01 '*' , 0.05 '.', 0.1 '' ..... 221

**Table A.2.2** Compact Letter Display (CDL) from the Tukey HSD test performed on the data from the antibacterial tests. From the ANOVA results, we concluded that the average between groups is statistically different assuming $p<0.05$. To learn where are the differences, we performed a post-hoc test, Tukey, which did a multiple comparisons between the $\log_{10}$ reduction values. To facilitate visualization, we employed CLD analysis which groups similar treatments into letter groups. Controls light were the NPs incubated in 5 % LB only and exposed to the light. ..... 222

# List of Abbreviations

| | |
|---|---|
| 3-NA | 3-Nitroanisole |
| 7-HC | 7-Hydroxycoumarin |
| DR | Diffuse Reflectance |
| EDS | Energy-Dispersive Spectrometer |
| AOP | Advanced Oxidation Process |
| APTES | (3-Aminopropyl) Triethoxysilane |
| ATR | Attenuated Total Reflectance |
| BenzA | Benzaldehyde |
| BET | Brunauer–Emmett–Teller |
| CB | Conduction Band |
| CDT | Chemodynamic Therapy |
| CFU | Colony Forming Units |
| DMEM | Dulbecco's Modified Eagle Medium |
| DMSO | Dimethyl Sulfoxide |
| $e^-$ | Electron |
| Ea | Activation Energy |
| Ebg | Band-Gap Energy |
| EDS | Energy Dispersive X-Ray |
| EtOH | Ethanol |
| FCS | Fetal Bovine Serum |

| | |
|---|---|
| FLIM | Fluorescence Lifetime Imaging Microscopy |
| FTIR | Fourier Transformed Infrared |
| GC-MS | Gas Chromatography-Mass Spectrometry |
| GF | Glass Filter Fibres |
| GW | Glass Wool |
| $h^+$ | Holes |
| HPLC | High-Performance Liquid Chromatography |
| I.D. | Inner Diameter |
| ICP-OES | Inductively Coupled Plasma Optical Emission Spectrometry |
| IR | Infra-Red |
| LB | Luria-Bertani |
| LCo | Lignin@Co |
| LED | Light Emitting Diode |
| LFe | Lignin@Fe |
| LFeAg | Lignin@FeAg |
| LFeCo | Lignin@FeCo |
| LSPR | Localized Surface Plasmon Resonance |
| $M^0$ | Atomic Metal |
| MH | Mueller Hinton |
| MIC | Minimal Inhibitory Concentration |
| $M^{n+}$ | Metal Ion |
| MNP | Magnetic Nanoparticles |

| | |
|---|---|
| MTT | 2,5-Diphenyl-2H-Tetrazolium Bromide |
| NIR | Near Infra-Red |
| NM | Nanomaterial |
| NMR | Nuclear Magnetic Resonance |
| NP | Nanoparticle |
| PBS | Phosphate-Buffered Saline |
| PDT | Photodynamic Therapy |
| PM | Particulate Matter |
| PTFE | Polytetrafluoroethylene |
| PTT | Photothermal Therapy |
| PVC | Polyvinyl Chloride |
| PVP | Polyvinylpyrrolidone |
| QD | Quantum Dots |
| ROS | Reactive Oxygen Species |
| RT | Residence Time |
| SEA | Sacrificial Electron Acceptor |
| SED | Sacrificial Electron Donnor |
| SEM | Scanning Electron Microscopy |
| SERS | Surface-Enhanced Raman Scattering |
| SSA | Specific Surface Area |
| $T_0$ | Time Zero |
| TEM | Transmission Electron Microscope |

| | |
|---|---|
| TGF | $TiO_2$@Glass Filter Fibres |
| TGW | $TiO_2$@Glasswool |
| TiP | Titanium Isopropoxide |
| TMB | 1,3,5-Trimethylbenzene |
| TNF | $TiO_2$ Nanofibres |
| TSPC | Time Correlated Photon Counting |
| UVA | Ultraviolet A (315-400 nm) |
| UVB | Ultraviolet A (280-315 nm) |
| VB | Valence Band |
| Vis | Visible |
| VOCs | Volatile organic compounds |
| XPS | X-Ray Photoelectron Spectroscopy |
| XRD | X-Ray Diffraction |
| $\Delta G$ | Free Energy |
| $\Delta G^{\dagger}$ | Free Energy Barrier |
| $\lambda$ | Wavelength |
| $\tau_{avg}$ | Average Lifetime |
| $\lambda_{ex}$ | Excitation Wavelength |

# 1. Introduction

## 1.1 Open remarks

The work presented in this dissertation addresses pressing issues by proposing innovative fabrication methodologies and applications for materials containing two earth-abundant elements, iron and titanium. These elements offer sustainable alternatives to at-risk materials across various fields. The following chapters will detail the synthetic methodologies, demonstrate their effectiveness, and discuss potential limitations. This doctoral thesis is composed of two peer-reviewed publications (Chapters 2 and 3) and two manuscripts undergoing peer review process (Chapters 4 and 5). These chapters include the manuscripts, supporting information, and additional commentaries and alterations to provide further insights and highlight the research context. First, this introductory chapter will discuss some basic concepts of nanomaterials, their properties, and their significance. This foundational understanding is crucial for appreciating the versatility and importance of these materials in various contexts, and how the proposed materials in this thesis can assist in these applications.

## 1.2 Nanomaterials

In December of 1959, Nobel laureate Richard Feynmann gave his famous lecture entitled "*There's Plenty of Room at the Bottom",* where he discussed the creation and exploration of technology in a smaller size.[1] In his talk he shared his vision to develop small machines and work at the atomic and molecular level, seedling then the concept of a modern technology. Fifteen years later, in 1974, the term nanotechnology was first used, by Professor Norio Taniguchi who defined it as "*the processing of separation, consolidation, and deformation of materials by one atom or one molecule*".[2,3] Nowadays, nanomaterials are described as materials that have at least one dimension in the nanoscale, which ranges between 1-100 nm.[4,5] The technologies that utilize those materials in practical applications are called nanotechnology.[6] Despite the great impact of those two lectures, explorations and development of nanotechnology only rose in the 1980s with the invention of scanning tunnelling microscopy and atomic force microscopy.[3,7,8] Two different tools

used in imaging and manipulation surfaces at the atomic level bringing to life Feynman's ideas. Over the years several revolutionary discoveries and developments have been made with the use and application of nanomaterials.

With the advancement in state-of-the-art technologies and the improvement of analytic instrumentation, we can now trace the use of nanomaterials back to the ancient world. Humans have been successfully employing nanostructures way before the concept of synthesizing materials at the nanoscale level was established. There are records of asbestos nanofibres being used to reinforce ceramic mixtures from 4500 years ago.[9] Au and Ag nanoparticles (NPs) were employed by the Romans in dichroic glasses in the 4$^{th}$ century A.D.[10,11] Similarly, late medieval church windows, that exhibit shining luminous red and yellow colours, are a result of the infusing of Au and Ag NPs into glass.[3] The first report on the experimental synthesis of nanomaterials was made by Michael Faraday in 1857. In his work *"Experimental Relations of Gold (and other Metals) to Light",*[12] Faraday prepared "ruby" gold solutions to study their interaction with light. In his analysis, Faraday concluded that the ruby colour was a result of finely divided Au.[13] Those solutions are now known to be colloidal AuNP suspensions.[13]

The previous sentence may sound intriguing because gold is not typically associated with the red colour; rather, bulk Au is known for its characteristic golden hue. The fact that gold, and other metals, can exhibit different colours at the nanoscale is one of the remarkable features of nanostructures and serves to justify the keen interest in those materials.[9] Some of the unique properties displayed by nanosized structures arise from the influence of electron motions on the physical and chemical properties of a certain material. In the example of the AuNPs, their small size relative to the wavelength of electromagnetic radiation triggers a collective oscillation of electrons at the nanoparticle's surface, generating a Localized Surface Plasmons Resonance (LSPR).[14] This phenomenon leads to strong light absorption in the visible range, which gives strong and characteristic colours to these materials. This is also true for other plasmonic materials such as Pd and Ag.

The motion of electrons is also significantly affected by the small sizes of nanometric structures. In such confined spaces, the freedom for electron motion is notably restricted, leading

to quantization.[15] Thus, the allowed type of electron motion is well-defined within discrete energy levels. The degree of confinement directly impacts the energy separation between these allowed levels, with stronger confinement resulting in larger energy gaps.[16] An important threshold between these energy levels is the band gap, which separates the highest occupied collection of energy levels, known as the valence band (VB) and the conduction band (CB).[17] The size of the band gap determines the conductivity properties of materials, categorizing them as conductors, semiconductors, and insulators. Figure 1.2.1 shows an illustrative diagram of the difference in band-gap energy for the three materials. Within the scope of this dissertation, the focus will be on semiconductors—materials that occupy an intermediate position between conductors and insulators.

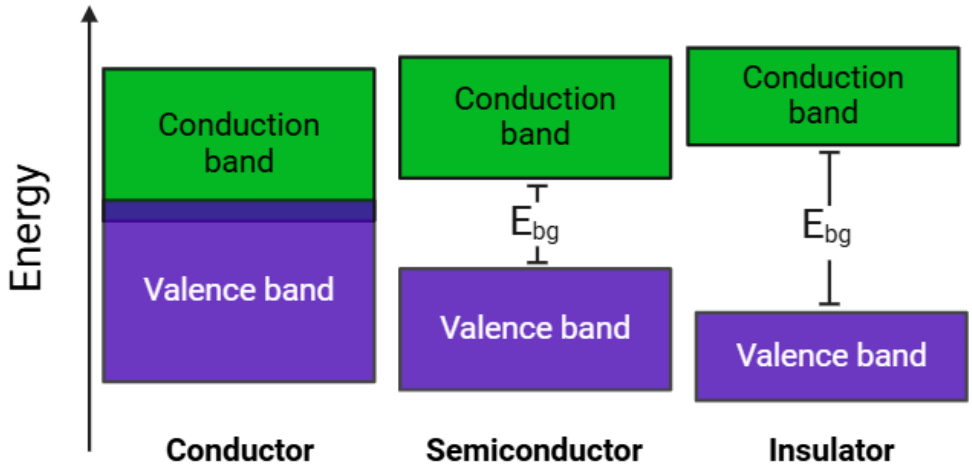


**Figure 1.2.1.** Illustrative diagram showing the band-gap energies (Ebg) for conductors, semiconductors, and insulators.

Electrons can move from the valence band to the conduction band through the absorption of energy, which can be supplied in the form of heat, an electric field or light excitation.[18,19] In light absorption, photons must possess energies above the band-gap energy ($E_{bg}$) to promote the electron ($e^-$) from the VB to the CB. While there is no precise threshold for the band-gap energy of a semiconductor, these materials typically exhibit band-gaps below 4 eV.[20,21] Upon excitation, the hot electron leaves behind a positively charged 'hole' ($h^+$),[19] which is often treated as a charge carrier.

Post-excitation, the charge carriers can follow various pathways. Initially, both carriers may recombine, releasing the absorbed energy in the form of light or heat, a process occurring within a time scale of 1-10 picoseconds.[22] Charge carriers can also migrate toward the material's surface and be trapped in surface sites, usually generated by crystal defects. Trapped charge carriers undergo recombination at a slower rate.[22] Alternatively, they can undergo redox reactions with compounds in the surrounding solution, $e^-$ are transferred to electron acceptors, while holes receive electrons from donors (Figure 1.2.2). The redox characteristics of semiconductors, along with the resultant energy emission from charge carrier recombination, hold significance across various applications, which will be described later in this manuscript.

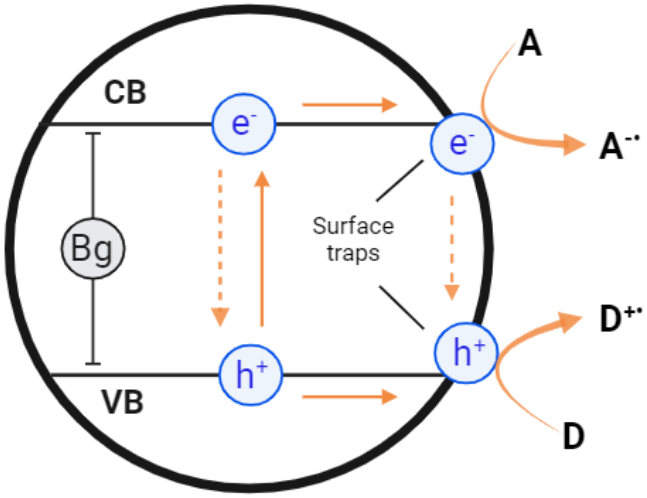


**Figure 1.2.2.** Illustration of the electronic structure of a semiconductor, showing the valance band (VB) and the conduction band (CB), separated by the band gap (Bg). Recombination events are shown as dashed lines. When in the surface the electrons ($e^-$) can be transferred to electron acceptors (A), which are reduced. Holes ($h^+$) receive electrons from electron donors (D), which become oxidized.

Another important feature of nanosized materials is the increased surface-to-volume ratio, leading to a higher proportion of surface atoms than bulk materials. These surface atoms exhibit distinct behaviour due to their reduced number of neighbouring atoms.[23] Consequently, nanomaterials exhibit unique physicochemical properties distinct from their bulk counterparts, such as higher reactivity and lower melting points. Moreover, a large surface area promotes

enhanced interactions with the surrounding environment, also influencing their reactivity.[23,24] Those properties together collaborate for the superior performance of nanomaterials compared to their bulk counterparts in many applications, combined with the facility to tailor physical and chemical properties by changing the size and shape of the nanostructures.[9,15] Therefore, the development of advanced synthetic routes for nanomaterials becomes an essential element in nanotechnology to exploit and utilize their unique features.

### 1.3 Synthesis of Nanomaterials

Following several decades of intense research efforts on the fabrication of new nanomaterials, scientists have developed various synthetic approaches. Different approaches yield materials with distinct structures and properties. In general, techniques for nanomaterials synthesis can be categorized into two synthetic principles: top-down and bottom-up.

The first approach is top-down in which bulk materials are broken down into nanosized materials.[3] The bulk breakdown is achieved by using advanced techniques, such as lithography, laser ablation, etching and mechanical milling.[25–27] The latter is an example of a mechanical strategy, in which a precursor powder is placed into a milling vial along with small balls. The kinetic energy generated by the ball movement is transferred to the powder leading to breakage of chemical bonding, reduction of particle size and modification of particle shape.[25,27] Another top-down approach is lithography, which is a physical strategy. One example is the work by Yue and colleagues,[26] where they described the synthesis of nanostructured substrates for surface-enhanced Raman scattering (SERS). In their work, pattern gold nanostructures were formed by coating a silicon wafer with a thin Au layer covered by a beam resist pattern. Upon exposure to a focused electron beam, followed by etching of the pattern, the nanometric gold layer is revealed.[26]

Bottom-up methods involve the build-up of nanostructures by assembling atoms or molecules.[3] Examples of these methods are sol-gel processes, chemical vapour deposition, and chemical reduction.[24,28–30] Metal and metal-oxide NPs are commonly synthesized by chemical reduction, where a metal-containing salt ($M^{n+}$) is reduced to its atomic form ($M^0$), using a reducing agent. Once the concentration $M^0$ reaches the super saturation ($C_{ss}$) level, marked as the green line in Figure 1.3.1, the atoms undergo fast nucleation, forming small clusters that grow by consuming $M^0$, represented in orange in Figure 1.3.1. Ultimately $M^0$ concentration drops, below $C_{ss}$, starting the growth of the clusters and ultimately resulting in the formation of NPs.[24,27,31] By controlling each of these steps, one can achieve various sizes and morphologies of nanostructures. Reduction of a metal salt can also be achieved photochemically in the presence of a photosensitizer.

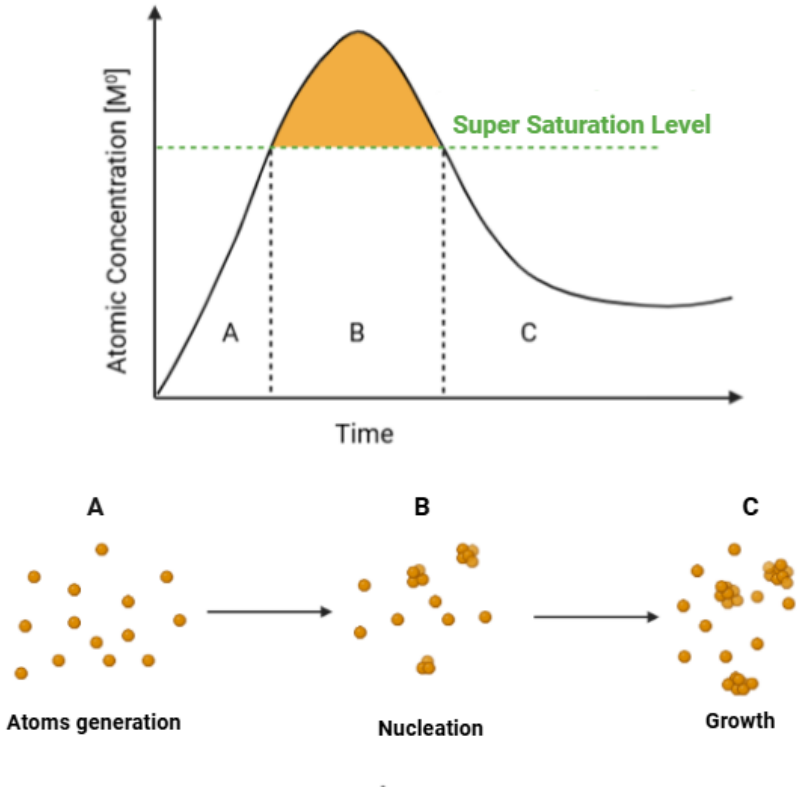


**Figure 1.3.1.** Representations of nanoparticle formation via chemical reduction. On top, a plot of the La Mer model for the generation of atoms (A), nucleation (B) and growth (C). On the bottom is an illustrative diagram of particle formation according to the steps described by the La Mer model. $M^0$ atoms are represented by the orange circles.

In the Scaiano group, we have explored the synthetic pathway for various nanoparticles using electron-donating radicals photochemically generated. For instance, the photocleavage of Irgacure-2959 under Ultraviolet A (UVA) irradiation yields ketyl radicals, which are strong electron-donating radicals capable of reducing metal ions to zero-valent species.[32–34]

Another photochemical approach is the photochemical deposition of metal NPs onto the surface of other nanostructures. This approach enables the fabrication of co-catalysts by depositing metals onto semiconductors under mild conditions. Upon exposure to light, semiconductors such as $TiO_2$, ZnO, $BiCo_4$, and $WO_3$, generate at their surface electrons and holes with sufficient energy to respectively reduce and oxidize metal precursors, depositing the metal NPs on the surface of the semiconductor.[35]

Additionally, surface modifications can be done by adding capping agents, during or after the synthesis of nanostructures. These modifications serve various purposes, such as stabilizing unstable and aggregative nanoparticles within a medium, facilitating surface functionalization for a targeted application, or aiding in nanoparticle assembly.[24,36] For instance, in drug-delivery systems, coating nanoparticles with target-specific molecules enhances their selectivity toward targeted tissues.[37] Common surface modifications are the use of thiolate surfactants or polymers, the attachment of biological molecules such as DNA, peptides, proteins and antigens or coating with polymer films.[24] Capping agents that act on the stabilization of NPs, are called stabilizing agents, and they prevent the formation of aggregates through several mechanisms, including steric hindrance, electrostatic repulsion, hydration forces, and van der Waals forces.[36] The selection of an appropriate capping agent is critical as it can significantly influence the size, shape, and interactions of nanoparticles.

Most of the techniques described pertain to 0D nanomaterials, those with all dimensions within the nanoscale. However, 1D and 2D materials, which have one or two dimensions extended beyond the nanoscale, are equally significant and require distinct synthetic methods. For instance, 2D materials like thin films and graphene can be produced using mechanical exfoliation, chemical vapour deposition, solution-based chemical approach, hydrothermal and solvothermal methods.[38]

Conversely, 1D nanomaterials, characterized by tubular shapes such as nanowires, nanotubes, and nanofibres, can be synthesized through processes like vapour–liquid-solid, template methods, sol-gel, hydrothermal methods, and electrospinning.[39,40]

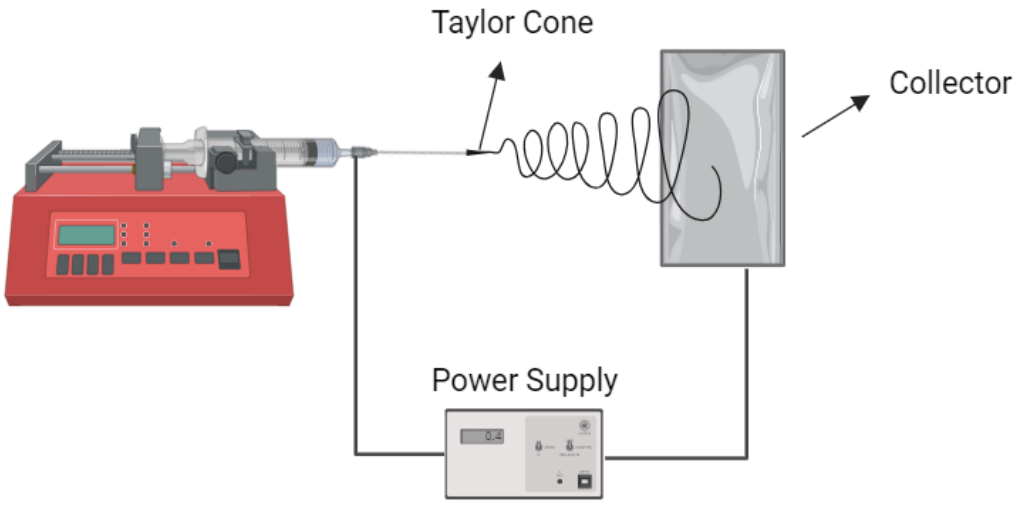


**Figure 1.3.2.** Schematic illustration of the electrospinning setup. A syringe is loaded with a polymer solution and attached to a syringe pump. An electric field is generated between the needle and the metallic collector, by an external power supply. Under the electric current, the polymer is ejected forming the Taylor cone, which is elongated, forming long fibres. The produced nanofibres are accumulated in the collector.

Electrospinning is a commonly used technique for nanofibres fabrication, which involves loading a polymer solution into a syringe and injecting it through a needle under the influence of a strong electric field generated by the high-voltage power supply.[41] A common electrospinning setup can be observed in Figure 1.3.2. During solution ejection, electrostatic charges build up on the surface of the forming droplet. When these charges exceed surface tension, a cone, known as the Taylor cone, is formed. This cone is further stretched, producing continuous ultrathin fibres as the solvent evaporates. The jet of fibres is collected by a conductive collector connected to the negative terminal of the power supply (Figure 1.3.2).[41] By employing a continuous-feeding mode, numerous fibre copies can be produced rapidly.[42,43] The success of the electrospinning depends on the choice of solvent, solution viscosity and applied voltage.[41] Moreover, the polymer solutions can be supplemented with additives to tailor the properties for specific applications, some

examples are the addition of organic compounds, metals, metal-oxide nanoparticles, or their precursors.

## 1.4 Applications of Nanomaterials

Due to their unique features and combined with the ability to tailor their physicochemical properties, nanomaterials have found widespread applications across various sectors. For instance, modern high-resolution displays benefit from the narrow emissions bands and tunability of quantum dots (QDs), which are small fluorescent semiconductors characterized by their high degree of quantum confinement.45 Electronics also utilize silicon and carbon-based nanomaterials in advanced transistor technology.[45,46] In the energy sector, graphene shows promising potential as supercapacitors for storing renewable energy.[46] In agriculture nanoparticles like Silicon NPs (SiNPs) serve as carriers for pesticides and carbon nanotubes have been shown to enhance seed germination.[47–49] SiNPs also play a role in the food industry, serving as anti-cracking and thickening agents.[9,50] Additionally, the cosmetic industry benefits from the optical properties of semiconductors such as ZnO and $TiO_2$, which are used as light-scattering agents in sunscreens.[51,52]

Beyond these applications, nanomaterials also have pivotal roles in biomedical, environmental, and catalysis fields, which will be the focus of the materials fabricated in this thesis. Therefore, we will delve deeper into the discussion of these applications.

### 1.4.1 Catalytic applications

Catalytic methodologies help reduce synthetic steps, enabling the realization of the reactions that once seemed too slow or even impossible. Through these processes, it becomes possible to reduce reaction temperatures, minimize reagent waste, and enhance the selectivity of desired reactions, which have significant impacts on sectors like pharmaceuticals and fine chemicals.[53] Catalysts function by reducing the activation energy (Ea) necessary for a chemical reaction to occur, often achieved by interaction with reagents, stabilization of intermediaries or by providing an alternative reaction pathway. Thermodynamically, catalyzed reactions exhibit a lower free energy barrier ($\Delta G^{\ddagger}$) compared to uncatalyzed reactions, while there is no alteration in

the overall change in free energy (ΔG).[54] Following product formation, catalysts are regenerated unchanged. Catalysts are typically classified as homogeneous, where all components (reactants, products, and catalyst) are in the same phase, or heterogeneous, where the catalyst exists in a different phase from its reactants.[53] However here we bring an interesting discussion since this classification oversimplifies the reality, as processes can occur in multiple phases. For example, catalytic species, such as ions, may leach from heterogeneous catalysts, and interact with the reactants in a homogeneous phase; homogeneous catalysts can generate *in situ* heterogeneous active catalytic species; and some heterogeneous catalysts may leach active species that after catalysis are redeposited on the catalyst surface.[55–59] Recognizing these diverse mechanisms is crucial for accurately determining reaction pathways.

Nanomaterials (NMs) hold particular significance in catalytic applications due to their increased surface area and abundance of reactive surface atoms, which make them great candidates for various catalytic reactions. As is the scope of this thesis we will be talking about photocatalysts, in special, semi-conductor photocatalysts. As previously mentioned, generated charge carriers can undergo different fates. For instance, the heat generated at NM's surface, after charge carrier recombination, can be used as an alternative heat source for organic reactions.[60,61] Moreover, the strong redox properties of the $e^-/h^+$ pair can be used for both redox reactions. For this, the redox potential of the band edge as well as the $E_{bg}$ of the catalysts must be aligned with the required redox potential and energy necessary for the desired reaction to occur.[22,62]

The photogenerated $h^+$ is utilized for the oxidative transformation of organic compounds, such as the oxidation of alcohols, benzene, and amines.[63] Enhancing its efficacy involves minimizing the formation of secondary oxidative species like $O_2^{\bullet-}$ and $^{\bullet}OOH$. These destructive species are formed from the reaction of $O_2$ with the photogenerated electron. One strategy is to eliminate the $e^-$ using sacrificial electron acceptors (SEA), such as benzoquinone, $Ag_2SO_4$ or loaded-metal NPs. Conversely, the photo-generated $h^+$ can be removed by sacrificial electron donors (SED), for successful reductive organic transformations, like electron transfer to halides, carbonyls, or nitro compounds. This prevents the formation of $^{\bullet}OH$ radicals formed from the reaction of water and the $h^+$.[64,65] Although desirable, the simultaneous utilization of photo-generated $h^+$ and $e^-$ in bond

formation reactions is challenging. It requires precise reagent selection and band-gap engineering to simultaneously use the $e^-$ and $h^+$.[65]

Recombination rates heavily influence the efficiency of reactions dependent on the photogenerated charge carriers. Faster recombination reduces the likelihood of carriers encountering electron donors or acceptors. To mitigate this, metallic nanoparticles such as Pd, Pt, and Au can be strategically placed on catalytic surfaces.[22,66] By doing so, electrons in the conduction band of semiconductors migrate to the metals, facilitating charge separation.[22]

### 1.4.2 Biomedical Applications

Medicine takes advantage of the large surface area of nanomaterials, stability, and optical properties. Light-emitting nanomaterials are great alternatives for imaging applications. An example is quantum dots (QDs), which are used as imaging agents for cell tracking and in imaged-guided surgeries due to their great photostability, and narrow emission.[67] NPs can also be employed as nanosensors in biological systems. Their small sizes give us the ability to sense and detect at the single-molecule scale in living systems.[68] Drug delivery is another important application of nanomaterials. NPs can be functionalized to reach specific targets, besides enhanced drug solubility, and stability.[24,36] Additionally, NPs facilitate trans-membrane transportation, prolonged circulation time and enable controlled release of therapeutics. In vaccine technology, nanomaterials proved to be a great alternative to carry immune-stimulating agents and triggering cellular and humoral immune responses.[69] The most notable example is the use of lipid nanoparticles encapsulating mRNA-12734 and BNT162b25 in the COVID-19 vaccines produced by Moderna and Pfizer-BioNTech, respectively.[69,70]

Besides acting as great drug carriers, nanomaterials possess therapeutic properties themselves. For example, nanoparticles (NPs), such as AgNPs exhibit anti-infective activities, by preventing the binding of HIV to host cells.[71,72] Studies have also demonstrated that NPs can act as anti-angiogenic agents by inhibiting heparin-binding proteins or cell proliferation, thus preventing the formation of new blood vessels that could support cancerous cells.[73–75]

However, the most remarkable health application of nanomaterials lies in combating bacterial infections. The antibacterial mechanisms of NPs are the subject of an ongoing discussion,

similar to the debate about homogenous and heterogenous catalysts, on whether the activity is generated by the NP *per se*, by leached ions, or a combination of both. It is known that nanomaterials can directly interact with the bacterial cell wall acting as a focal and continuous source of ions.[75,76] Once inside the cells, certain ions like $Ag^{+}$ and $Cu^{2+}$ can bind to thiol groups in proteins, thereby, disrupting essential cellular functions.[75,77] They can also induce oxidative stress by reacting with molecular oxygen, water, or other cellular components, generating reactive oxygen species (ROS).[77,78] For instance, one of the main radicals produced, $^{\bullet}OH$, is known to initiate hydrogen abstraction from amino acid side chains, which can lead to side chain functionalization, protein cross-linking or fragmentation.[78] Hydrogen can also be abstracted from allylic hydrogen forming a carbon-centred radical that can rapidly propagate resulting in a chain reaction.[79] As a result, NPs can cause generalized injury to cellular structures in the bacterial cytoplasm besides depleting ATP and inhibiting DNA synthesis.[79,80] Furthermore, aside from ion release, the nanostructures themselves have demonstrated antibacterial effects as membrane disruptors, forming pits in cell walls, and accumulating both, internally and externally, contributing further to their antibacterial effects.[76,81]

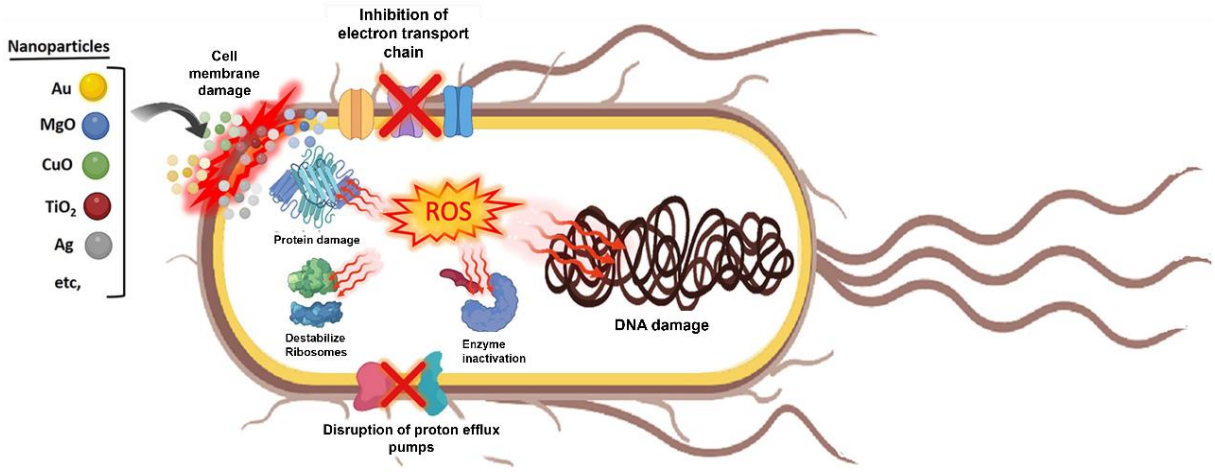


**Figure 1.4.1.** Diagram illustrating the potential bactericidal effects of metallic NPs. Once in contact with the cells, NPs can directly interact with bacterial membranes increasing permeability and causing membrane dysfunction. Inside the cell, they can trigger oxidative stress via ROS production, disrupting cellular functions and damaging DNA and RNA, culminating in cell death. Image adapted from reference,[80] under the Creative Commons license (CC-BY 4.0)

Alternatively, NMs can also act as therapeutic agents due to their interaction with light. Certain materials like AuNPs, Au nanorods (AuNRs), $Fe_3O_4$NPs and carbon nanotubes, exhibit great light-to-heat conversion capabilities.[82–84] When these materials absorb light, they rapidly convert it into heat through non-radiative decay, a process utilized in photothermal therapy (PTT) for treating infectious diseases and cancer.[83,85,86] The localized heat generated at the surface of the nanomaterial can impede pathogens' growth, disrupt cellular membranes, and denature proteins, ultimately causing cell (or pathogen death).[85,87] Additionally, nanostructures can serve as photosensitizing agents in photodynamic therapy (PDT). Upon activation by light at specific wavelengths, photosensitizers generate reactive oxygen species (ROS) like singlet oxygen ($^1O_2$), superoxide anion ($O_2^{\bullet-}$), and hydroxyl radicals ($^{\bullet}OH$) at cancer or infectious sites, damaging membranes, altering cellular functions, and inducing apoptotic responses.[88,89] Traditional photosensitizers are often organic molecules, such as phthalocyanine, and metalloporphyrin. However, in 2014, the research group of Dr. Hwang, demonstrated that Au nanorods (AuNRs) can generate singlet oxygen under NIR (915 nm) excitation leading to the destruction of B16F0 melanoma tumours.90 Since then, various nanomaterials including silver AgNPs, SiNPs, QDs, and upconversion nanoparticles (UCNPs) have been explored as effective photosensitizers in cancer therapy,[88] and as antibacterial agents.[91,92]

### 1.4.3 Environmental applications

Due to industrial processes coupled with inadequate waste management, environmental pollution has emerged as a significant threat to public health and ecological sustainability. Daily, large quantities of hazardous materials are discharged into water, air, and soil, including agrochemicals, dyes, antibiotics, VOCs, and heavy metals.[93–95] Furthermore, the depletion of potable water sources exacerbates the challenge of providing safe water to numerous communities.[94,96,97] Nanotechnology presents promising solutions for sustainable environmental management and protection in this pressing scenario. NMs can function as nanosensors, to monitor water and soil pollutant remediation processes, simplifying the need for complex analytical tools.[98] They serve as adsorbers or are integrated into filtration systems for contaminants removal. For instance,

electrospun nanofibres, leveraging their large surface area, demonstrate remarkable efficacy in capturing airborne particulate matter.[95]

Our focus will be the catalytic features of NPs for environmental remediation. More specifically, NMs are great catalysts for the advanced oxidation process (AOP), which is an important route to degrade contaminants via hydroxyl radical (•OH) generation. These radicals initiate a series of oxidation reactions potentially leading to the complete mineralization of organic compounds into $CO_2$ and $H_2O$.[99] AOP utilizes various approaches such as cavitation, photocatalysis, and Fenton chemistry.[99]

$$Fe^{2+} + H_2O_2 \longrightarrow {}^{\bullet}OH + OH^- + Fe^{3+} \qquad \text{(Equation 1)}$$

$$Fe^{3+} + H_2O_2 \longrightarrow Fe^{2+} + H^+ + HOO^{\bullet} \qquad \text{(Equation 2)}$$

**Scheme 1.4.1**. Main equations for iron-catalysed Fenton reaction.

Fenton reactions are a series of chemical reactions catalyzed by Fe-based compounds, which, in the presence of $H_2O_2$ yield •OH. In a typical Fenton reaction mechanism ferrous ion ($Fe^{2+}$) is oxidized by $H_2O_2$ forming a ferric ion ($Fe^{3+}$), hydroxyl radical, and a hydroxyl anion (Scheme 1.4.1, eq. 1). $Fe^{3+}$ is reduced by the same $H_2O_2$ recovering $Fe^{2+}$ (Scheme 1.4.1, eq. 2).[99] Traditionally, iron salts are used as Fenton catalysts, posing challenges in catalyst recovery and reusability. However, heterogeneous nanomaterials containing Fe offer a viable alternative.

When previously discussing the photocatalytic properties of semiconductors (Section 1.4.1) we described their role in molecule building, inversely, nanocatalysts can also break down harmful compounds into harmless products. The photogenerated $e^-/h^+$ pairs can directly interact with the target contaminant, which due to its high redox potential has the energy to break C-C and C-H bonds.[19,64] Alternatively, the charge carriers with enough energy can react with $e^-$ donors or acceptors, such as $O_2$ and $H_2O$, forming secondary ROS.[22] Those species have the energy to react with several organic substances, leading to bond breakage (Figure 1.4.2). The pollutants are then

degraded into less harmful intermediaries, and if given enough time and energy can be completely mineralized into $CO_2$ and $H_2O$.

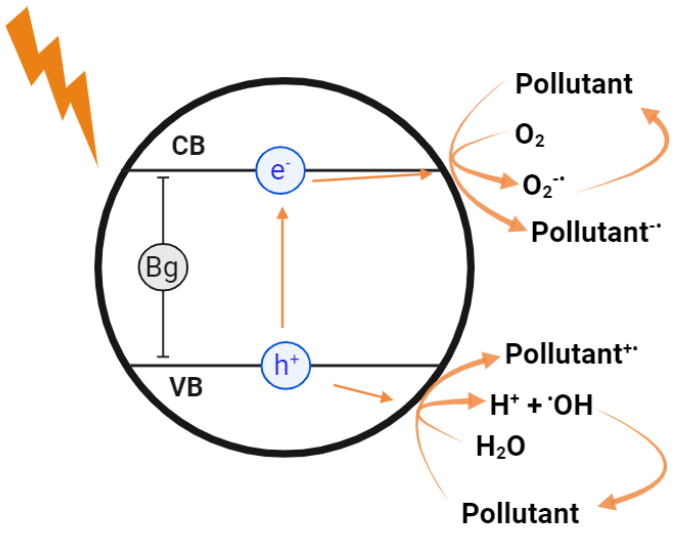


**Figure 1.4.2** Diagram of the potential photocatalytic degradation routes of pollutants using semiconductors nanomaterials. Upon light excitation, excited electrons are generated, and they can be transferred to adsorbed pollutants producing reduced compounds. Electrons can also be transferred to other electron donors, in this example, $O_2$ is reduced producing superoxide anion ($O^{-}$ •). The excited $e^-$ leaves behind a positively charged hole that oxidizes adsorbed molecules, such as pollutants or other electron donors, like water, producing hydroxyl radicals (•OH) and a proton. The produced radicals $O^{-}$ • and •OH, can also react with the pollutants. Bg: Bandgap; $e^-$: electron; $h^+$: hole; VB: valence band; CB: conduction band.

It is important to clarify that the same system is effective against various contaminants beyond organic molecules. Hydroxyl radicals (•OH), for instance, have great antibacterial properties, killing several microorganisms, which are the key reasons behind waster-boiling advisories across the country.[97] Additionally, this system can be employed to oxidize heavy metals, converting them into less harmful oxidative states or insoluble precipitates.[100,101]

## 1.5 Choice of elements

Now it is clear that nanotechnology is a fascinating and wide field with promising applications that impact several aspects of our lives. However, the implementation of

nanomaterials-based technologies often overlooks the criticality of the elements involved. Several elements have supply risks and environmental implications associated with their extraction and refinement casting doubt on their long-term sustainability.[102] Criticality of metallic elements evaluate not only their earth-abundance, but also their demand, and the associated environmental, social, and political risks. For instance, minerals from conflict zones help perpetuate the uncertainty in the region, and their extraction is often associated with the exploitation of forced labour, unsafety, and abuse of local communities.[102,103] Environmental risks include the high energy demands, potential pollutant emissions, eutrophication risks and human toxicity concerns associated with the minerals' extraction and refinement.[104] Recognizing the criticality of elements highlights the need to find alternatives for overly exploited elements. In 2015, Graedel and collaborators published periodic tables classifying the chemical elements according to their criticality,[102] which can be seen in Figure 1.5.1 A-C. Upon closer examination of the periodic tables and considering the intrinsic toxicity of the elements, it became clear that titanium and iron consistently emerge as low-risk elements, making them excellent candidates to explore their potential across various applications.

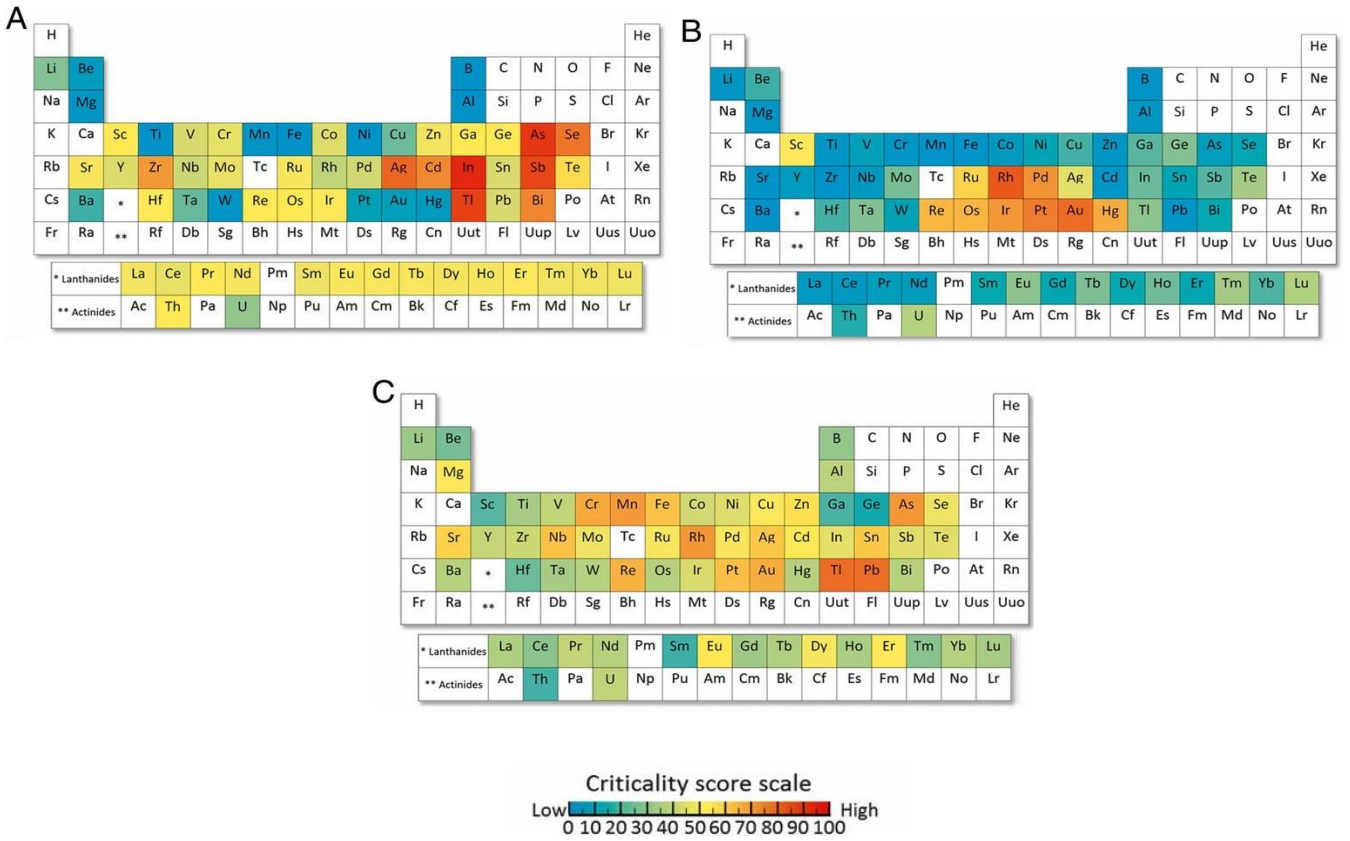


**Figure 1.5.1.** Periodic table representing the critically of 62 metals according to (A) supply risk, (B) environmental implications, and (C) vulnerability to supply restriction. Adapted from reference[102] with permission from Proceedings of the National Academy of Sciences (PNAS)

### 1.5.1 Iron

Iron is the most abundant element on Earth in terms of mass, constituting a significant portion of both the planet's outer and inner cores. Pure metallic iron is rarely found in the lithosphere due to its propensity to oxidize readily in the presence of oxygen and moisture. Iron's incomplete D orbital configuration ([Ar] $3d^6$ $4s^2$) is one of the contributors for its ferromagnetic properties. Exhibiting a range of oxidation states, iron's most prevalent forms are ferrous ($Fe^{2+}$) and ferric ($Fe^{3+}$).[105]

Iron oxides are the predominant form of iron found in nature. This term encompasses oxides, hydroxides, and oxyhydroxides containing Fe (II) and/or Fe (III) cations along with $OH^-$ and/or $O^{2-}$ anions.[106] Among the most common oxides is ferrous oxide (FeO), known as grayback ore, characterized by its cubic crystal structure. Ferric oxide ($Fe_2O_3$), is known as rust, thus having a reddish colour. $Fe_2O_3$ exists in different crystalline morphologies such as α-$Fe_2O_3$ (hematite), β-$Fe_2O_3$, γ-$Fe_2O_3$ (maghemite), and ε-$Fe_2O_3$. Despite sharing the same chemical composition, being $Fe_2O_3$, all ferric oxides have unique crystalline structures. Additionally, iron oxide can manifest as ferrous ferric oxide ($Fe_3O_4$), or magnetite, a dark material formed by Fe (II) and Fe (III).[105]

Magnetite and maghemite are the iron oxides most utilized in nanotechnology. Magnetite features a cubic inverse spinel crystal structure, spinels are described by the formula $AB_2O_4$, where A represents $Fe^{2+}$ and B represents $Fe^{3+}$, occupying tetrahedral or octahedral cation sites, respectively, while oxygen fills the anion sites (Figure 1.5.2 A).[107,108] Magnetite is sensitive to oxidation, transforming into maghemite, which shares a similar cubic spinel structure. However, in maghemite, most of the iron exists in the trivalent state, resulting in cation vacancy sites in some of the octahedral positions (Figure 1.5.2 B).[107] Despite a few structural differences, both, $Fe_3O_4$ and γ-$Fe_2O_3$ exhibit similar magnetic properties, a topic to be explored further in the subsequent section.

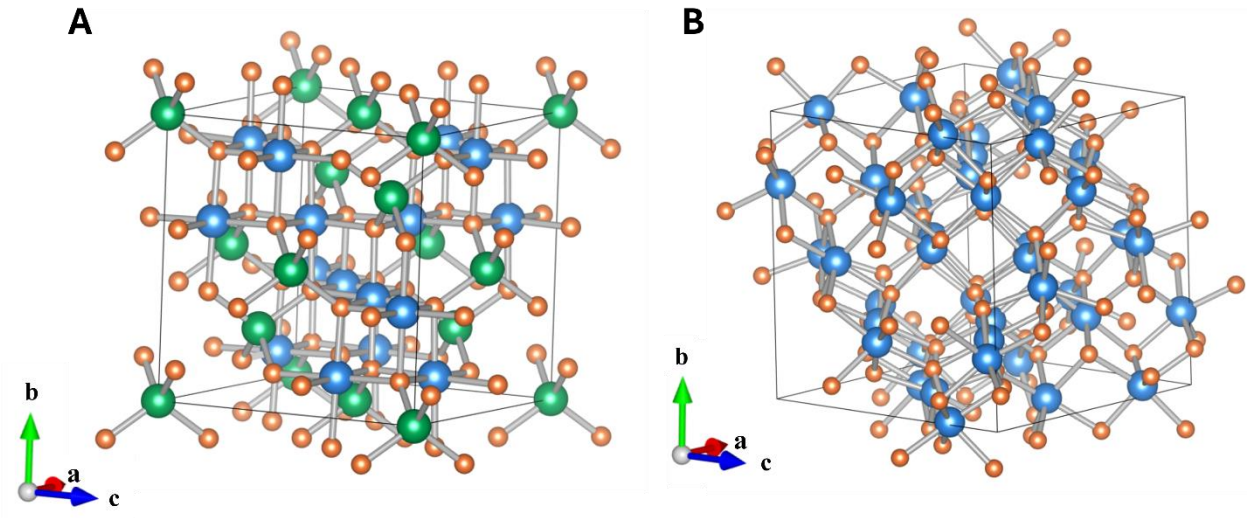


**Figure 1.5.2.** Crystal structure of (A) magnetite ($Fe_3O_4$), and (B) maghemite ($\gamma$-$Fe_2O_3$). In magnetite, $Fe^{2+}$ ions (green spheres) occupy the tetrahedral interstices, each bound to four $O^{2-}$ ions (orange spheres). $Fe^{3+}$ ions (blue spheres) occupy the octahedral positions, each bound to six $O^{2-}$ ions. In maghemite, $Fe^{3+}$ ions (blue spheres) can be surrounded by either six or four $O^{2-}$ ions. Crystal structures were drawn with the VESTA software,[102] using data from the Materials Project for $Fe_2O_3$ (mp-565814) and for $Fe_3O_4$ (mp-19306) from database version v2023.11.1.[121]

### 1.5.2 Iron oxide nanoparticles

One of the most interesting properties of nanosized iron oxides is their distinctive magnetic behaviour. While bulk magnetite exhibits ferromagnetic properties, at the nanoscale, it transitions to a superparamagnetic material. To comprehend this shift in magnetic behaviour it is essential to explore some fundamental concepts of magnetism. First, the magnetic effect arises from the movement of particles possessing mass and electric charge, such as electrons, holes, protons, and ions, implying that all materials exhibit some level of magnetism.[109] How materials behave to an external magnetic field will depend on how those particles align under its influence. In bulk materials, the particles can aggregate and align in the same direction, forming multiple domains,[109] which can be seen in the multi-domain structure in Figure 1.5.3. Typically, due to varying

alignment directions of each domain, the magnetic orientations cancel each other out. However, in ferromagnetic materials, their crystalline structures allow for coupled interaction between domains, all having magnetic moments of equal magnitude, thus allowing for permanent magnetization.[110] Ferromagnetic materials are characterized by their high coercivity, which is the resistance of the material to changes in magnetization, thus having permeant magnetization, even after the external magnetic field is removed.

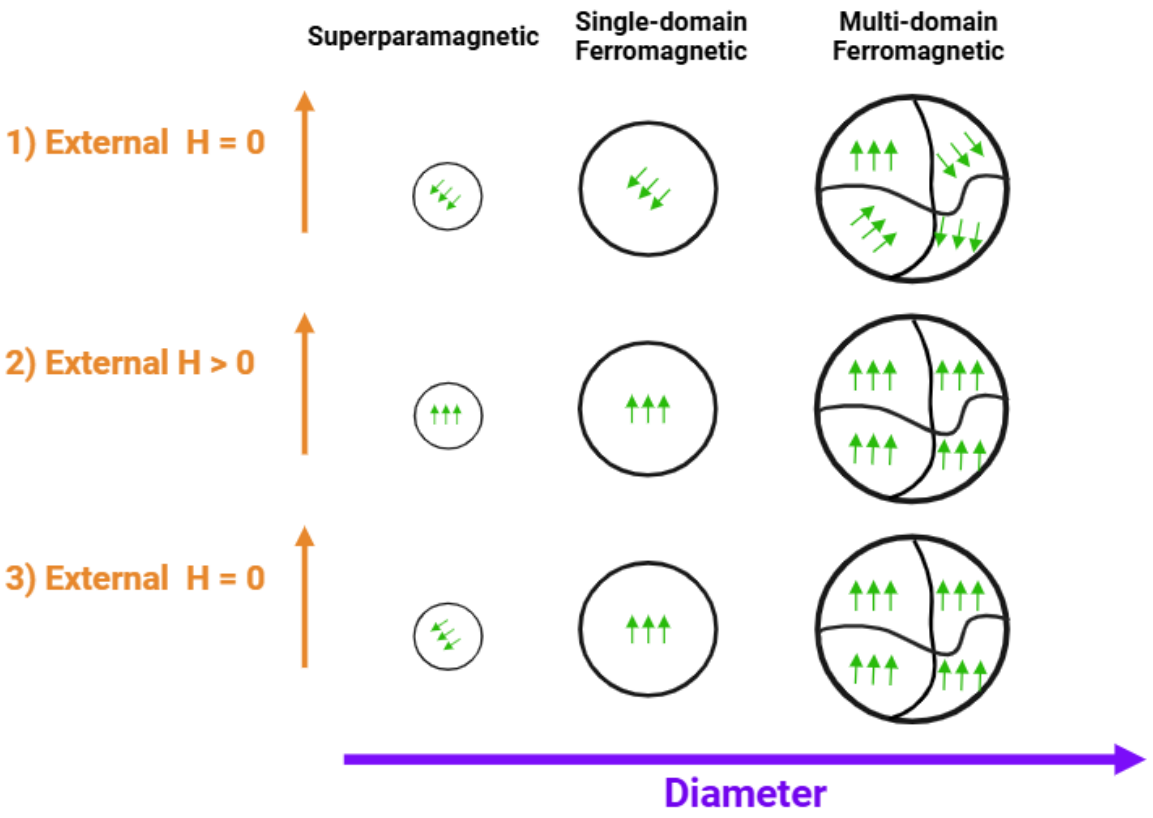


**Figure 1.5.3.** Diagram illustrating the transition of the magnetic states with changes in particle diameter. Bulk ferromagnetic materials consist of a multi-domain structure, which transitions to a single domain and eventually to a superparamagnetic as the particle diameter decreases. From top to bottom, the behaviour of particles under an external magnetic field (with strength H) is shown. Ferromagnetic materials retain their magnetization even after the magnetic field is removed (H=0, bottom), while superparamagnetic materials lose magnetization. Green arrows represent particles with mass and electronic charges.

As material size decreases, it becomes increasingly challenging to form domain walls. Below a critical size, particles become single-domain structures (Figure 1.5.3). Further reduction in size leads to a critical particle diameter where coercivity reaches zero. In simpler terms, at room temperature, the thermal energy for particle rearrangement surpasses the anisotropic energy for particle alignment, consequently, the material is easily demagnetized once the magnetic field is removed (Figure 1.5.3).[109,110] This behaviour characterizes superparamagnetic materials, which appear in iron oxide nanoparticles with diameters below 20 nm.

For the synthesis of nanometric iron oxides, various methods have been established, but the most used is coprecipitation. This approach offers the advantage of being a convenient means to synthesize MNP in aqueous solutions without generating toxic intermediates or requiring organic solvents. Additionally, coprecipitation can be performed at relatively low temperatures (up to 100°C) and does not require complex precursors. In coprecipitation, stoichiometric quantities of Fe (III) and Fe (II) are mixed in an aqueous medium, under an inert atmosphere, to produce $Fe_3O_4$, a 2:1 ratio of $Fe^{3+}$ to $Fe^{2+}$ must be used. Subsequently, a base is introduced to raise the pH level. At higher pH levels, the stable iron ions combine and precipitate out of the solution, forming solid $Fe_3O_4$ (Scheme 1.5.1).[108,109] By adjusting the pH to lower values, changing iron ions stoichiometry, or conducting the precipitation under air one obtains other iron oxides. Additionally, post-synthetic calcination can modify the crystalline structure of the final material.

$$Fe^{2+} + 2Fe^{3+} + 8OH^- \longrightarrow Fe_3O_{4\,(s)} + 4H_2O \qquad \text{(Equation 1)}$$

**Scheme 1.5.1**. General chemical balanced equation for the co-precipitation method using $Fe^{2+}$ and $Fe^{3+}$ in alkaline environment.

Despite its simplicity, the synthesis of MNP presents challenges related to achieving monodispersed size and shape, controlling crystallinity, preventing agglomeration, and ensuring long-term stability. To exert control over the resulting product, various parameters must be carefully adjusted, including the speed of base addition, temperature, concentration of reagents,

pH, and reaction time. Furthermore, stabilizing agents, such as surfactants and polymers, are often incorporated to prevent particle aggregation.[110]

### 1.5.3 Titanium

Titanium is the 9$^{th}$ most abundant element in Earth's crust. Pure bulk Ti has a silver colour, and it is known for its strength and low density, properties that find applications in aircraft and submarine manufacture, as a pure metal or an alloy. Titanium alloys, like Ti-6Al-4V, also due to their low toxicity, and high resistivity are ideal candidates for joint replacements and tooth implants.[111] Titanium easily interacts with oxygen, generating titanium (IV) dioxide ($TiO_2$), that different from pure metal, and presents a white colour. Similar to pure titanium, $TiO_2$ also have important commercial applications, being used as white pigments in house paint, plastic, and food colouring.

Titanium dioxide exists in three primary crystal forms: anatase, rutile, and brookite. Anatase is the most active form due to its high surface energy and abundance of active sites. When heated, anatase undergoes an irreversible transformation to rutile, which is the most thermostable crystalline structure. Brookite is characterized by its orthorhombic crystal structure (Figure 1.5.4 B) and it has less applications than the other two structures due to its challenging synthetic process, as it often appears as a by-product during precipitation in acidic conditions, rarely forming a pure crystal structure.[112] Both anatase and rutile exhibit tetragonal structures with titanium atoms arranged in octahedral coordination (Figure 1.5.4 A and C). In anatase, each Ti octahedra shares four edges, forming zigzag chains parallel to the [221] plane (Figure 1.5.4 A).[113] In rutile, the octahedra share only two edges, forming long octahedral chains along the [001] plane (c-axis) (Figure 1.5.4 C).[114] The transition from anatase to rutile involves the rotation of half of the titanium octahedra, resulting in a structural rearrangement.[115]

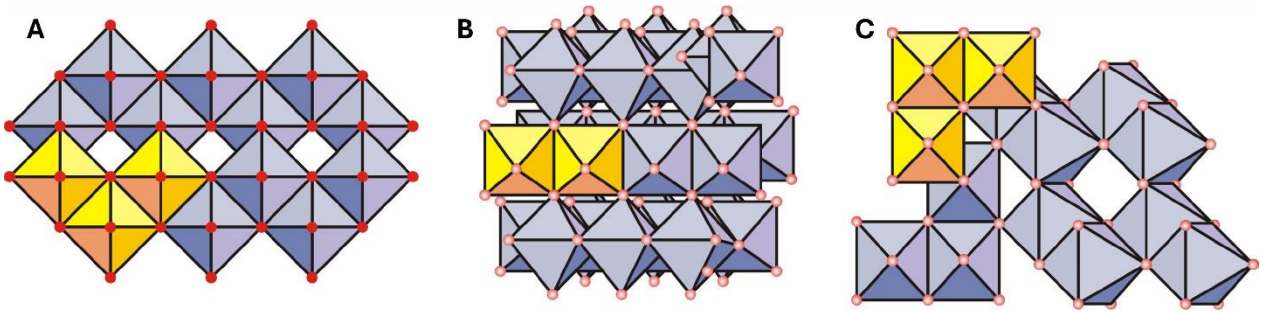


**Figure 1.5.4.** Representation of the crystal structure of anatase (A), brookite (B) and rutile (C) $TiO_2$. $TiO_6$ octahedra are represented by purple and yellow octahedra. Red spheres represent $O^{2-}$ ions. The highlighted yellow octahedra show 4 edge sharing forming zig-zag chains in anatase (A), the edge and corner sharing in brookite (B) and the edge sharing along the c-axis, interlinked by corner sharing in rutile (B). Image reproduced with permission from reference[113] Copyright 2010, Elsevier

### 1.5.4 Titanium dioxide nanoparticles

Nanometric $TiO_2$ is a well-known semiconductor recognized for its pivotal role in photocatalysis. Its significance as a photocatalyst rises from its large band-gap energy, measured at 3.2 eV and 3.0 eV, for anatase and rutile respectively. This characteristic enables photoexcitation in the UV spectrum (< 400 nm). Its large band gap means that the produced $e^-/h^+$ pair has sufficient energy for several redox processes, that can be used in synthetic organic chemistry, pollutant degradation, and energy generation.[22] Despite its remarkable potential, the photocatalytic efficacy of $TiO_2$ photocatalysts often encounters limitations due to the rapid recombination of photogenerated charge carriers, which primarily occur through non-radiative decay. To circumvent this challenge and optimize the utilization of charge carriers, $TiO_2$ NPs are commonly decorated with metal nanoparticles, serving as electron traps.

The synthesis of nanometric $TiO_2$ is primarily accomplished through the sol-gel process.[117]This can be performed using either an alcohol-based method, which employs a metal alkoxide as a precursor, or an aqueous-based route, which uses an inorganic metal salt.[118,119] Metal alkoxides are highly polar due to their metal-oxygen bonds. When water is added, these bonds undergo simultaneous hydrolysis and polycondensation reactions, leading to the formation of a gel

matrix with a continuous lattice structure, such as M-O-M or M-H-M.[118] Complexing agents can be employed to control the hydrolysis and condensation steps by enhancing the precursor's stability in the presence of water. For example, the acetate ions, in acetic acid, can act as a chelating agent, coordinating with titanium leading to more stable bonds. As a result, the speed of gel formation can be controlled.[120] Once the gel is formed, it can be molded into various shapes such as fine particles, thin films, fibres, or membranes. The final crystalline material is obtained by drying the gel under heat or supercritical conditions.

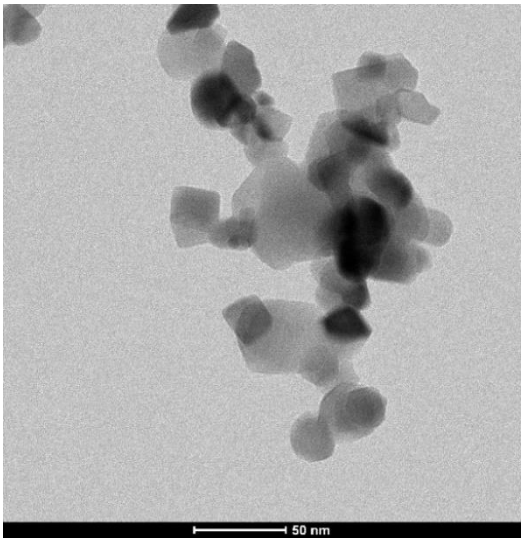


**Figure 1.5.5.** Representative TEM image of commercial P25 nanoparticles. Scale Bar = 50 nm.

$TiO_2$ is frequently commercially available as the nanopowder Degussa P25. This material consists of nanoparticles with diameters ranging from 10 to 50 nm (Figure 1.5.5), composed of anatase and rutile crystallites, typically in ratios of 70:30 or 80:20.[121] The polycrystalline structure of P25 enhances its photocatalytic activity due to the smaller band gap and crystal size of rutile, as well as the higher charge separation induced by the different crystal phases. Consequently, P25 gained recognition as a benchmark photocatalyst.[120,121] Despite its excellent photocatalytic properties, P25's powder form presents challenges for scaling up, due to its laborious separation process. Addressing these challenges by developing new formats and compositions of $TiO_2$ to

facilitate separation is one of the objectives of this thesis and will be discussed in subsequent chapters.

## 1.6 Objectives

This thesis seeks to expand the understanding and improve the application potential of iron- and titanium-based nanomaterials, with a focus on their roles in medical, environmental, and catalytic fields. Noble metals are traditionally preferred for many of these applications, however, they are increasingly recognized as critical, high-risk resources, so this research aims to establish iron and titanium nanostructures as sustainable and viable alternatives. The primary objectives of this work are as follows:

1) To develop and optimize environmentally friendly fabrication methods for iron- and titanium-based nanomaterials. Emphasis will be placed on one-pot synthesis methods wherever possible, aiming for cost-effectiveness and reduced environmental impact.
2) To quantify the light-driven activity of these nanomaterials for targeted applications, such as antimicrobial effects against specific microorganisms, degradation of organic pollutants, or catalysis in the synthesis of novel molecules. This includes assessing efficiency under varied light sources and intensities to establish their suitability for practical applications.
3) To evaluate the performance of these nanomaterials in their intended application settings, focusing on stability, toxicity, and reusability. This includes assessing their biocompatibility for medical applications, resilience under operational conditions for environmental uses, and durability for repeated catalytic cycles.

## 1.7 References


(1) Feynman, R. P. There's Plenty of Room at the Bottom—An Invitation to Enter a New Field of Physics. *Caltech Eng. Sci.* 1960, *23*, 5.

(2) Taniguchi, N. On the Basic Concept of'nano-Technology'. In *Proc. Intl. Conf. Prod. Eng. Tokyo, Part II, 1974*; Japan Society of Precision Engineering, 1974.

(3) Bayda, S.; Adeel, M.; Tuccinardi, T.; Cordani, M.; Rizzolio, F.; Baeza, A. The History of Nanoscience and Nanotechnology: From Chemical-Physical Applications to Nanomedicine. *Molecules* 2020, *25*, 112.

(4) Baig, N.; Kammakakam, I.; Falath, W.; Kammakakam, I. Nanomaterials: A Review of Synthesis Methods, Properties, Recent Progress, and Challenges. *Mater. Adv.* Royal Society of Chemistry March 21, 2021, pp 1821–1871.

(5) Mansoori, G. A.; Soelaiman, T. A. F. Nanotechnology-An Introduction for the Standards Community. *J. ASTM Int.* 2005, *2* (6).

(6) Bayda, S.; Adeel, M.; Tuccinardi, T.; Cordani, M.; Rizzolio, F. The History of Nanoscience and Nanotechnology: From Chemical–Physical Applications to Nanomedicine. *Molecules* 2019, *25* (1), 112.

(7) Binnig, G.; Quate, C. F.; Gi, E. L.; Gerber, C. Atomic Force Microscope. *Phys. Rev. Lett.* 1986, *56* (9), 930–934.

(8) Binnig, G.; Rohrer, H. The Scanning Tunneling Microscope. *Sci. Am.* 1985, *253* (2), 50–58.

(9) Heiligtag, F. J.; Niederberger, M. The Fascinating World of Nanoparticle Research. *Mater. Today* 2013, *16*, 262–271.

(10) Colomban, P. The Use of Metal Nanoparticles to Produce Yellow, Red and Iridescent Colour, from Bronze Age to Present Times in Lustre Pottery and Glass: Solid State Chemistry, Spectroscopy and Nanostructure. *J. Nano Res.* 2009, *8*, 109–132.

(11) Freestone, I.; Meeks, N.; Sax, M.; Higgitt, C. The Lycurgus Cup - A Roman Nanotechnology. *Gold Bull.* 2008, *40* (4), 270–277.

(12) Edwards, P. P.; Thomas, J. M. Gold in a Metallic Divided State - From Faraday to Present-Day Nanoscience. *Angew. Chem. Int. Ed.* 2007, *46* (29), 5480–5486.

(13) Thompson, D. Michael Faraday's Recognition of Ruby Gold: The Birth of Modern Nanotechnology: His 1857 Lecture to the Royal Society in London. *Gold Bull* 2007, *40* (4), 267–269.

(14) Jana, J.; Ganguly, M.; Pal, T. Enlightening Surface Plasmon Resonance Effect of Metal Nanoparticles for Practical Spectroscopic Application. *RSC adv.* 2016, *6* (89), 86174–86211.

(15) El-Sayed, M. A. Small Is Different: Shape-, Size-, and Composition-Dependent Properties of Some Colloidal Semiconductor Nanocrystals. *Acc. Chem. Res.* 2004, *37* (5), 326–333.

(16) El-Sayed, M. A. Some Interesting Properties of Metals Confined in Time and Nanometer Space of Different Shapes. *Acc. Chem. Res.* 2001, *34* (4), 257–264.

(17) M. Smith, A.; Nie, S. Semiconductor Nanocrystals: Structure, Properties, and Band Gap Engineering. *Acc. Chem. Res.* 2009, *43* (2), 190–200.

(18) Paranjape, V. V; Paranjape, B. V. Phonon Excitation by Electric Field in Semiconductors. *Phys. Rev.* 1968, *166* (3), 757.

(19) Mills, A.; Le Hunte, S. An Overview of Semiconductor Photocatalysis. *J. Photochem. Photobiol. A* 1997, *108* (1), 1–35.

(20) Li, J.; Zhang, J. Z. Optical Properties and Applications of Hybrid Semiconductor Nanomaterials. *Coord. Chem. Rev.* 2009, *253* (23–24), 3015–3041.

(21) Nayak, M. K.; Singh, J.; Singh, B.; Soni, S.; Pandey, V. S.; Tyagi, S. Introduction to Semiconductor Nanomaterial and Its Optical and Electronics Properties. In *Metal Semiconductor Core-Shell Nanostructures for Energy and Environmental Applications*; Elsevier, 2017; pp 1–33.

(22) Schneider, J.; Matsuoka, M.; Takeuchi, M.; Zhang, J.; Horiuchi, Y.; Anpo, M.; Bahnemann, D. W. Understanding TiO2 Photocatalysis: Mechanisms and Materials. *Chem. Rev.* 2014, *114* (19), 9919–9986.

(23) Roduner, E. Size Matters: Why Nanomaterials Are Different. *Chem. Soc. Rev.* 2006, *35* (7), 583–592.

(24) Nagarajan, R. Nanoparticles: Building Blocks for Nanotechnology. In *Nanoparticles: Synthesis, Stabilization, Passivation, and Functionalization*; 2008; Vol. 996, pp 2–14.

(25) Lyu, H.; Gao, B.; He, F.; Ding, C.; Tang, J.; Crittenden, J. C. Ball-Milled Carbon Nanomaterials for Energy and Environmental Applications. *ACS Sustain. Chem. Eng.* 2017, *5* (11), 9568–9585.

(26) Yue, W.; Wang, Z.; Yang, Y.; Chen, L.; Syed, A.; Wong, K.; Wang, X. Electron-Beam Lithography of Gold Nanostructures for Surface-Enhanced Raman Scattering. *J. Micromech. Microeng.* 2012, *22* (12), 125007.

(27) Abid, N.; Khan, A. M.; Shujait, S.; Chaudhary, K.; Ikram, M.; Imran, M.; Haider, J.; Khan, M.; Khan, Q.; Maqbool, M. Synthesis of Nanomaterials Using Various Top-down and Bottom-up Approaches, Influencing Factors, Advantages, and Disadvantages: A Review. *Adv. Colloid Interface Sci.* 2022, *300*, 102597.

(28) Palgrave, R. G.; Parkin, I. P. Aerosol Assisted Chemical Vapor Deposition Using Nanoparticle Precursors: A Route to Nanocomposite Thin Films. *J. Am. Chem. Soc.* 2006, *128* (5), 1587–1597.

(29) Mohammadi, S.; Harvey, A.; Boodhoo, K. V. K. Synthesis of $TiO_2$ Nanoparticles in a Spinning Disc Reactor. *J. Chem. Eng.* 2014, *258*, 171–184.

(30) Reiser, J. T.; Ryan, J. V; Wall, N. A. Sol−Gel Synthesis and Characterization of Gels with Compositions Relevant to Hydrated Glass Alteration Layers. *ACS Omega* 2019, *4* (15), 16257–16269.

(31) Turkevich, J.; Stevenson, P. C.; Hillier, J. A Study of the Nucleation and Growth Processes in the Synthesis of Colloidal Gold. *Faraday Discuss.* 1951, *11* (0), 55–75.

(32) Stamplecoskie, K. G.; Scaiano, J. C. Silver as an Example of the Applications of Photochemistry to the Synthesis and Uses of Nanomaterials. *Photochem. Photobiol.* 2012, *88* (4), 762–768.

(33) Scaiano, J. C.; Stamplecoskie, K. G.; McGilvray, K. L.; Pacioni, N. L. A Paradigm for the Radical-Mediated Photochemical Synthesis of Metal Nanostructures. In *Encyclopedia of Radicals in Chemistry, Biology and Materials*; John Wiley & Sons, Ltd, 2012.

(34) McGilvray, K. L.; Decan, M. R.; Wang, D.; Scaiano, J. C. Facile Photochemical Synthesis of Unprotected Aqueous Gold Nanoparticles. *J. Am. Chem. Soc.* 2006, *128* (50), 15980–15981.

(35) Chen, G.; Li, R.; Huang, L. Advances in Photochemical Deposition for Controllable Synthesis of Heterogeneous Catalysts. *Nanoscale* 2023, *15*, 13909.

(36) Pedroso-Santana, S.; Fleitas-Salazar, N. The Use of Capping Agents in the Stabilization and Functionalization of Metallic Nanoparticles for Biomedical Applications. *Part. Syst. Charact.* 2023, *40* (2), 2200146.

(37) Nik, A. B.; Zare, H.; Razavi, S.; Mohammadi, H.; Ahmadi, P. T.; Yazdani, N.; Bayandori, M.; Rabiee, N.; Mobarakeh, J. I. Smart Drug Delivery: Capping Strategies for Mesoporous Silica Nanoparticles. *Micropor. Mesopo. Mater.* 2020, *299*, 110115.

(38) Yadav, A.; Kumar, H.; Sharma, R.; Kumari, R. Synthesis, Processing, and Applications of 2D (Nano) Materials: A Sustainable Approach. *Surf. Interfaces* 2023, *39*, 102925.

(39) Jin, T.; Han, Q.; Wang, Y.; Jiao, L.; Jin, T.; Han, Q.; Wang, Y.; Jiao, L. 1D Nanomaterials: Design, Synthesis, and Applications in Sodium-Ion Batteries. *Small* 2018, *14* (2), 1703086.

(40) Garnett, E.; Mai, L.; Yang, P. Introduction: 1D Nanomaterials/Nanowires. *Chem. Rev.* 2019, *119* (15), 8955–8957.

(41) Reneker, D. H.; Chun, I. Nanometre Diameter Fibres of Polymer, Produced by Electrospinning. *Nanotechnology* 1996, *7* (3), 216.

(42) Li, D.; Xia, Y. Fabrication of Titania Nanofibers by Electrospinning. *Nano Lett* 2003, *3* (4), 555–560.

(43) Ziabari, M.; Mottaghitalab, V.; Haghi, A. K. Application of Direct Tracking Method for Measuring Electrospun Nanofiber Diameter. *Braz. J. Chem. Eng.* 2009, *26* (01), 53–62.

(44) Rocca, D. M.; Vanegas, J. P.; Fournier, K.; Becerra, M. C.; Scaiano, J. C.; Lanterna, A. E. Biocompatibility and Photo-Induced Antibacterial Activity of Lignin-Stabilized Noble Metal Nanoparticles. *RSC adv.* 2018, *8* (70), 40454–40463.

(45) Liu, Z.; Lin, C. H.; Hyun, B. R.; Sher, C. W.; Lv, Z.; Luo, B.; Jiang, F.; Wu, T.; Ho, C. H.; Kuo, H. C.; He, J. H. Micro-Light-Emitting Diodes with Quantum Dots in Display Technology. *Light sci. appl.* 2020, *9* (1), 1–23.

(46) Jariwala, D.; Sangwan, V. K.; Lauhon, L. J.; Marks, T. J.; Hersam, M. C. Carbon Nanomaterials for Electronics, Optoelectronics, Photovoltaics, and Sensing. *Chem. Soc. Rev.* 2013, *42*, 2824.

(47) Khot, L. R.; Sankaran, S.; Maja, J. M.; Ehsani, R.; Schuster, E. W. Applications of Nanomaterials in Agricultural Production and Crop Protection: A Review. *Crop Prot.* 2012, *35*, 64–70.

(48) Lima, A. C.; Ceragioli, H. J.; Cardoso, K. C.; Peterlevitz, A. C.; Zanin, H. G.; Baranauskas, V.; Silva, M. J. Synthesis and Application of Carbon Nanostructures on the Germination of Tomato Seeds. In *International Conference on Food and Agriculture: Applications of Nanotechnologies NanoAgri*; 2010.

(49) LIU, X. mei; Feng, Z. bin; Zhang, F. dao; Zhang, S. qing; He, X. sheng. Preparation and Testing of Cementing and Coating Nano-Subnanocomposites of Slow/Controlled-Release Fertilizer. *Agr. Sci. China* 2006, *5* (9), 700–706.

(50) Dekkers, S.; Krystek, P.; Peters, R. J. B.; Lankveld, D. P. K.; Bokkers, B. G. H.; van Hoeven-Arentzen, P. H.; Bouwmeester, H.; Oomen, A. G. Presence and Risks of Nanosilica in Food Products. *Nanotoxicology* 2011, *5* (3), 393–405.

(51) Morsella, M.; d'Alessandro, N.; E. Lanterna, A.; C. Scaiano, J. Improving the Sunscreen Properties of $TiO_2$ through an Understanding of Its Catalytic Properties. *ACS Omega* 2016, *1* (3), 464–469.

(52) Bashir, S.; Liu, J. Nanomaterials and Their Application. In *Advanced Nanomaterials and Their Applications in Renewable Energy*; Elsevier: Neitherlands, 2015; pp 1–50.

(53) Khalil, M.; Kadja, G. T. M.; Ilmi, M. M. Advanced Nanomaterials for Catalysis: Current Progress in Fine Chemical Synthesis, Hydrocarbon Processing, and Renewable Energy. *J. Ind. Eng. Chem.* 2021, *93*, 78–100.

(54) Jha, R.; Pal, R.; Chakraborty, D.; Chattaraj, P. K. Principles of Catalysis. *Eng. Mater.* 2023, 95–113.

(55) Scaiano, J. C.; Lanterna, A. E. Is Single-Molecule Fluorescence Spectroscopy Ready to Join the Organic Chemistry Toolkit? A Test Case Involving Click Chemistry. *J. Org. Chem.* 2017, *82* (10), 5011–5019.

(56) Costa, P.; Sandrin, D.; Scaiano, J. C. Real-Time Fluorescence Imaging of a Heterogeneously Catalysed Suzuki-Miyaura Reaction. *Nat. Catal.* 2020, *3*, 427–437.

(57) Phan, N. T. S.; Van Der Sluys, M.; Jones, C. W. On the Nature of the Active Species in Palladium Catalyzed Mizoroki–Heck and Suzuki–Miyaura Couplings – Homogeneous or Heterogeneous Catalysis, A Critical Review. *Adv. Synth. Catal.* 2006, *348* (6), 609–679.

(58) Melody Esfandiari, N.; A. Blum, S. Homogeneous vs Heterogeneous Polymerization Catalysis Revealed by Single-Particle Fluorescence Microscopy. *J. Am. Chem. Soc.* 2011, *133* (45), 18145–18147.

(59) Dery, S.; Friedman, B.; Shema, H.; Gross, E. Mechanistic Insights Gained by High Spatial Resolution Reactivity Mapping of Homogeneous and Heterogeneous (Electro) Catalysts. *Chem. Rev.* 2023, *123* (9), 6003–6038.

(60) Liu, H.; Han, L.; Duan, X.; Sun, H.; Wang, S.; Zhang, J. Photothermal Catalytic C1 Conversion on Supported Catalysts. *Energy adv.* 2023, *2*, 1541–1564.

(61) Shihao, D. U.; Xuanang, B.; Yunxuan, Z.; Run, S.; Tierui, Z. Progress and Prospect of Photothermal Catalysis. *Chem. Res. Chin. Univ.* 2021, *2022* (3), 723–734.

(62) Sarina, S.; Jaatinen, E.; Xiao, Q.; Ming Huang, Y.; Christopher, P.; Cai Zhao, J.; Yong Zhu, H. Photon Energy Threshold in Direct Photocatalysis with Metal Nanoparticles: Key Evidence from the Action Spectrum of the Reaction. *J. Phys. Chem. Lett.* 2017, *8* (11), 2526–2534.

(63) Xiong, L.; Tang, J. Strategies and Challenges on Selectivity of Photocatalytic Oxidation of Organic Substances. *Adv. Energy Mater.* 2021, *11* (8), 2003216.

(64) Fagnoni, M.; Dondi, D.; Ravelli, D.; Albini, A. Photocatalysis for the Formation of the C−C Bond. *Chem. Rev.* 2007, *107* (6), 2725–2756.

(65) Ma, D.; Liu, A.; Li, S.; Lu, C.; Chen, C. $TiO_2$ Photocatalysis for C–C Bond Formation. *Catal. Sci. Technol.* 2018, *8* (8), 2030–2045.

(66) Luna, M.; Barawi, M.; Gómez-Moñivas, S.; Colchero, J.; Rodríguez-Peña, M.; Yang, S.; Zhao, X.; Lu, Y.-H.; Chintala, R.; Reñones, P. Photoinduced Charge Transfer and Trapping on Single Gold Metal Nanoparticles on $TiO_2$. *ACS Appl. Mater. Interfaces.* 2021, *13* (42), 50531–50538.

(67) Lio, H.; Gil, M.; Price, T. W.; Chelani, K.; Bouillard, J.-S. G.; Calaminus, S. D. J.; Stasiuk, G. J. NIR-Quantum Dots in Biomedical Imaging and Their Future. *iScience* 2021, *24* (1), 102189.

(68) Ray, P. C. Size and Shape Dependent Second Order Nonlinear Optical Properties of Nanomaterials and Their Application in Biological and Chemical Sensing. *Chem. Rev.* 2010, *110* (9), 5332–5365.

(69) L.C. Guimaraes; P. A. C. Costa; S. R. A. S. Júnior; H. A. S. Ferreira; A. C. S. Braga; L. C.de Oliveira; M. M.Figueiredo; S. Shepherd; A. Hamilton; C. M. Queiroz-Junior; W. N. da Silva; N.J. A. da Silva; M. T. R. Alves; A. K. Santos; K. K. S. de Faria; F. M. Marim; H. Fukumasu; A. Birbrair; A. Teixeira-Carvalho;

P. P. G. Guimaraes. Nanoparticle-Based DNA Vaccine Protects against SARS-CoV-2 Variants in Female Preclinical Models. *Nat. Commun.* 2024, *15* (1), 590.

(70) Polack, F. P.; Thomas, S. J.; Kitchin, N.; Absalon, J.; Gurtman, A.; Lockhart, S.; Perez, J. L.; Pérez Marc, G.; Moreira, E. D.; Zerbini, C.; Bailey, R.; Swanson, K. A.; Roychoudhury, S.; Koury, K.; Li, P.; Kalina, W. V.; Cooper, D.; Frenck, R. W.; Hammitt, L. L.; Türeci, Ö.; Nell, H.; Schaefer, A.; Ünal, S.; Tresnan, D. B.; Mather, S.; Dormitzer, P. R.; Şahin, U.; Jansen, K. U.; Gruber, W. C. Safety and Efficacy of the BNT162b2 MRNA Covid-19 Vaccine. *N. Engl. J. Med.* 2020, *383* (27), 2603–2615.

(71) Elechiguerra, J. L.; Burt, J. L.; Morones, J. R.; Camacho-Bragado, A.; Gao, X.; Lara, H. H.; Yacaman, M. J. Interaction of Silver Nanoparticles with HIV-1. *J. Nanotechnol.* 2005, *3* (1), 1–10.

(72) Lara, H. H.; Ixtepan-Turrent, L.; Garza-Treviño, E. N.; Rodriguez-Padilla, C. PVP-Coated Silver Nanoparticles Block the Transmission of Cell-Free and Cell-Associated HIV-1 in Human Cervical Culture. *J. Nanobiotechnology* 2010, *8* (1), 1–11.

(73) Bhattacharya, R.; Mukherjee, P.; Xiong, Z.; Atala, A.; Soker, S.; Mukhopadhyay, D. Gold Nanoparticles Inhibit VEGF165-Induced Proliferation of HUVEC Cells. *Nano Lett* 2004, *4* (12), 2479–2481.

(74) Mukherjee, P.; Bhattacharya, R.; Wang, P.; Wang, L.; Basu, S.; Nagy, J. A.; Atala, A.; Mukhopadhyay, D.; Soker, S. Antiangiogenic Properties of Gold Nanoparticles. *Clin. Cancer Res.* 2005, *11* (9), 3530–3534.

(75) Arvizo, R. R.; Bhattacharyya, S.; Kudgus, R. A.; Giri, K.; Bhattacharya, R.; Mukherjee, P. Intrinsic Therapeutic Applications of Noble Metal Nanoparticles: Past, Present and Future. *Chem. Soc. Rev.* 2012, *41* (7), 2943–2970.

(76) Neal, A. L. What Can Be Inferred from Bacterium-Nanoparticle Interactions about the Potential Consequences of Environmental Exposure to Nanoparticles? *Ecotoxicol.* 2008, *17*, 362–371.

(77) Letelier, M. E.; Lepe, A. M.; Faúndez, M.; Salazar, J.; Marín, R.; Aracena, P.; Speisky, H. Possible Mechanisms Underlying Copper-Induced Damage in Biological Membranes Leading to Cellular Toxicity. *Chem. Biol. Interact.* 2005, *151* (2), 71–82.

(78) Quinteros, M. A.; Aristizábal, V. C.; Dalmasso, P. R.; Paraje, M. G.; Páez, P. L. Oxidative Stress Generation of Silver Nanoparticles in Three Bacterial Genera and Its Relationship with the Antimicrobial Activity. *Toxicol. in vitro* 2016, *36*, 216–223.

(79) Liu, Y.; Lee, P. K. H.; Nah, T. Emerging Investigator Series: Aqueous Photooxidation of Live Bacteria with Hydroxyl Radicals under Cloud-like Conditions: Insights into the Production and Transformation of Biological and Organic Matter Originating from Bioaerosols. *Environ. Sci.: Process. Impacts.* 2023, *25* (7), 1150–1168.

(80) Ayala, A.; Muñoz, M. F.; Argüelles, S. Lipid Peroxidation: Production, Metabolism, and Signaling Mechanisms of Malondialdehyde and 4-Hydroxy-2-Nonenal. *Oxid. Med. Cell. Longev.* 2014, *2014*, 1–31.

(81) Abo-zeid, Y.; Williams, G. R. The Potential Anti-infective Applications of Metal Oxide Nanoparticles: A Systematic Review. *Wiley Interdiscip. Rev. Nanomed. Nanobiotechnol.* 2020, *12* (2), 1592.

(82) Aflakian, F.; Mirzavi, F.; Aiyelabegan, H. T.; Soleimani, A.; Navashenaq, J. G.; Karimi-Sani, I.; Zomorodi, A. R.; Vakili-Ghartavol, R. Nanoparticles-Based Therapeutics for the Management of Bacterial Infections: A Special Emphasis on FDA Approved Products and Clinical Trials. *Eur. J. Pharm. Sci.* 2023, 106515.

(83) Linklater, D. P.; Baulin, V. A.; Le Guével, X.; Fleury, J.-B.; Hanssen, E.; Hong Phong Nguyen, T.; Juodkazis, S.; Bryant, G.; Crawford, R. J.; Stoodley, P.; Ivanova, E. P.; Linklater, D. P.; Bryant, G.; Crawford, R. J.; Ivanova, E. P.; Juodkazis, S.; Baulin, V. A.; Guével, X. L.; Fleury, J.; Hanssen, E.; P Nguyen, T. H.; Chi Minh City, H.; Stoodley, V. P.; Stoodley, P. Antibacterial Action of Nanoparticles by Lethal Stretching of Bacterial Cell Membranes. *Adv. Mater.* 2020, *32* (52).

(84) Chen, J.; Ning, C.; Zhou, Z.; Yu, P.; Zhu, Y.; Tan, G.; Mao, C. Nanomaterials as Photothermal Therapeutic Agents. *Prog. Mater. Sci.* 2019, *99*, 1–26.

(85) Ramasamy, M.; Lee, S. S.; Yi, D. K.; Kim, K. Magnetic, Optical Gold Nanorods for Recyclable Photothermal Ablation of Bacteria. *J. Mater. Chem. B* 2014, *2* (8), 981–988.

(86) Mocan, T.; Matea, C. T.; Cojocaru, I.; Ilie, I.; Tabaran, F. A.; Zaharie, F.; Iancu, C.; Bartos, D.; Mocan, L. Photothermal Treatment of Human Pancreatic Cancer Using PEGylated Multi-Walled Carbon Nanotubes Induces Apoptosis by Triggering Mitochondrial Membrane Depolarization Mechanism. *J. Cancer* 2014, *5* (8), 679.

(87) Sztandera, K.; Gorzkiewicz, M.; Klajnert-Maculewicz, B. Gold Nanoparticles in Cancer Treatment. *Mol. Pharmaceutics* 2018, *16* (1), 1–23.

(88) Chen, Y.; Gao, Y.; Chen, Y.; Liu, L.; Mo, A.; Peng, Q. Nanomaterials-Based Photothermal Therapy and Its Potentials in Antibacterial Treatment. *J. Control. Release* 2020, *328*, 251–262.

(89) Zou, L.; Wang, H.; He, B.; Zeng, L.; Tan, T.; Cao, H.; He, X.; Zhang, Z.; Guo, S.; Li, Y. Current Approaches of Photothermal Therapy in Treating Cancer Metastasis with Nanotherapeutics. *Theranostics* 2016, *6* (6).

(90) Chen, J.; Fan, T.; Xie, Z.; Zeng, Q.; Xue, P.; Zheng, T.; Chen, Y.; Luo, X.; Zhang, H. Advances in Nanomaterials for Photodynamic Therapy Applications: Status and Challenges. *Biomaterials* 2020, *237*, 119827.

(91) Dougherty, T. J.; Gomer, C. J.; Henderson, B. W.; Jori, G.; Kessel, D.; Korbelik, M.; Moan, J.; Peng, Q. Photodynamic Therapy. *J Natl. Cancer Inst.* 1998, *90* (12), 889–905.

(92) Vankayala, R.; Huang, Y. K.; Kalluru, P.; Chiang, C. S.; Hwang, K. C. First Demonstration of Gold Nanorods-Mediated Photodynamic Therapeutic Destruction of Tumors via Near Infra-Red Light Activation. *Small* 2014, *10* (8), 1612–1622.

(93) Bourgonje, C. R.; da Silva, D. R. C.; McIlroy, E.; Calvert, N. D.; Shuhendler, A. J.; Scaiano, J. C. Silver Nanoparticles with Exceptional Near-Infrared Absorbance for Photoenhanced Antimicrobial Applications. *J. Mater. Chem. B* 2023, *11* (26), 6114–6122.

(94) Zain, M.; Yasmeen, H.; Yadav, S. S.; Amir, S.; Bilal, M.; Shahid, A.; Khurshid, M. Applications of Nanotechnology in Biological Systems and Medicine. In *Nanotechnology for Hematology, Blood Transfusion, and Artificial Blood*; 2021; Vol. 30.

(95) Ternes, T. A.; Meisenheimer, M.; McDowell, D.; Sacher, F.; Brauch, H. J.; Haist-Gulde, B.; Preuss, G.; Wilme, U.; Zulei-Seibert, N. Removal of Pharmaceuticals during Drinking Water Treatment. *Environ. Sci.Technol.* 2002, *36* (17), 3855–3863.

(96) WHO; UNICEF; World Bank. State of the World's Drinking Water: An Urgent Call to action to Accelerate Progress on Ensuring Safe Drinking Water for All.; Geneva, 2022.

(97) Li, J.; Zhang, D.; Jiang, X.; Zhao, X.; Hu, R.; Zhong, Y.; Zhu, H. Nest-like Multilevel Structured Graphene Oxide-on-Polyacrylonitrile Membranes for Highly Efficient Filtration of Ultrafine Particles. *J. Materiomics* 2019, *5* (3), 422–427.

(98) Chong, M. N.; Jin, B.; Chow, C. W. K.; Saint, C. Recent Developments in Photocatalytic Water Treatment Technology: A Review. *Water Res.* 2010, *44* (10), 2997–3027.

(99) Galway, L. P. Boiling over: A Descriptive Analysis of Drinking Water Advisories in First Nations Communities in Ontario, Canada. *Int. J. Environ. Res. Public Health* 2016, *13* (5), 505.

(100) Mahmoud, A. E. D.; Fawzy, M. Nanosensors and Nanobiosensors for Monitoring the Environmental Pollutants. In *Waste Recycling Technologies for Nanomaterials Manufacturing*; Springer, 2021; pp 229–246.

(101) Saharan, V. K.; Pinjari, D. V; Gogate, P. R.; Pandit, A. B. Advanced Oxidation Technologies for Wastewater Treatment: An Overview. *Curr. Pollut. Rep.* 2015, *1*, 167–176.

(102) Lomberg, M.; Ruiz-Trejo, E.; Offer, G. Heavy Metal Ions Removal Using Advanced Oxidation ($UV/H_2O_2$ ) Technique Characterization of Ni-Infiltrated GDC Electrodes for Solid Oxide Cell Applications. *IOP Conf. Ser. Mater. Sci. Eng.* 2020, *870* (1), 012026.

(103) Qasem, N. A. A.; Mohammed, R. H.; Lawal, D. U. Removal of Heavy Metal Ions from Wastewater: A Comprehensive and Critical Review. *NPJ Clean Water* 2021, *4* (1), 1–15

(104) Graedel, T. E.; Harper, E. M.; Nassar, N. T.; Nuss, P.; Reck, B. K. Criticality of Metals and Metalloids. *PNAS* 2015, *112* (14), 4257–4262.

(105) Rhodes, C. J. Endangered Elements, Critical Raw Materials and Conflict Minerals. *Sci. Prog.* 2019, *102* (4), 304–350.

(106) Nuss, P.; Eckelman, M. J. Life Cycle Assessment of Metals: A Scientific Synthesis. *PLoS One* 2014, *9* (7), 101298.

(107) Taghizadeh, S.-M.; Berenjian, A.; Zare, M.; Ebrahiminezhad, A. New Perspectives on Iron-Based Nanostructures. *Process* 2020, *8* (9).

(108) Kharisov, B. I.; Kharissova, O. V.; Rasika Dias, H. V.; Ortiz Méndez, U.; de la Fuente, I. G.; Peña, Y.; Vázquez Dimas, A. Iron-Based Nanomaterials in the Catalysis. In *Advanced Catalytic Materials - Photocatalysis and Other Current Trends*; InTech, 2016; pp 35–68.

(109) Zboril, R.; Mashlan, M.; Petridis, D. Iron(III) Oxides from Thermal Processes Synthesis, Structural and Magnetic Properties, Mössbauer Spectroscopy Characterization, and Applications. *Chem. Mater.* 2002, *14* (3), 969–982.

(110) Ghosh, A.; Srinivas, V.; Sundara, R. Comprehensive Structural and Magnetic Properties of Iron Oxide Nanoparticles Synthesized through Chemical Routes. *J. Alloys Compd.* 2020, *818*, 152931.

(111) Akbarzadeh, A.; Samiei, M.; Davaran, S. Magnetic Nanoparticles: Preparation, Physical Properties, and Applications in Biomedicine. *Nanoscale Res. Lett.* 2012, *7*, 1–13.

(112) Bedanta, S.; Barman, A.; Kleemann, W.; Petracic, O.; Seki, T. Magnetic Nanoparticles: A Subject for Both Fundamental Research and Applications. *J. Nanomater.* 2013, *2013*, 22.

(113) Veiga, C.; Davim, J. P.; Loureiro, A. J. R. Properties and Applications of Titanium Alloys: A Brief Review. *Rev. Adv. Mater. Sci.* 2012, *32* (2), 133–148.

(114) Di Paola, A.; Bellardita, M.; Palmisano, L. Brookite, the Least Known $TiO_2$ Photocatalyst. *Catalysts* 2013, *3*, 36–73.

(115) Khataee, A. R.; Kasiri, M. B. Photocatalytic Degradation of Organic Dyes in the Presence of Nanostructured Titanium Dioxide: Influence of the Chemical Structure of Dyes. *J. Mol. Catal. A Chem.* 2010, *328* (1–2), 8–26.

(116) Hanaor, D. A. H.; Sorrell, C. C. Review of the Anatase to Rutile Phase Transformation. *J. Mater. Sci.* 2011, 855–874.

(117) Lee Penn, R.; Banfield, J. F. Formation of Rutile Nuclei at Anatase {112} Twin Interfaces and the Phase Transformation Mechanism in Nanocrystalline Titania. *Am. Min.* 1999, *84*, 871–876.

(118) Ullattil, S. G.; Periyat, P. Sol-Gel Synthesis of Titanium Dioxide. In *Sol-Gel Materials for Energy, Environment and Electronic Applications*; 2017; pp 271–283.

(119) Livage, J.; Henry, M.; Sanchez, C. Sol-Gel Chemistry of Transition Metal Oxides. *Prog. Solid State Chem.* 1988, *18* (4), 259–341.

(120) Cargnello, M.; Gordon, T. R.; Murray, C. B. Solution-Phase Synthesis of Titanium Dioxide Nanoparticles and Nanocrystals. *Chem. Rev.* 2014, *114* (19), 9319–9345.

(121) Ohtani, B.; Prieto-Mahaney, O. O.; Li, D.; Abe, R. What Is Degussa (Evonik) P25? Crystalline Composition Analysis, Reconstruction from Isolated Pure Particles and Photocatalytic Activity Test. *J. Photoch. Photobio. A* 2010, *216*, 179–182.

(122) Ishigaki, T.; Nakada, Y.; Tarutani, N.; Uchikoshi, T.; Tsujimoto, Y.; Isobe, M.; Ogata, H.; Zhang, C.; Hao, D. Enhanced Visible-Light Photocatalytic Activity of Anatase-Rutile Mixed-Phase Nano-Size Powder given by High-Temperature Heat Treatment. *R. Soc. Open Sci.* 2020, *7* (1), 191539.

(123) Momma, K.; Izumi, F. VESTA 3 for Three-Dimensional Visualization of Crystal, Volumetric and Morphology Data. *J. Appl. Crystallogr.* 2011, *44* (6), 1272–1276.

(124) Jain, A.; Ong, S. P.; Hautier, G.; Chen, W.; Richards, W. D.; Dacek, S.; Cholia, S.; Gunter, D.; Skinner, D.; Ceder, G. Commentary: The Materials Project: A Materials Genome Approach to Accelerating Materials Innovation. *APL mater.* 2013, *1* (1).

# 2. Exploring The Antibacterial Properties of Lignin-Coated Magnetic Nanoparticles Synthesized in a One-Pot Process

This chapter has been adapted from Photochemistry and Photobiology, 2023, 99 (2), 706-715 with permission from Wiley Online Library. To allow for consistent formatting and clarity, some changes have been made.

## 2.1 Preamble to Chapter 2

The following chapter describes the development and characterization of four distinct magnetic nanoparticles (MNPs) utilizing lignin as a capping agent, alongside their applications as potent antibacterial agents. These MNPs exhibited bactericidal responses during extended incubation periods of 16 hours, under dark incubation. However, upon exposure to the near-infrared wavelengths, their antibiotic activity increased to remarkable levels, reaching up to 99.9999% efficacy within a few minutes of treatment. Further enhancements in the bactericidal performance were achieved by incubating bacterial cells and nanoparticles with $H_2O_2$ which augmented •OH production, consequently reducing necessary incubation times to as short as 1-5 min. Magnetic NPs coated with lignin emerge as promising alternatives for fighting infectious diseases given efficiency, manipulability, and biocompatibility.

Our initial efforts to explore earth-abundant elements started with the development of iron oxide NPs coated with lignin. In the early stages of my graduate studies, I was dedicated to learning and testing various synthetic approaches for MNPs. Driven both by personal and by our group's interest we sought to explore the potential health-related applications of the novel materials. Although the synthesis of iron oxides was proven to be relativity straightforward, our initial antibacterial tests revealed that while iron oxide presented a safer alternative, its efficacy against bacterial cells was somewhat compromised. To address this limitation, I then turned my attention to the optimization of the synthetic approach for bimetallic NPs, leveraging the safety and magnetic behaviour of iron oxides while incorporating metals with superior bactericidal

efficiency. To stabilize the nanostructures, we chose to use lignin, a natural byproduct of the pulp industry. Lignin was employed instead of commonly used capping agents like PVP, PEG, oleic acid, or citric acid. Not only does lignin offer a more sustainable alternative, but it also supports ongoing efforts within Canadian industries to add value to this abundant commodity. Expanding applications for lignin could further strengthen Canada's economy by promoting sustainable innovation.

We successfully fabricated hybrids Fe and Ag, as well as Fe and Co with a one-pot synthetic route. These hybrids retained the magnetic properties of Fe while presenting improved antibiotic properties. We also synthesized CoNPs, due to their known antimicrobial activity and magnetic behaviour. Through the implementation of light treatment and Chemo-Dynamic Therapy, we achieved more than 4-log units' bacterial reduction, under short incubation times.

This work culminated in my first publication, which we were honoured to be invited to publish on Photochemistry and Photobiology as part of the special issue celebrating the 50$^{th}$ Anniversary of the American Society for Photobiology.

### 2.2 Post-print version of Manuscript

First published in: Photochemistry and Photobiology, 2023, 99 (2), 706-715

## ABSTRACT

Given the current serious problems with antibiotic resistance, the discovery of novel, unconventional antibacterial drugs are not just important, but also urgent. In this contribution, we report on the synthesis and testing of several composite nanomaterials that may find applications as therapeutic drugs or surface disinfectants. These materials are based on magnetic nanostructures coated with lignin, for example, lignin@FeCo. The magnetic properties of these nanocomposites facilitate removal or localization, while the lignin shell provides biocompatibility. These nanomaterials are mild antibacterials in the absence of light, but when illuminated become powerful antibacterial agents with typically ≥6 log units bacterial reduction in 1 to 5 minutes of irradiation. These materials are strongly absorbing, including in the very useful NIR biological

window, which we illustrate using 810 nm LED irradiation. We also show that in the short time required for antibacterial action, thermal changes are very small (≤5°C). Further, biocompatibility tests using fibroblasts show very limited cell damage and no enhanced adverse effect during 810 nm NIR illumination. As a surface coating for the active material, lignin provides a "trojan horse" strategy to facilitate the antibacterial action.

## INTRODUCTION

The constant emergence of antibiotic resistance and slow development of alternatives is a major threat to global health.[1,2] Traditional antibiotics can easily trigger the development of resistant bacterial strains, limiting their efficiency. Therefore, efficient, and safe solutions for infectious diseases are needed urgently to control future outbreaks. Among the strategies being developed, the use of nano-sized structures has been shown to be a promising solution. Materials such as silver nanoparticles (AgNP) have exceptional antimicrobial properties; however, their colloidal form often limits some applications. In contrast, magnetic nanoparticles (MNPs) are easily separated from solutions or guided using an external magnetic field. MNPs are used in magnetic resonance imaging (MRI), drug delivery, and cancer treatments and have proven effective *in vivo* applications.[2,3] Yet, the use of MNPs as antimicrobial agents is still underexplored; beyond any therapeutic uses, MNPs may find applications in antimicrobial surface treatments.

The use of iron oxide magnetic NPs alone does not have high intrinsic antibacterial properties. Their application in combating bacterial proliferation is often associated with metal doping or light irradiation. In the presence of near-infra-red (NIR) and infra-red light (IR), iron oxide nanoparticles convert the absorbed energy into heat. The use of photo-generated heat to combat infectious diseases and/or cancer cells is the basis of photothermal therapy (PTT).[4,5] It is a convenient treatment since it uses wavelengths that are within the biological window, allowing applications on deep tissues and precisely treating the desired area. However, long-time exposure to the irradiated light may damage normal tissues.

Liu and colleagues[6] demonstrated that the combination of PTT with chemodynamic therapy (CDT) has a synergic effect increasing the antibacterial potency of nanostructures.[6] CDT

explores the nanoenzymatic behaviour of nanoparticles to convert hydrogen peroxide ($H_2O_2$) into toxic hydroxyl radical (•OH) through Fenton/Fenton-like reactions. When compared with natural enzymes, nanoenzymes have higher stability, scoring better antibacterial activity. Yet the high toxicity of •OH is due to its fast reactivity, which also makes it short-lived, limiting the bactericidal performance. Thus, the combination of both therapies takes advantage of local heat generation and radical production to increase cell membrane permeability and lead to cell death.

Here we synthesized MNPs in one pot using lignin as a capping agent. Lignin is produced as a by-product of the pulp and paper industry, that is often discarded. The abundance and underutilization of this biopolymer make it an inexpensive resource to be explored.[7] Lignin has been employed in nanocomposites and has proven to increase the biodegradability and biocompatibility of nanostructures.[7,8] Lignin has a variety of structures depending on the biomass source and pulping process, but in general, they are formed by a complex polyaromatic structure.[9] Lignin-capped nanomaterials, in special AgNPs, have shown controlled ion release, reducing toxicity towards human cells, but keeping effective antibacterial activities[7,10] Despite recent efforts on the valorization of this biopolymer, studies on nanomaterials are limited to the coating of noble metals colloidal nanoparticles.

In this study, we investigated the use of lignin as a capping agent for several magnetic nanoparticles synthesized under mild conditions. We further explored the antibacterial properties of those nanoparticles against Gram-negative and Gram-positive bacteria, searching for the optimal conditions for their applications in the fight against resistant pathogens.

## MATERIALS AND METHODS

### Materials:

Lignin A samples were kindly supplied by FP Innovations (Pointe-Claire, Quebec, Canada), and were produced in Hinton, Alberta. Complete lignin characterization was previously published by our group.[11] Iron chloride II ($FeCl_2$), iron chloride III ($FeCl_3$), cobalt chloride anhydrous ($CoCl_2$) (further dried in the oven), iron nitrate ($Fe(NO)_3$), iron sulphate ($Fe(SO)_4$), silver nitrate ($AgNO_3$), trisodium Citrate, Luria-Bertani (LB) broth, 1,2-benzopyrone (coumarin), and Dulbecco's modified eagle's

medium (DMEM), penicillin-streptomycin were purchased from Sigma-Aldrich. Mueller Hinton (MH) from BD Life Sciences. Dulbecco's phosphate-buffered saline (DPBS), Fetal Calf Serum (FCS), Gentamicin and Trypsin-EDTA (0.25 %) were purchased from Gibco™. Unless specified the chemicals were used as received.

**Synthesis:**

***Lignin@Fe,*** in a 50mL round bottom flask 0.66 g (4.07 mM) (1.4 mM of $Fe^{3+}$) of $FeCl_3$ and 0.20 g (1.59 mM) (0.7 mM of $Fe^{2+}$) of $FeCl_2$ were added to 20 mL of distilled water. The sample was heated at 85°C under argon flow; after approximately 30 minutes 900 µL of a 28% solution of $NH_4^+$ was slowly added, resulting in a black precipitate. Subsequently, 200 µL of Lignin A solution (100 mg/L) was added dropwise. The samples were then kept under heating and argon flow for 30 minutes. The resulting black material was washed 3 times with distilled water at pH 10 and dried under vacuum.

***Lignin@FeAg,*** in a 50mL round bottom flask 1.80 g of $Fe(NO_3)_3 \cdot 9H_2O$ and 0.355 g of $Fe(SO_4) \cdot 7H_2O$ were mixed in 25 mL of distilled water. The solution was heated at 85°C under an argon flow; after approximately 30 minutes 900 µL of a 28% solution of $NH_4^+$ was added, resulting in a black precipitate. To the same pot, 2 mL of 0.16M of aqueous $AgNO_3$ was added, followed by the addition of 2 mM of Tri-sodium citrate. Lastly, 200 µL of Lignin A solution (100 mg/L) was added dropwise and the mixture was kept under heating and argon flow for 30 minutes. The resulting black material was washed 3 times with distilled water at pH 10 and dried under vacuum.

***Lignin@FeCo,*** in a 50 mL round bottom flask, 0.542 g (2 mM of $Fe^{3+}$) of $FeCl_3$ 0.1988 g (1 mM of $Fe^{2+}$) of $FeCl_2$, and 0.909 g $CoCl_3$ (7 mM of $Co^{2+}$) were mixed in 20 mL of distilled water. The solution was heated at 85°C under an argon flow; after approximately 30 minutes, 900 µL of a 28% solution of $NH_4^+$ was added, resulting in a black precipitate. Finally, 200 µL of Lignin A solution (100 mg/L) was added dropwise and the solution was kept under heating and argon flow for 30 minutes. The resulting black material was washed 3 times with distilled water at pH 10 and dried under vacuum.

***Lignin@Co,*** in a round bottom flask 0.236 g of $CoCl_2$ (Anhydrous) (1.8 mM) was added to 100 mL of water. The solution was added to an ice bath (5°C) and purged with argon for 30 min. After 0.155g of $NaBH_4$ (4 mM) was added under constant sonication, forming a black precipitate. Lastly, 1 mL of Lignin A solution (1 g/L) was added, and the solution was kept under sonication for an extra 20 min.

**Characterization:** Transmission electron microscopy (TEM) images were collected on a JEM2100F FETEM (JEOL) operating at 200 kV. Diffuse reflectance measurements were carried out using an Agilent Cary 7000 UV-Vis-NIR Universal Measurement Spectrophotometer coupled with an Agilent praying Mantis accessory. The metal composition of the materials was determined by Inductively Coupled Plasma Optical Emission Spectrometry (ICP-OES), using an Agilent Vista Pro ICP Emission Spectrometer. Approximately 10 mg portions were accurately weighed in triplicate and digested with *aqua regia*. Solutions were further diluted and measured by ICP-OES. The following emission lines were used for quantification when applicable: Fe 238.20 nm, Ag 338.29 nm, and Co 238.89 nm. The percentage of lignin in the nanomaterials was measured using Thermogravimetric analysis (TGA), using a Q5000 IR instrument (TA Instruments; New Castle, DE, USA) under $N_2$ or airflow (120 mL/min) with a heating rate of 10 °C/min (balance gas with nitrogen 10.0 ml/min; sample gas with nitrogen 25.0 ml/min). TGA data were analyzed by using TA Instruments Universal Analysis 2000 Version 4.5 A. Powder X-ray diffraction analysis was carried out at room temperature on Rigaku Ultima IV powder diffractometer in Bregg Brentano geometry, using Cu Kα radiation (λ = 1.5418 Å). Two theta range of 20° to 90° was covered with 0.02° step width and 0.5°/min scan speed.

**Antibacterial tests:**

***Bacterial strains and growth conditions,*** the experiments were performed using *Escherichia coli* CF073 (ATCC700928) and *Staphylococcus aureus (*ATCC25923) Stock cultures were maintained in Tryptone soy broth (TSB) and stored at -80°C in 10 % glycerol.

***Minimum Inhibitory Concentration (MIC)***, Minimum Inhibitory Concentration (MIC) was determined by the broth microdilution method. The initial bacterial inoculum was prepared at a concentration of 1.6 x $10^8$ CFU/mL ($OD_{600}$ = 0.2) in LB broth. Using a 96 well-plate 100 µL of

the bacterial suspension was mixed with 100 µL of MNPs solutions, at concentrations ranging from 1000 to 31.25 mg/L. The MNP stock solution was prepared by dispersing the nanomaterials on sterilized PBS and sonicated for 10 min. All experiments were run in triplicates. The plates were incubated in the dark for up to 16 h at 37°C. After incubation, the drop plate method was used to count viable cells. In brief, aliquots of each sample were properly diluted in phosphate-buffered saline (PBS) and seeded in Mueller Hinton (MH) agar plates. Colony Forming Units (CFU) were counted from the agar plates after 14 h of incubation at 37°C. Only samples with colony counts ranging from 3 to 30 were counted for 10 µL drops. Biological replicates were used to obtain statistical analysis

***Bactericidal activity,*** antibacterial activity of MNPs was tested against *E. coli* and *S. aureus* under dark and light conditions. Photothermal therapy (PTT), was performed using glass vials. 500 µL of the bacterial suspension, at 1.6 x $10^8$ CFU/mL (OD600 = 0.2) in LB, was mixed with 500 µL of MNP solution, in PBS, with a final concentration of 125 mg/L. For light experiments, the solutions were irradiated for up to 30 min using LED illuminator (Luzchem Research Inc.) at 810 nm (0.99 W/$cm^2$). Dark experiments were run under the same conditions but protected from light. Chemical dynamic therapy (CDT) was done under similar conditions, however 10 mM of $H_2O_2$ was added to the vials containing the bacterial cells to a final concentration of 100 µM and nanocomposites. Viable cells were counted using the drop plate method, only samples with colony counts ranging from 3 to 30 were counted for 10 µL drops. Technical replicates were used to obtain statistical analysis. Antibacterial activity was expressed as log reduction; conversion was made using the following equation:

$$Log\ reduction = Log_{10}\left(\frac{viable\ cells\ before\ \ treatment\ \ (CFU/mL)}{viable\ cells\ after\ treatment\ \ (CFU/mL)}\right)$$

**Hydroxyl radical detection:**

Detection of •OH radicals was done using coumarin as a probe. In the presence of •OH, coumarin is hydroxylated into 7-hydroxycoumarin (7-HC) which has strong fluorescence at 454 nm. The experiments were run in the same conditions as antibacterial tests, with 125 mg/L of catalysts and 10 mM of $H_2O_2$. 0.5 mM of aqueous Coumarin solution at pH 3 was mixed with the NPs solution

in PBS and $H_2O_2$. The solutions were vortexed and incubated under dark and light (810 nm, 0.99 W/cm$^2$) for 1, 5, 15 or 30 min. Fluorescence spectra were obtained in a PTI instrument. The excitation wavelength was set at 340 nm, and the emission wavelength at 454 nm.

**Cell Toxicity:**

***Cell line and growth conditions,*** for the cytotoxicity assays, we used fibrosarcoma cell line HT1080 (ATCC CCL-121™) that were generously donated by the Pratt Research Group (University of Ottawa). Cells were maintained in liquid $N_2$, and stored in a freezing solution containing FCS, DMEM, and DMSO (80:10:10). After defrosting the cells were grown in T75 flasks using supplemented DMEM (10 % FCS, 1 % penicillin-streptomycin, and 0.1 % gentamicin). Cells were incubated in a $CO_2$ incubator (Thermo Forma 370 Steri-Cycle) at 37$^o$C and 5 % $CO_2$.

***Cell toxicity assay,*** the human fibroblasts were cultured in supplemented DMEM until 85–95 % confluence, then washed with DPBS and trypsinized with 3 mL Trypsin-EDTA. Trypsinization was stopped by adding a fresh medium to the reaction. Cells were washed by centrifugation with DMEM, resuspended in medium, and plated in 24 well-plates at approximately $10^5$ cells/ well after proper cell counting in an improved Neubauer chamber. They were incubated overnight to allow attachment and then treated with MNP. The cells were kept in the dark for 48 h at 37 °C, 5% $CO_2$, and 95 % humidity. A solution containing 125 mg/L of MNPs in DPBS, and 50 % DMEM was then added to each well and irradiated for 5 min using a LED-illuminator (Luzchem Research Inc.) at 810 nm (0.99 W/cm$^2$). After irradiation, the MNPs were removed using an external magnet and the cells were incubated for 24h. Following incubation, the media was removed, and the cells were washed 3x with DPBS. MTT reagent was added into the wells with media to a final concentration of 0.5 mg/mL. Plates were incubated for 2 h to allow the reduction of tetrazolium salt to formazan crystals in living cells. The media was substituted for DMSO, and the absorbance was measured at 590 nm using a microplate reader (Molecular Devices™). Tests were run in 3 independent experiments.

**Statistics:**

Statistical analysis was done with R studio (version 1.4.1717). The comparison of multiple groups was done by one-way analysis of variance (ANOVA with Tukey's Post Hoc test), *p*-values less than 0.05 were considered statistically significant.

## RESULTS AND DISCUSSION

### Characterization

There are various published methods to fabricate magnetic nanoparticles including, sol-gel,[12] microemulsion,[13,14] thermal decomposition,[15-17] and co-precipitation.[18-21] In this work, we selected co-precipitation and reduction-precipitation, which allowed the synthesis in one pot under low temperatures and using a non-toxic solvent, water. The synthetized nanocomposites were, Lignin@Fe (LFe), Lignin@FeAg (LFeAg), Lignin@Co (LCo) and Lignin@FeCo (LFeCo).

To investigate the crystalline structures of the synthesized NPs we performed powder X-ray diffraction (PXRD) measurements using Cu Kα radiation. Figure 2.2.1 shows the XRD diffractograms of the MNPs. Lignin@Fe NPs (LFe) were the only NPs composed of a single crystalline phase, cubic $Fe_3O_4$, according to the ICDD card #04-013-9808. The presence of magnetite as the main phase is in accordance with the accepted mechanisms for the formation of iron oxides by co-precipitation. The formation of iron oxide nanoparticles is done by the addition of a base, forming iron hydroxide and oxyhydroxide intermediaries, followed by oxidation into iron oxides. At pH above 8, it is expected the formation of $Fe_3O_4$, which is the most stable phase, when compared with the goethite ($Fe_2O_3$).[22,23]

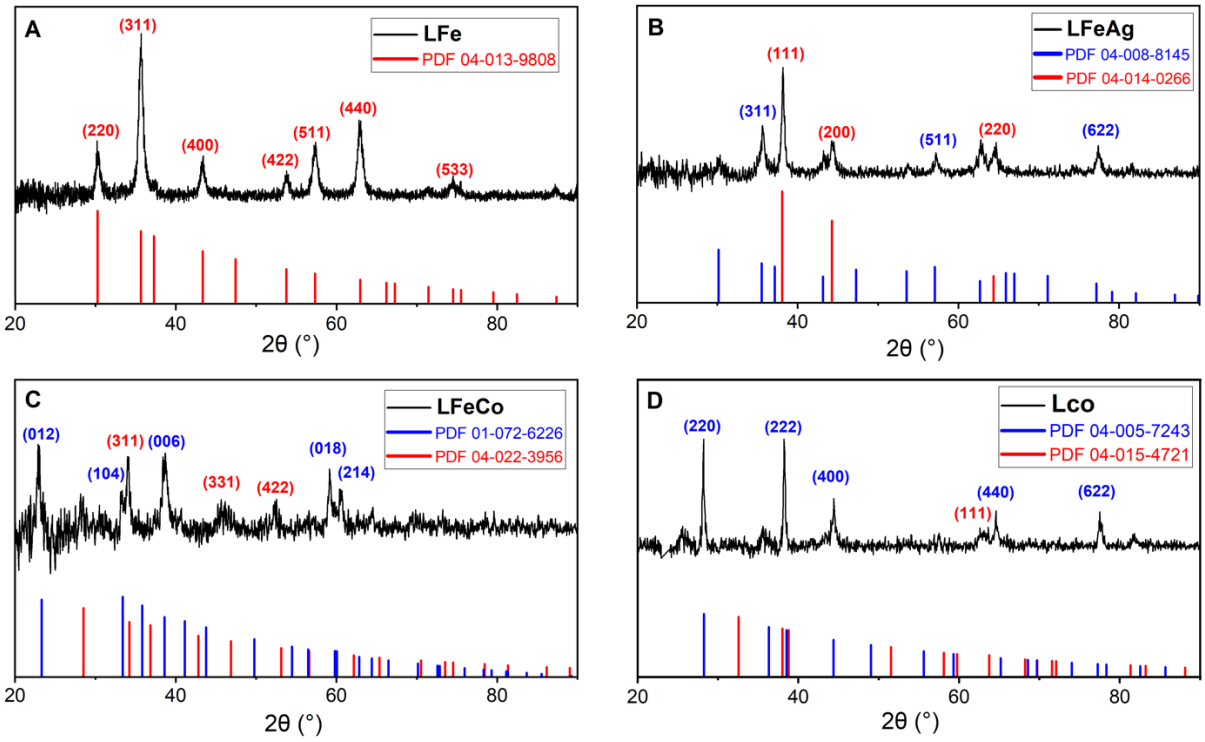


**Figure 2.2.1** XRD patterns for the MNPs LFe (A), LFeAg (B), LFeCo (C) and LCo (D). Crystalline structures were analyzed from the XRD diffractograms and compared with the existing profiles on the ICDD database. LFe: $Fe_3O_4$ (PDF 04-013-9808 - red), LFeAg: Ag (PDF 04-014-0266 - blue) and $Fe_3O_4$ (PDF04-008-8145 - red), LCo: $Co_3O_4$ (PDF 04-015-4721 - red) and CoOH (PDF 04-005-7243 - blue), and LFeCo: $Fe_2O_3$ (PDF 01-072-6226 - blue) and $CoFe_2O_4$ (PDF 04-022-3956 - blue).

Lignin@FeAg NPs (LFeAg) were formed by two crystalline phases, Ag [ICDD #04-014-0266] and $Fe_3O_4$ [ICDD #04-008-8145]. For this composite, the iron oxide NPs were first formed followed by the addition of Ag precursor and Tri-Sodium citrate. The latter helps with the reduction of Ag into AgNPs that were incorporated into the nanocomposite. XRD diffractogram of lignin@Co (LCo), assigned the peaks to $Co_3O_4$ [ICDD #04-015-4721]. Additionally, the broad peak at 63° was assigned to the (111) plane of CoOH [ICDD #04-005-7243]. Different from the other NPs the synthesis of the CoNPs relied only on the reduction of the Co precursor using a reduction agent, $NaBH_4$. Although the cobalt NPs synthesis was done under a nitrogen atmosphere, once under atmospheric conditions, $Co^0$ is easily oxidized into cobalt oxides and hydroxides, even in the presence of capping agents.[24-26] Although with weaker magnetic properties, $Co_3O_4$, also

presents a response to an external magnetic field (Figure 2.2.2 E). To balance the magnetic properties of iron oxides and the excellent antibacterial properties of cobalt-based nanomaterials, we synthesized a hybrid material, Lignin@FeCo (LFeCo). Using XRD (Figure 2.2.1) we confirmed the presence of two phases, $Fe_2O_3$ [PDF 01-072-6226] and $CoFe_2O_4$ [PDF 04-022-3956]. The presence of both phases can also be seen in the TEM images (Figure 2.2.2 D) and the presence of two distinct populations on the size distribution (Figure 2.3.2).

The morphology of the NPs was investigated using TEM (Figure 2.2.2) and their magnetic behaviour can be seen in Figure 2.2.2 E. Due to the magnetic nature of these materials and the presence of organic material, the NPS tends to agglomerate. Figure 2.2.2 A-D shows the spherical LFe, LFeAg, and LCo nanoparticles. Interestingly, the ones with lower amounts of lignin, LFe, and LFeAg with 3.5 and 8%, respectively (Figure 2.3.3 and Table 2.2.1), also presented better dispersibility. In fact, lower amounts of lignin during the synthesis resulted in less agglomeration, as shown in Supporting information (Figure 2.3.1). This tendency was also demonstrated in previously published papers using different metals.[27,28]

From the TEM image of LFeCo (Figure 2.2.2 D), we note that the nanoparticles are enclosed within a hexagon shape, which is one of the common shapes of $CoFe_2O_4$. The hexagon-shaped nanoparticles are formed by the competition between the growth rates of different crystallographic facets, in this case, the favourable growth of the [100] and [111] planes.[15,29,30] The shape control is a result of surface energy alterations caused by the presence of capping agents, such as lignin.[29]

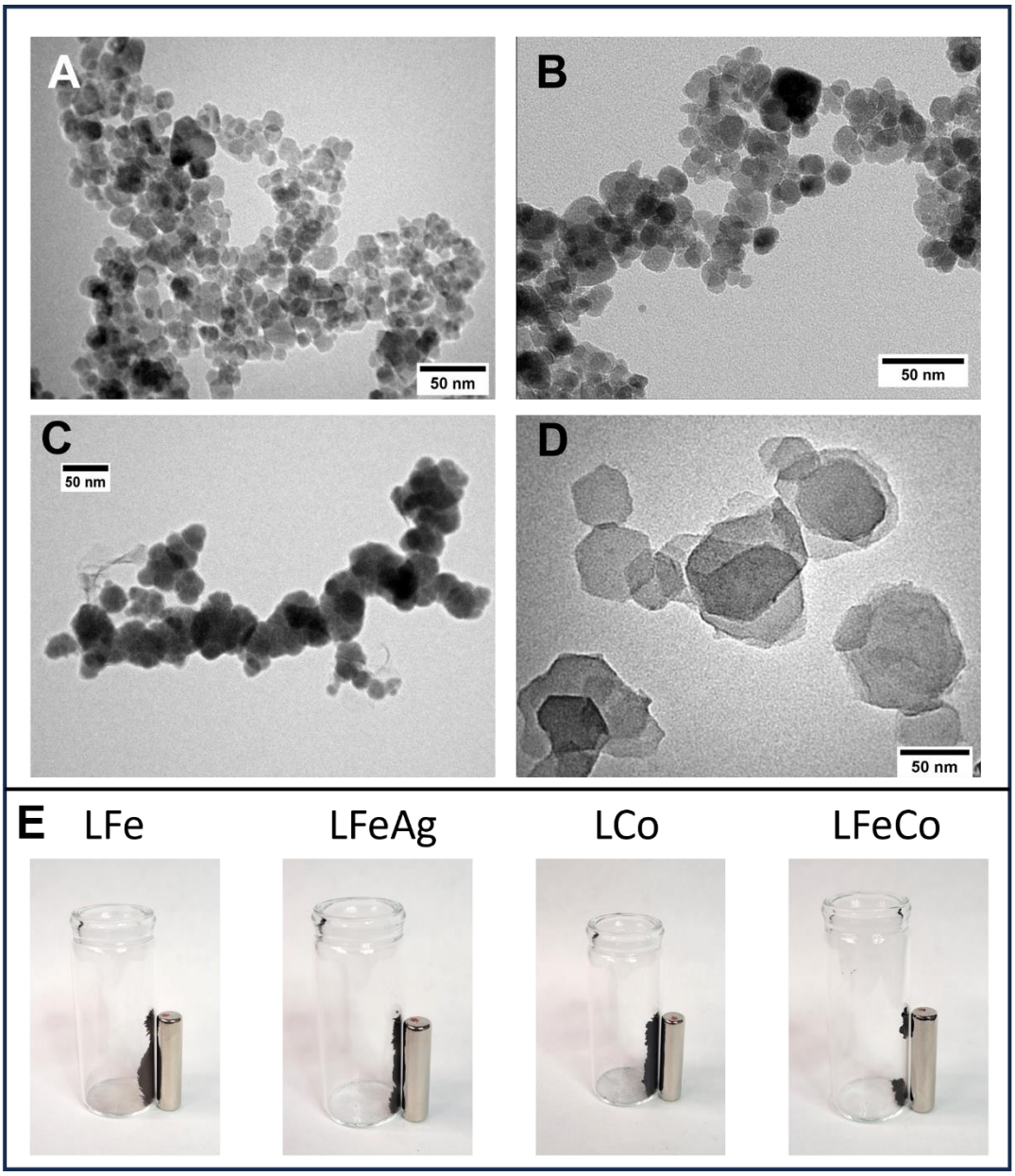


**Figure 2.2.2** Representative TEM images for the synthesized magnetic nanoparticles: (A) LFe, (B) LFeAg, (C) LFeCo and (D) LCo. Scale bars: 50 nm. (E) Photographs showing the magnetic behaviour of the MNPs in the presence of an external magnetic field.

Using their TEM images, we calculated the particles' average diameter estimated from the largest dimension of each NP. The particle sizes were different among the materials, ranging from 4.9 nm for LCO to 17.9 nm for LFeCo (Table 2.2.1). The MNPs had a wide size distribution which is attributed to the method chosen. Although one of the most used methods for the synthesis of magnetic NPs, co-precipitation's main challenge is to control the size and shape of the resulting particles. Average crystallite sizes were calculated using the Scherrer equation, to be 12.6, 12.5, 17.2, and 17.6 nm, for LFe, LFeAg, LCo and LFeCo, respectively. The sizes are similar to the particle sizes measured by TEM (Table 2.2.1), in agreement with the fact that each particle is a crystal.

**Table 2.2.1** Summary of the characterizations for MNP. Particle size was obtained from the TEM images of the nanomaterials. Crystalline structures were analyzed from the XRD diffractograms and compared with the existingprofiles on the ICDD database. LFe: $Fe_3O_4$ [PDF 04-013-9808], LFeAg: Ag [PDF 04-014-0266] and Fe3O4 [PDF04-008-8145], LCo: $Co_3O_4$ [PDF 04-015-4721] and CoOH [PDF 04-005-7243] and LFeCo: $Fe_2O_3$ [PDF 01-076-4579] and $CoFe_2O_4$ [PDF 04-022-3956]. Crystallite size was calculated using the Scherrer equation using data from the XRD diffractograms. Lignin content was obtained using Thermogravimetric analysis (TGA), measured between 25-300°C under $N_2$. Metal quantification was done using ICP-OES following Fe, Ag and Co emission line.

| Nanomaterial | Size (nm) | Crystalline Phases | Crystallite Size (nm) | Lignin Content (wt %) | ICP (%) |
|---|---|---|---|---|---|
| LFe | 13.2 ± 5.7 | $Fe_3O_4$ | 12.6 ± 2.9 | 3.5 | Fe: 74.0 |
| LFeAg | 11.4 ± 4.6 | Ag and $Fe_3O_4$ | 12.5 ± 2.6 | 8.0 | Fe: 70.0<br>Ag: 12.0 |
| LCo | 15.8 ± 8.0 | $Co_3O_4$ and CoOH | 17.2 ± 5.6 | 10.0 | Co: 56.0 |
| LFeCo | 17.3 ± 16.7 | $Fe_2O_3$ and $CoFe_2O_4$ | 17.6 ± 8.1 | 12.0 | Fe: 24.0<br>Co: 48.8 |

The optical properties of these nanomaterials were investigated using diffuse reflectance between 300-1200 nm. The MNPs (Figure 2.2.3) show strong absorbance in the entire visible range

and into the NIR region. This feature makes these NPs ideal for applications using solar light and NIR irradiation into the biological window I (700-950 nm).

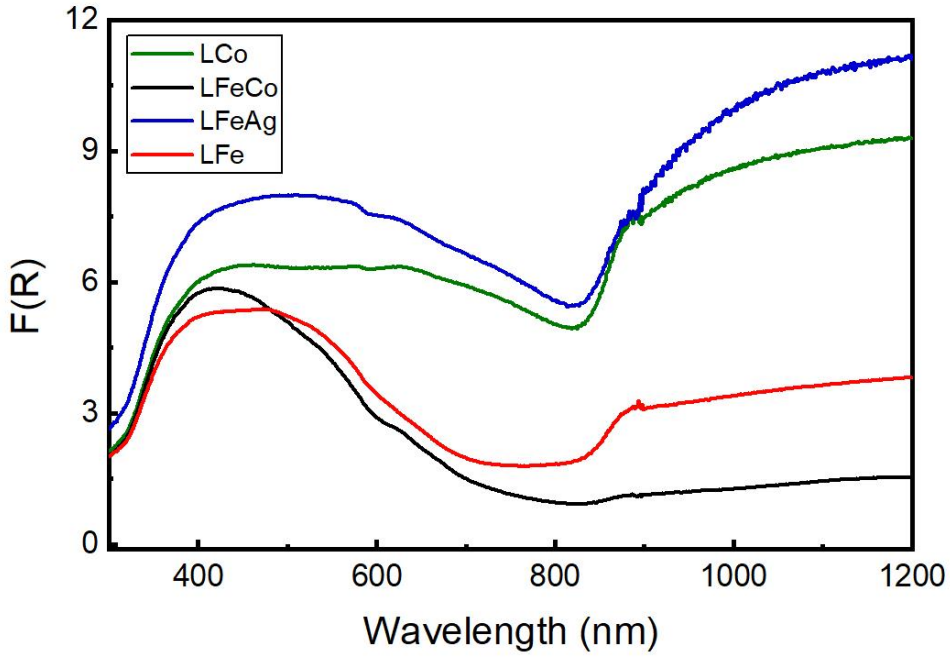


**Figure 2.2.3** Diffuse Reflectance spectra (arbitrary but comparable units) of the MNP measured at room temperature between 300-1200 nm: LFe (red), LFeAg (blue), LFeCo (black) and LCo (green).

**Minimal Inhibitory Concentration (MIC)**

The antimicrobial properties of the MNPs were tested by performing Minimal Inhibitory Concentration (MIC) experiments via a microdilution assay. The MIC is defined as the minimal concentration capable of inhibiting any bacterial growth, compared to the control. We evaluated nanoparticles at concentrations ranging from 1000 to 31.25 mg/L. The effect of lignin alone was also investigated, incubating the bacterial cells with the biopolymer.

Statistically, all concentrations of lignin alone presented no effect on bacterial growth, for both species, when compared with the control (0 log reduction) ($p > 0.05$). Although previously reported as antibacterial,[9,31,32] lignin structures and properties vary according to the biomass

sources and extraction methods as investigated by Alzagameem et.al.[9] and Guo et.al.[131] Its capacity to inhibit bacterial growth is due to the presence of phenolic hydroxyl and methoxy groups.[9,32] Our research group has previously discussed the influence of the lignin structures on their antibacterial activity. In fact, their structures can facilitate the interaction with the bacterial cell wall.[10] In the meanwhile, this heterogenic biopolymer also presents antioxidant properties that may protect the bacteria against oxidative stress. [9,31,32]

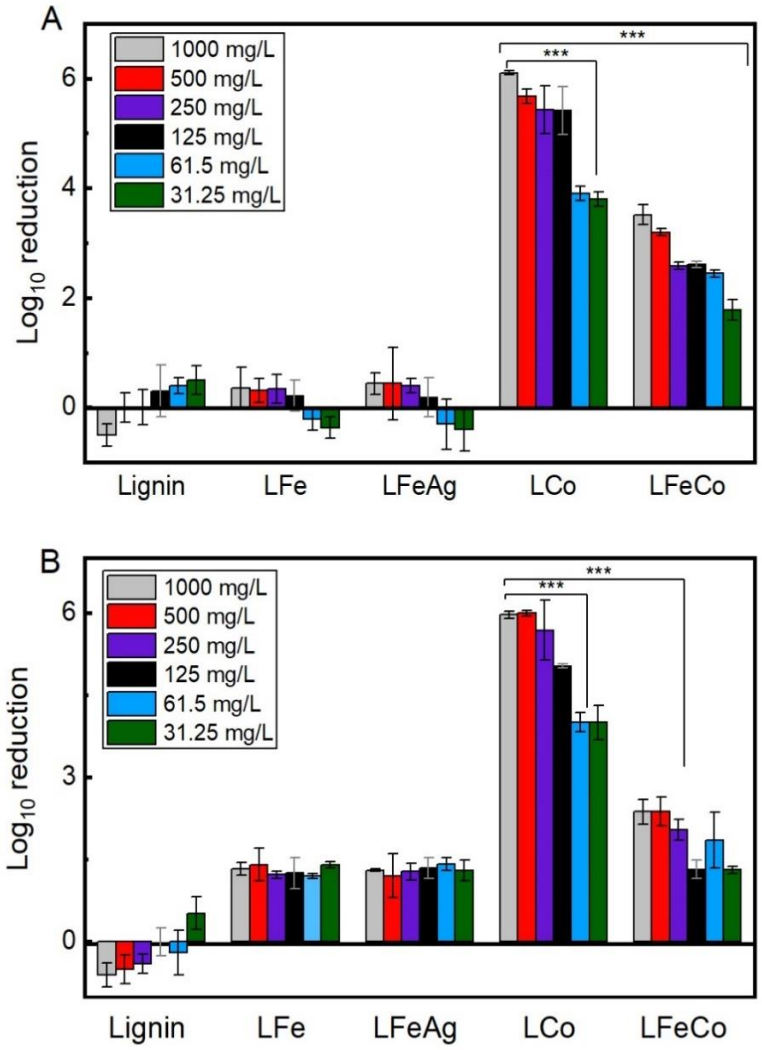


**Figure 2.2.4** $Log_{10}$ reduction of (A) *E. coli* (B) *S. aureus*, after treatment with MNPs or lignin A alone (31.5-1000 mg/L) for 16 h in 50 % LB at 37°C and 140 rpm, under dark. Cell growth was determined by the plate counting method and log reduction was obtained by comparing bacterial growth in presence of nanoparticles to a control incubated without the NPs. Error bars represent standard deviations of the log reduction, n=5. (*p < 0.05, **p < 0.01, ***p < 0.001)

The synthesized nanomaterials exhibited effective inhibitory and bactericidal activity after 16 h incubation with *E. coli* and *S. aureus*, a Gram-negative and a Gram-positive model, respectively. In general, NPs performed better against *E. coli*, presumably due to the thinner peptidoglycan cell wall of Gram-negative. LCo outperformed the other NPs ($p = 0.00$), having a minimum of 7 log reductions at 31.25 mg/L. This may be due to the leaching of cobalt ions that can interact with thiol groups of essential bacterial enzymes. Nanostructures are also known to induce the formation of reactive oxygen species that damage DNA, lipids, and proteins.[24] Hybrid nanocomposites contained lower amounts of toxic metals, Ag and Co (Table 2.2.1), which justify the reduced antibacterial activity of LFeCo and LFeAg in comparison to LCo.

Regarding the experiment with *S. aureus*, both LCo and LFeCo had great antibacterial effects, with a minimum reduction of 2.6 log units for LFeCo and 3.4 log units for LCo. LFe and LFeAg did present statically similar growth to the control ($p > 0.05$). Compared with the other materials, iron oxide shows lower antibacterial activity, mostly due to the lower toxicity of iron ions. In fact, the greater antibacterial activity of iron oxide nanoparticles is often obtained by surface modifications, doping and synthesis of nanohybrids.[33-37]

Based on these data we determined that concentrations higher than 31.25 mg/L were able to inhibit *E. coli* growth for all NPs. As *S. aureus* although similar to the control, concentrations above 125 mg/L did show some level of inhibition. For this reason, we continued the next experiments by using NPs at concentrations of 125 mg/L.

**Photothermal activity**

We sought to investigate the photothermal activity of the MNPs by using NIR irradiation (810 nm) with a power of 0.99 W/cm$^2$. The wavelength of choice is within the biological window, which allows deep tissue penetration, ideal for *in situ* applications. Iron and cobalt-based materials are known for their exceptional photothermal properties, being vastly studied for cancer therapies.[2,4,25,38] The nanocomposites, LFeAg and LCo presented great photothermal properties eventually achieving solution temperatures up to 50°C, Figure 2.2.5. It should be noted that in the

times required for potent antibacterial activity (6 log reduction or more), temperature changes were small, typically ≤5°C.

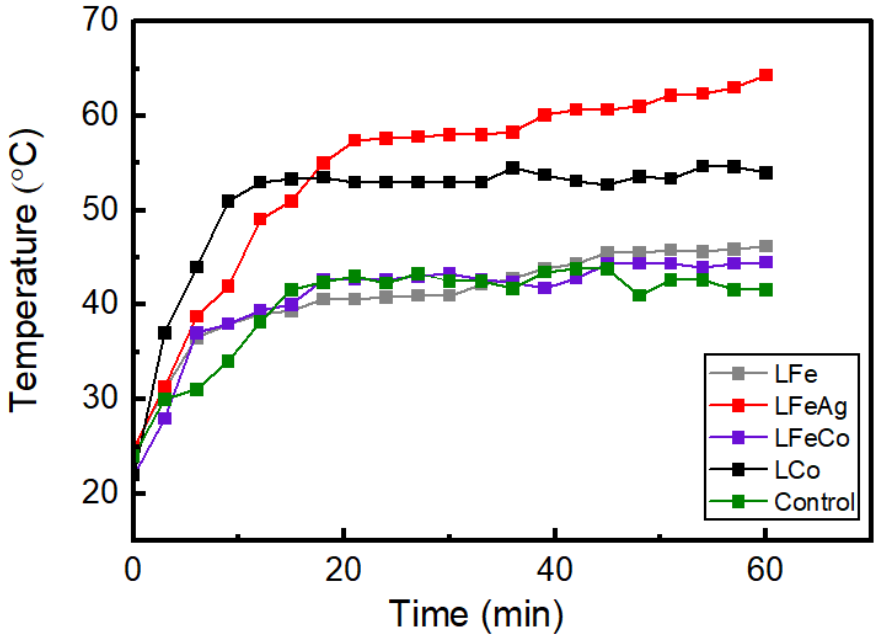


**Figure 2.2.5** Temperature changes over time of aqueous solutions of MNPs (125 mg/mL) after irradiation with 810 nm LED (0.99 W/cm$^2$). Temperature was measured with an IR thermometer every 5 min. The control sample (green) was pure water.

As demonstrated in Figure 2.2.6, in the presence of light, the MNPs were able to kill the bacteria at shorter times than the MIC experiments. In times as short as 1-5 minutes, LFeCo and LFeAg could cause up to 99.9999 % reduction for *E. coli* and 99.9 % for *S. aureus*. Following Health Canada guidelines, a minimum of 4-log (99.99 %) removal is required for water disinfection and 3-log reduction for surface disinfectant.[39,40]

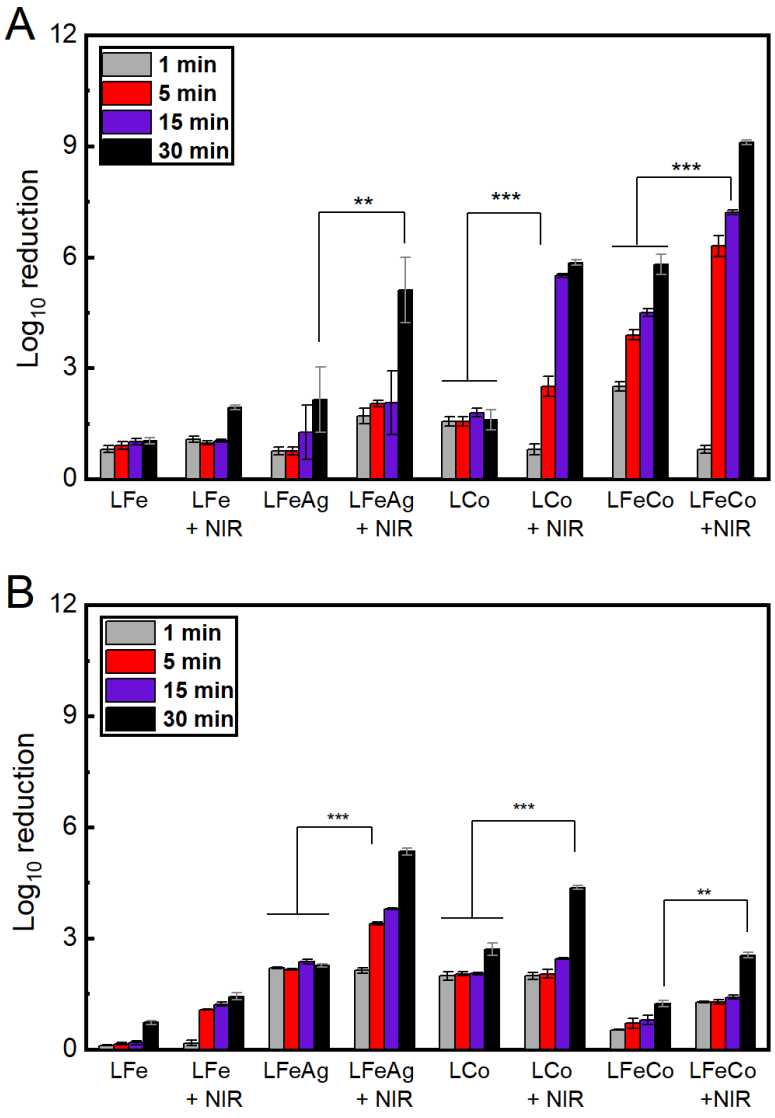


**Figure 2.2.6** Bactericidal activity against *E.coli* (A) and *S. aureus* (B) after treatment with MNPs (125 mg/L) alone ( LFe, LFeAg, LCo, and LFeCo) and with MNP and NIR (810 nm - 0.99 W/cm$^2$) irradiation (LFe + NIR, LFeAg + NIR, LCo + NIR, and LFeCo + NIR). Treatment was done 1, 5, 15 and 30 min, and cell growth was determined by the plate counting method. Log reduction was compared to the initial bacterial inoculum. Error bars represent standard deviations of the log reduction, n=3. (*p < 0.05, **p < 0.01, ***p < 0.001).

A possible cause of the antibacterial effect is the local heat, that is generated as the excited nanomaterial releases the energy absorbed upon NIR irradiation. Temperatures, above 50°C, cause

membrane disruption, protein denaturation, and increased permeability, eventually causing bacterial death.

Note that at longer times the log reduction achieved reaches a maximum of around 9 log units. Those data points do not have any error bars, since in all the experiments there were no bacteria to count. For this we use the initial bacterial concentration, $OD_{600}$ = 0.1, to estimate the total log reduction.

The composite with the highest antibacterial activity against *E. coli* was LFeCo, with a 7-log reduction in 15 min. Interestingly, this nanomaterial did not have higher temperature increases, when compared to the other NPs, with a maximum of 45°C (but < 20 °C at 15 minutes). Trying to understand the antibacterial mechanism of these nanostructures, we incubated *E. coli* at 45°C for up to 30 min and measured the bacterial growth. As demonstrated in Figure 2.3.4, the heat alone does not cause the massive bactericidal effect that is observed in the presence of the LFeCo. Furthermore, the presence of light does influence the higher antibacterial rate for LFeCo and LCo ($p = 0.00$). We then measured if the presence of the light would accelerate the release of toxic ions, such as $Co^{2+}$. Table 2.3.1 shows that the percentage of Co ions released for LCo is not affected by the presence of light. Thus, the high antibacterial effect can be a combination of the heat generated, which increases bacterial membrane permeability, leading to further permeation to the nanomaterials or the released ions.

**Chemodynamic therapy (CDT)**

Exploring the full potential of our NPs we then investigated the nanoenzymatic behaviour of these materials. A few nanomaterials, such as superparamagnetic NPs have peroxidase-like activity, which catalyzes the one-electron reduction of $H_2O_2$, generating $^{\bullet}OH$ radicals through a Fenton-like reaction.[41] We first tested our lignin@MNPs' ability to catalyze the oxidation of 1,3,5-trimethylbenzene (TMB) in the presence of $H_2O_2$. TMB is translucent in its natural form, but in the presence of $^{\bullet}OH$, it is oxidized into oxi-TMB which has a strong characteristic peak at 652 nm. The resulting blue colour indicates the successful colorimetric reaction.

Here the nanoparticles were tested at the concentrations used for PTT assays (125 mg/ L) and with $H_2O_2$ (0.1 mM). As can be seen in Figure 2.2.7-A, all tested composites could catalyze TMB oxidation. Lignin and $H_2O_2$ alone were not able to induce the formation of oxi-TMB.

Particularly, solutions treated with LCo and LFeAg, resulted in a higher absorbance intensity for oxi-TMB, showing better enzymatic activity of these NPs. Both nanomaterials, CoNPs and FeAg nanohybrids were previously reported as suitable catalysts for TMB oxidation.[42,43]

The peroxidase-like activity can be used to improve NPs' capability to kill bacteria through oxidative stress. The hydroxyl radicals produced are strong oxidant agents that react with lipids, DNA, and proteins. Hydrogen peroxide in the absence of MNP, with and without NIR irradiation had low antibacterial activity. In addition, CDT treatment alone (no NIR) had less bactericidal effect efficiency than the PTT (Figure 2.2.7-B and C) which can be due to the low stability of •OH radicals that easily react with other molecules in the solution, such as the media constituents (LB broth) or the lignin present in the NPs. Note that the $H_2O_2$ concentration used, 0.1 mM, is significantly lower than that previously used for bactericidal experiments.[6,44]

**Combination of PTT and CDT**

When combining the presence of NIR irradiation with $H_2O_2$, the bactericidal effect of the NPs was enhanced by reducing the necessary time for the treatment. Similar to the previous tests, *E. coli* was more sensitive to the treatments achieving total eradication with LFeAg and 6 log units with LCo within only 1 min (Figure 2.2.7-B and Table 2.2.2). Meanwhile, the MNPs were able to eradicate a maximum of 4.5 and 5 log units of *S. aureus* in 15 and 30 min using LFeAg and LCo, respectively (Figure 2.2.7-C), indicating that the different cell wall constitution does influence the bacteria sensibility, emphasizing the role of membrane permeabilization on the antibacterial mechanism of the fabricated NPs.

To evaluate the proposed mechanisms, •OH production and ion leaching with the combination of CDT and PTT were evaluated. The fluorescent probe, coumarin, was used to observe the production of hydroxyl radicals. The fluorescence of 7-hydroxycoumarin (7-HC) at 454 nm was used and analyzed for the presence of this radical. Figure 2.3.5 shows the increased production of •OH radicals over time, with higher fluorescence at 30 min. Control experiments without $H_2O_2$ yield lower concentrations of 7-HC. For iron containing NPs, LFe, LFeCo and LFeAg, the presence of light did not interfere with the •OH radical amounts, emphasizing that the higher antibacterial activity under light, is due to other mechanisms such as the photothermal effect

(Figure 2.2.5) or ions leaching. As for LCo, the light treatment accelerated the formation of 7-HC, which can be due to the heat generated.

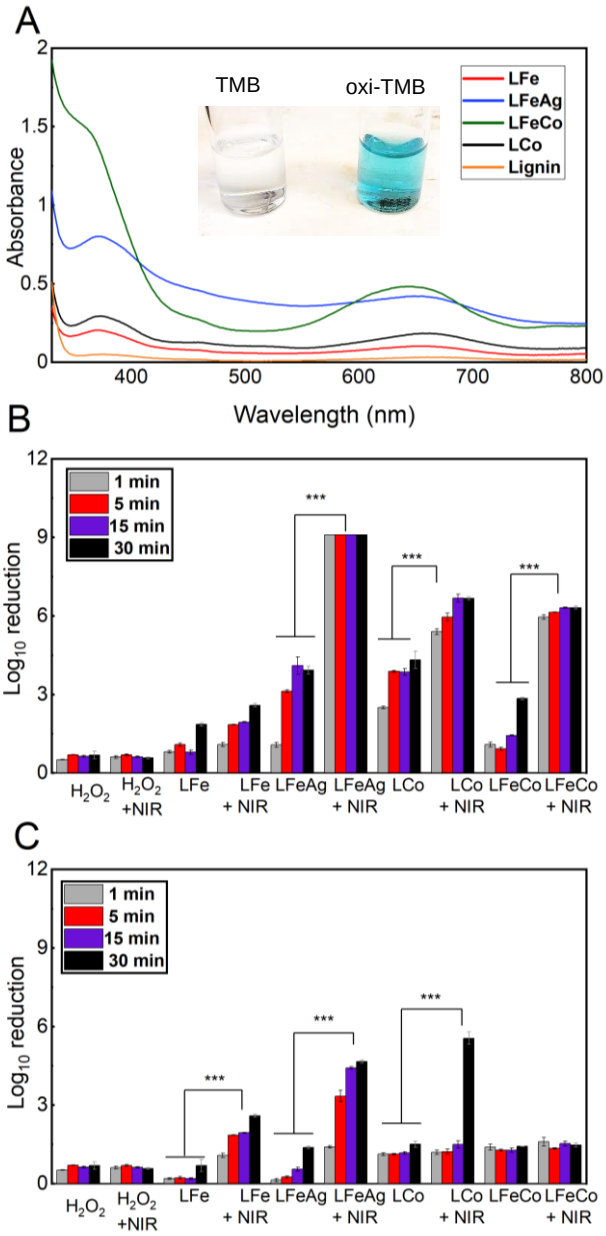


**Figure 2.2.7** (A) Oxidation of TMB (1 mM) in the presence of the MNPs (125 mg/L) or Lignin A and 0.1 mM of $H_2O_2$, after 20 min of reaction in PBS. In the inset, images of TMB solutions before and after reaction with MNPs. Bactericidal activity against *E. coli* (A) and *S. aureus* (B) after treatment with MNPs (125 mg/L) and 0.1 mM of $H_2O_2$ (LFe, LFeAg, LCo, and LFeCo). And in the presence of the MNP, $H_2O_2$ and NIR irradiation (810 nm) (LFe + NIR,

LFeAg + NIR, LCo + NIR, and LFeCo + NIR). Treatments were done for up to 30 min. Bacterial viability was determined by the plate counting method and log reduction was determined by comparing the cell viability to initial bacterial inoculum. Error bars represent standard deviations of the log reduction, n=3. (*p < 0.05, **p < 0.01, ***p < 0.001).

**Table 2.2.2** Summary of the bactericidal activity against *E. coli and S. aureus* after treatment with MNPs (125 mg/L) and NIR (0.99 W/cm$^2$) for 1 and 5 min, determined by the plate counting method. Bactericidal activity was measured as $\log_{10}$ reduction, by comparing cell viability after treatment with the initial bacterial inoculum. PTT treatment was done with solely NIR irradiation in the presence of the MNPs. CDT treatment was a combination of NIR irradiation presence of 0.1 mM $H_2O_2$.

| | ***Escherichia coli*** | | | |
|---|---|---|---|---|
| | **PTT** | | **CDT** | |
| **Nanomaterials** | 1 min | 5 min | 1 min | 5 min |
| LFe | 1.1 | 1.0 | 1.1 | 1.8 |
| LFeAg | 1.7 | 2.4 | 9.1 | 9.1 |
| LFeCo | 1.2 | 6.7 | 5.9 | 6.1 |
| LCo | 1.2 | 2.9 | 0.8 | 2.5 |
| | ***Staphylococcus aureus*** | | | |
| | PTT | | CDT | |
| | 1 min | 5 min | 1 min | 5 min |
| LFe | 0.2 | 1.1 | 0.1 | 0.1 |
| LFeAg | 2.1 | 3.4 | 1.4 | 3.3 |
| LFeCo | 1.3 | 0.8 | 1.6 | 1.3 |
| LCo | 2.0 | 2.0 | 1.2 | 1.2 |

CDT, chemodynamic therapy; LFe, Lignin@Fe; LFeAg, Lignin@FeAg; LFeCO, Lignin@CO; MNP, magnetic nanoparticle; NIR, near-infra-red; PTT, photothermal therapy.

## Cell toxicity

To evaluate the toxicity of the nanocomposites we treated human fibroblasts with synthesized nanomaterials. Previous experiments demonstrated that long irradiation times can be

damaging to mammalian cells.[45] The advantage of the Lignin@MNPs is that at short irradiation times, such as 1 and 5 min, we could see effective antibacterial activity. Considering this, we choose 5 min irradiation to evaluate the toxicity of our composites toward human cells. Using their magnetic properties, we removed the NPs after the 5-minute irradiation (light) or dark incubation. Cellular viability was inferred using the MTT assay, which measures cellular metabolism. Cells treated with DPBS, and no light (dark) were assumed as 100 % viable.

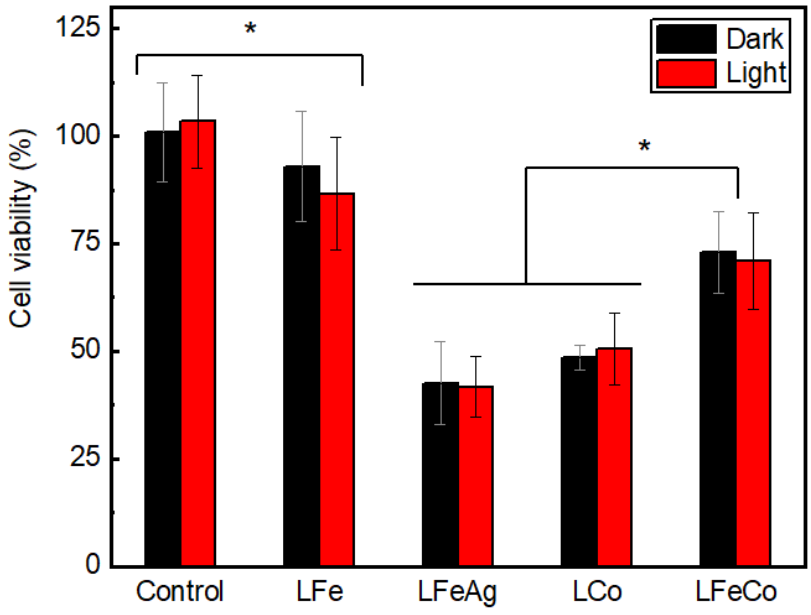


**Figure 2.2.8** Cell viability of human fibroblasts (HT1080) measurements were carried out using the MTT colorimetric assay. Cells were treated with 125 mg/L of the nanocomposites, and 0.1 mM of $H_2O_2$ in the presence (red) and absence (black) of NIR (810 nm - 0.99 W/cm$^2$) irradiation for 5 min. Nanocomposites were removed with an external magnet and cells were incubated for 24 h before viability tests. Error bars represent standard deviations, n=3. (*$p < 0.05$)

The presence of light did not affect the viability of the cells ($p > 0.05$) (red bars, Figure 2.2.8) meaning that the short NIR irradiation is a safe tool to combat bacterial infections. The composites, LFeAg and LCo, were the ones with lower cell viability with respectively, 42 % and 50 % survival in both, dark and light, indicating the intrinsic toxicity of these materials. Differently, in the presence of LFe, cells presented a survival rate of 87 %, similar to the controls ($p < 0.05$). Cell compatibility of iron oxides is a known feature of the nanostructures, which can make them suitable for medical applications such as MRI imaging.[46-48] However, the antibacterial activities of LFe were limited in both PTT and CDT, with a maximum of 1.8 log reduction.

Combining the antibacterial efficiency of cobalt and the biocompatibility of iron oxides, we synthesized the LFeCo composite. The hybrid material maintained cell viability at 70 % while keeping an excellent antibacterial performance (Figures 2.2.6 and 2.2.7). In fact, for PTT against *E. coli*, LFeCo performed better than the other composites, achieving almost 7 log reduction in only 5 min (Table 2.2.2). For this reason, we evaluated the toxicity of these composites using only PTT (810 nm - 0.99 W/cm$^2$). Cellular viability remained at 80% in the dark and 75 % in light (Figure 2.3.5), slightly higher than in the presence of $H_2O_2$ (Figure 2.2.8). Further, we explored the impact of lignin as a capping agent, for FeCo NPs, on cell viability. In the presence of lignin (LFeCo), the cellular survival remained at 75 %. However, on FeCo NPs, with no capping agent, the survival rate drastically dropped to 21 % (Figure 2.3.5). Meaning that by using a biocompatible capping agent we were able to modulate the toxicity of this composite. As previously mentioned, lignin is known for its antioxidant behaviour which can protect the cells. Also, biopolymers as capping agents act to reduce the leach of ions and the different contact of the NPs with the cell membrane.[7,9,10,32]

## CONCLUSION

Several magnetic nanostructures coated with lignin have been prepared and their antibacterial properties against Gram-positive and Gram-negative bacteria tested. The magnetic properties of these nanocomposites facilitate removal or localization, while the lignin shell

provides biocompatibility. In the dark, these nanomaterials are mild antibacterials, but when illuminated become powerful antibacterial agents with typically ≥6 log units bacterial reduction in 1 to 5 minute irradiations. These materials absorb strongly in the very useful NIR biological window, which we illustrate using 810 nm LED irradiation. Biocompatibility tests using fibroblasts show limited cell damage and no enhanced adverse effect during 810 nm NIR illumination. A comparison of the data in Figures 2.2.6 and 2.2.8 suggests that LFeCo offers the best compromise of very high antibacterial.

## REFERENCES

(1) Ten threats to global health in 2019. World Health Organization. https://www.who.int/news-room/spotlight/ten-threats-to-global-health-in-2019 (accessed 2021-11-21).

(2) Fu, G.; Sanjay, S. T.; Zhou, W.; Brekken, R. A.; Kirken, R. A.; Li, X. Exploration of Nanoparticle-Mediated Photothermal Effect of TMB-$H_2O_2$ Colorimetric System and Its Application in a Visual Quantitative Photothermal Immunoassay. Anal. Chem. 2018, 90 (9), 5930–5937.

(3) Rodrigues, G. R.; López-Abarrategui, C.; de la Serna Gómez, I.; Dias, S. C.; Otero-González, A. J.; Franco, O. L. Antimicrobial Magnetic Nanoparticles Based-Therapies for Controlling Infectious Diseases. Int. J. Pharm. 2019, 555, 356–367.

(4) Chen, Y.; Gao, Y.; Chen, Y.; Liu, L.; Mo, A.; Peng, Q. Nanomaterials-Based Photothermal Therapy and Its Potentials in Antibacterial Treatment. J. Control. Release 2020, 328 (August), 251–262.

(5) Cieplik, F.; Deng, D.; Crielaard, W.; Buchalla, W.; Hellwig, E.; Al-Ahmad, A.; Maisch, T. Antimicrobial Photodynamic Therapy–What We Know and What We Don't. Crit. Rev. Microbiol. 2018, 44 (5), 571–589.

(6) Liu, Z.; Zhao, X.; Yu, B.; Zhao, N.; Zhang, C.; Xu, F. J. Rough Carbon-Iron Oxide Nanohybrids for Near-Infrared-II Light-Responsive Synergistic Antibacterial Therapy. ACS Nano 2021, 15 (4), 7482–7490.

(7) Hoyo, J.; Ivanova, K.; Torrent-Burgues, J.; Tzanov, T. Interaction of Silver-Lignin Nanoparticles With Mammalian Mimetic Membranes. Front. Bioeng. Biotechnol. 2020, 8, 439.

(8) Richter, A. P.; Brown, J. S.; Bharti, B.; Wang, A.; Gangwal, S.; Houck, K.; Cohen Hubal, E. A.; Paunov, V. N.; Stoyanov, S. D.; Velev, O. D. An Environmentally Benign Antimicrobial Nanoparticle Based on a Silver-Infused Lignin Core. Nature Nanotechnology 2015 10:9 2015, 10 (9), 817–823.

(9) Alzagameem, A.; Klein, S. E.; Bergs, M.; Do, X. T.; Korte, I.; Dohlen, S.; Hüwe, C.; Kreyenschmidt, J.; Kamm, B.; Larkins, M.; Schulze, M. Antimicrobial Activity of Lignin and Lignin-Derived Cellulose and Chitosan Composites against Selected Pathogenic and Spoilage Microorganisms. Polym. 2019, 11 (4), 670.

(10) Rocca, D. M.; Vanegas, J. P.; Fournier, K.; Becerra, M. C.; Scaiano, J. C.; Lanterna, A. E. Biocompatibility and Photo-Induced Antibacterial Activity of Lignin-Stabilized Noble Metal Nanoparticles. RSC adv. 2018, 8 (70), 40454–40463.

(11) Fournier, K.; Marina, N.; Joshi, N.; Berthiaume, V. R.; Currie, S.; Lanterna, A. E.; Scaiano, J. C. Scale-up of a Photochemical Flow Reactor for the Production of Lignin-Coated Titanium Dioxide as a Sunscreen Ingredient. J. Photochem. Photobiol. 2021, 7, 100040.

(12) Wang, X.; Zhang, P.; Gao, J.; Chen, X.; Yang, H. Facile Synthesis and Magnetic Properties of $Fe_3C$/C Nanoparticles via a Sol–Gel Process. Dyes Pigm. 2015, 112, 305–310.

(13) Barad, J. M.; Kohli, H. P.; Chakraborty, M. Adsorption of Hexavalent Chromium from Aqueous Stream by Maghemite Nanoparticles Synthesized by the Microemulsion Method. Energy Nexus 2022, 5, 100035.

(14) Lopez Perez, J. A.; Lopez Quintela, M. A.; Mira, J.; Rivas, J.; Charles, S. W. Advances in the Preparation of Magnetic Nanoparticles by the Microemulsion Method. J. Phys. Chem. B. 1997, 101 (41), 8045–8047.

(15) Tomar, D.; Jeevanandam, P. Synthesis of Cobalt Ferrite Nanoparticles with Different Morphologies via Thermal Decomposition Approach and Studies on Their Magnetic Properties. J. Alloys Compd. 2020, 843, 155815.

(16) Unni, M.; Uhl, A. M.; Savliwala, S.; Savitzky, B. H.; Dhavalikar, R.; Garraud, N.; Arnold, D. P.; Kourkoutis, L. F.; Andrew, J. S.; Rinaldi, C. Thermal Decomposition Synthesis of Iron Oxide Nanoparticles with Diminished Magnetic Dead Layer by Controlled Addition of Oxygen. ACS Nano 2017, 11 (2), 2284–2303.

(17) Wu, W.; He, Q.; Jiang, C. Magnetic Iron Oxide Nanoparticles: Synthesis and Surface Functionalization Strategies. Nanoscale Res. Lett. 2008, 3 (11), 397–415.

(18) Basak, M.; Rahman, M. L.; Ahmed, M. F.; Biswas, B.; Sharmin, N. Calcination Effect on Structural, Morphological and Magnetic Properties of Nano-Sized $CoFe_2O_4$ Developed by a Simple Co-Precipitation Technique. Mater. Chem. Phys. 2021, 264, 124442.

(19) Carvalho, M. D.; Henriques, F.; Ferreira, L. P.; Godinho, M.; Cruz, M. M. Iron Oxide Nanoparticles: The Influence of Synthesis Method and Size on Composition and Magnetic Properties. J. Solid State Chem. 2013, 201, 144–152.

(20) Siddiqui, M. T. H.; Baloch, H. A.; Nizamuddin, S.; Mubarak, N. M.; Hossain, N.; Zavabeti, A.; Mazari, S. A.; Griffin, G. J.; Srinivasan, M. Synthesis and Optimization of Chitosan Supported Magnetic Carbon Bio-Nanocomposites and Bio-Oil Production by Solvothermal Carbonization Co-Precipitation for Advanced Energy Applications. Renew. Energy 2021, 178, 587–599.

(21) Wu, S.; Sun, A.; Zhai, F.; Wang, J.; Xu, W.; Zhang, Q.; Volinsky, A. A. Fe3O4 Magnetic Nanoparticles Synthesis from Tailings by Ultrasonic Chemical Co-Precipitation. Mater. Lett. 2011, 65 (12), 1882–1884.

(22) Ahn, T.; Kim, J. H.; Yang, H. M.; Lee, J. W.; Kim, J. D. Formation Pathways of Magnetite Nanoparticles by Coprecipitation Method. J. Phys. Chem. C 2012, 116 (10), 6069–6076.

(23) Besenhard, M. O.; LaGrow, A. P.; Hodzic, A.; Kriechbaum, M.; Panariello, L.; Bais, G.; Loizou, K.; Damilos, S.; Margarida Cruz, M.; Thanh, N. T. K.; Gavriilidis, A. Co-Precipitation Synthesis of Stable Iron Oxide Nanoparticles with NaOH: New Insights and Continuous Production via Flow Chemistry. J. Chem. Eng. 2020, 399, 125740.

(24) Alahmadi, N. S.; Betts, J. W.; Cheng, F.; Francesconi, M. G.; Kelly, S. M.; Kornherr, A.; Prior, T. J.; Wadhawan, J. D. Synthesis and Antibacterial Effects of Cobalt–Cellulose Magnetic Nanocomposites. RSC Adv. 2017, 7 (32), 20020–20026.

(25) Ansari, S. M.; Bhor, R. D.; Pai, K. R.; Sen, D.; Mazumder, S.; Ghosh, K.; Kolekar, Y. D.; Ramana, C. V. Cobalt Nanoparticles for Biomedical Applications: Facile Synthesis, Physiochemical Characterization, Cytotoxicity Behavior and Biocompatibility. Appl. Surf. Sci. 2017, 414, 171–187.

(26) Iravani, S.; Varma, R. S. Sustainable Synthesis of Cobalt and Cobalt Oxide Nanoparticles and Their Catalytic and Biomedical Applications. Green Chem. 2020, 22 (9), 2643–2661.

(27) Klapiszewski, Ł.; Nowacka, M.; Milczarek, G.; Jesionowski, T. Physicochemical and Electrokinetic Properties of Silica/Lignin Biocomposites. Carbohydr. Polym. 2013, 94, 345–355.

(28) Klapiszewski, Ł.; Zdarta, J.; Antecka, K.; Synoradzki, K.; Siwińska-Stefańska, K.; Moszyński, D.; Jesionowski, T. Magnetite Nanoparticles Conjugated with Lignin: A Physicochemical and Magnetic Study. Appl. Surf. Sci. 2017, 422, 94–103.

(29) Kumar, Y.; Sharma, A.; Shirage, P. M. Shape-Controlled $CoFe_2O_4$ Nanoparticles as an Excellent Material for Humidity Sensing. RSC Adv. 2017, 7 (88), 55778–55785.

(30) Lo, A.; Lottini, E.; de Julia, sar; Sangregorio, C. Exploring the Magnetic Properties of Cobalt-Ferrite Nanoparticles for the Development of a Rare-Earth-Free Permanent Magnet. Chem. Mater. 2015, 27 (11), 4048–4056.

(31) Guo, M.; Jin, T.; Nghiem, N. P.; Fan, X.; Qi, P. X.; Jang, C. H.; Shao, L.; Wu, C. Assessment of Antioxidant and Antimicrobial Properties of Lignin from Corn Stover Residue Pretreated with Low-Moisture Anhydrous Ammonia and Enzymatic Hydrolysis Process. Appl. Biochem. Biotechnol. 2018, 184 (1), 350–365.

(32) Kaur, R.; Uppal, S. K.; Sharma, P. Antioxidant and Antibacterial Activities of Sugarcane Bagasse Lignin and Chemically Modified Lignins. Sugar Tech 2017, 19 (6), 675–680.

(33) Bhushan, M.; Kumar, Y.; Periyasamy, L.; Viswanath, A. K. Antibacterial Applications of α-Fe2O3/Co3O4 Nanocomposites and Study of Their Structural, Optical, Magnetic and Cytotoxic Characteristics. Appl. Nanosci 2018, 8 (1), 137–153.

(34) Karki, H. P.; Ojha, D. P.; Joshi, M. K.; Kim, H. J. Effective Reduction of P-Nitrophenol by Silver Nanoparticle Loaded on Magnetic $Fe_3O_4$/ATO Nano-Composite. Appl. Surf. Sci. 2018, 435, 599–608.

(35) Manna, P. K.; Nickel, R.; Wroczynskyj, Y.; Yathindranath, V.; Li, J.; Liu, S.; Thliveris, J. A.; Klonisch, T.; Miller, D. W.; Van Lierop, J. Simple, Hackable, Size-Selective, Amine-Functionalized Fe-Oxide Nanoparticles for Biomedical Applications. Langmuir 2018, 34 (8), 2748–2757.

(36) Sangaiya, P.; Jayaprakash, R. A Review on Iron Oxide Nanoparticles and Their Biomedical Applications. J. Supercond. Nov. Magn. 2018, 31 (11), 3397–3413.

(37) Shah, S. T.; Yehye, W. A.; Saad, O.; Simarani, K.; Chowdhury, Z. Z.; Alhadi, A. A.; Al-Ani, L. A. Surface Functionalization of Iron Oxide Nanoparticles with Gallic Acid as Potential Antioxidant and Antimicrobial Agents. Nanomater. 2017, 7 (10), 306.

(38) Jaque, D.; Martínez Maestro, L.; Del Rosal, B.; Haro-Gonzalez, P.; Benayas, A.; Plaza, J. L.; Martín Rodríguez, E.; García Solé, J. Nanoparticles for Photothermal Therapies. Nanoscale 2014, 6 (16), 9494–9530.

(39) ARCHIVED Guidance document - Safety and efficacy requirements for hard surface disinfectant drugs - Canada.ca. https://www.canada.ca/en/health-canada/services/drugs-health-products/drug-products/applications-submissions/guidance-documents/disinfectants/safety-efficacy-requirements-hard-surface-disinfectant-drugs.html (accessed 2022-05-13).

(40) Page 8: Guidelines for Canadian Drinking Water Quality: Guideline Technical Document – Enteric Viruses - Canada.ca. https://www.canada.ca/en/health-canada/services/publications/healthy-

living/guidelines-canadian-drinking-water-quality-guideline- technical-document-enteric-viruses.html (accessed 2022-05-13).

(41) Gao, L.; Zhuang, J.; Nie, L.; Zhang, J.; Zhang, Y.; Gu, N.; Wang, T.; Feng, J.; Yang, D.; Perrett, S.; Yan, X. Intrinsic Peroxidase-like Activity of Ferromagnetic Nanoparticles. Nat. Nanotechnol 2007, 2 (9), 577–583.

(42) Mu, J.; Wang, Y.; Zhao, M.; Zhang, L. Intrinsic Peroxidase-like Activity and Catalase-like Activity of Co3O4 Nanoparticles. Chem. Comm. 2012, 48 (19), 2540–2542.

(43) Sloan-Dennison, S.; Laing, S.; Shand, N. C.; Graham, D.; Faulds, K. A Novel Nanozyme Assay Utilising the Catalytic Activity of Silver Nanoparticles and SERRS. Analyst 2017, 142 (13), 2484–2490.

(44) Alkawareek, M. Y.; Bahlool, A.; Abulateefeh, S. R.; Alkilany, A. M. Synergistic Antibacterial Activity of Silver Nanoparticles and Hydrogen Peroxide. PLoS One 2019, 14 (8), e0220575.

(45) González-Béjar, M.; Liras, M.; Francés-Soriano, L.; Voliani, V.; Herranz-Pérez, V.; Duran-Moreno, M.; Garcia-Verdugo, J. M.; Alarcon, E. I.; Scaiano, J. C.; Pérez-Prieto, J. NIR Excitation of Upconversion Nanohybrids Containing a Surface Grafted Bodipy Induces Oxygen-Mediated Cancer Cell Death. J. Mater. Chem. B 2014, 2 (28), 4554–4563.

(46) Quan, Q.; Xie, J.; Gao, H.; Yang, M.; Zhang, F.; Liu, G.; Lin, X.; Wang, A.; Eden, H. S.; Lee, S.; Zhang, G.; Chen, X. HSA Coated Iron Oxide Nanoparticles as Drug Delivery Vehicles for Cancer Therapy. Mol. Pharmaceutics 2011, 8 (5), 1669–1676.

(47) Caruso, F.; Hyeon, T.; Rotello, V.; Lee, N. Designed Synthesis of Uniformly Sized Iron Oxide Nanoparticles for Efficient Magnetic Resonance Imaging Contrast Agents. Chem. Soc. Rev. 2012, 41 (7), 2575–2589.

(48) Shen, Z.; Wu, A.; Chen, X. Iron Oxide Nanoparticle Based Contrast Agents for Magnetic Resonance Imaging. Mol. Pharmaceutics 2017, 14 (5), 1352–1364.

## 1.8 Post-print Version of Supporting Information

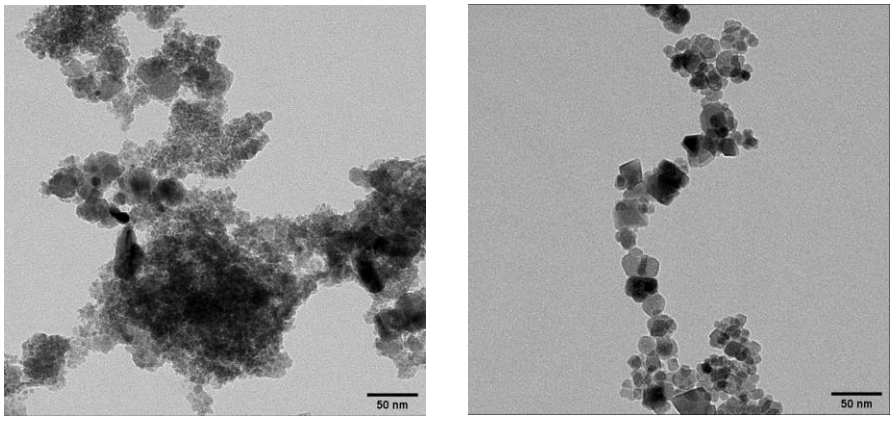


**Figure 2.3.1** Representative TEM images comparing LFeAg NPs synthesized using different initial concentrations of lignin A: 10 mg/L (left) and 1 mg/L (right). Before the imaging, the NPs were dispersed on EtOH and sonicated for 30 min. 20 μL of the ethanolic MNPs solution was dropped on the copper side of TEM grids and air dried overnight before being inserted on a JEM2100F FETEM (JEOL) instrument. Scale bars: 50 nm.

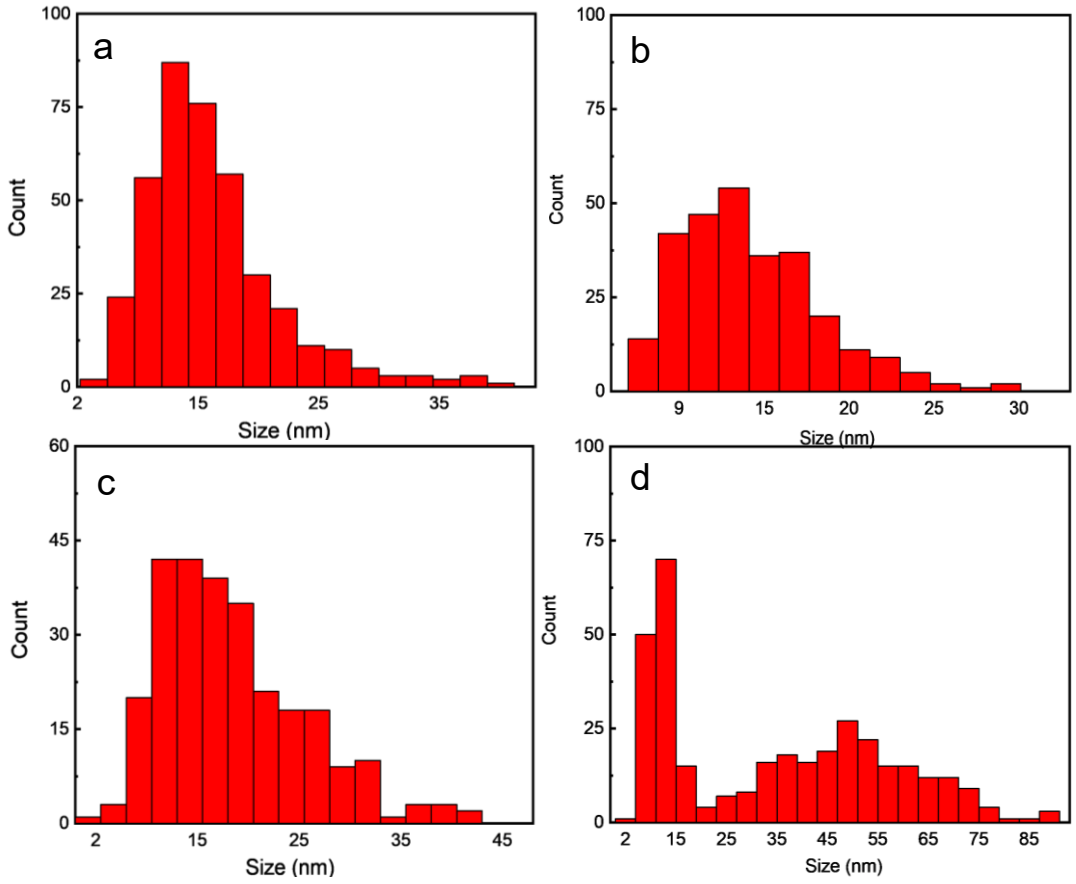


**Figure 2.3.2** Size distribution of the MNPs: LFe (a), LFeAg (b), LCo (c), and LFeCo (d). Particle sizes were obtained using their TEM images. The measurements were estimated from the largest diameter of a minimum of 300 individual particles.

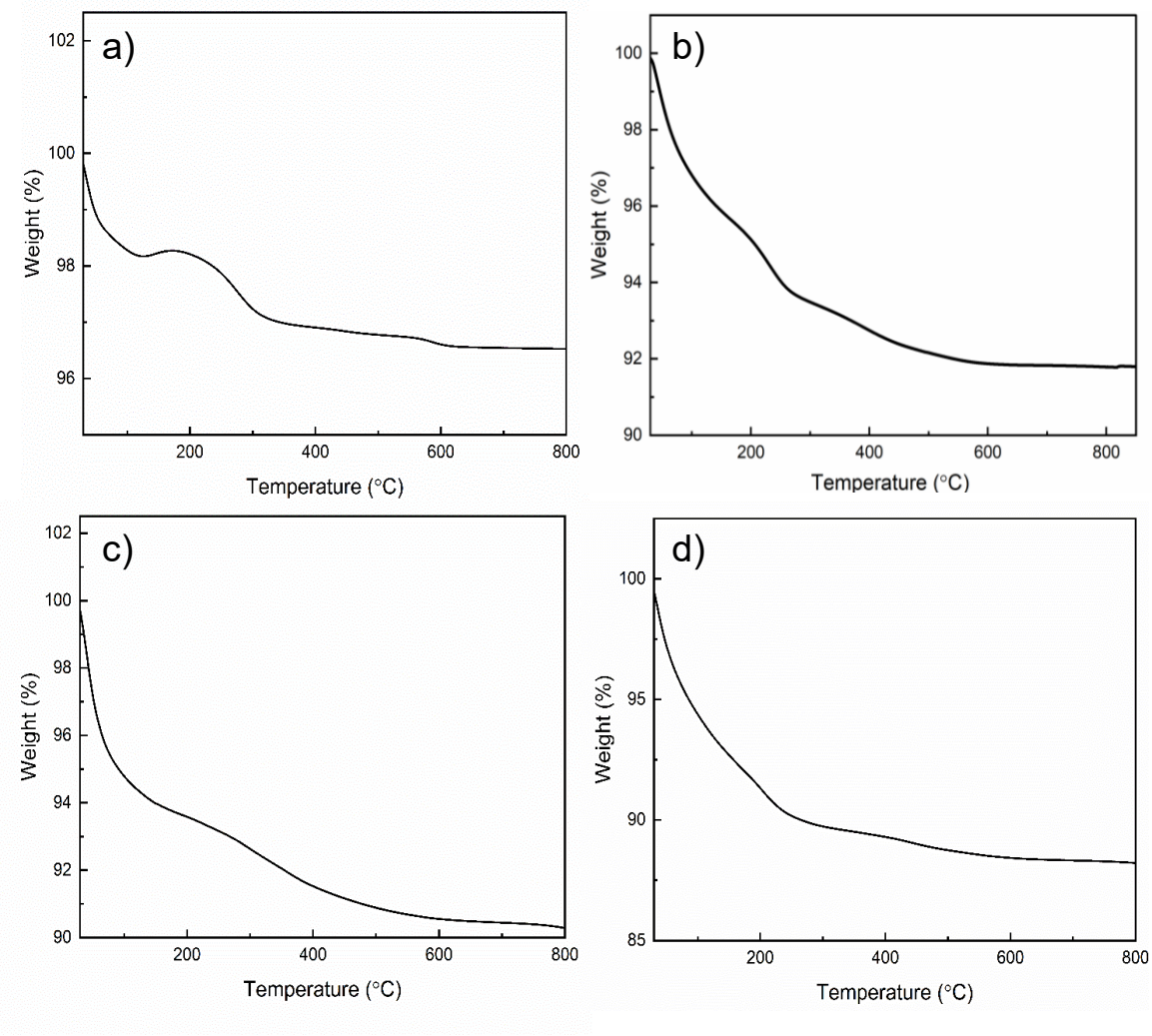


**Figure 2.3.3** Thermogravimetric analysis (TGA) graphs of the MNPs, evaluating the lignin content of LFe (a), LFeAg (b), LCo (c), and LFeCo (d). 10 mg of each sample was loaded into a Q5000 IR instrument under $N_2$, or airflow (120 mL/min) and the weight changed as the function of temperature was measured between 25-850°C with a heating rate of 10 °C/min.

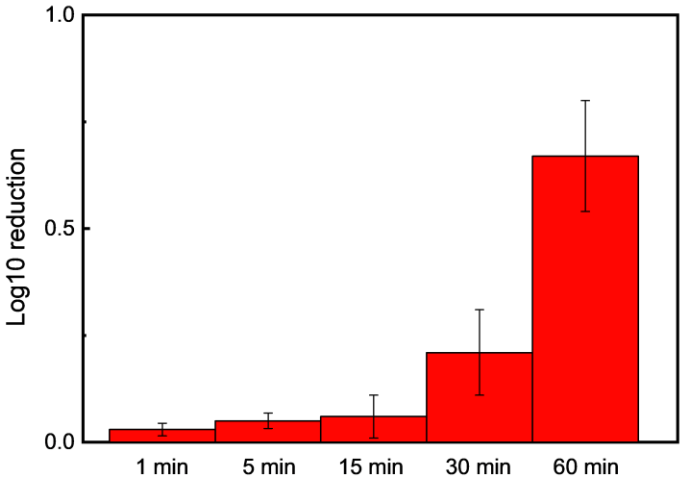


**Figure 2.3.4** Log reduction of *E. coli* incubated at higher temperatures. The Initial bacterial solution at 0.1$OD_{600}$ was incubated at 45°C for 1, 5, 15, 30, and 60 min. Log reduction was calculated relative to the number of viable cells before the experiment (CFU/mL). Error bars indicate means ± standard deviations (n=3).

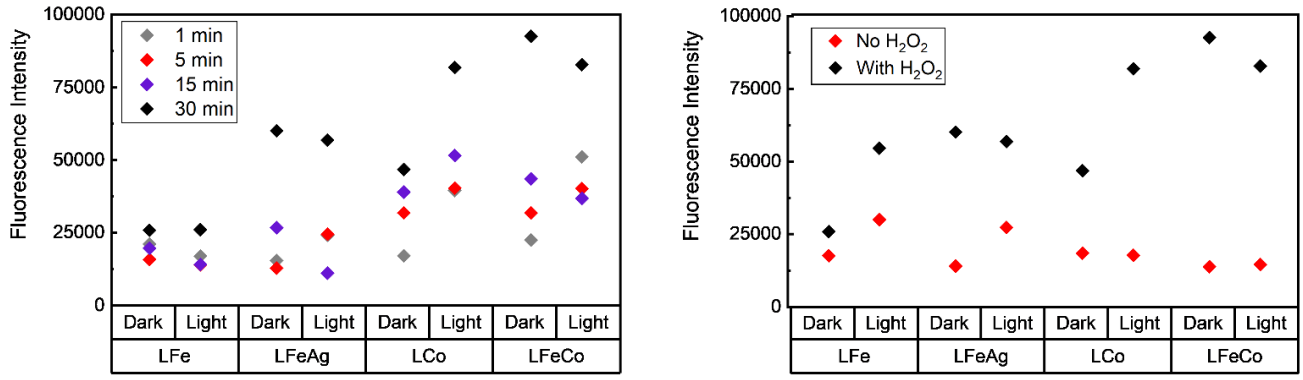


**Figure 2.3.5** Hydroxyl radicals detection using coumarin as a standard probe. Presence of the hydroxylated product, 7-hydroxycoumarin was detected by following the fluorescence at 454 nm (ex 340 nm). On the left, the fluorescence of 7HC, at 454 nm, after incubation with 125 mg/L of MNP and 0.1 mM of $H_2O_2$, in dark and under NIR irradiation (810 nm) for 1, 5, 15 and 30 min. On the right, fluorescence at 454 nm after incubation with 125 mg/L of MNP with and without $H_2O_2$ (0.1 mM) for 30 min in dark and under NIR irradiation (light) (810 nm)

**Table 2.3.1** The cumulative released amount of ions (iron, silver and cobalt) from the MNP solutions (125 mg/L) after 30 min irradiation with 810 nm LEDi (0.99 W/cm$^2$) (light) or after incubation in the dark for 30 min (dark). Ions in solution were measured using ICP-OES following the Fe, Ag and Co emissions line at 238.20 nm, 338.29 nm, and 238.89 nm respectively. Percentages were calculated based on the total amount of NPs added to the solution.

| Nanomaterial | Iron | Silver | Cobalt |
|---|---|---|---|
| **LFe Dark** | 10.7 ppm (8.5 %) | - | - |
| **LFe light** | 15.7 ppm (12.6 %) | - | - |
| **LFeAg Dark** | 7.4 ppm (5.9 %) | 0.2 ppm (0.2 %) | - |
| **LFeAg Light** | 5.9 ppm (4.7 %) | 0.2 ppm (0.2 %) | - |
| **LFeCo Dark** | 1.0 ppm (0.8 %) | - | 3.6 ppm (3.0 %) |
| **LFeCo Light** | 1.1 ppm (0.8 %) | - | 4.0 ppm (3.2 %) |
| **LCo Dark** | - | - | 9.4 ppm (7.7 %) |
| **LCo Light** | - | - | 12.1 ppm (9.9 %) |

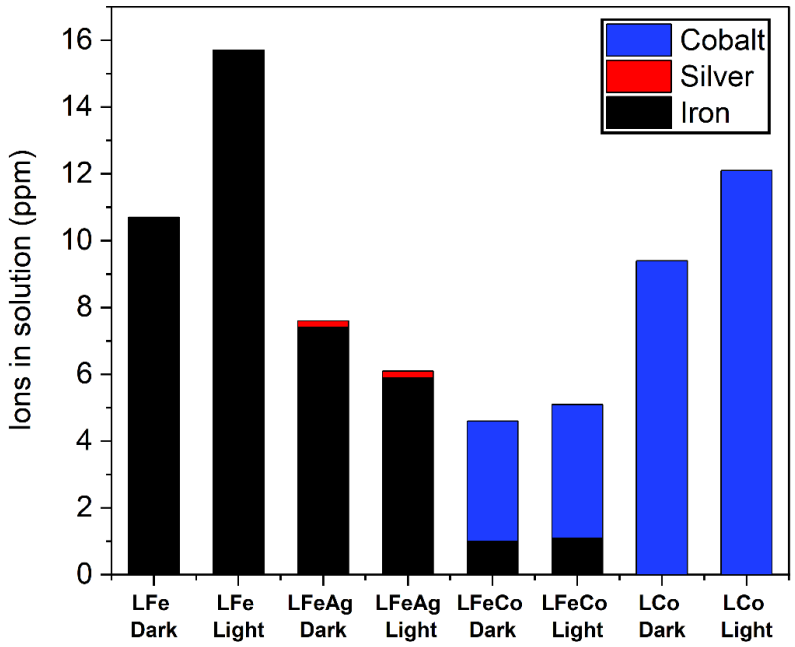


**Figure 2.3.6** The cumulative released amount of ions (iron, silver and cobalt) from the MNP solutions (125 mg/L) after 30 min irradiation with 810 nm LEDi (0.99 W/cm$^2$) (light) or after incubation in the dark for 30 min (dark). Ions in solution were measured using ICP-OES following the Fe, Ag and Co emissions line at 238.20 nm, 338.29 nm, and 238.89 nm respectively. Amounts of released ions are expressed in parts per million (ppm).

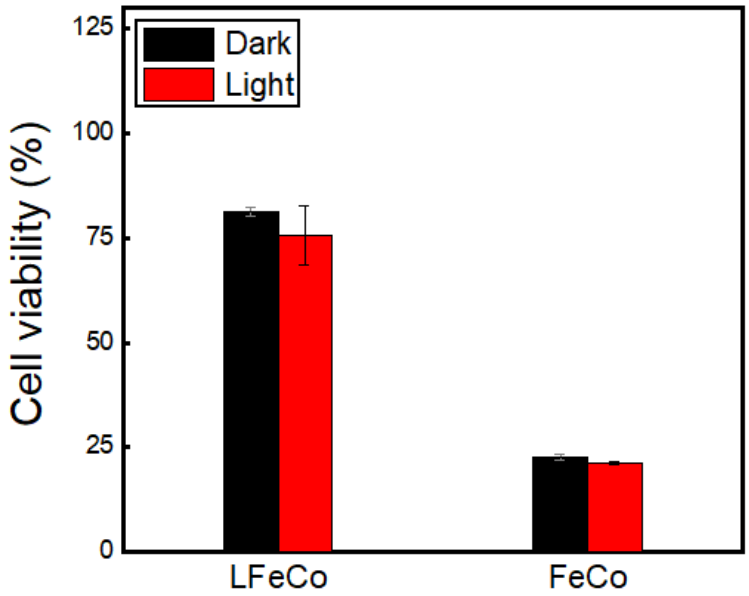


**Figure 2.3.7** Cell viability of human fibroblasts (HT1080) treated with 125 mg/L of Lignin@FeCo (LFeCo) and uncapped FeCo nanocomposites in the presence (red) and absence (black) of NIR (810 nm - 0.99 W/cm$^2$) irradiation for 5 min. Nanocomposites were removed with an external magnet and cells were incubated for 24 h prior to viability tests. For cell viability, MTT (0.5 mg/mL) reagent was added to the treated cells. After 2 h incubation, the produced formazan crystals were dissolved in DMSO, and the absorbance was measured at 590 nm. The viability percentage was calculated by comparing the absorbances of treated cells to untreated controls incubated in the dark. Error bars represent standard deviation.

## 1.9 Accompaniment to Chapter 2

Here we explored four simple approaches to fabricate magnetic NPs. The synthetic approach developed for bimetallic NPs will be further revisited in Chapter 5. Interestingly the use of lignin was proven to be a great choice of biocompatible capping agent facilitating NPs stabilization while reducing toxicity towards human cells. In addition, it repurposes a material that is often discarded by pulp and paper industries. Thus, contributing to the quest for more sustainable alternatives.

The remarkable bacterial cell reduction above 3-log units in short periods for PTT and CDT treatments highlights the exceptional bactericidal properties of those materials. Moreover, the combination of PTT and CDT further reduces the necessary treatment duration to 1-5 min, which is great for reducing potential damage to mammalian cells. Particularly, FeCo had great performance across all antibacterial tests while maintaining cell viability at about 80 %.

# 3. Fibrous $TiO_2$ Alternatives for Semiconductor-Based Catalysts for Photocatalytic Water Remediation Involving Organic Contaminants

This chapter has been adapted from ACS Omega, 2023, 8, 21585-21593, with permission from the American Chemical Society. To allow for consistent formatting and clarity, some changes have been made.

## 3.1 Preamble to Chapter 3

The following chapter describes the synthesis and comparison of three fibrous $TiO_2$ catalysts for water purification, evaluating their catalytic performance and morphological features. The three developed fibres—$TiO_2$ nanofibres (TNF), $TiO_2$ glass wool (TGW), and $TiO_2$ glass filter (TGF)—are highlighted as promising alternatives for water purification due to their macroscopic dimensions, which make them ideal candidates for fixed-bed reactors compared to traditional powder $TiO_2$ such as P25. We developed standardized tests for both batch and continuous flow systems, using crocin as a surrogate molecule for organic contaminants. The catalysts demonstrated impressive catalytic performance in batch tests, achieving degradation values above 80%. Notably, in continuous flow systems, they showed significantly faster degradation rates. For example, TGW bleached 43% of the dye within just 35 seconds of irradiation, a process that would take at least 1 hour in our batch system. The chapter also includes a comparative analysis of these materials in terms of synthesis convenience, affordability, and efficiency, considering their potential for scaling up production and application.

The second element of interest, titanium (Ti), is particularly significant in its oxide form, $TiO_2$. This semiconductor nanomaterial is predominantly used as a powder. To broaden its applications, we focused on fabricating new $TiO_2$ nanostructures that facilitate separation from solutions. My initial interest in titanium dioxide-based materials began with an opportunity to develop metal-oxide nanofibres at Rhodes University in South Africa as part of an IDRC grant

with groups from Kenya and South Africa. During my time at Rhodes University, I learned how to develop and characterize semiconductor-based electro-spun nanofibres, and $TiO_2$ was highlighted for its efficient synthesis.

Upon returning to the University of Ottawa, my interest shifted towards exploring other macroscopic alternatives for $TiO_2$-based catalysts for water remediation. This led to the development of $TiO_2$ deposited on glass wool. This supporting material was previously employed by our group for supporting noble metals and ruthenium complexes, proving to be an excellent candidate. Additionally, with my colleagues' collaboration, we successfully developed $TiO_2$ deposited on a glass filter. Both syntheses were surprisingly straightforward and resulted in a great $TiO_2$ deposition on the glass materials.

We then became interested in comparing the three materials as potential candidates for water remediation. For photocatalytic molecule degradation, dyes are great alternatives for simple spectroscopic quantification. From prior studies from our group, we learned that traditional dyes used as surrogate molecules were unsuitable for tests with glass-based catalysts. We quickly identified crocin as an effective surrogate molecule, thanks to its characteristic peak in the visible range, and lower adsorption onto glass. In the batch experiments, we utilized degradation rates during light exposure to determine the best-performing catalysts, which were the TNFs. Interestingly, their catalytic performances and suitability differed significantly in flow tests. We observed that TGW adapted more easily to various flow systems, compared to the other fibrous materials. Additionally, the glass wool's shape allowed for more contact with the solution inside the tube, significantly enhancing TGW's degradation potential compared to the other materials.

### 3.2 Post-print version of Manuscript

First published in ACS Omega, 2023, 8, 21585-21593

## ABSTRACT

Water decontamination remains a challenge in several developed and developing countries. Affordable and efficient approaches are needed urgently. In this scenario, heterogeneous photocatalysts appear as one of the most promising alternatives. This justifies the extensive attention that semiconductors, such as $TiO_2$, have gained over the last decades. Several studies have evaluated their efficiency for environmental applications; however, most of these tests rely on the use of powder materials that have minimal to no applicability for large-scale applications. In this work, we investigated three fibrous $TiO_2$ photocatalysts, $TiO_2$ nanofibres (TNF), $TiO_2$ on glass wool (TGW), and $TiO_2$ in glass fibre filters (TGF). All materials have macroscopic structures that can be easily separated from solutions or that can work as fixed beds under flow conditions. We evaluated and compared their ability to bleach a surrogate dye molecule, crocin, under batch and flow conditions. Using black light (UVA/visible), our catalysts were able to bleach a minimum of 80% of the dye in batch experiments. Under continuous flow experiments, all catalysts could decrease dye absorption under shorter irradiation times: TGF, TNF, and TGW could, respectively, bleach 15, 18, and 43% of the dye with irradiation times as short as 35 s. Catalyst comparison was based on the selection of physical and chemical criteria relevant for application on water remediation. Their relative performance was ranked and applied to a radar. The features evaluated here had two distinct groups, chemical performance, which related to the dye degradation, and mechanical properties, which described their applicability in different systems. This comparative analysis gives insights into the selection of the right flow-compatible photocatalyst for water remediation.


## INTRODUCTION

Universal access to safe water is still a major challenge for nations around the globe. According to the United Nations, the lack of sufficient water treatment plants and sanitation is responsible for letting more than 1.5 billion people consume unsafe water every year.[1] Human activities are one of the main sources of contamination, introducing a growing number of compounds into the water bodies. Such contaminants range from pathogens, heavy metal ions, and

organic pollutants.[1-3] Among the latter are pharmaceuticals, endocrine disrupters, personal care products, dyes, phenols, and benzene compounds.[1,4-6] Addressing this challenge calls for affordable and efficient alternatives while being safe for humans and having minimal environmental impact.

Among the most promising alternatives for water remediation, the use of heterogeneous catalysts is one of the most developed alternatives due to their stability, low cost, and nontoxicity. Since the discovery of photocatalytic water splitting using $TiO_2$, in 1972, by Honda and Fujishima,[7-8] this semiconductor has gained great attention for photocatalytic uses. It is widely used for energy purposes and environmental applications.[9-11] Its large band gap (3.19 eV) gives it enough energy to perform catalytic reactions that is generally require large energy inputs, such as water oxidation and radical formation. In particular, hydroxyl radicals and other radicals originating from them are of great interest due to their high antimicrobial nature,[12] which also finds utilization in degrading organic materials. These two applications combined can make $TiO_2$ a promising catalyst for water remediation.[13-15]

Most of the research has been performed with powder $TiO_2$, frequently commercial P25 grade which is mostly anatase phase with particles of around 25 nm in size. This is generally suitable for small-scale batch applications and many interesting “proof-of-concept" reports are available.[16-22] For environmental applications, particularly if they involve water treatment, batch strategies with powder catalysts are unlikely to find practical applications. For this, flow methods are essential for suitable scale-up to be viable. Further, if illumination is required, batch systems present additional challenges because of limited light penetration and the need for surface exposure to incident light. In our recent research, we have found that fibrous materials, including $TiO_2$–rich components have excellent properties for flow catalysis, as they present a fixed bed catalyst, that allows liquids to flow without loss of catalytic materials.[23] In a typical test, the fibrous material is not exposed to mechanical challenges, so it simply needs to be robust enough to maintain its integrity in the presence of liquid flow, a frequently reducing environment and simultaneous illumination.[23]

Flow-suitable catalysts can be achieved by the preparation of fibrous $TiO_2$, such as nanofibres and microfibres,[24-26] or by using a support material to deposit the $TiO_2$ photocatalyst. The latter is a supported catalyst. The *in-situ* synthesis, deposition, impregnation, and precipitation of catalytic material on inert surfaces introduces compatibility with flow systems, and thus easy separation from solutions. Some of the supports developed include glass wool, glass beads, glass filters, and cellulose filters.[16,21,23,27–29]

In our group, we are investigating the use of glass supports for titanium dioxide, due to their inert, non-toxic, and inexpensive characteristics. In this contribution, we tested three $TiO_2$-rich materials. The first one consists of $TiO_2$ fibres (about 1 μm diameter) produced by electrospinning ($TiO_2$NF). The other two materials are preceded by *in-situ* depositing $TiO_2$ on glass fibres. In one of them, the substrate is glass wool pretreated with APTES with fibres of about 10 μm of diameter ($TiO_2$@GW), and in the other $TiO_2$ was deposited on glass filters, a fibrous cardboard-like material consisting of glass fibres of about 100 nm in diameter. Our tests include bleaching of an organic dye, crocin, which is the pigment present in saffron. For illumination, we use a 30 cm long black light (UVA/Visible ~400 nm), a safe source, that emits at the edge of the absorption profile of $TiO_2$. Our work involves batch studies and a bench-scale flow system to evaluate and compare these materials aiming at future applications in large-scale flow systems. Here we compared and discussed the performance of those materials using parameters such as flow compatibility, availability, convenience (including synthesis), photochemical activity, mechanical properties and reusability.

## MATERIALS AND METHODS

### Materials

Unless otherwise specified, all chemicals and glass wool fibres were purchased from Sigma-Aldrich and used without further purification. Glass fibre filters were purchased from Pall Corporation, and APTES (3-aminopropyl triethoxysilane) from Tokyo Chemical Industry Co., Ltd. (TCI).

## Catalyst Preparation

### $TiO_2$ nanofibres (TNF)

A 10% PVP (polyvinylpyrrolidone) solution was prepared in 20 mL of ethanol (EtOH) with vigorous stirring for 2 h. A mixture of 5 mL (60 mM) TiP (titanium isopropoxide) and 5 mL acetic acid was made by stirring them until a transparent solution was obtained, which was then added to the PVP/EtOH solution, followed by vigorous stirring for 8 h. This polymeric solution was loaded into a 20 mL plastic syringe for electrospinning. Fibres were spun applying a positive voltage of 18 kV at the needle tip with respect to the collector metal (aluminum tray) with tip to collector distance (TCD) of 12 cm. A syringe pump was used to flow the solution at a flow rate of 1 mL/h. After the entire solution was spun, the collected material was removed from the aluminum tray and calcined to obtain anatase $TiO_2$. The calcination was done under air, at 500°C for 2 h.

### $TiO_2$@Glass Wool (TGW)

A 10% PVP solution was prepared in 20 mL of EtOH with vigorous stirring for 2 h. A mixture of 5 mL (60 mM) titanium isopropoxide and 5 mL acetic acid was made by stirring them until a transparent solution was obtained, which was then added to the PVP/EtOH solution, followed by vigorous stirring for 2 h. The $TiO_2$ precursor solution was added to a 30 cm glass tube, with 1.5 g HCl (6 M) and APTES-treated glass wool as previously described.[23] The solution was stirred using a rotator overnight at room temperature; the slow rotation ensured adequate mixing without mechanical stress for the fibres. After this period, the glass wool was removed and carefully washed 3x with EtOH and 3x with distilled water and let dry in the oven at 80 °C overnight. The dry TGW was then calcined under air using a tube furnace heated at 500 °C for 2 h followed by 5 min at 600 °C. The material was left to cool down at room temperature, washed 5x or until a clear solution was obtained with distilled water and dried at 80 °C.

### $TiO_2$@Glass Filter (TGF)

TGF catalyst was synthesized directly onto the glass fibre filter. Glass fibres (with long fibres about 300 nm in diameter), were cut by hand into strips (0.60 cm in width and ranging from 5.50 to 25.0 cm in length) using ceramic scissors to avoid contamination. These were weighed and placed in an aluminum foil tray. Once in the tray, 3 to 5 mL of TiP was added on both sides of the

filter strips to ensure saturation. Following this, the aluminum tray was filled with deionized water. The saturated strips were left submerged in water for 15 minutes, on each side. The loaded filter strips were then removed from the aluminum tray and placed between two sheets of aluminum foil. Using a clothing iron, the sandwiched filter strips were ironed at medium heat (140-160 °C) until dry. To obtain anatase $TiO_2$, the dried glass filter strips of $TiO_2$ supported on the glass fibre filter paper were placed inside a tube furnace and heated at 500 °C for 2 h followed by 5 min at 600 °C. The material was left to cool down at room temperature, washed 5x or until a clear solution was obtained with distilled water and dried at 80 °C.

**Photocatalytic activity**

The photocatalytic performance of the three catalysts was evaluated using a UVA/visible black light composed of 9 LEDs with maximum emission at 400 nm (Viugreum). The irradiance of each LED was measured at a 3 cm distance using a spectroradiometer (Luzchem, SPR-4002, Ottawa, Canada) The energy distribution for a single LED is described in Table 2.2.1.

**Table 3.2.1** Energy distribution of a single LED measured with a spectroradiometer.

| Region | Power W/m$^2$ |
|---|---|
| UVB | Traces |
| UVA | 12.9 |
| Visible | 5.1 |
| Total | 18.0 |

**Characterization**

SEM images were acquired using a JSM-7500F field emission scanning electron microscope from JEOL Ltd. Elemental identification mapping was done using a Zeiss Gemini SEM 500 equipped with an energy dispersive X-ray spectrometer (EDS) system (QUANTAX, Bruker). Diffuse reflectance (DR) measurements were carried out in VARIAN Cary 100 UV-VIS Spectrophotometer coupled with an integrating sphere accessory and absorption spectroscopy was performed in a Cary-60 UV-Visible spectrophotometer. Fourier Transformed Infrared (FTIR)

spectra were obtained on a Nicolet IS5 FTIR spectrometer equipped with an iD7 Attenuated Total Reflectance (ATR) accessory. For each sample 64 scans were recorded with resolution of 4 $cm^{1}$. Powder X ray diffraction analysis was carried out at room temperature on Rigaku Ultima IV powder diffractometer in Bregg Brentano geometry, using Cu Kα radiation (λ = 1.5418 Å). Two theta range of 20° to 90° was covered with 0.02° step width and 0.5°/min scan speed. The specific surface area was measured using the Brunauer–Emmett–Teller (BET) $N_2$ isotherms collected on a Micromeritics 3Flex adsorption analyzer at 77 K (liquid $N_2$ bath). Prior to measurements, all samples (0.030 – 0.050 g) were activated using a Micromeritics Smart VacPrep under a high vacuum at 100 °C for 24 h. We aimed to study the charge separation using the photoluminescence technique. However, the glass wool utilized has luminesce that interfered with the emission from $TiO_2$ (Figure 3.3.13), thus we decided not to use this technique to compare the photocatalysts used.

**Degradation of an organic dye**

The photocatalytic activity of the fibrous $TiO_2$ materials was evaluated by following the photodegradation of crocin ($C_{44}H_{64}O_{24}$, see Scheme 3.3.1); we note that "degradation" does not imply complete mineralization. The reaction vessel was maintained at ambient temperature. In a typical experiment, aqueous solutions of crocin (5 mL, 8.1 μM) were mixed with the fibrous $TiO_2$ catalysts in a glass vial. Since each material has different $TiO_2$ loading we weighed the materials to obtain a final concentration of 10 mg/mL of $TiO_2$ in the solution. The solutions were stirred constantly, using a microplate shaker. Before irradiation, the suspension was kept in the dark to establish adsorption/desorption equilibrium. At 30 min intervals, 1 mL of the suspension was collected, and dye absorbance was measured. The change in absorbance at 440 nm was plotted against time.

Degradation under an inert atmosphere was run similarly to the batch experiments. Samples were purged with $N_2$ for 20 min prior to illumination. During the three hours of the experiment, samples had $N_2$ balloons attached to guarantee the inert atmosphere.

We note that methylene blue is a frequent choice for photodegradation work. However, we noted that methylene blue absorbs strongly on glass-based materials, thus masquerading as dark bleaching of the dye. This led to the choice of crocin as the dye for degradation studies.

**Reuse of $TiO_2$ catalysts**

To study the reusability of the catalysts, all the experimental parameters were kept constant, and the experiments were repeated for 5 sets using the same catalyst and fresh dye solutions. After each photodegradation assay, the catalyst was rinsed with distilled water to remove any organic contaminant. The catalysts were dried at 100° C overnight, before each use.

**Continuous flow degradation**

Flow experiments were performed in a bench-scale system. Catalysts were placed inside a 15.9 cm long tube (I.D.: 3 mm) connected through a PVC tubing (I.D.: 4 mm). Catalyst amounts were set to obtain 8 mg of $TiO_2$ inside the tube. A total volume of 20 mL of crocin solution was fed into the system using a syringe pump (NE-300 Just Infusion™ Syringe Pump) at 10, 30, 50, or 100 mL/h. The solution flowed in the dark until a steady state was achieved. For irradiation experiments, the tube was placed between two UVA/Visible black lights and 3 LEDs from each lamp were used as light sources, while the other six LEDs were covered with aluminum foil. Residence time (the time in which the solution spends in contact with the catalyst and is exposed to light) was determined by dividing the volume of the flow tube by the flow rate. Note that due to the different volumes filled by the catalyst itself, the total liquid capacity inside the tube is different for each material. The total exposure (from three LEDs) is thus three times that indicated in Table 3.2.1. The outlet samples were examined every minute using a Cary-60 spectrometer equipped with a flow cuvette that allows in-line monitoring. The absorbance at $\lambda$= 440 nm was recorded and compared with the initial absorbance of the crocin solution.

**High-performance Liquid Chromatography (HPLC)**

Analysis. To evaluate the resulting solution, from the single-pass flow experiment, we irradiated an aqueous solution of crocin 1 mM in the presence of TGW until 90% bleaching was observed. The treated solution was then evaluated using high-performance chromatography. HPLC was performed on an Agilent 1260 infinity II series HPLC instrument, using a ZORBAX SB-C18 column (2.1 × 50 mm−1.8 μm particle size). Acetonitrile and water were used as mobile phases using the gradual change from 10:90 (acetonitrile:water) to 80:20 at a flow rate of 1 mL/h.

## RESULTS

### Characterization

The use of photocatalysts in water remediation is generally limited by their powder morphology, which makes it hard to separate them from solution and is not suitable for flow reactors. Knowing the importance and effectiveness of $TiO_2$ we designed three new fibrous $TiO_2$ materials that are compatible with flow systems. For all materials, $TiO_2$ was fabricated *in situ* using Titanium isopropoxide (TiP) as a precursor followed by calcination. Titanium dioxide nanofibres (TNF) were made up of only $TiO_2$. The two catalysts on glass supports, $TiO_2$ on glass wool (TGW) and on glass filter (TGF) had $TiO_2$ loading determined gravimetrically. TGW has 48 % and TGF 62 % of the semiconductor. Photographs of the materials can be found in Figure 3.3.1, all fibrous materials have large macroscopic structures and can be easily removed from the reactions using tweezers or stay in flow tubes without moving with the solutions. $TiO_2$ nanofibres were made with support polymer (PVP), which was used to give the viscosity to the precursor solution, allowing it to be electrospun and as support for the semiconductor precursor. Before calcination, fibres had an average diameter of 1.5 μm (± 0.3 μm) (Figure 3.3.3A), which decreased to 0.98 μm (± 0.4 μm) after annealing. Macroscopically, the fibres were flake-like in shape and were very light.

Using the same polymer support (PVP) and precursor solution for the nanofibres, we loaded $TiO_2$ to the APTES-treated glass wool (9.4 ± 1.8 μm), giving the catalyst a fibrous support. APTES was bonded to the glass through the silicon moieties, leaving free amino groups on the glass surface which undergo hydrogen bonding with the available hydroxyl groups on $TiO_2$.[30] Calcination at 500 ℃ allows the formation of crystalline $TiO_2$ without damaging the glass. Tests with different annealing temperatures (data not shown), demonstrated that at temperatures closer to the GW melting point (680 °C) the semiconductor had better adherence to the support. Thus, we selected a short time at 600 °C to avoid the conversion of anatase into the rutile form of $TiO_2$. After synthesis, $TiO_2$ can be seen covering and connecting the glass wool fibres (Figure 3.2.1B). Close-up photos comparing the original support, and the final material highlight the presence of a $TiO_2$ net in the fabricated material (Figure 3.3.2). Using SEM, we can also observe that $TiO_2$ formed a film-like coverage on the fibres (Figure 3.2.1). At breakage spots, the fibre and its coating

are readily distinguishable. The location of the semiconductor on the glass support is further confirmed using EDS mapping (Figure 3.3.4).

The third material, $TiO_2$@Glass filter (TGF), used commercially available glass fibre filters as support. Originally the glass fibres had 0.36 µm in diameter with a polydisperse size distribution. After $TiO_2$ addition we can see that the photocatalyst was deposited between the glass fibres on the support (Figures 3.2.1C and 3.3.5). Moreover, even after the $TiO_2$ treatment, the final material maintained the macroscopic features of the original glass filter (Figure 3.3.1). Different from the previous TGW, no APTES treatment was required, in this case since the intricate glass fibres arrangement was able to retain the semiconductor.

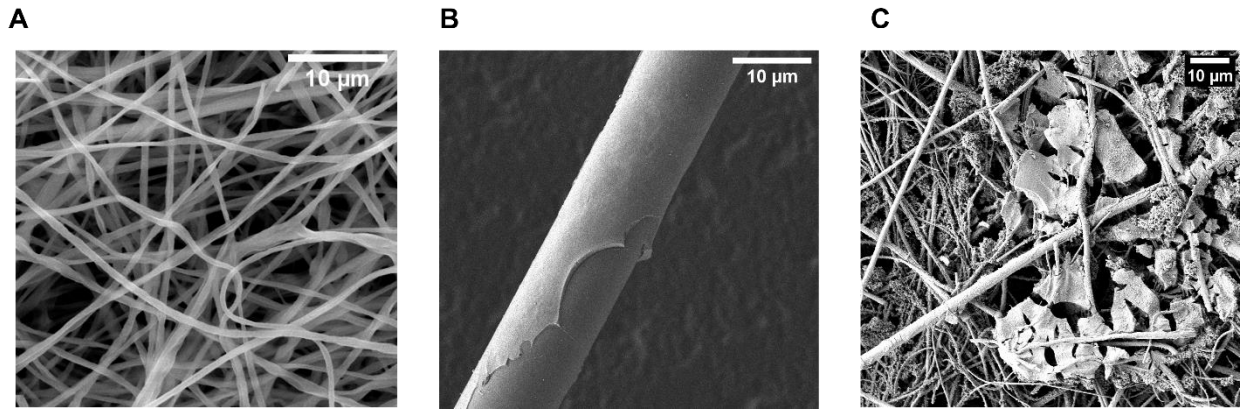


**Figure 3.2.1.** Representative SEM images of fibrous $TiO_2$: (A) $TiO_2$ nanofibres (TNF), (B) $TiO_2$ Deposited on a glass wool fibre (TGW), and (C) $TiO_2$ deposited on glass filter fibre (TGF). All the SEM images were taken after materials calcination at 500 °C. Scalebar: 10µm

FTIR spectra of the fibrous photocatalysts can be found in the supporting information (Figure 3.3.7). For the materials containing glass (TGW and TGF) we can see the characteristic bands for silicate glass, with the prominent vibration band at ~1000 $cm^{-1}$ for the asymmetric stretch of Si-O, the weak band at ~ 800 $cm^{-1}$ assigned to the Si-O bending and the band at ~ 480 $cm^{-1}$ corresponding to the rocking bend of Si-O-Si. Note that the vibration at ~ 1000 $cm^{-1}$ shifted between the two glass materials (GW and GF). This band is the most sensitive to changes in the structure since it is affected by the Si-O-Si bonding angle. In all samples containing $TiO_2$ (TNF,

TGF and TGW) we see the band corresponding to Ti-O stretching located ~ 438 $cm^{-1}$. In glass-containing samples, this band is overlapped with the Si-O-Si rocking vibration from the support.

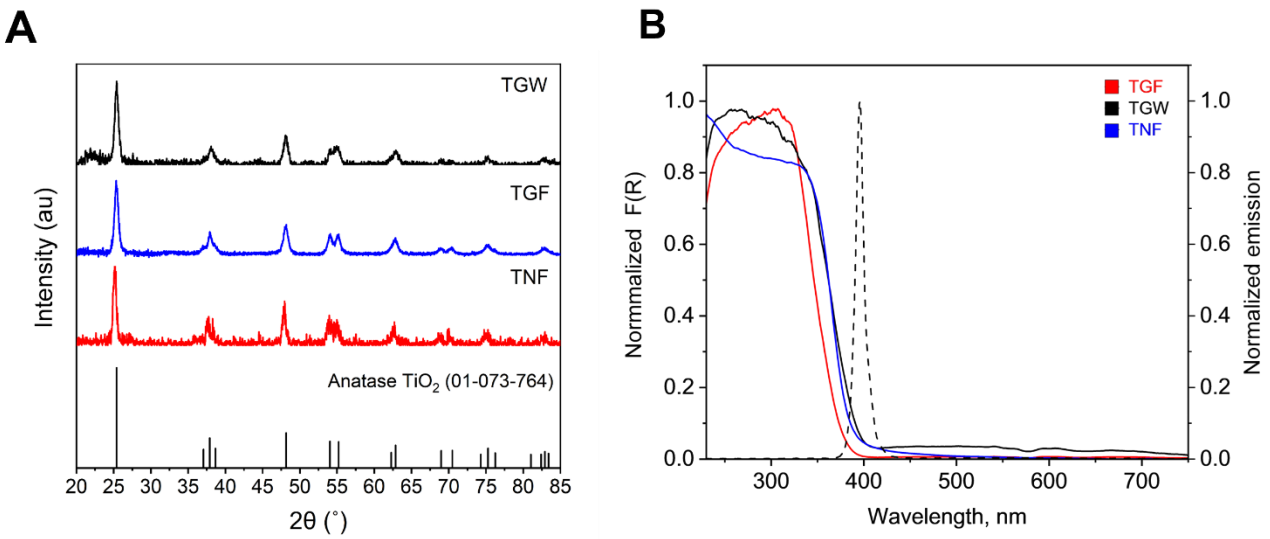


**Figure 3.2.2.** (A) XRD diffractogram of the produced fibrous materials: $TiO_2$ NF (red) $TiO_2$@GF (blue) and $TiO_2$@GW (black) and the PDF card 01-073-1764 pattern for anatase $TiO_2$. (B) Normalized diffuse reflectance of the fibrous $TiO_2$ materials (solid line) and emission of the black light used in the experiments (dashed line). Tauc plots are shown in Figure 3.3.8.

X-ray diffractograms reveal that all materials are composed of the anatase crystalline phase, which is the most photocatalytic active.[31-34] The position of the peaks at 2θ = 25.4, 37.9, 48.1, 55.05, 55.2, and 62.9° correspond to the respective planes (101), (004), (200), (105), (211), (204) of tetragonal anatase $TiO_2$ (ICDD: 01-073-1754) (Figure 3.2.2A). Using the Scherrer equation, we calculated the crystalline sizes of the photocatalysts finding 13.2 nm, 10.3 and 9.5 nm for TNF, TGW and TGF, respectively. Interestingly, TGW and TGF, which were treated at 600 °C for 5 min did not show any peak corresponding to the rutile phase, which is the most thermally stable form. Lastly, optical properties were measured with diffuse reflectance.

As expected for anatase $TiO_2$ all three materials have strong absorbance in the UVA range (Figure 3.2.2B) with band gaps between 3.12 and 3.22 eV (Figure 3.3.8), in agreement with typical values for anatase $TiO_2$. The emission of the light source chosen for the experiments can also be seen in Figure 3.2.2B (dashed line). The maximum at 400 nm matches with the absorption tail of

the nanostructures, utilizing the photocatalyst ability of this semiconductor while emitting a safer wavelength for users.

Part of the catalyst efficiency is defined by its surface area. To compare these catalysts, we analyzed the $N_2$ isotherms using the Brunauer–Emmett–Teller (BET) method to obtain their specific surface area (SSA). All materials revealed typical type IV isotherms (according to IUPAC classification) with a hysteresis loop (capillary condensation).[35] Table 3.2.2 summarizes the results for all the fibrous materials, before and after $TiO_2$ treatment (when applicable). The first observation is the difference between the SSA of both glass supports alone, glass filter and glass wool. The larger surface area of the glass fibre filters justifies the higher loading of $TiO_2$ when compared with TGW. Moreover, for the glass wool, the addition of APTES not only created better adherence to $TiO_2$ but also led to some increase in the surface area of the material.

**Table 3.2.2** Specific surface area ($m^2/g$) of the fibrous catalysts and their support materials (if applicable)[a].

| Sample | SSA ($m^2/g$) |
|---|---|
| TNF | 15.8 ± 0.2 |
| GF | 20.2 ± 0.4 |
| TGF | 25.0 ± 0.7 |
| GW | 6.8 ± 0.2 |
| APTES-GW | 12.4 ± 0.2 |
| TGW | 17.4 ± 0.3 |

[a] Obtained by BET analysis of the $N_2$ adsorption-desorption isotherms acquired at 77K

TGF had the higher surface area out of the three $TiO_2$-rich materials with 25.02 $m^2/g$, followed by TGW and TNF with 17.4 and 15.8 $m^2/g$ respectively. Part of this difference is justified by the crystallite sizes of each material, where smaller crystallite sizes lead to larger SSA.[36] Among the three materials, TGF had the smaller average crystallite sizes (9.5 nm). Another reason is the presence and type of glass support. We can see that GF alone had already a large surface area that was impregnated with the semi-conductor. Interestingly for both glass-supported catalysts, the addition of $TiO_2$ increased the total surface area of the material, which is due to the higher porosity of $TiO_2$, when compared to the glass supports.

## Crocin degradation

While all the catalysts are flow-compatible, we developed a set of batch experiments in small batch systems to evaluate catalyst performance. We used crocin, a carotenoid extracted from Saffron, as a surrogate molecule. The high presence of delocalized electrons makes it strongly absorbent in the visible range with a maximum at 440 nm (Figure 3.3.15-dashed line). Under light irradiation (λ ~ 400 nm, 18 W/m$^2$ for each of the 9 LEDs), crocin solution alone (8.1 μM in water) bleaches slowly, ~20% during 3h of light exposure (Fig. 3.3.9), probably mediated by singlet oxygen or cis-trans isomerization.[37,38]

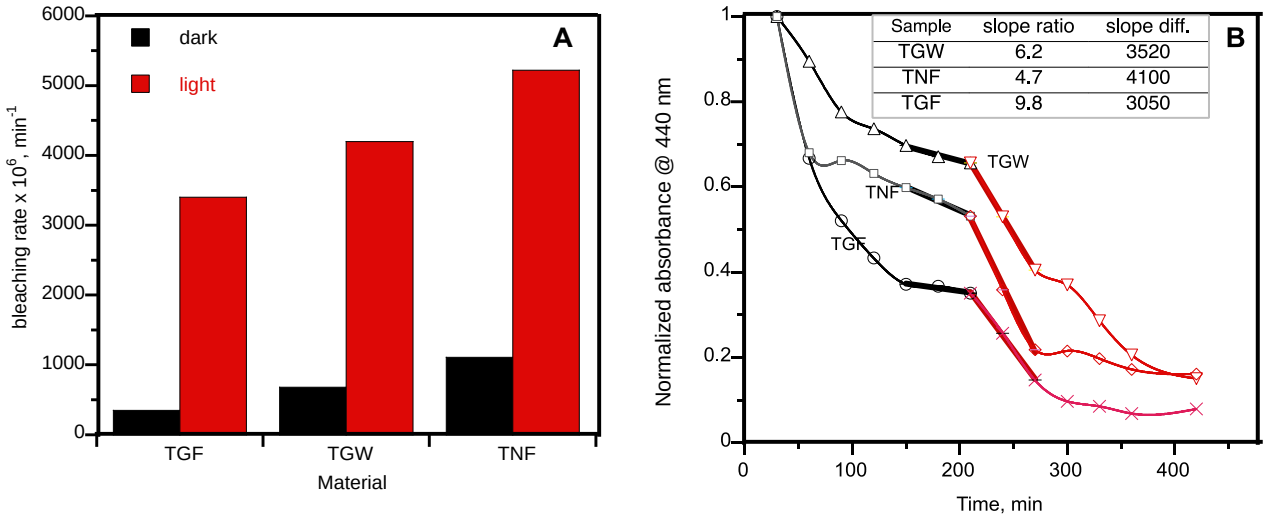


**Figure 3.2.3.** A) Crocin bleaching rates, in the dark (black) and un-der irradiation using a black light (red), in the presence of the fibrous $TiO_2$-rich materials. Crocin remaining based on the absorbance at 440 nm over time. B) Decay of crocin absorption as a function of time in the presence of the fibrous $TiO_2$-rich mate-rials. Insert: slope ratio and the difference between dark and light treatment for the three fibrous catalysts. Slopes (rates) are based on the last 3 points (black heavy line) before turning on the 400 nm light and the three points immediately after the lights are turned on (red heavy line). All rates in units of $10^{-6}$ min$^{-1}$.

The dye solution and catalysts were incubated in the dark for 3 h to allow adsorption equilibration. Change in absorbance in the dark can be seen in Figure 3.2.3A. The dark adsorption order followed the SSA order for all the materials (Figure 3.2.4). Catalysts were impregnated with the yellow dye, in particular TGF which had the highest surface area (Figure 3.3.11), proving that the bleaching in the dark is due to adsorption on the photocatalyst. Note little to no decrease in

absorbance was not observed when the dye was incubated with the glass support alone (Figure 3.3.10)

As the light was turned on (at 200 min), the degradation rate increased (Figure 3.2.3B), and after 3 h of irradiation (18 W/m$^2$), the maximum absorbance dropped 84 % in the presence of TNF, 85 % for TGW and 92 % for TGF. It is noteworthy, the higher degradation rates are related to the materials showing absorption profiles that overlap better with the excitation wavelengths (*cft*. Figures 3.2.2B and 3.3.7). Mechanistically, irradiation on the photocatalyst generates electron-hole pairs which can respectively, reduce and oxidize other molecules such as water, $O_2$ and the dye itself. $TiO_2$-mediated organic dye degradation is a result of the redox reactions mediated by the photo-generated electron/holes, adsorption on the catalyst and in the case of visible light irradiation, the excitation of the dye itself. The latter was previously studied elsewhere and showed that excited electrons generated by the dye can be transferred to the photocatalyst assisting the degradation. However, this mechanism is less prevalent than the direct excitation on the photocatalyst.[39,40]

To better understand the mechanisms behind the dye bleaching we first evaluated the $^{\bullet}OH$ production among all catalysts. We used coumarin, which is a probe that is oxidized by hydroxyl radicals forming 7-hydroxycoumarin (7-HC) which has strong fluorescence at 454 nm ($\lambda_{ex}$ = 332 nm).[41] The emission spectrum from the production of 7-HC is in the Supporting Information (Figure 3.3.12). After 3 hours of dark incubation, the fluorescence produced by all catalysts is approximately the same as time zero ($T_0$), showing that light is necessary to induce the formation of hydroxyl radicals from the catalyst. Samples that were irradiated had increasing fluorescence emission over time. The higher fluorescence from the samples treated with TGF, especially because their degradation rates were lower than the other materials. TGF has a significantly higher SSA (Table 3.2.1) which increases the chances of the encounter between the target molecules, adsorbed on the catalyst, and the short-lived photogenerated holes and $^{\bullet}OH$. The latter tend to react with nearby molecules with virtually no selectivity. Further, we evaluated crocin photodegradation under anaerobic conditions. In the absence of oxygen, there is a decrease in the overall photocatalytic activity (Figure 3.3.13). The 8.2 %, 22.3 % and 33.9 % decrease in photocatalytic activity for TNF, TGW and TGF, respectively, emphasize that most of the bleaching is non-$O_2$

related. Possibly by $^{\bullet}OH$ radicals and by the adsorption of the dye on the catalyst. In the absence of oxygen, the lower bleaching values can be assigned to the decrease in OH radicals' production as previously described by other authors.[42,43] $O_2$ also acts by trapping excited electrons, thus decreasing recombination rates, and generating oxygen-centred radicals, such as superoxide ($O_2^{\bullet -}$) or other ROS, that also act on the dye degradation.[44-46]

**Reuse Experiments**

Aiming at the practical application of the fibrous $TiO_2$-rich materials, the dye discoloration capability of the reused fibrous $TiO_2$ structures was evaluated for five catalytic cycles (Figure 3.2.4). The tests were run in the same conditions as the batch experiments under UVA/visible irradiation. The dye bleaching was measured after 3 h by following the absorbance at 440 nm and compared with the initial absorbance. All materials kept similar degradation capabilities, even after 5 cycles. TNF efficiency went from 61 to 65 %, TGW dropped from 89 to 78 % and TGF from 88 to 81 %. The slight decrease in degradation efficiency for TGW and TGF may reflect some $TiO_2$ leaching from the supported materials, something that did not happen with TNF which is made of 100 % $TiO_2$.

**Continuous flow degradation**

Solutions for photocatalytic water treatment are ideally processed under a continuous flow using a fixed bed catalyst that allows for uniform light distribution, easy scale-up, fast mixing, and faster reactions. Here we compared the performance of our three fibrous materials using crocin as our surrogate dye. Using a single-pass approach, we evaluated the performance of the catalysts at 4 different flow rates, 10, 30, 50 and 100 mL/h. The summary of the removal efficiency in the different flow rates can be seen in Figure 3.2.5. Overall, slower flow rates lead to higher degradation, which is attributed to the longer residence/irradiation time (RT). A similar trend was also observed in previous reports for the degradation of other dyes like azo compounds and methyl orange. [47-49]

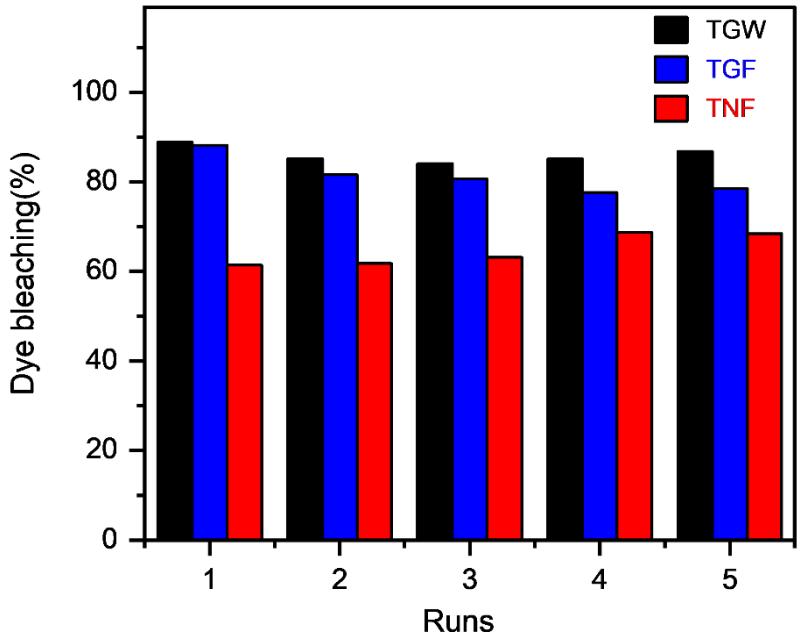


**Figure 3.2.4.** Reusability test results of the 5 cycles of crocin bleaching, followed at 440 nm. Experiments run in batch with an initial dye concentration of 8.1 μM, and under UVA irradiation (18 W/m$^2$).

Since we chose to use the same $TiO_2$ amount for all catalysts, the volumes of each fibrous material were different inside the tubes, changing the residence time (RT) for the catalysts analyzed. All fibrous materials were able to be used in the flow system and were capable of bleaching the dye in shorter times. In general, for all rates, TGW outperformed the other photocatalysts with a maximum dye removal of 89 % at 10 mL/h. As a comparison, at 50 mL/h, TGW bleached 43 % of the dye with 35 s of RT, which would take at least 1 hour of irradiation in our batch system. At the same flow rate, TGF removed 15 % of the dye with an RT of 90 s, and TNF removed 18 % of the crocin with an RT of 115 s. The longer retention time together with better $TiO_2$ distribution, resulted in better photocatalytic activity for TGW. TNF which also had high degradation rates in the batch experiments did not perform as well in flow. Continuous flow systems enable better light distribution favouring materials with higher volumes, and better

photocatalyst distribution such as TGW. On the other hand, TNF has a compact form, due to the higher $TiO_2$ content, not being as favoured with improvements in light distribution.

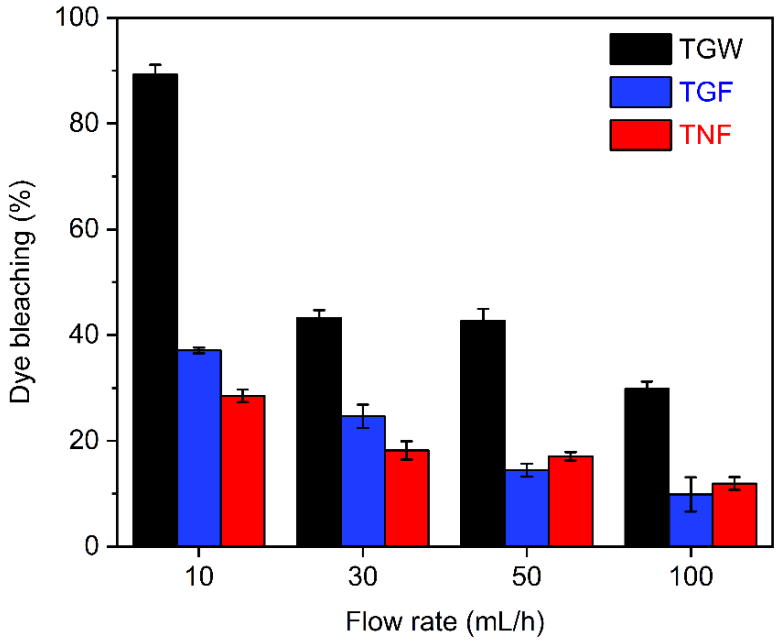


**Figure 3.2.5.** Crocin bleaching (%) using TGW (black), TGF (blue) or TNF (red) in a continuous flow system. The initial dye concentration was 8.1 μM in water and under Blacklight irradiation (λ=400 nm) (18 W/m$^2$). Bleaching is calculated based on the absorbance on the decrease at the absorbance at 440 nm

Interested in the results from the single-pass degradation, we selected the best working catalyst, TGW to observe the results from the degradations. After 90% bleaching at 440 nm, no colour could be seen in the liquid. We then proceeded to observe the changes in the solution using HPLC. In Figure 3.3.15, we can see the HPLC peaks at 400 nm for the initial solution (in black). The conjugated structure of crocin allows for the formation of several isomers, which can be seen in peaks 1−5. Their absorbance profile (insert) shows similar absorbance spectra. After treatment with TGW and light, no other peak is visible proving the degradation of the molecule.

**Catalyst Comparison**

The development of suitable photocatalysts for water treatment reactors is a complex challenge that comprises catalytic performance, durability, cost-efficiency, and range of action, among others.[50] In this study, we investigated and compared three fibrous $TiO_2$-rich structures that are suitable for flow systems. Aiming for their real-life application we selected five categories, mechanical properties, price/synthesis convenience, dye degradation in batch and flow, as well as compatibility with flow systems, and ranked the three catalysts from 1 to 3 for each of those categories. The data were then plotted in a radar plot for easy visualization.

The first category is mechanical properties, which we compared to how easy it is to manipulate those materials. For example, TNFs are made of 100 % $TiO_2$ which is a brittle material that can be easily broken when moved between surfaces and added into the treatment tubes. In contrast, TGF is a flexible paper that can be easily manipulated and breaks less easily. The second aspect evaluated is how flow-compatible are those materials. This category considers how easy it is to position them into glass flow tubes, and how stable they are inside those tubes. In this category, TNF also scored lower than the other materials since it can be broken when transferred into the tubes and it tends to move with the flow. Both glass-supported $TiO_2$ materials were easier to insert into tubes and keep inside as the liquid flowed. In particular, TGW, which ranks in the first place for this criterion, can be easily packed into the tubes, allowing the use of more catalysts, and can take different shapes adapting to the system being used. Moving to dye degradation performance in batch tests, we compared their performance bleaching crocin under UVA/visible (~400 nm) irradiation. Using the data displayed in Figure 3.2.3 we can see that TNF had a higher degradation rate under light irradiation, followed by TGW and TGF. Higher degradation rates mean that short treatment times are necessary using the same amount of catalyst.

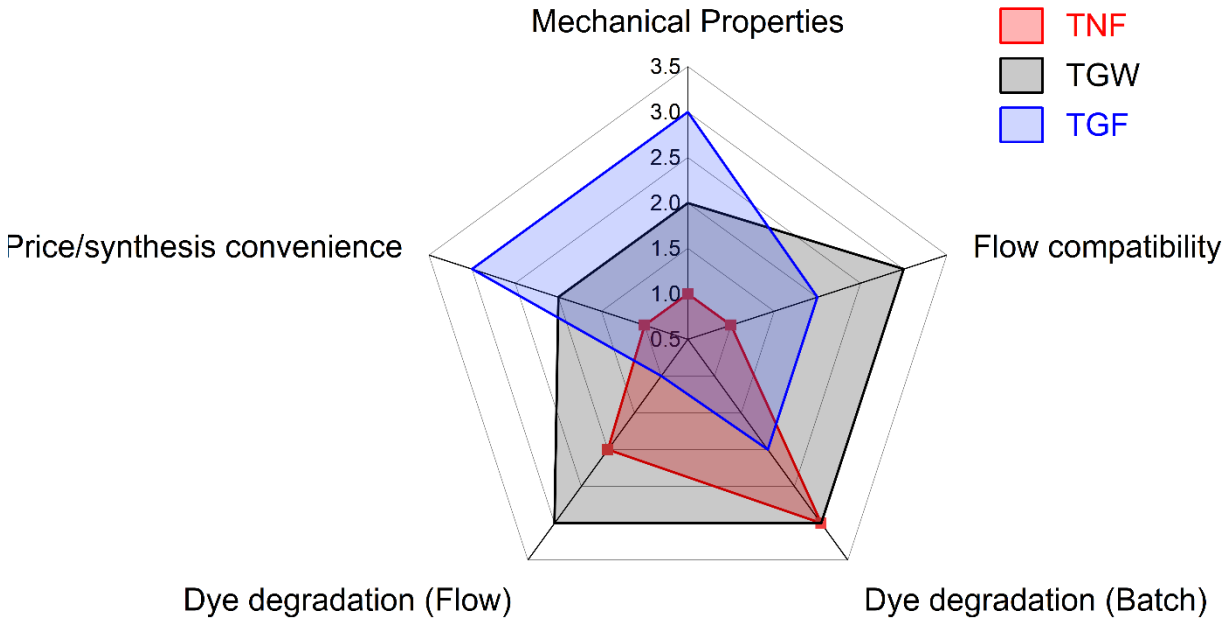


**Figure 3.2.6.** Radar plot of the fibrous catalysts for a relative comparison according to their physical features and chemical activity. The $TiO_2$-rich catalysts were ranked from 1 to 3 in the five categories, based on the results from this contribution.

Finally, we ranked the catalysts according to their synthesis convenience (availability, cost, scalability, and safety). TNFs are synthesized using electrospinning that requires high voltages together with flammable solvents. Although it is a low-cost technique,[51] it imposes a fire hazard that requires specialized labour and higher safety environments. For safety reasons, TNF was placed last in this category. Moving to TGW, the synthesis is done inside a glass tube, which does not require any special apparatus or equipment. However, glass wool must be treated with acid (HCl), followed by APTES attachment and overnight treatment with $TiO_2$ precursors. Compared to the other methods, it takes longer to obtain the final material. However, it is important to emphasize that the synthesis of TGW can be easily scaled up. Lastly, TGF came in first for this category as there is no preparation of the supporting material. The high surface area of the commercial glass fibres filter allows for effective $TiO_2$ deposition. Moreover, the material can be

cut and shaped in the desired size and $TiO_2$ precursors are added using a clothing iron, proving to be a simpler and inexpensive solution. Note that calcination treatment was not used as a comparison since all the materials undergo similar processes.

Based on the radar plot (Figure 3.2.6), the catalysts were divided into two main categories, chemical descriptors, which are related to their catalytic activity, with TGW and TNF shown in the upper level of the right and bottom quadrants. On the other hand, there are physical descriptors, which are associated with the mechanical and synthetic aspects. In this case, TGF was placed in the upper level of the left and upper quadrants. The exception is TGW which took the upper level of flow compatibility, which makes it a great candidate for flow applications, due to its high performance and compatibility with continuous flow reactors.

## CONCLUSION

The photochemical treatment of contaminated waters requires the discovery of safe, durable and cost-efficient catalysts that can operate in the UVA or visible regions. The materials reported here operate at the edge of these spectral regions, are fully compatible with flow methods and can be prepared from readily available materials. Among the materials tested here, glass wool is the recommended support for flow-related applications, although glass filter materials offer some advantages relating to mechanical and synthetic properties, for example, no APTES treatment is required. The dye crocin serves as an excellent screening material, although ultimately the complete photodegradation of drug contaminants and the potential killing of bacteria will need to be evaluated. Overall, the three new photocatalysts studied offer a major advantage over the powder catalysts frequently used.

## REFERENCES


(1) WHO; UNICEF; World Bank. *State of the World's Drinking Water: An Urgent Call to action to Accelerate Progress on Ensuring Safe Drinking Water for All.*; Geneva, 2022.

(2) Ding, Q.; Li, C.; Wang, H.; Xu, C.; Kuang, H. Electrochemical Detection of Heavy Metal Ions in Water. *Chem. Commun* **2021**, *57*, 7215.

(3) Chakraborti, D.; Rahman, M. M.; Paul, K.; Chowdhury, U. K.; Sengupta, M. K.; Lodh, D.; Chanda, C. R.; Saha, K. C.; Mukherjee, S. C. Arsenic Calamity in the Indian Subcontinent: What Lessons Have Been Learned? *Talanta* **2002**, *58* (1), 3–22.

(4) Menon, N. G.; George, L.; Tatiparti, S. S. V.; Mukherji, S. Efficacy and Reusability of Mixed-Phase TiO2–ZnO Nanocomposites for the Removal of Estrogenic Effects of 17β-Estradiol and 17α-Ethinylestradiol from Water. *J Environ Manage.* **2021**, *288*, 112340.

(5) Sun, J.; Luo, Q.; Wang, D.; Wang, Z. Occurrences of Pharmaceuticals in Drinking Water Sources of Major River Watersheds, China. *Ecotoxicol. Env. Safety* **2015**, *117*, 132–140.

(6) Ternes, T. A.; Meisenheimer, M.; McDowell, D.; Sacher, F.; Brauch, H. J.; Haist-Gulde, B.; Preuss, G.; Wilme, U.; Zulei-Seibert, N. Removal of Pharmaceuticals during Drinking Water Treatment. *Environ. Sci.Technol.* **2002**, *36* (17), 3855–3863.

(7) Kamat, P. V.; Sivula, K. Celebrating 50 Years of Photocatalytic Hydrogen Generation. *ACS Energy Lett.* **2022**, *7*, 3149–3150.

(8) Fujishima, A.; Honda, K. Electrochemical Photolysis of Water at a Semiconductor Electrode. *Nature* **1972**, *238* (5358), 37–38.

(9) Ge, M.; Cao, C.; Huang, J.; Li, S.; Chen, Z.; Zhang, K.-Q.; Al-Deyab, S. S.; Lai, Y. A Review of One-Dimensional $TiO_2$ Nanostructured Materials for Environmental and Energy Applications. *J. Mater. Chem. A* **2016**, *4* (18), 6772–6801.

(10) Tang, Z.-R.; Li, F.; Zhang, Y.; Fu, X.; Xu, Y.-J. Composites of Titanate Nanotube and Carbon Nanotube as Photocatalyst with High Mineralization Ratio for Gas-Phase Degradation of Volatile Aromatic Pollutant. *J. Phys. Chem. C* **2011**, *115* (16), 7880–7886.

(11) Jothi Prakash, C. G. ; P. R. TiO2-Based Devices for Energy-Related Applications. In *Titanium Dioxide ($Tio_2$) and Its Applications*; 2021; pp 241–464.

(12) Dell'Edera, M.; Lo Porto, C.; De Pasquale, I.; Petronella, F.; Curri, M. L.; Agostiano, A.; Comparelli, R. Photocatalytic $TiO_2$-Based Coatings for Environmental Applications. *Catal. Today* **2021**, *380*, 62–83.

(13) Mohadesi, M.; Sanavi Fard, M.; Shokri, A. The Application of Modified Nano-$TiO_2$ Photocatalyst for Wastewater Treatment: A Review. *J. Environ. Anal. Chem.* **2022**, 1–22.

(14) Riaz, S.; Park, S.-J. An Overview of TiO2-Based Photocatalytic Membrane Reactors for Water and Wastewater Treatments. *J. Ind. Eng. Chem.* **2020**, *84*, 23–41.

(15) Horikoshi, S.; Serpone, N. Can the Photocatalyst $TiO_2$ Be Incorporated into a Wastewater Treatment Method? Background and Prospects. *Catal. Today* **2020**, *340*, 334–346.

(16) Yaghmaei, M.; Lanterna, A. E.; Scaiano, J. C. Nitro to Amine Reductions Using Aqueous Flow Catalysis under Ambient Conditions. *iScience* **2021**, *24* (12), 103472.

(17) Tatsuma, T.; Tachibana, S. I.; Miwa, T.; Tryk, D. A.; Fujishima, A. Remote Bleaching of Methylene Blue by UV-Irradiated $TiO_2$ in the Gas Phase. *J. Phys. Chem. B* **1999**, *103* (38), 8034–8035.

(18) Sun, Q.; Li, K.; Wu, S.; Han, B.; Sui, L.; Dong, L. Remarkable Improvement of $TiO_2$ for Dye Photocatalytic Degradation by a Facile Post-Treatment. *New J. Chem.* **2020**, *44* (5), 1942–1952.

(19) Lee, S. Y.; Kang, D.; Jeong, S.; Do, H. T.; Kim, J. H. Photocatalytic Degradation of Rhodamine B Dye by $TiO_2$ and Gold Nanoparticles Supported on a Floating Porous Polydimethylsiloxane Sponge under Ultraviolet and Visible Light Irradiation. *ACS Omega* **2020**, *5* (8), 4233–4241.

(20) Naskar, S.; Pillay, S. A.; Chanda, M. Photocatalytic Degradation of Organic Dyes in Aqueous Solution with $TiO_2$ Nanoparticles Immobilized on Foamed Polyethylene Sheet. *J. Photochem. Photobiol. A: Chem* **1998**, *113* (3), 257–264.

(21) Barton, I.; Matejec, V.; Matousek, J. Photocatalytic Activity of Nanostructured $TiO_2$ Coating on Glass Slides and Optical Fibers for Methylene Blue or Methyl Orange Decomposition under Different Light Excitation. *J. Photochem. Photobiol. A: Chem* **2016**, *317*, 72–80.

(22) Oliveira, G. H.; Galante, M. T.; Martins, T. T.; dos Santos, L. F. L. S.; Ely, F.; Longo, C.; Gonçalves, R. V.; Muniz, S. R.; Nome, R. A. Real Time Single $TiO_2$ Nanoparticle Monitoring of the Photodegradation of Methylene Blue. *Solar Energy* **2019**, *190*, 239–245.

(23) Elhage, A.; Wang, B.; Marina, N.; Marin, M. L.; Cruz, M.; Lanterna, A. E.; Scaiano, J. C. Glass Wool: A Novel Support for Heterogeneous Catalysis. *Chem. Sci.* **2018**, *9* (33), 6844–6852.

(24) Lu, Y.; Ou, X.; Wang, W.; Fan, J.; Lv, K. Fabrication of TiO2 Nanofiber Assembly from Nanosheets ($TiO_2$-NFs-NSs) by Electrospinning-Hydrothermal Method for Improved Photoreactivity. *Chin. J. Catal.* **2020**, *41* (1), 209–218.

(25) Mapukata, S.; Hainer, A. S.; Lanterna, A. E.; Scaiano, J. C.; Nyokong, T. Decorated Titania Fibers as Photocatalysts for Hydrogen Generation and Organic Matter Degradation. *J. Photochem. Photobiol. A: Chem* **2020**, *388*, 112185.

(26) Lou, L.; Kendall, R. J.; Ramkumar, S. Comparison of Hydrophilic PVA/$TiO_2$ and Hydrophobic PVDF/TiO2 Microfiber Webs on the Dye Pollutant Photo-Catalyzation. *J. Environ. Chem. Eng.* **2020**, *8* (5), 103914.

(27) Shen, C.; Wang, Y. J.; Xu, J. H.; Luo, G. S. Facile Synthesis and Photocatalytic Properties of $TiO_2$ Nanoparticles Supported on Porous Glass Beads. *Chem. Eng. J.* **2012**, *209*, 478–485.

(28) Uddin, M. J.; Cesano, F.; Bonino, F.; Bordiga, S.; Spoto, G.; Scarano, D.; Zecchina, A. Photoactive $TiO_2$ Films on Cellulose Fibres: Synthesis and Characterization. *J. Photochem. Photobiol. A: Chem.* **2007**, *189* (2–3), 286–294.

(29) Lan, L.; Daly, H.; Jiao, Y.; Yan, Y.; Hardacre, C.; Fan, X. Comparative Study of the Effect of $TiO_2$ Support Composition and Pt Loading on the Performance of Pt/TiO2 Photocatalysts for Catalytic Photoreforming of Cellulose. *Int. J. Hydrogen Energy.* **2021**, *46* (60), 31054–31066.

(30) Meroni, D.; Presti, L. Lo; Liberto, G. Di; Ceotto, M.; Acres, R. G.; Prince, K. C.; Bellani, R.; Soliveri, G.; Ardizzone, S. A Close Look at the Structure of the $TiO_2$-APTES Interface in Hybrid Nanomaterials and Its Degradation Pathway: An Experimental and Theoretical Study. *J. Phys. Chem. C* **2016**, *121* (1), 430–440.

(31) Chen, X.; Hosseini, S. N.; van Huis, M. A. Heating-Induced Transformation of Anatase $TiO_2$ Nanorods into Rock-Salt $TiO_2$ Nanoparticles: Implications for Photocatalytic and Gas-Sensing Applications. *ACS Appl. Nano Mat.* **2022**, *5* (1), 1600–1606.

(32) Riegal, G.; Bolton, J. R. Photocatalytic Efficiency Variability in $TiO_2$ Particles. *J. Phys. Chem.* **1995**, *99* (12), 4215–4224.

(33) Baiju, K. V.; Shukla, S.; Sandhya, K. S.; James, J.; Warrier, K. G. K. Photocatalytic Activity of Sol−Gel-Derived Nanocrystalline Titania. *J. Phys. Chem. C* **2007**, *111* (21), 7612–7622.

(34) L. Kavan; M.Grätzel; S. E. Gilbert; C. Klemenz; H. J. Scheel. Electrochemical and Photoelectrochemical Investigation of Single-Crystal Anatase. *J. Am. Chem. Soc.* **1996**, *118* (29), 6719–6723.

(35) Thommes, M.; Kaneko, K.; Neimark, A. V.; Olivier, J. P.; Rodriguez-Reinoso, F.; Rouquerol, J.; Sing, K. S. W. Physisorption of Gases, with Special Reference to the Evaluation of Surface Area and Pore Size Distribution (IUPAC Technical Report). *Pure Appl. Chem.* **2015**, *87* (9–10), 1051–1069.

(36) Kočí, K.; Obalová, L.; Matějová, L.; Plachá, D.; Lacný, Z.; Jirkovský, J.; Šolcová, O. Effect of $TiO_2$ Particle Size on the Photocatalytic Reduction of CO2. *Appl. Catal. B Environ.* **2009**, *89* (3–4), 494–502.

(37) Vickackaite, V.; Romani, A.; Pannacci, D.; Favaro, G. Photochemical and Thermal Degradation of a Naturally Occurring Dye Used in Artistic Painting. A Chromatographic, Spectrophotometric and Fluorimetric Study on Saffron. *Int. J. Photoenergy.* **2004**, *06* (4), 175–183.

(38) Winterhalter, P.; Straubinger, M. Saffron— Renewed Interest in an Ancient Spice. *Food Rev. Int.* **2007**, *16* (1), 39–59.

(39) Ma, Y.; Yao, J. Photodegradation of Rhodamine B Catalyzed by $TiO_2$ Thin Films. *J. Photochem. Photobiol. A Chem.* **1998**, *116* (2), 167–170.

(40) Ishibashi, K. ichi; Fujishima, A.; Watanabe, T.; Hashimoto, K. Quantum Yields of Active Oxidative Species Formed on $TiO_2$ Photocatalyst. *J. Photochem. Photobiol. A: Chem.* **2000**, *134* (1–2), 139–142.

(41) Leandri, V.; Gardner, J. M.; Jonsson, M. Coumarin as a Quantitative Probe for Hydroxyl Radical Formation in Heterogeneous Photocatalysis. *J. Phys. Chem. C* **2019**, *123* (11), 6667–6674.

(42) Holroyd, R. A.; Bielski, B. H. J. Photochemical Generation of Superoxide Radicals in Aqueous Solutions. *J. Am. Chem. Soc.* **1978**, *100* (18), 5796–5800.

(43) Shibata, H.; Ogura, Y.; Sawa, Y.; Kono, Y. Hydroxyl Radical Generation Depending on $O_2$ or $H_2O$ by a Photocatalyzed Reaction in an Aqueous Suspension of Titanium Dioxide. *Biosci. Biotechnol. Biochem.* **1998**, *62* (12), 2306–2311.

(44) Hayyan, M.; Hashim, M. A.; AlNashef, I. M. Superoxide Ion: Generation and Chemical Implications. *Chem. Rev.* **2016**, *116* (5), 3029–3085.

(45) Galindo, C.; Jacques, P.; Kalt, A. Photodegradation of the Aminoazobenzene Acid Orange 52 by Three Advanced Oxidation Processes: $UV/H_2O_2$, $UV/TiO_2$ and $VIS/TiO_2$. *J. Photochem. Photobiol.* **2000**, *130* (1), 35–47.

(46) Holroyd, R. A.; Bielski, B. H. J. Photochemical Generation of Superoxide Radicals in Aqueous Solutions. *J. Am. Chem. Soc.* **1978**, *100* (18), 5796–5800.

(47) Mahmoodi, N. M.; Arami, M.; Limaee, N. Y.; Tabrizi, N. S. Decolorization and Aromatic Ring Degradation Kinetics of Direct Red 80 by UV Oxidation in the Presence of Hydrogen Peroxide Utilizing TiO2 as a Photocatalyst. *Chem. Eng. J.* **2005**, *112* (1–3), 191–196.

(48) Behnajady, M. A.; Modirshahla, N.; Daneshvar, N.; Rabbani, M. Photocatalytic Degradation of an Azo Dye in a Tubular Continuous-Flow Photoreactor with Immobilized TiO 2 on Glass Plates. *J. Chem. Eng.* **2007**, *127*, 167–176.

(49) Zhang, X.; Su, · Xiaowen; Gao, W.; Wang, F.; Liu, Z.; Zhan, J.; Liu, B.; Wang, R.; Liu, H.; Sang, Y.; Zhang, X. Photocatalytic Quartz Fiber Felts with Carbon-Connected TiO 2 Nanoparticles for Capillarity-Driven Continuous-Flow Water Treatment Graphical Abstract. *Appl. Phys. A* **2018**, *124*, 459.

(50) Chong, M. N.; Jin, B.; Chow, C. W. K.; Saint, C. Recent Developments in Photocatalytic Water Treatment Technology: A Review. *Water Res.* **2010**, *44* (10), 2997–3027.

(51) Cui, J.; Li, F.; Wang, Y.; Zhang, Q.; Ma, W.; Huang, C. Electrospun Nanofiber Membranes for Wastewater Treatment Applications. *Sep. Purif. Technol.* **2020**, *250*, 117116.

### 3.3 Post-print Version of Supporting Information

## Supporting Information

## Fibrous $TiO_2$ alternatives for semiconductor-based catalysts for photocatalytic water remediation involving organic contaminants

Daliane R.C. da Silva[a], Sivuyisiwe Mapukata[b], Sara Currie[a], Alexandros A. Kitos[a], Anabel E. Lanterna[a†], Tebello Nyokong[b] and Juan C. Scaiano[a]

[a] Department of Chemistry and Biomolecular Sciences, University of Ottawa, Ottawa, Ontario K1N 6N5, Canada

[b] Institute for Nanotechnology Innovation, Rhodes University, Grahamstown 6140, South Africa.

[†] Present address (AEL) School of Chemistry, University of Nottingham, University Park, Nottingham NG7 2RD, U.K.

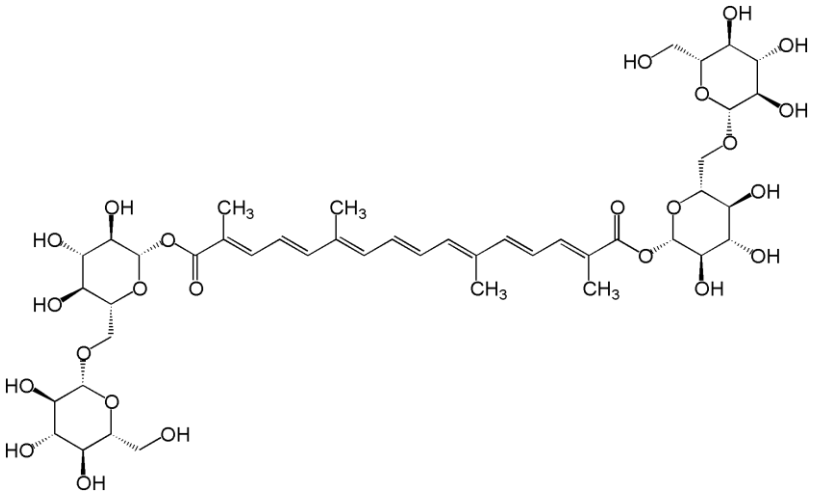

**Scheme 3.3.1**. Crocin chemical structure

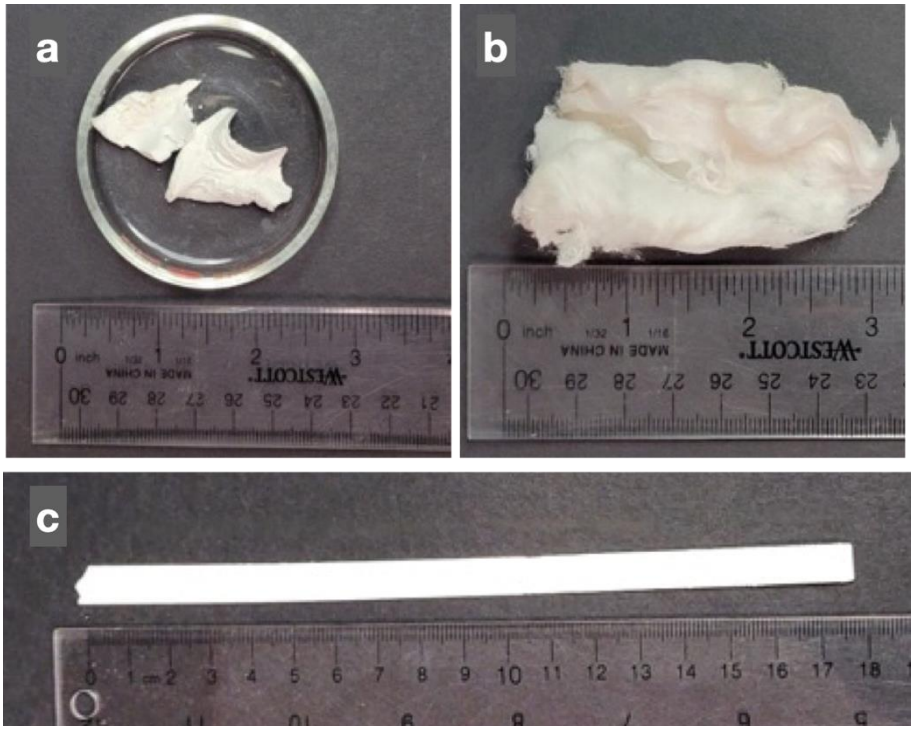


**Figure 3.3.1**. Photographs of the fibrous $TiO_2$ materials. (a) $TiO_2$ nanofibres (TNF), (b) $TiO_2$@Glass wool (TGW), and (c) $TiO_2$@Glass filter (TGF).

**Figure 3.3.2.** Close-up photographs of Glass wool alone, before the deposition of $TiO_2$ (left) and Glass wool after the deposition of $TiO_2$ (right).

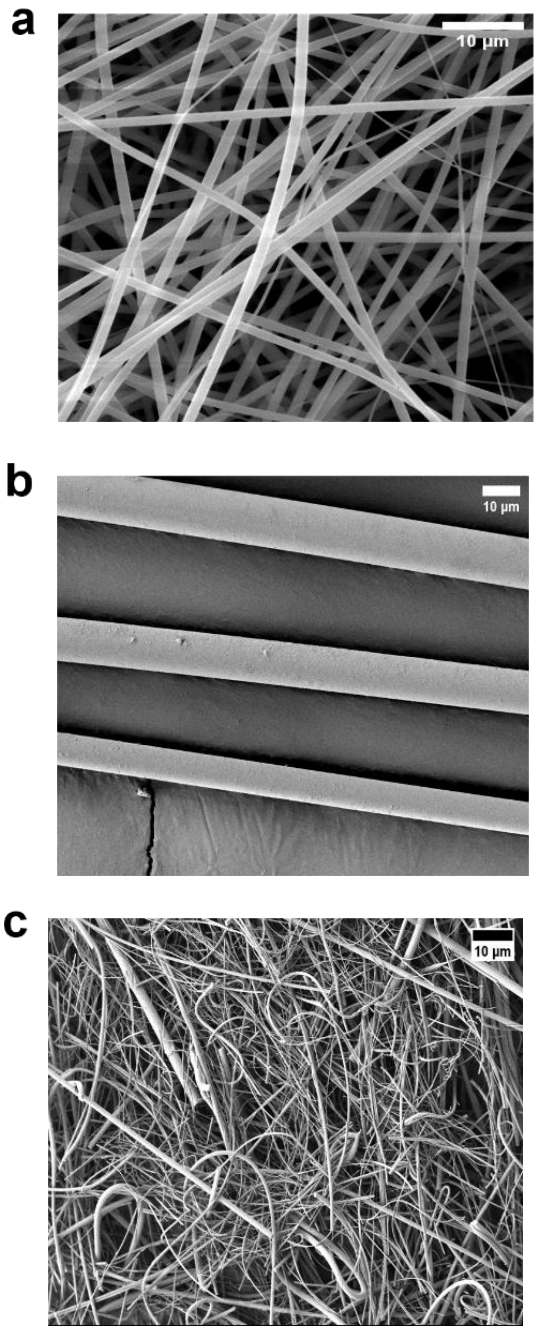


**Figure 3.3.3.** Representative SEM images of (a) the electrospun $TiO_2$/PVP nanofibres before calcination, (b) commercial glass wool fibres and (c) commercial glass fibres filter before pre-treatment and addition of $TiO_2$ precursors.

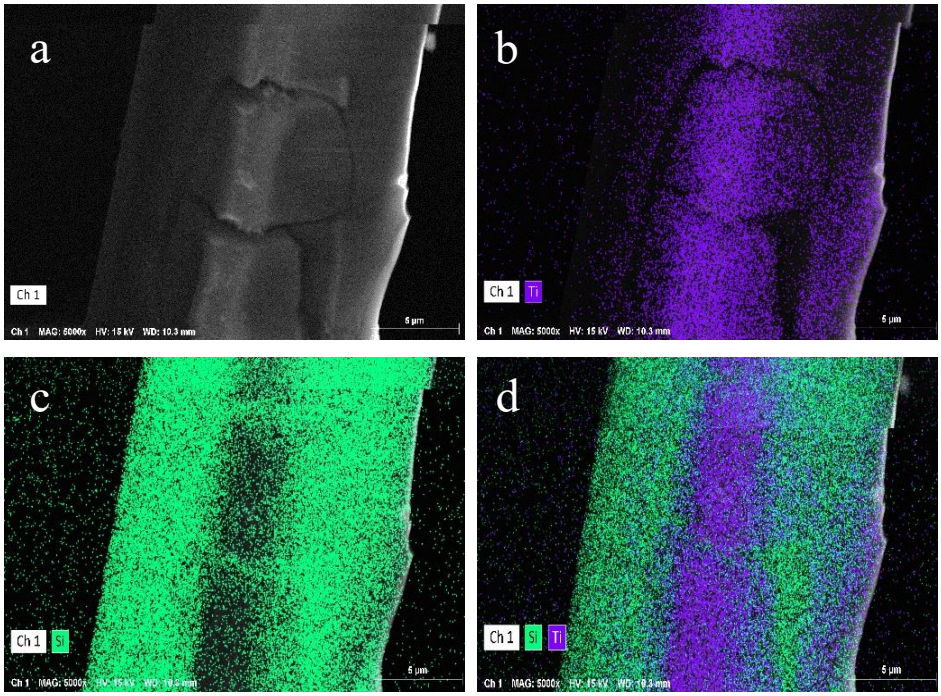


**Figure 3.3.4.** EDS mapping of TGW. SEM image used for the analysis (a) and elemental mapping showing Ti (b) and Si (c) distribution on TGW. EDS mapping overlap of Ti and Si components (d).

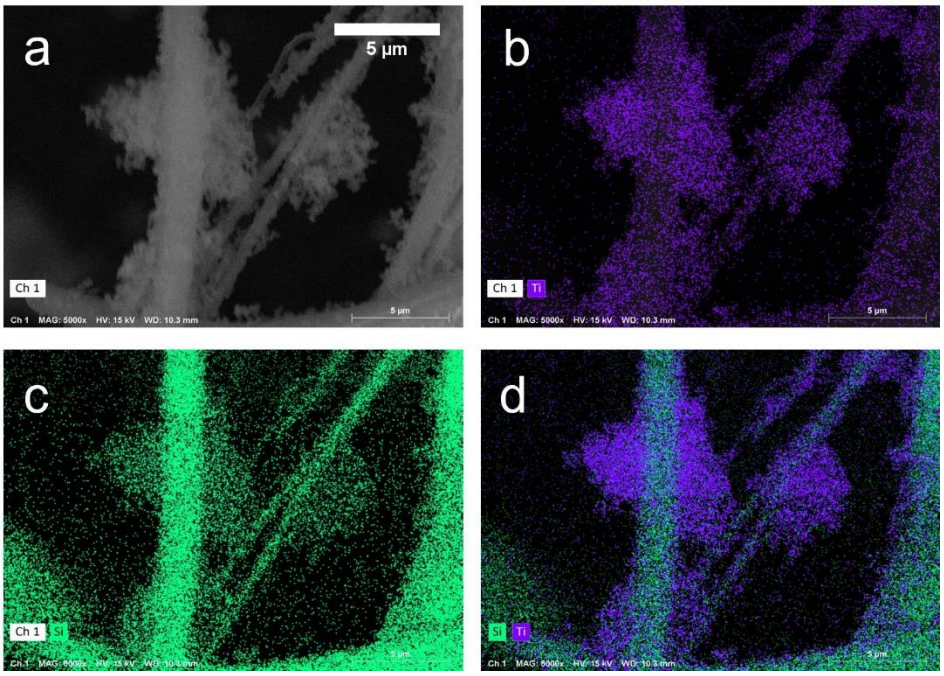


**Figure 3.3.5** EDS mapping of TGF. SEM image used for the analysis (a) and elemental mapping showing Ti (b) and Si (c) distribution on TGF. EDS mapping overlap of Ti and Si components (d).

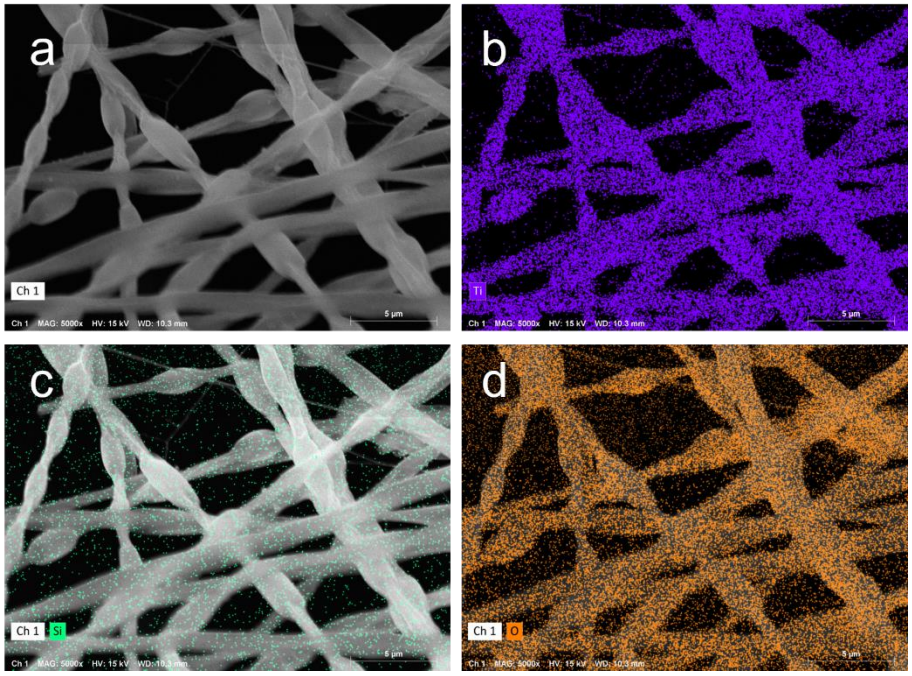


**Figure 3.3.6.** EDS mapping of TNF. SEM image used for the analysis (a) and elemental mapping showing Titanium (b) and Silica (c) and Oxygen (d).

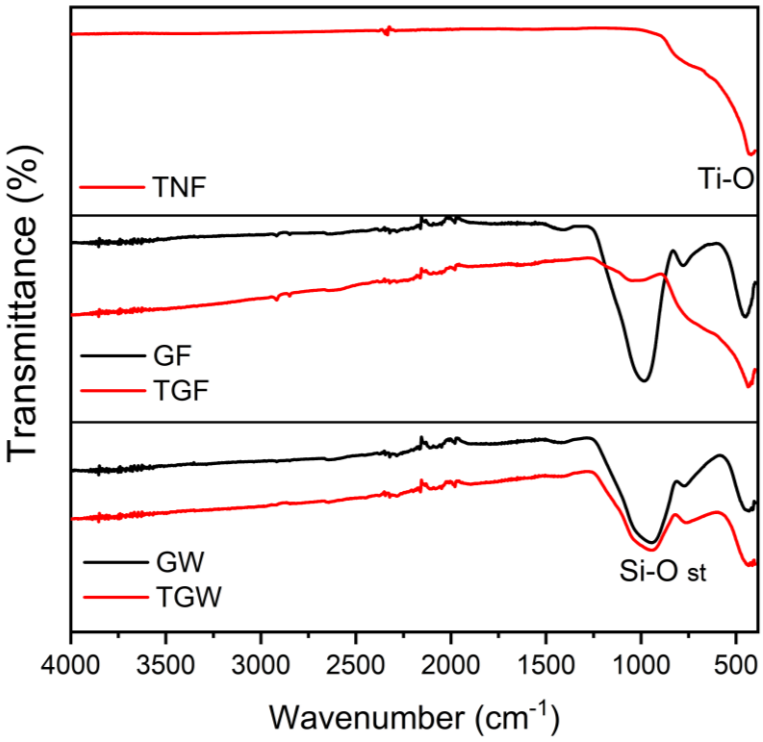


**Figure 3.3.7.** ATR FTIR spectra of the three fibrous materials (TNF, TGF and TGW) and their supports, glass filter (GF) and glass wool (GW). Solid samples were dried under vacuum before the measurements. Notice the presence of the Ti-O and Si-O signals, with the latter missing for TNF as expected.

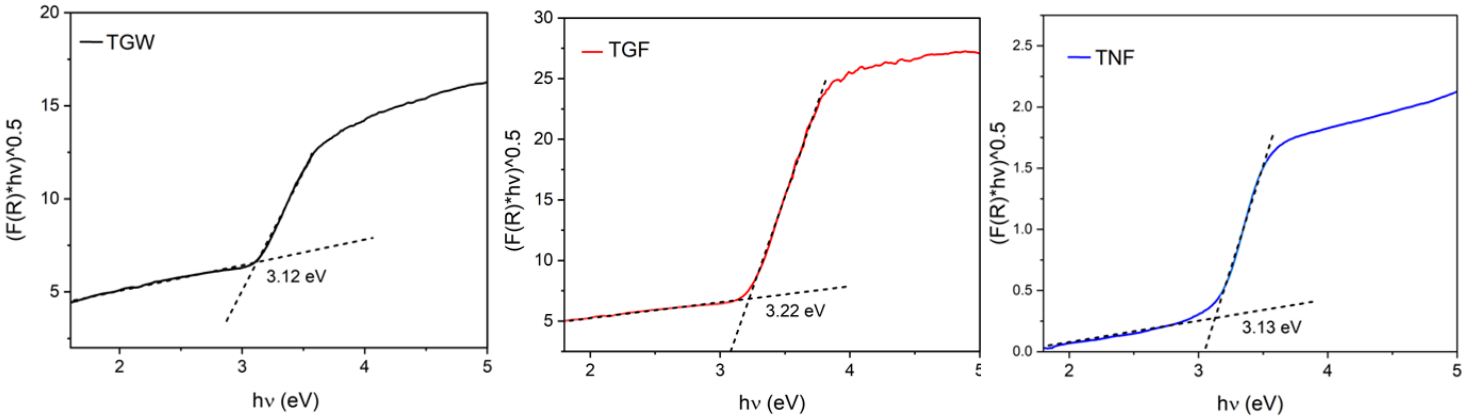


**Figure 3.3.8.** Tauc plots showing the determination of the band gaps for the three materials studied. The plots are based on the diffuse reflectance data shown in Figure 3.2.2B.

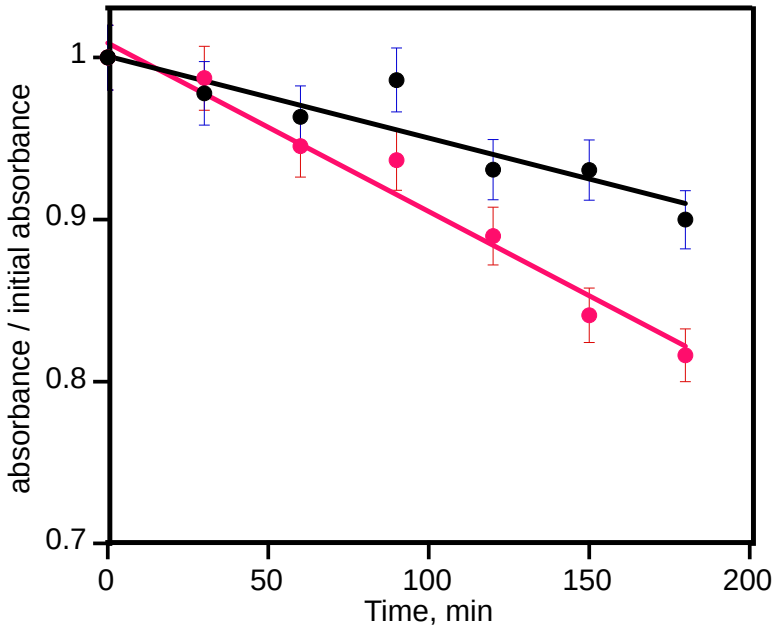


**Figure 3.3.9.** Decay of crocin absorbance as a function of time when irradiated with black light (λ ~ 400 nm, 18 W/m$^2$ for the single LED used) for 180 min (red). The dark control experiment is shown in black. Error bars show the estimated error of 2%. Crocin concentration used was 8.1 μM in water and the change in absorbance was measured using absorption maxima at 440 nm.

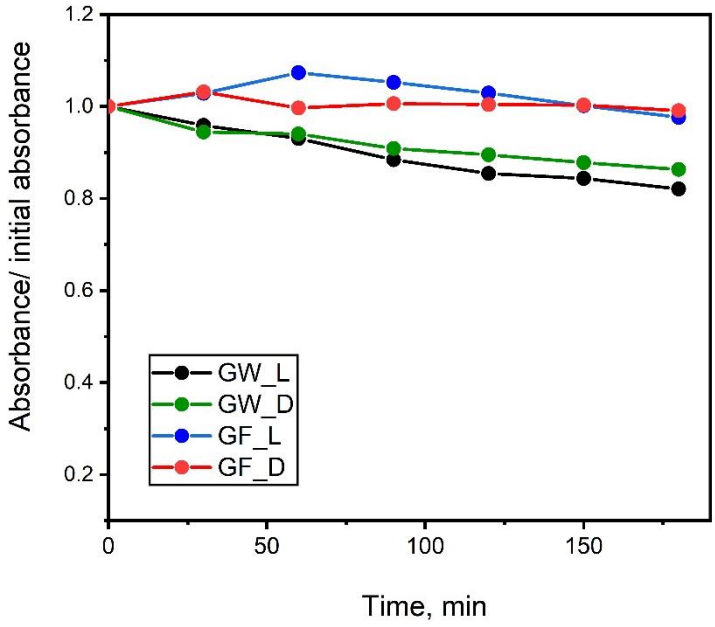


**Figure 3.3.10.** Decay of crocin absorbance as a function of time when incubated with the glass support catalyst used in this work: glass wool (GW) and glass filter (GF), under irradiation with black light (L) for 180 min or under dark for the same time (D). Crocin concentration used was 8.1 μM in water and the change in absorbance was measured using absorption maxima at 440 nm. Light source used had maximum emission at 400 nm, 18 W/m$^2$ for the single LED used.

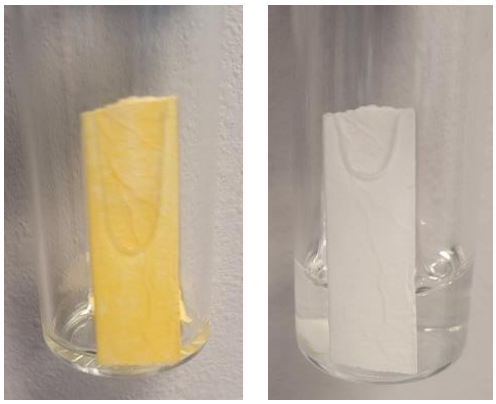

**Figure 3.3.11**. Photographs of TGF after 3 h dark incubation inside an aqueous crocin solution (8.1 μM) (left), and the same TGF piece after exposure to black light (UVA/Visible) illumination for 3 h (right).

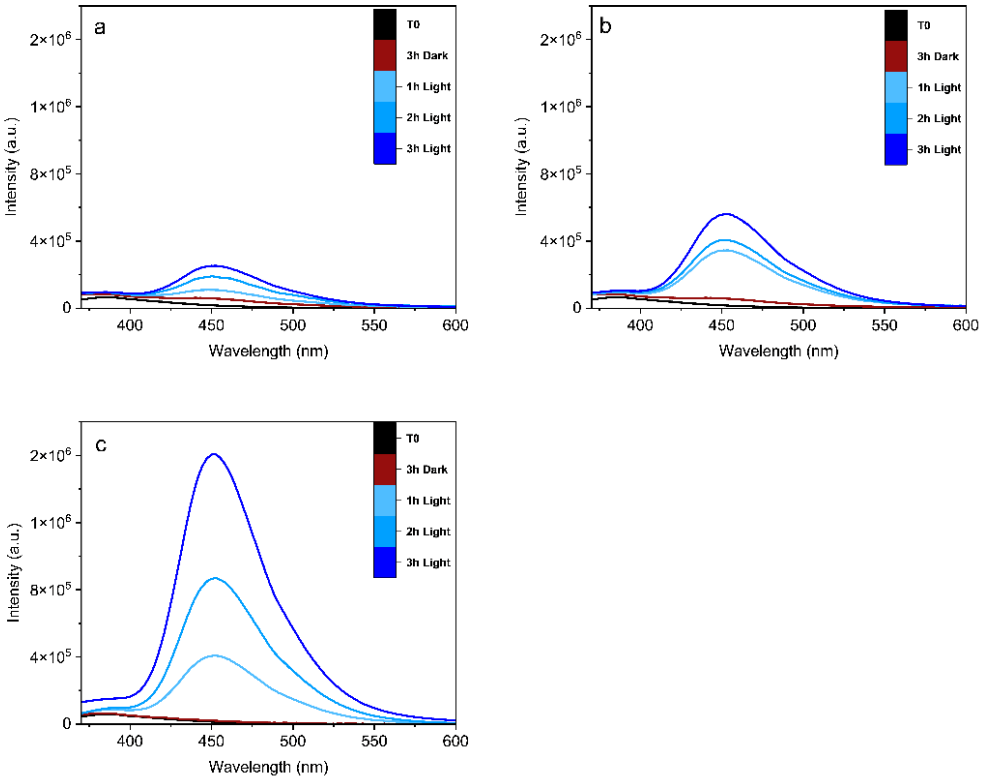


**Figure 3.3.12.** Hydroxyl radical production was evaluated using coumarin probe. Coumarin is oxidized to 7-hydroxyl coumarin in the presence of ˙OH, the product has strong fluorescence at 454 nm when excited at 332 nm. Graphs show the fluorescence spectra of aqueous solutions of coumarin irradiated in the presence of TNF (a), TGW (b) or TGF (c) for 1, 2 and 3 hours.

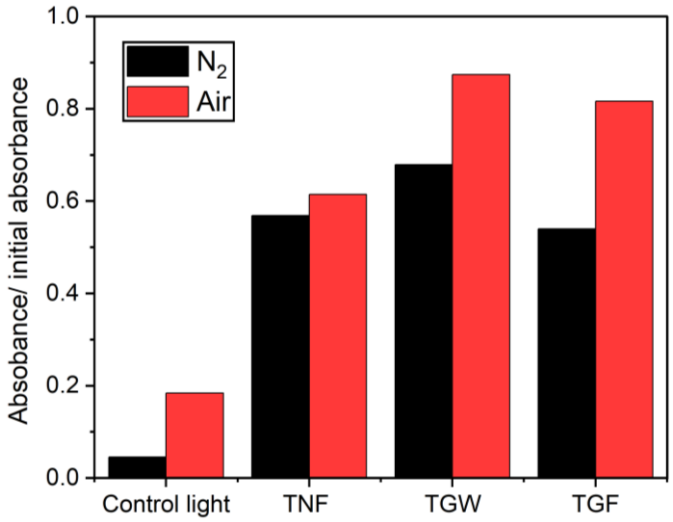


**Figure 3.3.13.** Crocin bleaching using the three fibrous $TiO_2$ catalysts, TNF, TGW and TGF under an inert atmosphere, $N_2$ (black) and under air (red). Samples were irradiated for 3 hours with a black light (λ ~ 400 nm, 18 $W/m^2$ for the single LED). Crocin concentration used was 8.1 μM in water and the change in absorbance was measured using maximum absorbance at 440 nm.

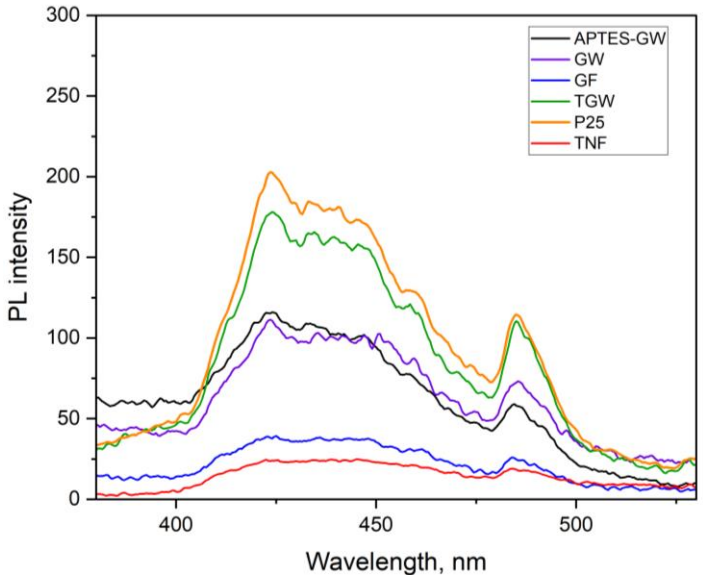


**Figure 3.3.14** Photoluminescence spectroscopy of the photocatalysts and supports excited at 300 nm. Analysis was carried out using a Perkin-Elmer LS-50 luminescence spectrometer, and fluorescence spectra were recorded between 320 and 580 nm using a front-face attachment. APTES- Glass wool (black), Glass wool (purple), Glass filter (blue), $TiO_2$@ Glass wool (green), $TiO_2$ P25 nanoparticles (orange) and $TiO_2$ nanofibres (red)

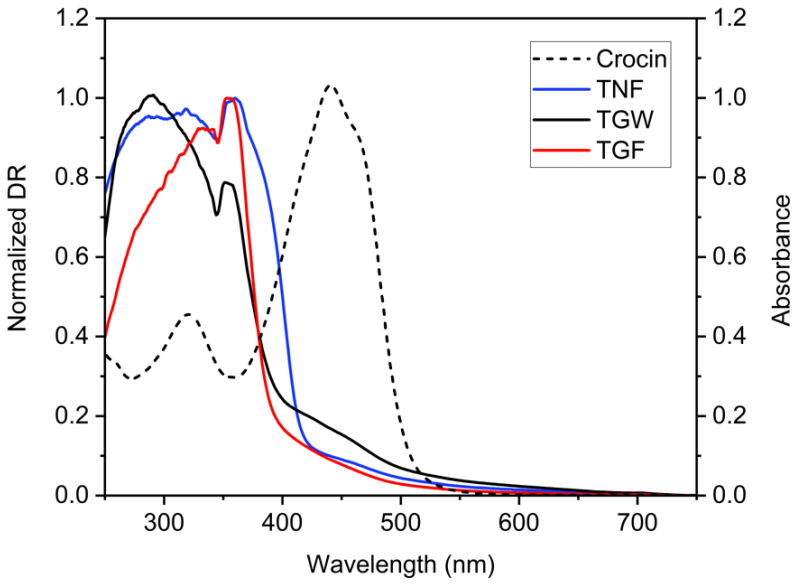


**Figure 3.3.15** Diffuse reflectance of the three fibrous materials after crocin adsorption under dark for three hours (solid lines). Dashed line: UV-vis spectra of an aqueous solution of crocin (8.1 μM).

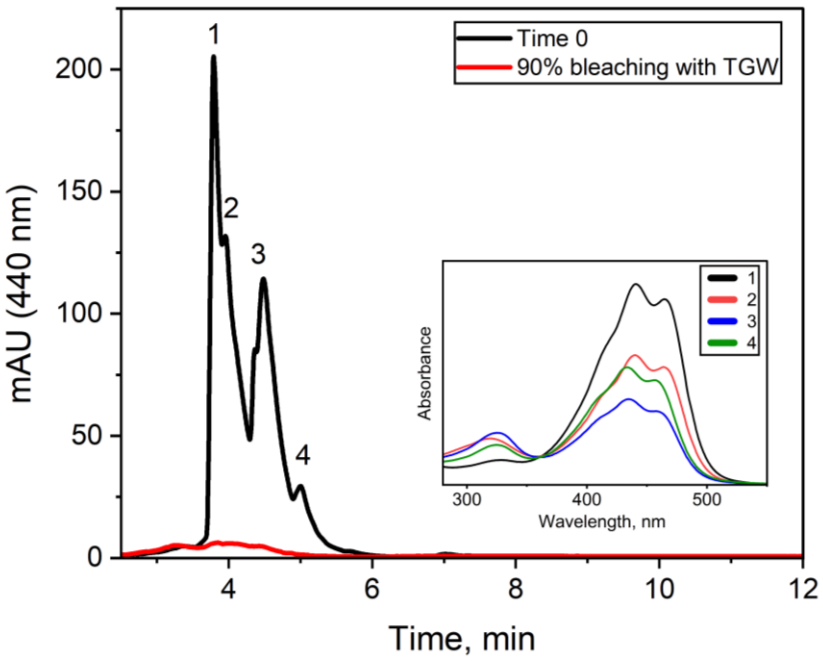


**Figure 3.3.16** HPLC-DAD analysis of an aqueous s solution of crocin 1 mM at 440 nm of the initial solution (black) and after degradation with TGW (red), The conjugated structure of crocin allows for several isomers that can be seen in peaks 1-5. The UV-vis spectra of those peaks are present in the insert, showing the similarity of the peaks. HPLC was done using a C18 column, and a mixture of acetonitrile and water as the mobile phase.

### 3.4 Accompaniment to Chapter 3

Semiconductors, particularly $TiO_2$, have been extensively researched for water and wastewater treatment processes.[97,175,178–181] Their exceptional ability to absorb light and generate charge carriers makes them ideal candidates for the degradation of organic pollutants. However, the practical application of suspended nanoparticles is limited due to issues such as catalyst agglomeration and challenges in separation after treatment, which hinder reusability. These challenges underscore the importance of finding effective and reliable alternatives to advance toward commercial-scale applications. Consequently, many researchers have explored the fabrication of macroscopic or supported titanium dioxide. However, a limited number of discussions are comparing the proposed materials, pondering catalytic performances and physicochemical attributes, which are crucial aspects for commercialization.

This chapter describes the synthesis of three fibrous materials, $TiO_2$ nanofibres and two glass-supported $TiO_2$ alternatives. Our work highlights the role of the support in enhancing catalytic activity, primarily due to differences in surface area. It also emphasizes that catalytic performance varies significantly between batch and continuous flow systems, underscoring the importance of selecting appropriate methods based on the desired system. Furthermore, we compare the physical aspects of these materials and their synthesis processes, often neglected in discussions of new catalysts but essential for real applications. For instance, we found that $TiO_2$ nanofibres exhibit high catalytic activity in batch systems, but their relatively complex fabrication, compared to other materials proposed, weighed against their selection for further studies. In our analysis, $TiO_2$@GW stood out for its good catalytic activity combined with excellent physical properties.

Some of the catalysts described here and the comparative methods developed are currently being used in our group to evaluate their potential degrading other contaminants such as estrogens and biological pollutants. Additionally, research on the interaction of $TiO_2$@GW with bacterial cells will be discussed in the following chapter.

# 4. Investigating the Antibacterial Performance of Supported $TiO_2$ on Glass Wool Fibres: Challenges and Optimization Strategies

This chapter is adapted from a final manuscript currently undergoing submission. The final published version may have small differences.

## 4.1 Preamble to Chapter 4

To build on the research discussed in Chapter 3, we focused on investigating the antibacterial activity of $TiO_2$@GW. This catalyst has demonstrated remarkable efficacy in degrading organic compounds, and we aimed to assess its performance against a realistic contaminant: microorganisms. The first modification from the previous tests was the working wavelength. Initially, we hypothesized that using UVA light, which perfectly matches the $TiO_2$ absorbance window, would optimize photocatalytic performance. However, even with a 370 nm lamp, we observed only a 1-log unit reduction in *E. coli* after 6 hours of irradiation, a result inferior to photoinactivation by UVA alone. This was unexpected, given $TiO_2$'s well-documented antibacterial properties. Consequently, we sought to understand why our photocatalyst exhibited lower bactericidal activity when deposited on a glass substrate, despite its proven efficiency in degrading organic dyes.

The initial goal of this chapter was to describe our investigations to enhance the bactericidal activity and determine optimal conditions for using supported $TiO_2$ as disinfection agents. As we tested different methodologies, explored other materials and reviewed literature, we noted common reports on the reduced photocatalytic ability of supported semiconductors. Recognizing the importance of this issue for the implementation of metal oxide in water remediation, we aimed to contribute to the development of efficient and reliable systems. For this, here we also discussed the factors limiting the photocatalytic performance of these materials and suggested modifications based on our results to improve these systems.

## 4.2 Pre-submission Version of Manuscript

This manuscript is currently in the process of submission.


## ABSTRACT

Improving clean water availability for many communities around the globe remains a significant challenge. Metal-oxide nanostructures, such as $TiO_2$ nanomaterials, have gained considerable attention due to their effective photocatalytic bacterial inactivation, generating toxic radicals without releasing harmful metals or compounds into the water. Practical applications of $TiO_2$ rely on immobilizing it on inert supports to avoid the need for extra separation steps. However, reports describing the bactericidal potential of supported metal oxides often overlook the limitations of these systems, which may suffer from poor optical properties and limited mass transfer. Additionally, the performance of such systems is highly dependent on water conditions and bacterial composition. This study investigates the antibacterial activity of $TiO_2$@Glass Wool (TGW) against *Escherichia coli*. Using techniques such as plate counting and fluorescence lifetime imaging (FLIM), we assessed the antibacterial performance of this material and the interaction between bacteria and TGW. Initial experiments revealed only a 1-log unit reduction in cell count after 6 hours of irradiation. These results highlighted the limitations of supported catalytic systems. Despite efforts to improve performance by increasing catalyst concentration, decreasing initial bacterial amounts, enhancing oxygen availability, and improving sample agitation, significant improvements were not observed. Our findings underscore the necessity of optimizing bacterial adhesion to the catalyst, improving light absorption, and enhancing mass transport to develop effective bactericidal-supported $TiO_2$ systems. Tailored methodologies that address these specific challenges are crucial for achieving effective bacterial disinfection and advancing the application of supported photocatalytic materials in decentralized water treatment technologies.


## INTRODUCTION

Consumption of unsafe water remains a reality for many communities. The absence of proper treatment forces millions of people to depend on untreated water from wells, springs, and surface water.[1] In many of these communities, the primary contaminants are opportunistic

pathogens. Ingesting contaminated water leads to waterborne disease and health issues such as diarrhea, vomiting, and gastroenteritis.[1] Those issues could be prevented with the existence of proper treatment systems. While urban areas benefit from centralized water treatment and distribution systems, these are poorly implemented in small and rural areas. Decentralized or point-of-use (POU) technologies could provide on-site water treatment to reduce the prevalence of pathogens in water sources.[2]

The design of such systems requires the implementation of antimicrobial agents. Among the potential options, metal and metal-oxide nanoparticles have proven to be excellent alternatives for water disinfection. Metals like gold, silver, and copper nanoparticles have shown significant antibiotic activity; however, the potential leaching of their ions raises concerns about health and environmental impacts.[3,4] In contrast, titanium dioxide-based nanomaterials are considered less harmful alternatives. Their antimicrobial activity arises from the photogeneration of hydroxyl radicals (•OH), hydrogen peroxide ($H_2O_2$), and superoxide anions $O_2^{\bullet-}$, which causes oxidative stress in microorganisms leading to cell death.[5]

Although $TiO_2$ presents excellent photocatalytic activity, its widespread application is primarily hindered by the fact that it is predominantly commercialized in powdered form. While these powders perform well in batch and laboratory-scale reaction models, they pose challenges for practical environmental applications due to the need for an additional separation step. Consequently, the concept of immobilizing photocatalysts on inert supports has gained significant attention, as it can help eliminate the cost associated with phase separation. [6] In particular, the use of glass materials as supports has seen increasing interest in these applications. [5,7–11]

Most studies have focused on the overall performance of supported $TiO_2$ catalysts in eliminating bacterial contaminants from water, without addressing some critical limitations.[10,12–15] Despite their promising antibacterial properties, supported catalyst systems often face challenges that are rarely discussed in the context of antibacterial applications. Some of these challenges include the attachment of bacteria to the catalyst, low light penetration, scattering from the support, and limited mass transfer.[16–21] To advance the development and scalability of supported catalysts for water treatment, it is essential to address these issues comprehensively.

In this contribution, we present a comprehensive analysis of our experimental findings on the antibacterial activity of $TiO_2$@Glass Wool (TGW). Our initial results showed unexpected outcomes, leading us to investigate four factors commonly discussed in optimizing photocatalytic bacterial inactivation:

- Increased catalyst concentration
- Decreased initial bacterial amounts
- Higher oxygen availability
- Enhanced sample agitation

Even more surprising, optimization experiments did not yield higher antibacterial activity. This prompted a discussion on the reasons for the lower activity and the key aspects to be considered when developing fixed-bed photocatalysts for water disinfection. By understanding these limitations and optimizing conditions, we aim to advance the design of photocatalytic materials for water treatment applications.

## MATERIALS AND METHODS

### Catalyst preparation

The material was synthesized as previously published.[22] In brief, to a 10% PVP in EtOH, we added 5 mL (60 mM) titanium isopropoxide and 5 mL acetic acid. The solution was stirred until a transparent homogenous solution was obtained. The $TiO_2$ precursor solution was added to a 30 cm glass tube, with 1.5 g HCl (6 M) and APTES-treated glass wool. The solution was stirred using a rotator overnight at room temperature. After the pre-incubation, the glass wool was removed, washed 3x with EtOH, and 3x with distilled water, and let dry at 80 °C overnight. The dry $TiO_2$@GW (TGW) was then calcined under air using a tube furnace heated at 500 °C for 2 h and 5 min at 600 °C. The material was left to cool down at room temperature, washed 5x or until a clear solution was obtained with distilled water and dried at 80 °C.

### Antibacterial tests:

***Bacterial strains and growth conditions,*** the experiments were performed using *Escherichia coli* O6:H1 (strain CF073) (ATCC700928), an uropathogenic isolate. Stock cultures were maintained

in LB and stored at -80°C in 10 % glycerol.

***Bactericidal activity,*** TGW was tested in batches under dark and light conditions. The initial bacterial suspension was prepared from an overnight culture grown in Luria-Bertani (LB) broth at 37°C, the solution was diluted in LB 5% (in PBS) until an $OD_{600}$ = 0.1. This solution was then diluted 200x to obtain a suspension of approximately $1x10^6$ CFU/mL. In a glass vial, 3 mL of the bacterial suspension was added to 30 mg of the catalyst. For light experiments, the solutions were irradiated for 24 hours with a Luzchem Expo panel fitted with four UVA bulbs (8W each), at a 3 cm distance. The environment temperature after 24 hours of irradiation reached 34°C. Dark experiments were run under the same conditions but protected from light using tin foil. Air experiments were done under the same conditions while bubbling air during the total incubation time. Agitation experiments were done using a circular rotator. Sonicated samples were treated as described and after the assigned irradiation the vials were sonicated for 3 minutes using an ultrasonic bath (40 kHz). Viable cells were counted using the drop plate method. Only samples with colony counts ranging from 3 to 30 were counted for 10 µL drops. Biological replicates were used to obtain statistical analysis

**Hydroxyl radical detection:** Detection of ˙OH radicals was done using a coumarin probe. In the presence of ˙OH, coumarin is hydroxylated into 7-hydroxycoumarin (7-HC) which has strong fluorescence at 454 nm. The experiments were run in the same conditions as antibacterial tests, with 10 mg/mL of catalysts in 5% LB. 0.25 mM of aqueous Coumarin in 5% LB solution (pH 3) was mixed with TGW in a glass vial. The solutions were irradiated with the UVA light source for light treatments or protected from illumination with tin foil for dark samples. Fluorescence spectra were obtained in a Photon Technology International (PTI) fluorimeter. The excitation wavelength was set at 340 nm, and the emission scanned between 380 nm and 660 nm.

**Fluorescence Lifetime Imaging Microscopy (FLIM) Study**

***Sample preparation:*** Samples were incubated in similar conditions to the antibacterial experiments, utilizing an initial bacterial concentration of $10^6$ CFU/mL, and incubated for three and 24 hours. After the incubation 400 µL of the cellular suspension and small pieces of glass wool were taken from the vials and added to a glass bottom dish (35 mm).

Cellular aliquots alone ($OD_{600}$ = 0.1) in 5 % LB were used as "live sample control" and the same solution was heated to 85 °C and imaged as "dead samples control". Bacterial growth on those samples was also confirmed by the Colony Forming Units (CFU) counting in MH agar plates.

For the lifetime fluorescence, we chose SYTO 9 which has strong fluorescence emission when bound to DNA.[238,239] The dye was obtained from Thermo Fisher as part of the BacLight™ bacterial viability kits. The initial solution of 3.34 mM in DMSO was kept protected from light and stored at -20°C until use. Immediately before use, 2 uL of the dye was mixed into the sample and incubated at room temperature for 5 min before imaging.

***Imaging:*** Images were taken using a Fluorescent Lifetime Imaging system (FLIM, PicoQuant MicroTime 200). The instrument was equipped with a frequency-doubled picosecond pulse diode laser (485 ± 10 nm, 70 ps, 40 MHz, LDH-D-C-485, PicoQuant). The laser beam was collimated and focused through a fiber-coupling unit. A beam splitter 500dcxr (Chroma) was used to reflect the excitation light into the oil immersion total internal reflection objective (100×, NA1.45, Olympus, PLAPO). The excitation dose (average power) was about 1.5 mW at the microscope. The generated images had 80 µm in the x and y axes.

***Image analysis:*** FLIM data were analyzed using SymPho Time software. Regions of interest (ROI) were designated on each image. Fits to a multiexponential model were used with $\chi^2$ and residuals were used to indicate goodness-of-fit of one-, two- and three-component decays for each ROI.

**Statistics**

Statistical analysis was done with R studio (version 4.1.2). The comparison of multiple groups was done by one-way analysis of variance (ANOVA with Tukey's Post Hoc test), p-values less than 0.05 were considered statistically significant.

## RESULTS:

**Initial antibacterial tests**

We previously worked with $TiO_2$@GW (TGW); a catalyst that proved to be highly effective for water remediation involving organic contaminants. Beyond its impressive catalytic activity, the glass wool support provided a versatile alternative for various reactor configurations.[22]

Our focus has since shifted to evaluating this new catalyst against more realistic contaminants, specifically microorganisms. We chose *Escherichia coli*, a Gram-negative bacterium, as our model. *E. coli* is not only easy to cultivate in a laboratory setting but also belongs to the coliform group, one of the main bacterial contaminants in wastewater, and is an indicator of fecal contamination.[25]

To explore the potential antibacterial activity of our catalyst, we employed a batch system containing 10 mg/mL of TGW, a concentration established in our previous work. The samples were irradiated with four UVA bulbs (8 W each), whose emission matched $TiO_2$ absorbance maxima at 370 nm. After the light treatments for 1 to 3, 6, and 24 hours, the viable bacteria concentration was assessed. All experiments were done using diluted LB (5 %) in PBS, as the rich composition of this media does not resemble the natural water environments. Using an initial bacterial concentration of 1 x $10^6$ CFU/mL, we first measured the growth pattern of the negative control, a bacterial solution incubated under the same conditions as the treatments, but without a catalyst and protected from light, assigned as dark control. Figure 4.3.1 illustrates the increase in the bacterial count in the dark control, compared to the initial inoculum during the treatment period. To account for the rise in the bacterial population, cell viability was compared to the counted cells in the dark control.

Figure 4.2.1 shows the overall change in viable bacteria under the treatment conditions. Bars above the x-axis correspond to a logarithmic decrease in the bacterial count compared to the dark control, while negative bars indicate bacterial growth. Bars near zero (0 log units) represent samples with cellular counts comparable to the control, indicating that the treatment did not affect the microorganisms' growth pattern.

When incubating the bacterial solution with APTES-treated glass wool in the dark (GW Dark), in the first 6 hours, no significant difference was found compared to incubating the bacteria alone ($p>0.05$), suggesting that the glass support was not harmful to the bacteria. This is in alignment with other research utilizing glass wool, which has shown that the material is not harmful to bacteria.[26,27] Moreover, it demonstrates that APTES treatment did not impact bacterial growth. In fact, Wang and colleagues[28] reported that *E. coli* cells could grow and multiply even

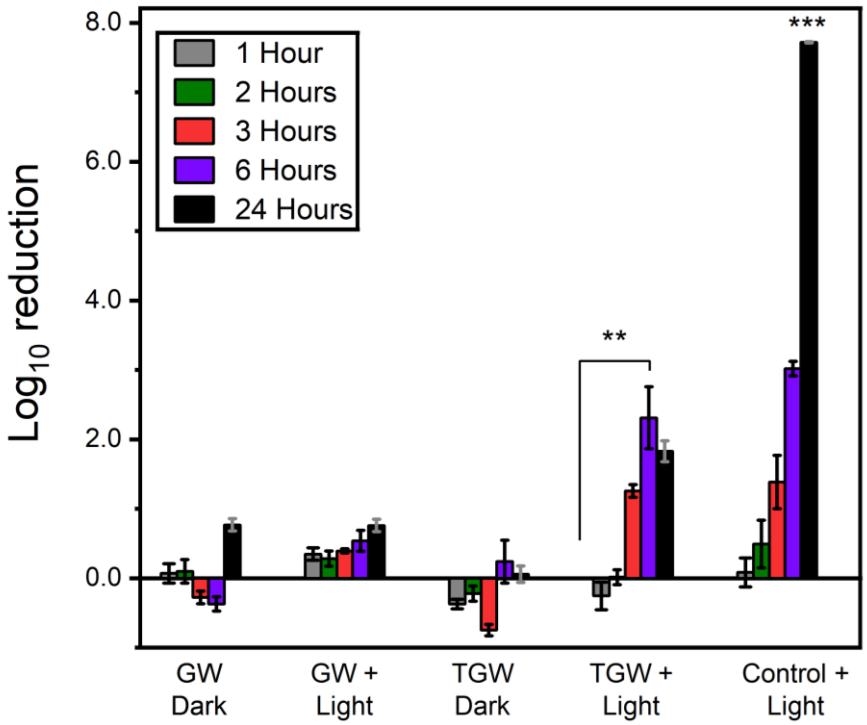


**Figure 4.2.1** Log reduction of *E.coli* bacterial count after incubation with 10 mg/mL APTES-Glass wool (GW) and $TiO_2$ deposited on glass wool (TGW), in the absence of light (dark) and irradiated with four UVA bulbs (8 W each) (Light) for 24 hours. Control light was measured in a bacterial solution exposed to the same light source but without a catalyst. Log reduction was calculated based on the bacterial count of a control incubated protected from the light. Error bars represent standard deviation, n= 3 (*$p < 0.05$, **$p < 0.001$, ***$p = 0.00$).

when attached to an APTES-coated glass surface. When the samples with the glass support were exposed to the light source, a slight, but no significant decrease in viable bacteria was observed (GW+Light) ($p>0.05$).

We then tested the material containing $TiO_2$ on glass wool (TGW). In the absence of illumination, we observed an initial small increase in recovered bacteria during the first 3 hours, however for all time points, the recovered bacteria were statistically the same as the control without treatment, with log reduction values approximately equal to zero ($p>0.05$). In the samples treated with TGW + Light, there was no bactericidal activity during the first two hours. However, a significant ($p<0.05$) reduction in bacterial count was noted at 3 and 6 hours, with a reduction of 1.3 and 2.3 log units, respectively. At longer times, however, the bactericidal remained at a similar value with 1.8 log units. Long irradiation times do not always result in higher bacterial inactivation, this is a previously observed phenomenon that can be a result of resistance development or photocatalyst inhibition produced by the competition with organic products released from cellular compartments.[29] Although the sample with the $TiO_2$ catalyst exhibited some bactericidal activity, the control exposed to UVA light alone (Figure 4.2.1: Control+ Light) showed the same log reduction activity after three and six hours ($p>0.05$). Moreover, at longer irradiation times, the control light sample demonstrated superior performance ($p<0.001$), with no bacterial cells recovered after 24 hours of irradiation.

It was expected a bactericidal effect from the irradiation alone, as wavelength within the UVA range photoexcites cellular chromophores which culminates in hydroxyl radicals (•OH) production and increased formation of cyclobutane pyrimidine dimers (CPD). [30-32] However, the presence of supported $TiO_2$ exposed to UVA light is reported to accelerate bacterial killing,[10,12,21,33] but this was not the case in our system. This unexpected outcome prompted us to conduct a series of investigations under different conditions to identify the factors contributing to the suboptimal performance of the catalyst. Based on these results we can then discuss which factors are influencing the performance of supported $TiO_2$ materials and propose improvements for such systems.

**Does Concentration Matter? Sometimes Less Means More**

First, the catalyst concentration was varied, with lower and higher concentrations set at 5 mg/mL and 20 mg/mL, respectively. Table 4.2.1 compares the effects of different catalyst concentrations with the no catalyst sample (0 mg/mL) designated as Control + Light. Interestingly, the sample with 5 mg/mL, achieved 1.8 log units, a larger log reduction than the 1.2 log units with

10 mg/mL of the catalyst, however, both are statistically comparable ($p>0.05$). On the other hand, increasing the concentration to 20 mg/mL resulted in a slight decrease in the antibacterial performance of TGW down to 0.9 log units, despite the higher amounts of $TiO_2$ in this treatment.

The negative correlation between photocatalytic activity and increasing $TiO_2$ loading has been previously reported for both suspended and supported $TiO_2$.[7,17,34] This phenomenon could be attributed to light scattering by the catalyst, which reduces overall photon absorption.[35] In the case of a supported catalyst system, the glass material may also act as a scattering center.[7] Light scattering would also explain why the GW+Light treatment exhibited a lower bactericidal effect compared to the control + Light treatment (Figure 4.2.1), as the glass could be shielding the cells. To further demonstrate this effect, we measured the light transmitted through the reaction vial with and without the glass support and observed a reduction in the transmitted light (Figure 4.3.2). This confirms that the presence of the glass support can impact the optical behaviour of the photocatalyst.

The next variation considered was the initial bacterial density. While coliform concentrations in surface and groundwater can reach up to $10^6$ CFU/mL in highly contaminated areas, it is more common to find concentrations ranging from $10^0$ to $10^3$ CFU/mL. [36-38] We then chose a lower initial concentration of approximately $10^3$ CFU/mL to represent typical contamination levels and assess any potential increase in bacterial inactivation.

The presence of high amounts of bacterial cells signifies stronger competition between living cells and higher turbidity, contributing to light attenuation. This also increases the chances of surface saturation with adhesion from live cells or cellular debris, all of which can compromise photocatalytic inactivation. Despite reports suggesting higher photocatalytic disinfection rates in solutions with lower bacterial density,[12,21] our experiments revealed that decreasing the initial concentration did not significantly alter the log unit reduction ($p>0.05$), achieving only a 0.9 log reduction. It is important to note that one log unit for a smaller initial bacterial concentration translates to a higher percentage of bacteria inactivation, thus having a higher impact on the bacterial community. Yet, our findings indicate that an initial bacterial concentration of $10^6$ CFU/mL does not significantly impact the catalyst's performance.

These results first evidenced that we were not employing a bacterial density above the catalyst limit. Therefore, we decided to maintain a concentration of $10^6$ CFU/mL for further tests as it also facilitates additional imaging tests. Secondly, this suggests that the photocatalytic generation of radicals may be compromised. For this reason, in the following section, we will evaluate hydroxyl radicals generation in our systems.

**Table 4.2.1** Log reduction of *E. coli* bacterial count after incubation with $TiO_2$@Glass wool (TGW) with different concentrations of catalyst (0-20 mg/mL) or different initial bacterial concentrations. Samples were irradiated with UVA light for 3 hours. Log reduction was calculated based on the bacterial count of a control incubated protected from the light. Standard deviation values are presented in parentheses.

| Catalyst Concentration (mg/mL) | Initial concentration (CFU/mL) | Log reduction ($Log_{10}$ CFU/mL) |
|---|---|---|
| 0 | $1x10^6$ | 1.4 (±0.4) |
| 5 | $1x10^6$ | 1.8 (±1.2) |
| 10 | $1x10^6$ | 1.2 (±0.1) |
| 20 | $1x10^6$ | 0.9 (±1.1) |
| 0 | $2x10^3$ | 1.2 (±0.4) |
| 10 | $2x10^3$ | 0.9 (±0.2) |
| 10[a] | $2x10^3$ | 1.07 (±0.2) |

[a] Sample incubated with APTES-GW only, no $TiO_2$.

**The Multiple Target Dispute for Hydroxyl Radicals**

Given the indications that the system with the supported material may absorb less light, combined with the fact that we are using a complex medium, LB broth, which contains various natural molecules, that could be scavenging the produced radicals. We wanted to test whether we were producing hydroxyl radicals as they are often considered one of the primary bactericidal mechanisms of semiconductors.[5] To test this, we employed a coumarin probe which is hydroxylated in the presence of $^{\bullet}OH$, forming 7-hydroxycoumarin (7-HC) which has a strong fluorescence at 454 nm.[39]

The fluorescence emission spectra of the initial solution and the resulting fluorescent product are shown in Figure 4.3.3. The initial solution exhibits slight fluorescence in the visible region due to the background fluorescence of coumarin and the LB medium.[39] Upon irradiation, the emission maximum shifts to around 454 nm, indicating the production of 7-HC. Figure 4.2.2 A summarizes the changes in fluorescence for the sample containing the glass materials and the controls. In the absence of a catalyst, minimal hydroxyl radical production occurs from the irradiation of coumarin. Similar fluorescence readings were found for the sample containing glass wool alone and the TGW catalyst without UVA irradiation. At all time points, the sample containing the supported $TiO_2$ catalyst showed superior 7-HC production, peaking at 6 hours. There was no change after 24 hours of irradiation, possibly due to the limited reagent, which was added at a lower concentration because of its low water solubility.

Comparing the fluorescence produced by TGW in the 5% LB medium versus in distilled water reveals a decrease in the produced hydroxyl radicals (Figure 4.2.2 B), suggesting that the medium may be scavenging some of the radicals. This is an interesting outcome that can be justified by the transient nature of $^{\bullet}OH$, which reacts with many molecules at a rate close to diffuse control.[40] The rich composition of LB broth, and the high ionic strength of the dilution medium, PBS, contribute to this effect. In the case of the buffer, the influence of the inorganic ions is variable depending on the ion. For example, $Cl^-$ has minimal impact on the photocatalytic disinfection,[41,42] while $PO_4^-$ strongly adorbs in $TiO_2$, occupying reactive sites and competing for $^{\bullet}OH$.[42] This explains the reduced photocatalytic activity of our catalyst compared to the previous results.[22] Natural and wastewater conditions, however, are more similar to the ones proposed in the antibacterial experiments, having inorganic ions and organic matter. The latter also displays variable effects on photocatalysis, leading to enhancement via photosensitization or inhibition through radical scavenging, depending on its composition.[43–45.] Despite having limited radical production under those conditions, these catalysts should still generate sufficient radicals for bacterial inactivation to be considered for realistic applications. Based on this understanding, in

the next section, we will explore methods to enhance radical production or improve its efficiency towards bacteria.

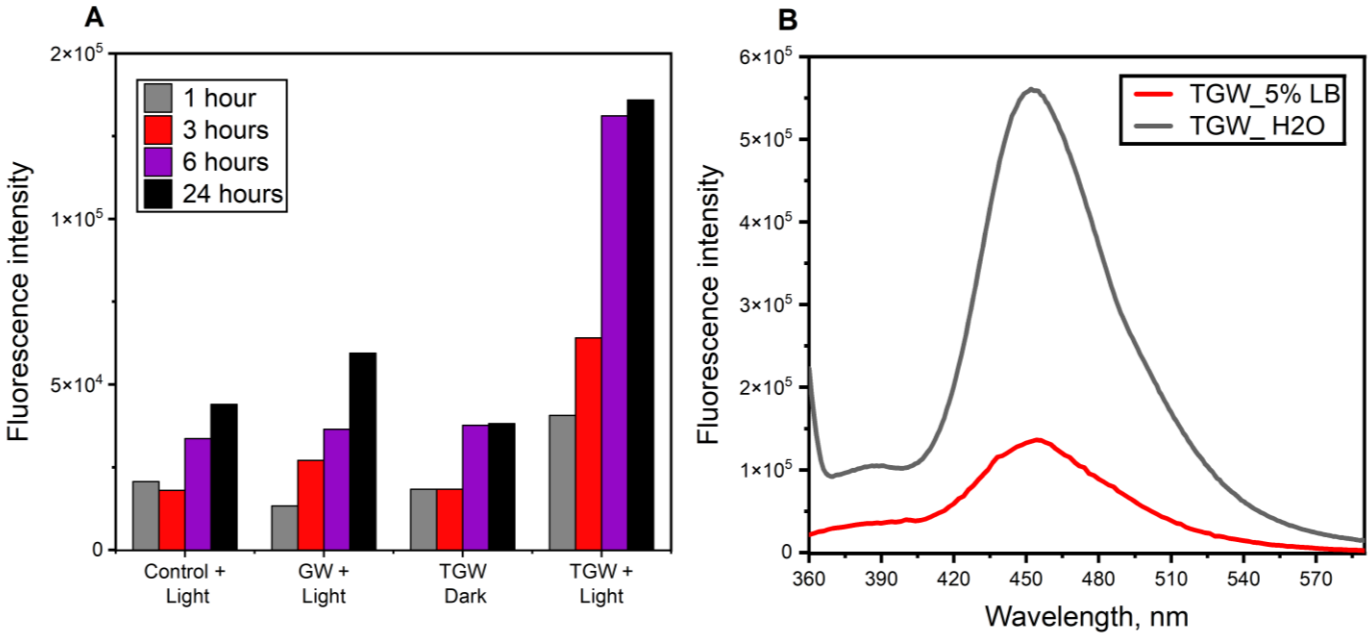


**Figure 4.2.2** (A) Hydroxyl radical detection using coumarin as a standard probe. The presence of the hydroxylated product, 7-hydroxycoumarin was detected by measuring the fluorescence at 454 nm (ex: 340 nm). Coumarin solution (0.25 mmol in 5 % LB) was irradiated with UVA light for 1, 3, 6 and 24 hours, without catalyst (Control+Light), with 10 mg/mL APTES Treated Glass wool (GW+Light), and with 10 mg/mL of $TiO_2$+GW in presence and absence of light (TGW+Light) and TGW Dark. (B) Fluorescence emission spectra of coumarin solution in LB 5 % (pH 3.0) (red) and in $dH_2O$ (grey), both samples were irradiated with UVA light irradiation for three hours with 10 mg/mL of TGW

**Stirring the Pot: The Impact of Aeration and Agitation**

Oxygen is an important electron acceptor for photocatalysts, decreasing the chances of charge recombination, and generating other ROS-centered radicals.[46] Low oxygen availability is demonstrated to decrease hydroxyl radical production thus affecting photocatalytic performance.[47-48] To test whether increased aeration would enhance photocatalytic bacterial inactivation, we conducted bacterial tests while bubbling air into the sample. After three hours of irradiation, the bacterial inactivation was 1.38 ± 0.28 log units, a value not significantly different

from the non-aeration sample at 1.26 ± 0.09 ($p>0.05$). In contrast, Yan and colleagues[261] found increased bactericidal activity when samples were purged with air, attributing this to higher levels of $H_2O_2$ and $^{\bullet}OH$ radicals. It is worth mentioning that the dark control under aeration displayed higher colony counts than the one in the closed system, with an increase of 1 log unit. Consequently, the log reduction calculation for the treatment sample was adjusted to account for the cellular increase. In a higher bacterial concentration, the same catalyst would require higher radical production to achieve greater bacterial activity, which does not occur in this system, as the added $O_2$ does not seem to produce sufficient radicals.

We also conducted experiments with constant mixing to enhance sample aeration and homogenization while reducing bacterial adhesion to the glass wool. To avoid damaging the glass wool support, we used a circular rotator instead of a stirring bar. Surprisingly, when comparing results from the static system to the system under agitation, we observed a decrease log reduction (Figure 4.2.3) for both the $TiO_2$-supported sample (grey) and the glass support alone (red). Thus, even with improved homogenization, which would facilitate the interaction of the surface-generated radicals with the target *E. coli*, the GW treatment did not exhibit enhanced bactericidal activity.

The decrease in log reduction for samples under agitation could be attributed to reduced bacterial attachment to the heterogeneous catalyst. To verify this, we conducted the reaction under static conditions and sonicated the samples before plating to remove potentially attached bacteria. After three minutes of sonication, we observed an increase in the number of viable bacteria, as indicated by the negative log reduction in Figure 4.2.3. This suggests the adhesion of bacterial cells on the catalyst. We anticipated some degree of bacterial attachment to the supported catalysts, as bacteria in natural environments prefer to grow on surfaces, forming aggregates known as biofilms.[50-51]

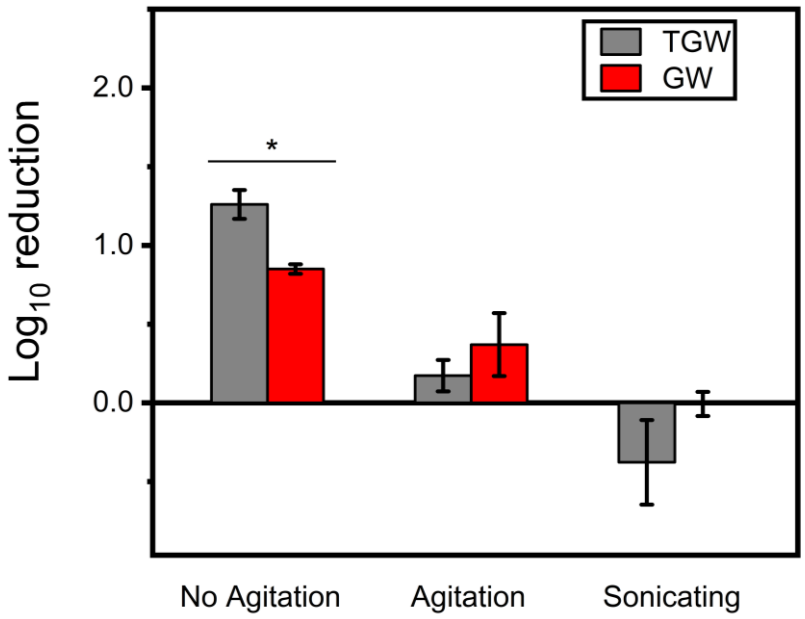


**Figure 4.2.3** Log reduction of *E. coli* bacterial count after incubation with 10 mg/mL APTES-Glass Wool (GW) (red) and $TiO_2$-deposited Glass Wool (TGW) (grey) under UVA irradiation for 3 hours. Agitation samples were mixed using a circular rotator for the full duration of irradiation. Sonicating samples were irradiated under static conditions and sonicated for three minutes before plating. Log reduction was calculated based on the bacterial count of a control incubated in the absence of light for the same duration. Error bars represent the standard deviation. * $p<0.05$

Although the incubation time and solution conditions in our system may not have been sufficient for mature biofilm formation, the supported catalyst appeared to provide a surface for bacterial attachment. Our $TiO_2$@GW has a 48% $TiO_2$ loading,[22] meaning both titanium dioxide and silica oxide surfaces were available for attachment, which has previously been shown to support bacterial growth.[22,19,52-54] Bacterial interactions with surfaces are a complex phenomenon driven by electrostatic forces, Van der Waals, hydrophobic and hydrogen interactions.[52,55] The degree of these interactions depends on the composition of the bacterial cell envelope, the catalyst surface properties, and the media composition.[52] For instance, *E.coli* and $TiO_2$ interactions vary greatly depending on the ionic strength of the surrounding medium, the ions composing the solution, pH and the presence of organic matter.[33] Due to the high degree of variability between systems, it is important to evaluate the interaction between the microorganisms and the catalyst

being studied. As observed, the cellular attraction and attachment to the photocatalysts and to the glass support influence the observed log reduction and may affect the overall bactericidal activity.

**Imaging Bacterial-catalyst interaction as it happens**

Interested in observing bacterial attachment to the catalyst, we utilized Fluorescence Lifetime Microscopy (FLIM), which allowed us to observe cells and infer the environment surrounding the fluorophore.[56] We began by measuring the average lifetimes for live and dead cells using SYTO 9, a cell-permeable dye that stains genetic material in both live and dead cells.[23,57] We could not establish a clear lifetime threshold for distinguishing between live and dead bacteria due to considerable overlap in lifetimes for both controls, as seen in Figure 4.3.4. However, we observed an overall decrease in the average lifetime ($\tau_{avg}$) of samples with dead cells. On average, the lifetime decreased from 2.8 ns in live cells to 2.3 ns in dead cells, this difference can also be seen in the decays represented in Figure 4.3.5. This trend was consistent with other nucleic acid-binding dyes, with the change in lifetime attributed to the fragmented and disorganized genetic material in necrotic cells, leading to less stabilization of the dye.[58,59] Additionally, utilizing a similar dye, SYTO 13, Walczysko et.al.[60] reported longer lifetime on cells in the logarithmic growth phase, due to the high RNA/DNA proportion. Samples with a high number of dead cells were also detected by the noisy background fluorescence due to the released cellular content in solution (Figure 4.3.6 B) and by the presence of large aggregates indicative of accumulated cellular debris. In contrast, live cells not only had longer lifetimes but also maintained the rod shape of *E. coli*, resulting in clearer images of the bacteria (Figure 4.3.6A).

We imaged the bacterial cells after incubating them for three and 24 hours, under the same conditions described in the first experiment, (Figure 4.2.1). Representative images of the samples are displayed in Figures 4.2.4 and 4.2.5, for 3 and 24 hours of incubation, respectively, and the average of the calculated lifetimes is listed in Table 4.3.1. For the no catalyst controls, we observed an increase in the number of cells in the dark, for both time points, with $\tau_{avg}$ of 2.6 ns and 2.4 ns for the 3-hour and 24-hour incubations, respectively. The control incubated under irradiation showed fewer observed cells and signs of substantial cellular death, such as a large mass of cellular debris, after 24 hours of incubation (Figure 4.2.5). This aligns with the data presented in Figure

4.2.1, where no viable bacteria were recovered. Additionally, the average lifetimes for the irradiated samples were shorter than those of the controls, with $\tau_{avg}$ = 2.2 ns and 2.1 ns for 3 and 24-hour incubations, respectively. The shorter lifetimes for the light-treated samples can also be seen in the histograms comparing the $\tau_{avg}$ for both controls in Figure 4.2.6. UVA irradiation is known to cause growth delays.[61] resulting from the suppression of RNA synthesis during stress stimuli.[62] The reduction in fluorescence lifetimes in the irradiated samples agrees with the findings from Walczysko et.al.,[60] previously mentioned, which indicates that a lower RNA/DNA ratio results in shorter fluorescence lifetimes.

Samples incubated with glass wool demonstrated significant interaction of *E. coli* cells with the support material in both dark and light conditions (Figures 4.2.4 and 4.2.5). This is expected, as glass is a common substrate for bacterial adhesion. Specifically, glass wool has been used as a support for biofilm formation due to its large surface area, which facilitates the exchange of nutrients and oxygen.[27] Additionally, the silanization process enhances cell deposition, as demonstrated by Sharma and Conrad,[54] *E. coli* cells attach more rapidly to APTES-treated surfaces than to untreated glass surfaces. Overall, a reduction in the lifetimes of cells attached to glass wool was observed. For instance, in samples incubated with glass wool (GW) in the dark for 3 hours, the lifetime of cells in the solution was 2.4 ns, while cells on the GW had $\tau_{avg}$ of 2.2 ns. This might suggest the presence of dead cells; however, when these samples were plated after sonication, the log reduction was close to zero (Figure 4.2.3), indicating that most cells remained viable. Also, it is important to note that dead bacteria, lacking metabolic activity and cellular integrity, generally do not exhibit the same attachment behaviour as live cells.[63,64]

Samples containing $TiO_2$ were distinguishable by the short lifetimes at the catalyst, demonstrated as blue areas in Figures 4.2.4, 4.2.5 and Figure 4.3.7. Those values are very similar to the instrument response function (IRF), $\tau$= 0.4 ns, and can be seen probably due to light scattering. Comparing irradiated and non-irradiated $TiO_2$ samples revealed a higher cell count in the dark samples, agreeing with the finding in Figure 4.2.1. Bacterial deposition was observed even in the semiconductor catalyst, for both dark and light treatment, consistent with findings from other studies. [12,29] However, as observed by Pablos et al.,[33] the extent of this interaction depends

not only on the properties of the bacteria and catalyst but also on the solution's composition. The fluorescent lifetime of cells attached to the material remained consistent at $\tau_{avg}$ of 2.5 ns for both samples. However, cells in the solution of irradiated samples showed a slight decrease in $\tau_{avg}$, to 2.3 ns after three hours and 2.1 ns after 24 hours (Figure 4.2.5).

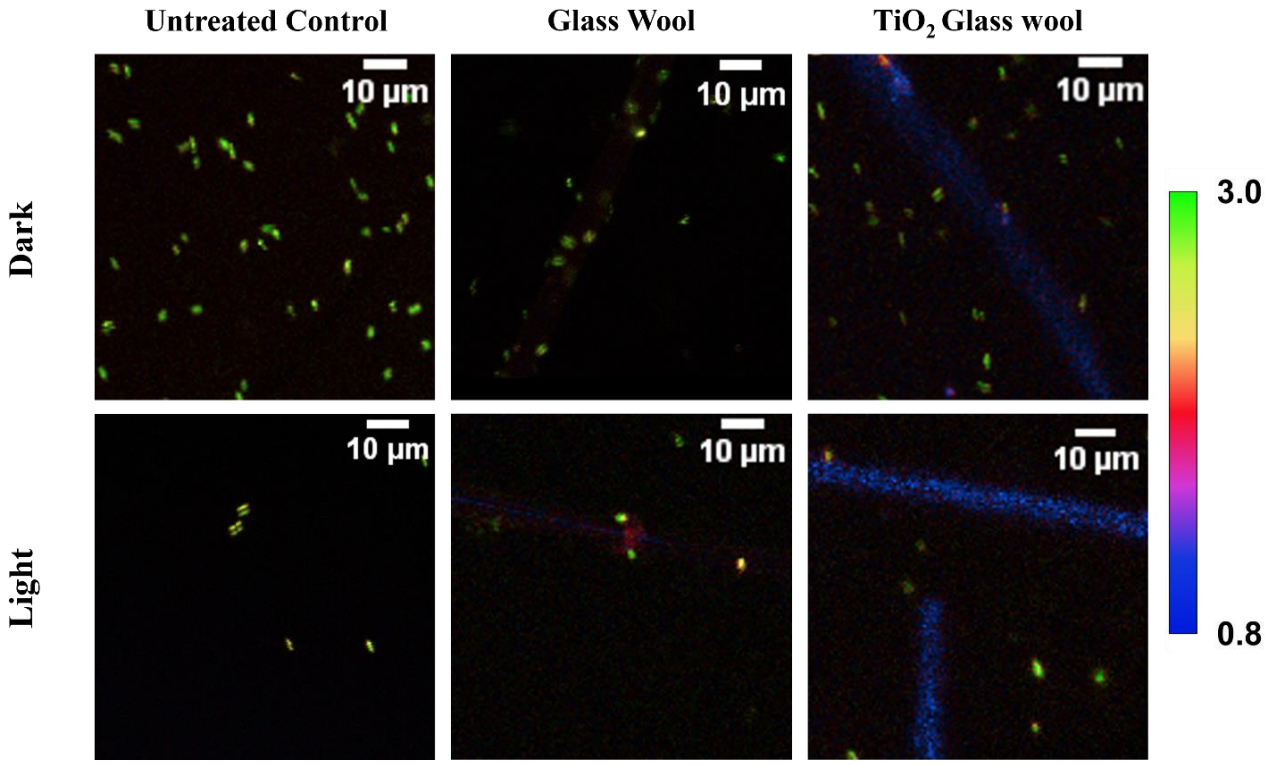


**Figure 4.2.4.** Characteristic Fluorescence lifetime images (FLIM) of *E. coli* cells stained with SYTO9 after 3 hours incubation. The images depict *E. coli* cells in 5 % LB in PBS, either untreated or treated, after three hours in the dark or irradiated with UVA light. Treated samples were incubated with either 10 mg/mL of APTES glass wool or $TiO_2$@glass wool (TGW). Different colours represent various lifetimes of the dye, excited at 485 nm. The colour bar scale ranges from 0.8 to 3 ns. The brightness of the images was enhanced by 20% to ensure all FLIM data is clearly visible.

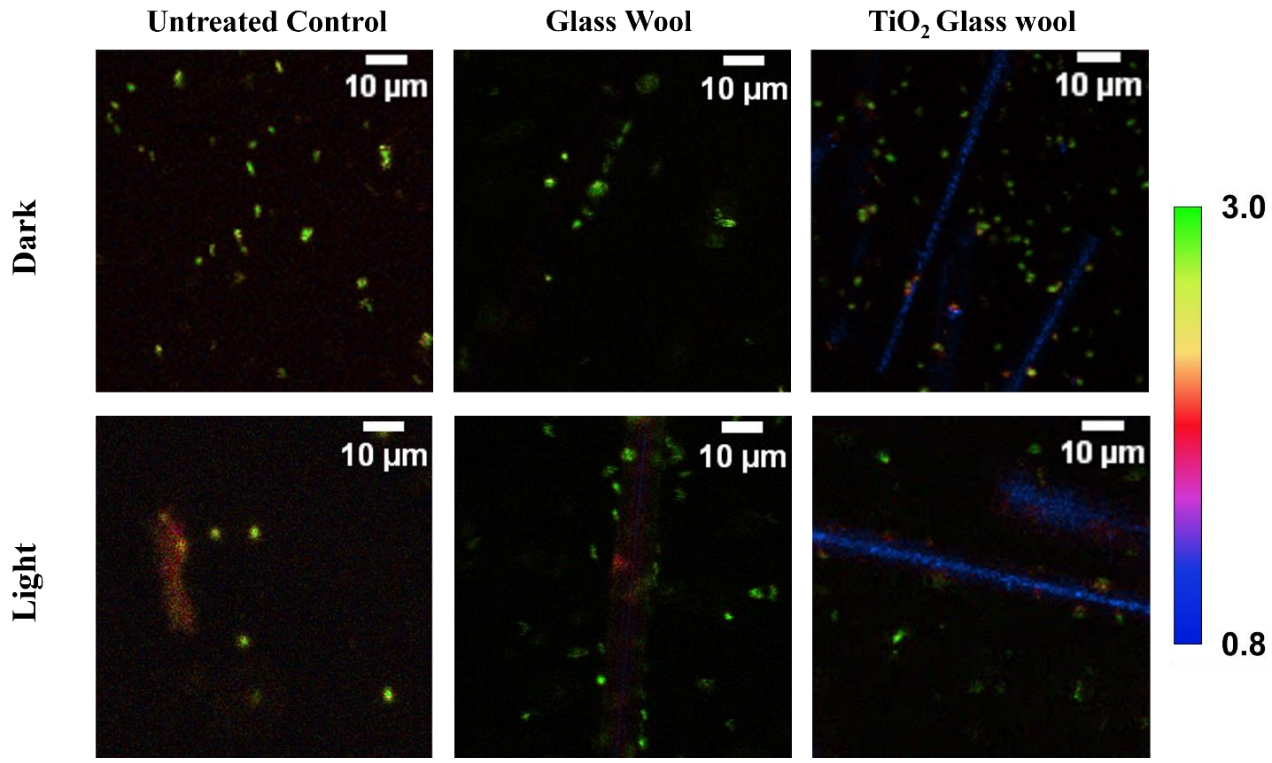


**Figure 4.2.5** Characteristic Fluorescence lifetime images (FLIM) of *E. coli* cells stained with SYTO9 after 24 hours of incubation. The images depict *E. coli* cells in 5 % LB in PBS, either untreated or treated, after 24 hours in the dark or irradiated with UVA light. Treated samples were incubated with either 10 mg/mL of APTES glass wool or $TiO_2$@glass wool (TGW). Different colours represent various lifetimes of the dye, excited at 485 nm. The colour bar scale ranges from 0.8 to 3 ns. The brightness of the images was enhanced by 20% to ensure all FLIM data is clearly visible

Additionally, after a long incubation, a few spots on the TGW displayed shorter lifetimes ($\tau_{avg}$=1.69 ns) than the ones found in the deposited bacteria, Figure 4.3.8 (yellow arrows). These spots did not resemble cellular shapes, possibly indicating the presence of cellular components released from lysed cells which might contain genetic material.[63] Notably, areas containing debris can still serve as attachment sites for viable bacteria, as demonstrated by Miwa et al., and they can act as protective layers, shielding the cells from the catalyst's action. In fact, a decrease in the bactericidal performance was observed after 24 hours of treatment with TGW + Light (Figure

4.2.1). In some samples, live cells were still detected ($\tau_{avg}$= 2.5 ns) (Figure 4.2.5), indicating that not all microorganisms were inactivated, which aligns with the data presented in Figure 4.2.1.

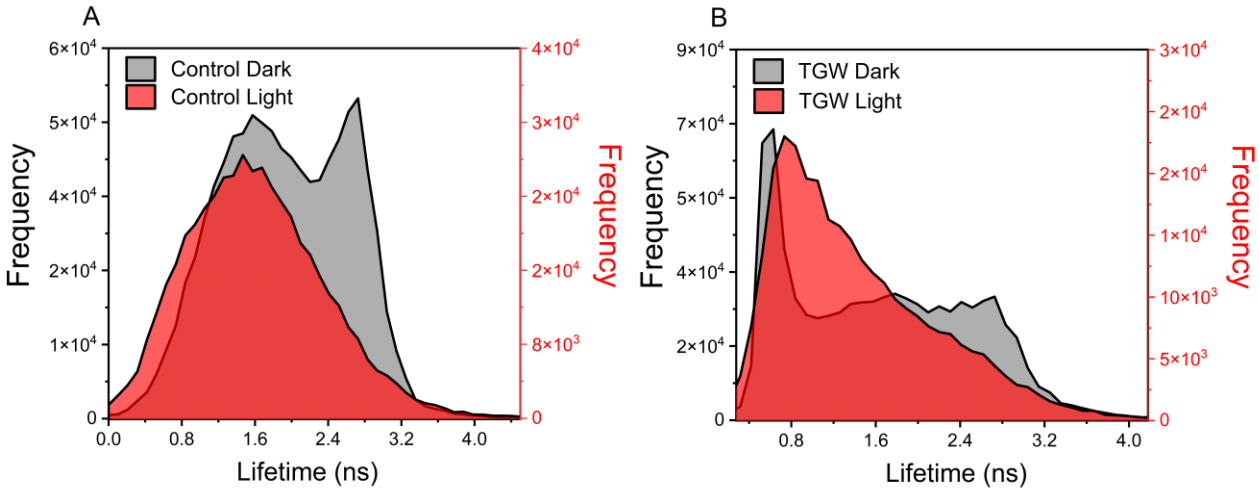


**Figure 4.2.6.** Histograms of fluorescence lifetime distribution on control samples (A) and on samples treated with 10 mg/mL of TGW. In grey are samples incubated and protected from light and in red samples irradiated with UVA light (370 nm). Bacteria concentration was set to $OD_{600}$=0.1 in 5 % LB.

**Plausible scenario and future improvements**

In this context, the catalyst surface provided a favourable environment for bacterial adherence. Alongside an overall low catalytic activity—likely due to insufficient ROS production, limited $O_2$ availability, and light scattering from the supporting material— this resulted in inadequate bactericidal performance against microorganisms in the solution and those in close contact with the catalyst. In cases where bacterial inactivation occurred after prolonged irradiation, the accumulated cellular debris seemed to further hinder catalytic activity.

From this perspective, while the catalyst was effective for dye degradation, its application for antimicrobial activity may require improved methodologies. As pointed out by Rimzhim and Modak,[65] catalysts that are effective for organic degradation may not be suitable for bacterial disinfection, and vice versa. This discrepancy is influenced by various factors that affect both photocatalytic degradation and disinfection. For bactericidal applications, variables such as bacterial adhesion, the quantity and lifetime of radicals formed, bacterial cell composition, and the

ionic strength of the solution play crucial roles.[7,12,21,29,33,65] Thus, troubleshooting for bacterial disinfection also differs from that for organic degradation.

Based on the observed results, several possible improvements can be discussed. One key factor is the bacterial adhesion to the catalyst. Here, it should be noted that the close contact of bacteria to $TiO_2$ was demonstrated to increase oxidative damage in bacteria, which is caused by surface-generated radicals,[20,66] in particular, when talking about wastewater, the excess ions and organic matter may act as radical scavengers,[33] as we observed in Figure 4.3.5. On the other hand, accumulated live cells or cellular debris on the photocatalyst surface may hinder the catalyst's effectiveness. Some researchers have reported modulating the semiconductor's surface to reduce bacterial deposition, with the formation of superhydrophobic $TiO_2$ being one of the most common strategies.[19,53,67] Furthermore, the attachment of bacteria raises concerns about biofilm formation, as these surfaces provide anchoring support for biofilm development. Those mature bacterial communities display increased adhesion to surfaces, extra protection against bactericidal agents,[68] and increased chances of horizontal gene transfer, potentially leading to resistance development.[68–70]

Certainly, most issues related to the attachment of live bacteria and biofilm formation arise from insufficient photocatalytic activity. A significant part of the problem stems from low light absorbance in the system,[17] which results from the limited photon penetration common in fixed catalyst structures.[20,35] This issue is exacerbated by the scattering effect from the glass support. Improving the optical properties of the catalyst can be achieved by increasing $TiO_2$ loading on the glass material, which would increase the radiation absorption-to-scattering ratio.[7] A possible alternative is evaluating other glass-supported $TiO_2$ materials, such as the $TiO_2$ on glass filter fibres that we previously fabricated, which have a higher $TiO_2$ loading, around 62 %.[22] Another effective strategy is the use of continuous flow systems, which, with the appropriate reactor design, allow for uniform light distribution compared to batch systems.[71,72] Additionally, immobilized catalysts limit the mass transport of the reactant to the irradiated catalyst surface.[18,29] Some researchers have described the synthesis of differently shaped glass-supported semiconductors, to increase surface-to-volume ratio, or the use of fluidized reactors to reduce mass transfer limitations.[18,73]

## CONCLUSIONS

In conclusion, supported $TiO_2$ catalysts offer the advantage of easy removal from solutions without additional separation steps, making them attractive for water remediation. However, our observations using supported $TiO_2$ in glass wool (TGW) reveal challenges in antibacterial applications. Specifically, the catalyst demonstrated low antibacterial activity, achieving only about a 1 log unit reduction in bacterial count, comparable to disinfection using UVA alone. This suboptimal performance is likely due to insufficient ROS production, limited $O_2$ availability, and light scattering from the support material, all of which result in inadequate bactericidal activity. Additionally, the protective attachment of the bacteria to the catalyst, and the accumulation of cellular debris further hinder catalytic efficiency. These findings underscore that catalysts effective for organic degradation may not be suitable for bacterial disinfection due to differing influencing factors. To enhance bactericidal efficacy, optimizing bacterial adhesion to the catalyst, improving light absorption, and enhancing mass transport are crucial. Therefore, tailored methodologies that address these specific challenges are potential improvements for effective bacterial disinfection.

## REFERENCES

(1) Pooi, C. K.; Ng, H. Y. Review of Low-Cost Point-of-Use Water Treatment Systems for Developing Communities. NPJ Clean Water 2018, 1 (1), 11.

(2) Chong, Y.; Ge, C. Rational Design of Metal-Based Antimicrobial Nanomaterials in Environmental Applications. Environ. Sci. Nano. 2021, 8 (12), 3478–3492.

(3) Biswas, P.; Bandyopadhyaya, R. Synergistic Antibacterial Activity of a Combination of Silver and Copper Nanoparticle Impregnated Activated Carbon for Water Disinfection. Environ. Sci. Nano 2017, 4 (12), 2405–2417.

(4) Nowack, B.; Bucheli, T. D. Occurrence, Behavior and Effects of Nanoparticles in the Environment. Environ. Pollut. 2007, 150 (1), 5–22.

(5) Mohadesi, M.; Sanavi Fard, M.; Shokri, A. The Application of Modified Nano-$TiO_2$ Photocatalyst for Wastewater Treatment: A Review. J. Environ. Anal. Chem. 2022, 1–22.

(6) Shan, A. Y.; Ghazi, T. I. Mohd.; Rashid, S. A. Immobilisation of Titanium Dioxide onto Supporting Materials in Heterogeneous Photocatalysis: A Review. Applied Catalysis A: Gen. 2010, 389 (1–2), 1–8.

(7) Marugán, J.; Hufschmidt, D.; Sagawe, G.; Selzer, V.; Bahnemann, D. Optical Density and Photonic Efficiency of Silica-Supported $TiO_2$ Photocatalysts. Water Res. 2006, 40 (4), 833–839.

(8) Cunha, D. L.; Kuznetsov, A.; Achete, C. A.; Machado, A. E. da H.; Marques, M. Immobilized TiO2 on Glass Spheres Applied to Heterogeneous Photocatalysis: Photoactivity, Leaching and Regeneration Process. Peer J 2018, 6, e4464.

(9) Erjavec, B.; Hudoklin, P.; Perc, K.; Tišler, T.; Dolenc, M. S.; Pintar, A. Glass Fiber-Supported TiO2 Photocatalyst: Efficient Mineralization and Removal of Toxicity/Estrogenicity of Bisphenol A and Its Analogs. Appl. Catal. B: Environ. 2016, 183, 149–158.

(10) Kongsong, P.; Sikong, L.; Niyomwas, S.; Rachpech, V. Photocatalytic Antibacterial Performance of Glass Fibers Thin Film Coated with N-Doped $SnO_2$ /$TiO_2$. Sci. World J. 2014, 2014, 1–9.

(11) Srikanth, B.; Goutham, R.; Badri Narayan, R.; Ramprasath, A.; Gopinath, K. P.; Sankaranarayanan, A. R. Recent Advancements in Supporting Materials for Immobilised Photocatalytic Applications in Wastewater Treatment. J. Environ. Manage. 2017, 200, 60–78.

(12) Rincón, A. G.; Pulgarin, C. Photocatalytical Inactivation of E. Coli: Effect of (Continuous–Intermittent) Light Intensity and of (Suspended–Fixed) $TiO_2$ Concentration. Appl. Catal. B: Environ. 2003, 44 (3), 263–284.

(13) Koli, V. B.; Ke, S.-C.; Dodamani, A. G.; Deshmukh, S. P.; Kim, J.-S. Boron-Doped $TiO_2$-CNT Nanocomposites with Improved Photocatalytic Efficiency toward Photodegradation of Toluene Gas and Photo-Inactivation of Escherichia Coli. Catal. 2020, 10 (6), 632.

(14) Pratap Reddy, M.; Venugopal, A.; Subrahmanyam, M. Hydroxyapatite-Supported Ag–$TiO_2$ as Escherichia Coli Disinfection Photocatalyst. Water Res. 2007, 41 (2), 379–386.

(15) Gelover, S.; Gómez, L. A.; Reyes, K.; Teresa Leal, Ma. A Practical Demonstration of Water Disinfection Using $TiO_2$ Films and Sunlight. Water Res. 2006, 40 (17), 3274–3280.

(16) Yu, H.; Song, L.; Hao, Y.; Lu, N.; Quan, X.; Chen, S.; Zhang, Y.; Feng, Y. Fabrication of Pilot-Scale Photocatalytic Disinfection Device by Installing $TiO_2$ Coated Helical Support into UV Annular Reactor for Strengthening Sterilization. J. Chem. Eng. 2016, 283, 1506–1513.

(17) Kacem, M.; Plantard, G.; Wery, N.; Goetz, V. Kinetics and Efficiency Displayed by Supported and Suspended $TiO_2$ Catalysts Applied to the Disinfection of Escherichia Coli. Chin. J. Catal. 2014, 35 (9), 1571–1577.

(18) Kabir, M. F.; Haque, F.; Vaisman, E.; Langford, C. H.; Kantzas, A. Disinfecting E.coli Bacteria In Drinking Water Using A Novel Fluidized Bed Reactor. Int. J. Chem. React. Eng. 2003, 1 (1).

(19) Wang, G.; Weng, D.; Chen, C.; Chen, L.; Wang, J. Influence of TiO2 Nanostructure Size and Surface Modification on Surface Wettability and Bacterial Adhesion. Colloids Interface Sci. Commun. 2020, 34, 100220.

(20) Gumy, D.; Rincon, A. G.; Hajdu, R.; Pulgarin, C. Solar Photocatalysis for Detoxification and Disinfection of Water: Different Types of Suspended and Fixed $TiO_2$ Catalysts Study. Sol. Energy 2006, 80 (10), 1376–1381.

(21) Rincón, A.-G.; Pulgarin, C. Bactericidal Action of Illuminated $TiO_2$ on Pure Escherichia Coli and Natural Bacterial Consortia: Post-Irradiation Events in the Dark and Assessment of the Effective Disinfection Time. Appl. Catal. B: Environ. 2004, 49 (2), 99–112.

(22) Da Silva, D. R. C.; Mapukata, S.; Currie, S.; Kitos, A. A.; Lanterna, A. E.; Nyokong, T.; Scaiano, J. C. Fibrous $TiO_2$ Alternatives for Semiconductor-Based Catalysts for Photocatalytic Water Remediation Involving Organic Contaminants. ACS Omega 2023, 8 (24), 21585–21593.

(23) Tárnok, A. SYTO Dyes and Histoproteins—Myriad of Applications. Cytom. Part A 2008, 73A (6), 477–479.

(24) BV, M. P. E. LIVE/DEAD BacLight Bacterial Viability Kit Product Information Sheet; Leiden, The Netherlands, 1996.

(25) Cabral, J. P. S. Water Microbiology. Bacterial Pathogens and Water. Int. J Environ. Res. Public Health 2010, 7 (10), 3657–3703.

(26) Ren, D.; Bedzyk, L. A.; Thomas, S. M.; Ye, R. W.; Wood, T. K. Gene Expression in Escherichia Coli Biofilms. Appl. Microbiol. Biotechnol. 2004, 64 (4), 515–524.

(27) Steyn, B.; Oosthuizen, M. C.; MacDonald, R.; Theron, J.; Brözel, V. S. The Use of Glass Wool as an Attachment Surface for Studying Phenotypic Changes InPseudomonas Aeruginosa Biofilms by Two-Dimensional Gel Electrophoresis. Proteomics 2001, 1 (7), 871–879.

(28) Wang, Y.-K.; Krasnopeeva, E.; Lin, S.-Y.; Bai, F.; Pilizota, T.; Lo, C.-J. Comparison of Escherichia Coli Surface Attachment Methods for Single-Cell Microscopy. Sci. Rep. 2019, 9 (1), 19418.

(29) Kacem, M.; Goetz, V.; Plantard, G.; Wery, N. Modeling Heterogeneous Photocatalytic Inactivation of E. Coli Using Suspended and Immobilized $TiO_2$ Reactors. AIChE J. 2015, 61 (8), 2532–2542.

(30) Xiao, Y.; Chu, X. N.; He, M.; Liu, X. C.; Hu, J. Y. Impact of UVA Pre-Radiation on UVC Disinfection Performance: Inactivation, Repair and Mechanism Study. Water Res. 2018, 141, 279–288.

(31) Song, K.; Mohseni, M.; Taghipour, F. Mechanisms Investigation on Bacterial Inactivation through Combinations of UV Wavelengths. Water Res. 2019, 163, 114875.

(32) Nyangaresi, P. O.; Rathnayake, T.; Beck, S. E. Evaluation of Disinfection Efficacy of Single UV-C, and UV-A Followed by UV-C LED Irradiation on Escherichia Coli, B. Spizizenii and MS2 Bacteriophage, in Water. Sci. Total Environ. 2023, 859, 160256.

(33) Pablos, C.; van Grieken, R.; Marugán, J.; Chowdhury, I.; Walker, S. L. Study of Bacterial Adhesion onto Immobilized TiO2: Effect on the Photocatalytic Activity for Disinfection Applications. Catal. Today 2013, 209, 140–146.

(34) Bamba, D.; Atheba, P.; Robert, D.; Trokourey, A.; Dongui, B. Photocatalytic Degradation of the Diuron Pesticide. Environ. Chem. Lett. 2008, 6 (3), 163–167.

(35) Chong, M. N.; Jin, B.; Chow, C. W. K.; Saint, C. Recent Developments in Photocatalytic Water Treatment Technology: A Review. Water Res. 2010, 44 (10), 2997–3027.

(36) Aram, S. A.; Saalidong, B. M.; Osei Lartey, P. Comparative Assessment of the Relationship between Coliform Bacteria and Water Geochemistry in Surface and Ground Water Systems. PLoS One 2021, 16 (9), e0257715.

(37) Some, S.; Mondal, R.; Mitra, D.; Jain, D.; Verma, D.; Das, S. Microbial Pollution of Water with Special Reference to Coliform Bacteria and Their Nexus with Environment. Ener. Nexus 2021, 1, 100008.

(38) Anh, N. T.; Can, L. D.; Nhan, N. T.; Schmalz, B.; Luu, T. Le. Influences of Key Factors on River Water Quality in Urban and Rural Areas: A Review. Case Stud. Chem. Environ. Eng. 2023, 8, 100424.

(39) Leandri, V.; Gardner, J. M.; Jonsson, M. Coumarin as a Quantitative Probe for Hydroxyl Radical Formation in Heterogeneous Photocatalysis. J. Phys. Chem. C 2019, 123 (11), 6667–6674.

(40) Kaur, H.; Halliwell, B. [6] Detection of Hydroxyl Radicals by Aromatic Hydroxylation. In Methods in Enzymology; Academic Press, 1994; Vol. 233, pp 67–82.

(41) Liu, N.; Zhu, Q.; Zhang, N.; Zhang, C.; Kawazoe, N.; Chen, G.; Negishi, N.; Yang, Y. Superior Disinfection Effect of Escherichia Coli by Hydrothermal Synthesized TiO2-Based Composite Photocatalyst under LED Irradiation: Influence of Environmental Factors and Disinfection Mechanism. Environ. Pollut. 2019, 247, 847–856.

(42) Rincon, A.; Pulgarin, C. Effect of PH, Inorganic Ions, Organic Matter and $H_2O_2$ on E. Coli K12 Photocatalytic Inactivation by $TiO_2$ Implications in Solar Water Disinfection. Appl. Catal. B: Environ. 2004, 51 (4), 283–302.

(43) Awfa, D.; Ateia, M.; Fujii, M.; Yoshimura, C. Photocatalytic Degradation of Organic Micropollutants: Inhibition Mechanisms by Different Fractions of Natural Organic Matter. Water Res. 2020, 174, 115643.

(44) Yang, W.; Bu, Q.; Zhao, R.; Xu, W.; Jia, N.; Yang, L.; Tang, J. A Novel Preparation of Trace Iron-Doped 3D Urchin-like $TiO_2$ for Efficient Degradation and Mineralization of Trimethoprim under Simulated Sunlight. Ceram. Int. 2024, 50 (7), 11138–11149.

(45) Liu, S.; Edara, P. C.; Schäfer, A. I. Influence of Organic Matter on the Photocatalytic Degradation of Steroid Hormones by $TiO_2$-Coated Polyethersulfone Microfiltration Membrane. Water Res. 2023, 245, 120438.

(46) Holroyd, R. A.; Bielski, B. H. J. Photochemical Generation of Superoxide Radicals in Aqueous Solutions. J. Am. Chem. Soc. 1978, 100 (18), 5796–5800.

(47) Galindo, C.; Jacques, P.; Kalt, A. Photodegradation of the Aminoazobenzene Acid Orange 52 by Three Advanced Oxidation Processes: UV/$H_2O_2$, UV/$TiO_2$ and VIS/$TiO_2$. J. Photochem. Photobiol. 2000, 130 (1), 35–47.

(48) Shibata, H.; Ogura, Y.; Sawa, Y.; Kono, Y. Hydroxyl Radical Generation Depending on O2 or H2O by a Photocatalyzed Reaction in an Aqueous Suspension of Titanium Dioxide. Biosci. Biotechnol. Biochem. 1998, 62 (12), 2306–2311.

(49) Yan, G.; Chen, J.; Hua, Z. Roles of $H_2O_2$ and OH Radical in Bactericidal Action of Immobilized $TiO_2$ Thin-Film Reactor: An ESR Study. J Photochem. Photobiol. A: Chem. 2009, 207 (2–3), 153–159.

(50) Beveridge, T. J.; Makin, S. A.; Kadurugamuwa, J. L.; Li, Z. Interactions between Biofilms and the Environment. FEMS Microbiol. Rev. 1997, 20 (3–4), 291–303.

(51) Costerton, J. W.; Stewart, P. S.; Greenberg, E. P. Bacterial Biofilms: A Common Cause of Persistent Infections. Science (1979) 1999, 284 (5418), 1318–1322.

(52) Elfazazi, K.; Zahir, H.; Tankiouine, S.; Mayoussi, B.; Zanane, C.; Lekchiri, S.; Ellouali, M.; Mliji, E. M.; Latrache, H. Adhesion Behavior of Escherichia Coli Strains on Glass: Role of

Cell Surface Qualitative and Quantitative Hydrophobicity in Their Attachment Ability. Int. J. Med. Microbiol. 2021, 2021, 1–9.

(53) Lai, Y.; Huang, J.; Cui, Z.; Ge, M.; Zhang, K.; Chen, Z.; Chi, L. Recent Advances in TiO2-Based Nanostructured Surfaces with Controllable Wettability and Adhesion. Small 2016, 12 (16), 2203–2224.

(54) Sharma, S.; Conrad, J. C. Attachment from Flow of Escherichia Coli Bacteria onto Silanized Glass Substrates. Langmuir 2014, 30 (37), 11147–11155.

(55) BinAhmed, S.; Hasane, A.; Wang, Z.; Mansurov, A.; Romero-Vargas Castrillón, S. Bacterial Adhesion to Ultrafiltration Membranes: Role of Hydrophilicity, Natural Organic Matter, and Cell-Surface Macromolecules. Environ. Sci. Technol. 2018, 52 (1), 162–172.

(56) Dunkers, J. P.; Iyer, H.; Jones, B.; Camp, C. H.; Stranick, S. J.; Lin, N. J. Toward Absolute Viability Measurements for Bacteria. J. Biophotonics 2021, 14 (12).

(57) Boulos, L.; Prévost, M.; Barbeau, B.; Coallier, J.; Desjardins, R. LIVE/DEAD® BacLightTM: Application of a New Rapid Staining Method for Direct Enumeration of Viable and Total Bacteria in Drinking Water. J. Microbiol. Methods 1999, 37 (1), 77–86.

(58) Silvero C., M. J.; Rocca, D. M.; de la Villarmois, E. A.; Fournier, K.; Lanterna, A. E.; Pérez, M. F.; Becerra, M. C.; Scaiano, J. C. Selective Photoinduced Antibacterial Activity of Amoxicillin-Coated Gold Nanoparticles: From One-Step Synthesis to in Vivo Cytocompatibility. ACS Omega 2018, 3 (1), 1220–1230.

(59) Schweitzer, C.; Scaiano, J. C. Selective Binding and Local Photophysics of the Fluorescent Cyanine Dye PicoGreen in Double-Stranded and Single-Stranded DNA. Phys. Chem. Chem. Phys. 2003, 5 (21), 4911.

(60) Walczysko, P.; Kuhlicke, U.; Knappe, S.; Cordes, C.; Neu, T. R. In Situ Activity of Suspended and Immobilized Microbial Communities as Measured by Fluorescence Lifetime Imaging. Appl. Environ. Microbiol. 2008, 74 (1), 294–299.

(61) Hollaender, A. Effect of Long Ultraviolet and Short Visible Radiation (3500 to 4900Å) on Escherichia Coli. J. Bacteriol. 1943, 46 (6), 531–541.

(62) Ramabhadran, T. V. Effects of Near-Ultraviolet and Violet Radiations (313–405 Nm) On DNA, RNA, and Protein Synthesis In E. Coli B/r: Implications For Growth Delay. Photochem. Photobiol. 1975, 22 (3–4), 117–123.

(63) Miwa, T.; Takimoto, Y.; Hatamoto, M.; Kuratate, D.; Watari, T.; Yamaguchi, T. Role of Live Cell Colonization in the Biofilm Formation Process in Membrane Bioreactors Treating Actual Sewage under Low Organic Loading Rate Conditions. Appl. Microbiol. Biotechnol. 2021, 105 (4), 1721–1729.

(64) Rowlett, V. W.; Mallampalli, V. K. P. S.; Karlstaedt, A.; Dowhan, W.; Taegtmeyer, H.; Margolin, W.; Vitrac, H. Impact of Membrane Phospholipid Alterations in Escherichia Coli on Cellular Function and Bacterial Stress Adaptation. J. Bacteriol. 2017, 199 (13).

(65) Gupta, R.; Modak, J. Bacterial Lysis via Photocatalysis - A Critical Mechanistic Review. ChemCatChem 2020, 12 (8), 2148–2170.

(66) Foster, H. A.; Ditta, I. B.; Varghese, S.; Steele, A. Photocatalytic Disinfection Using Titanium Dioxide: Spectrum and Mechanism of Antimicrobial Activity. Appl. Microbiol. Biotechnol. 2011, 90 (6), 1847–1868.

(67) Zhang, X.; Wang, L.; Levänen, E. Superhydrophobic Surfaces for the Reduction of Bacterial Adhesion. RSC Adv. 2013, 3 (30), 12003.

(68) Flemming, H.-C.; Neu, T. R.; Wozniak, D. J. The EPS Matrix: The “House of Biofilm Cells.” J Bacteriol. 2007, 189 (22), 7945–7947.

(69) Davies, D. Understanding Biofilm Resistance to Antibacterial Agents. Nat. Rev. Drug Discov 2003, 2 (2), 114–122.

(70) Hausner, M.; Wuertz, S. High Rates of Conjugation in Bacterial Biofilms as Determined by Quantitative In Situ Analysis. Appl. Environ. Microbiol. 1999, 65 (8), 3710–3713.

(71) Chanquia, S. N.; Valotta, A.; Gruber-Woelfler, H.; Kara, S. Photobiocatalysis in Continuous Flow. Front. catal. 2022, 1.

(72) Loubière, K.; Oelgemöller, M.; Aillet, T.; Dechy-Cabaret, O.; Prat, L. Continuous-Flow Photochemistry: A Need for Chemical Engineering. Chem. Eng. Process. Process Intensif 2016, 104, 120–132.

(73) Marinho, B. A.; Cristóvão, R. O.; Djellabi, R.; Caseiro, A.; Miranda, S. M.; Loureiro, J. M.; Boaventura, R. A. R.; Dias, M. M.; Lopes, J. C. B.; Vilar, V. J. P. Strategies to Reduce Mass and Photons Transfer Limitations in Heterogeneous Photocatalytic Processes: Hexavalent Chromium Reduction Studies. J. Environ. Manage. 2018, 217, 555–564.

## 4.3 Pre-submission Version of Supporting Information

# Supporting information

## Investigating the Antibacterial Performance of Supported $TiO_2$ on Glass wool fibres: Challenges and Optimization Strategies

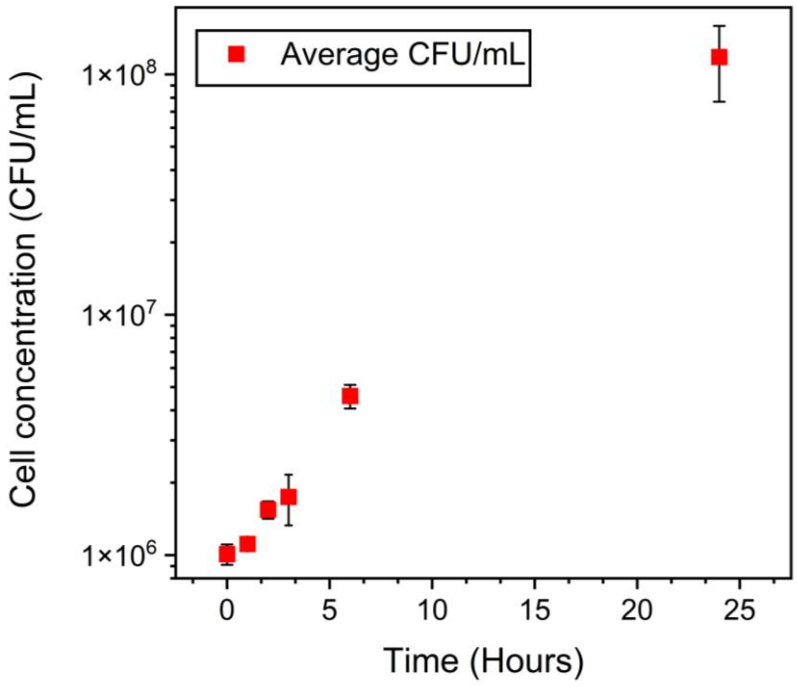


**Figure 4.3.1** Viable *E. coli* cells count for the control sample (dark control) incubated under the same conditions of the treatments but without catalyst and protected from light. The initial bacterial inoculum was $1x10^6$ CFU/mL in 5 % LB in PBS. Viables were incubated without agitation at room temperature, but due to the light exposure, the ambient temperature close to the light source was 34 °C after 24 hours. Viable cells were determined by plate counting colony forming units (CFU) and results were expressed as CFU/mL. Those viable bacterial counts were utilized to calculate log reduction for the treatment samples

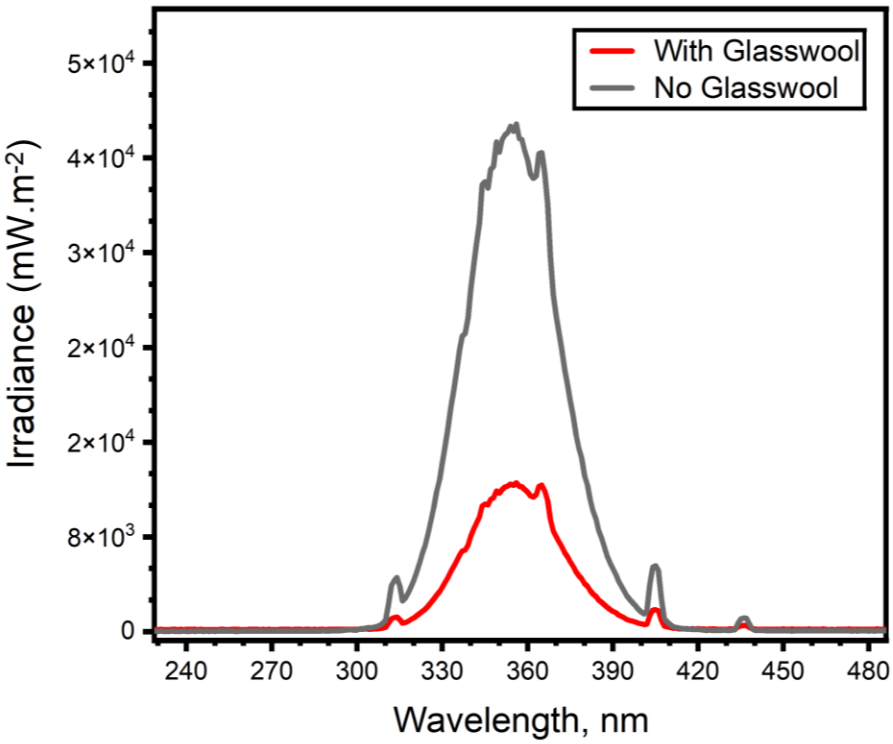


**Figure 4.3.2.** Emission spectra of the UVA bulb used in this work. Irradiance was measured after light was passed through the glass vial containing LB 5 % without glass wool (grey) and with 10 mg/mL of GW (red).

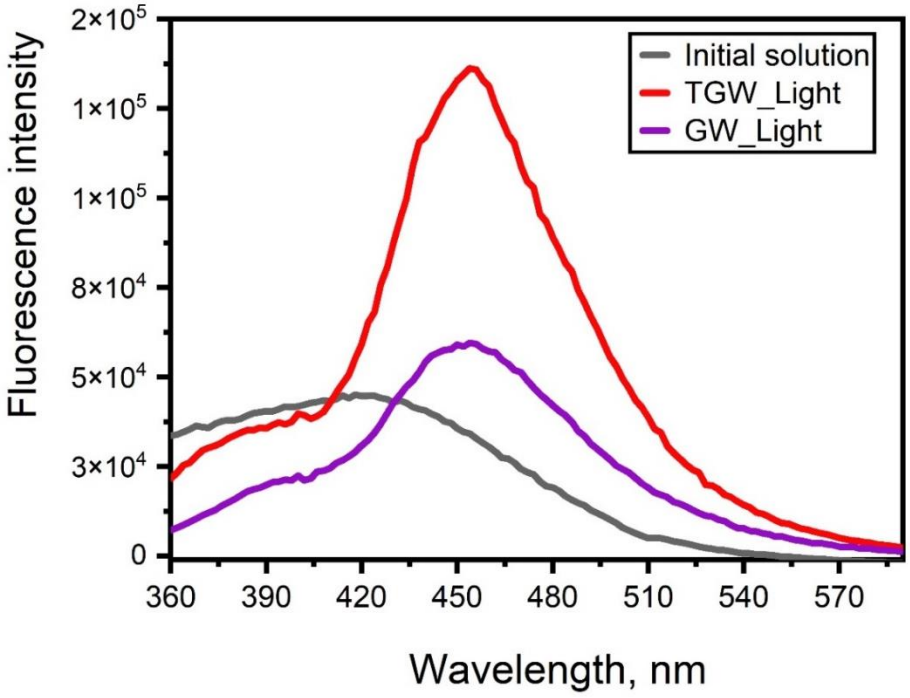


**Figure 4.3.3** Fluorescence emission spectra of a 0.25 mmol solution of coumarin in LB 5% (pH 3.0) before (grey) and after UVA irradiation for 24 hours with 10 mg/mL of $TiO_2$@glasswool (Red) and APTES-Treated glass wool (purple). The peak at 454 nm (ex: 340 nm) is indicative of the formation of 7-hydroxycoumarin (7-HC).

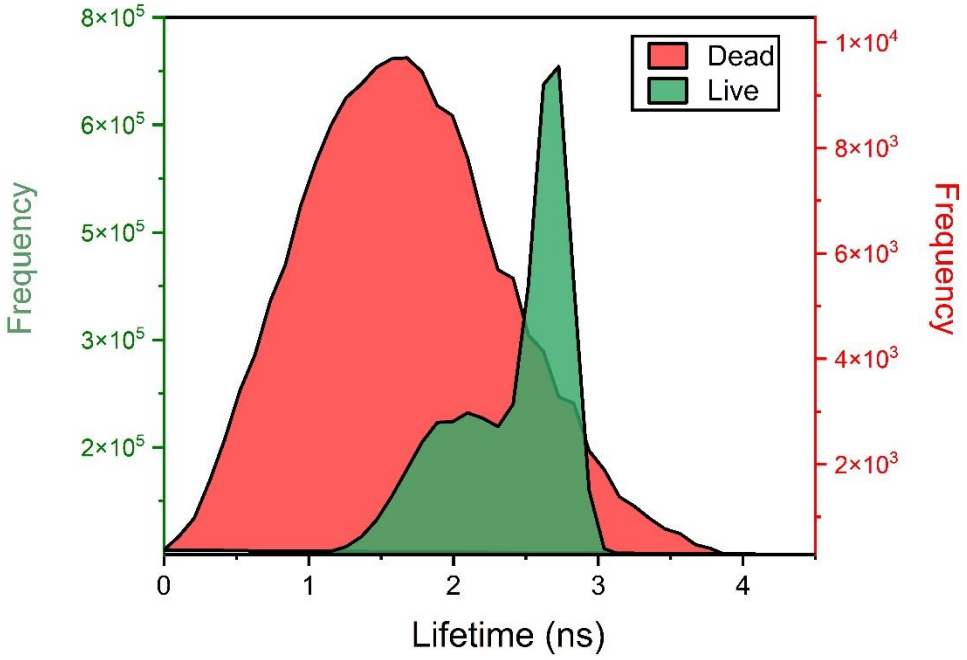


**Figure 4.3.4** Histograms of fluorescence lifetime distribution on samples containing Live *E. coli* (Green) and dead bacteria (red). Bacteria concentration was set to $OD_{600}$=0.1 in 5% LB. Dead cells were obtained by heating the bacterial solution, and the absence of viable bacteria was confirmed via plate counting.

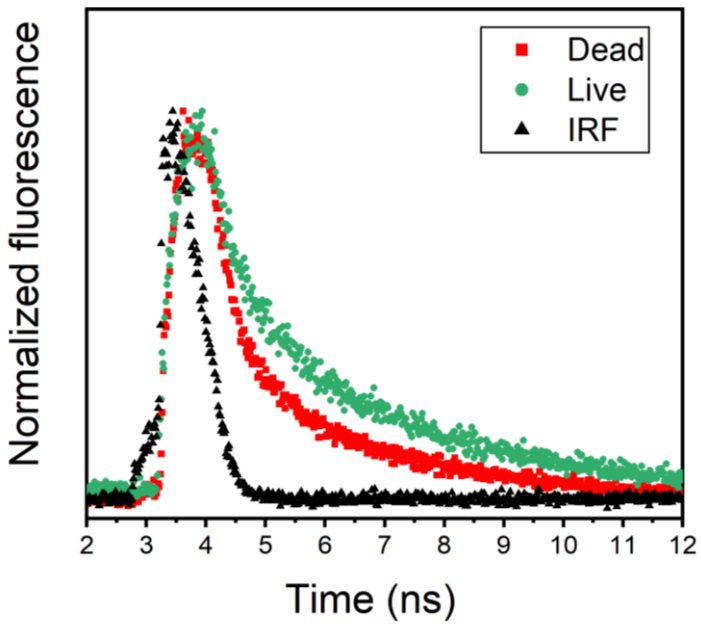


**Figure 4.3.5** Average TSCPC curves for samples containing live *E. coli* (green) and dead bacteria (red), and the Instrument response function (IRF) (black). Bacteria concentration was set to $OD_{600}$=0.1 in 5% LB. Dead cells were obtained by heating the bacterial solution, and the absence of viable bacteria was confirmed via plate counting.

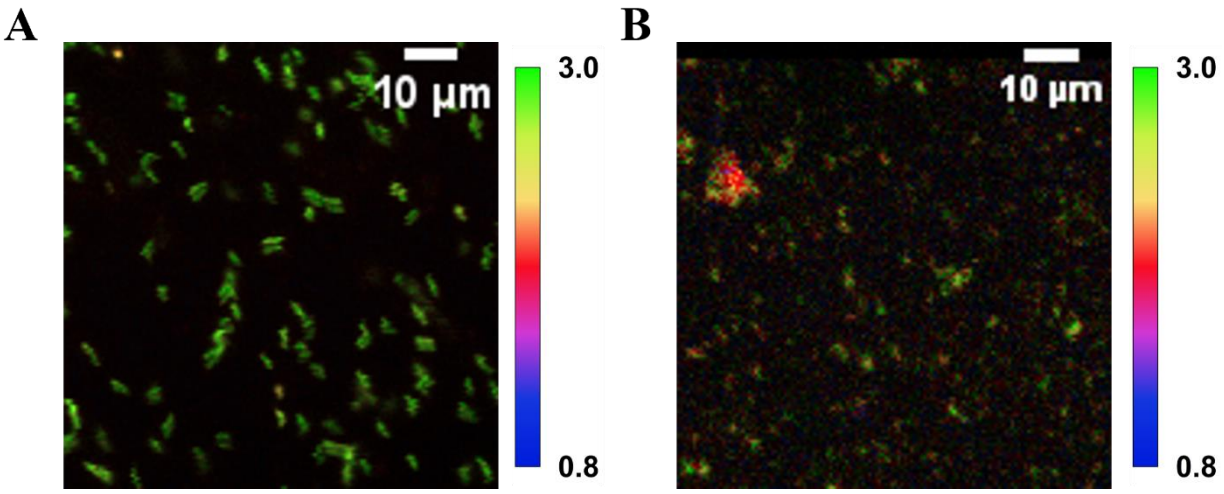


**Figure 4.3.6** Example of FLIM images of samples containing live (A) and dead (B) *E. coli* cells. Bacteria concentration was set to $OD_{600}$=0.1 in 5% LB. Dead cells were obtained by heating the bacterial solution, and the absence of viable bacteria confirmed via plate counting. Different colours represent various lifetimes of the dye, excited at 485 nm. The colour bar scale ranges from 0.8 to 3 ns. The brightness of the images was enhanced by 20% to ensure all FLIM data is clearly visible.

**Table 4.3.1** Average lifetime ($\tau_{average}$) calculated from the ROI from the treatment images shown in the main text. The total lifetime for each treatment was calculated as an average of 15 ROIs. Different lifetimes were calculated for cells found in solution from the ones found in close contact with the glass wool (Or TGW).

| Sample | Treatment Time (hours) | Location | $\tau_{average}$ (ns) | Standard deviation |
|---|---|---|---|---|
| Control Live | NA | Solution | 2.8 | 0.4 |
| Control Dead | NA | Solution | 2.3 | 0.6 |
| Initial Solution | 0 | Solution | 2.8 | 0.4 |
| Control Dark | 3 | Solution | 2.6 | 0.4 |
| Control Dark | 24 | Solution | 2.4 | 0.4 |
| Control + Light | 3 | Solution | 2.3 | 0.8 |
| Control + Light | 24 | Solution | 2.1 | 0.5 |
| Glass Wool Dark | 3 | Solution | 2.4 | 0.5 |
| Glass Wool Dark | 3 | Glass Wool | 2.2 | 0.4 |
| Glass Wool Dark | 24 | Solution | 2.5 | 0.6 |
| Glass Wool Dark | 24 | Glass Wool | 2.6 | 0.5 |
| Glass Wool + Light | 3 | Solution | 2.5 | 0.2 |
| Glass Wool + Light | 3 | Glass Wool | 2.2 | 0.4 |
| Glass Wool + Light | 24 | Solution | 2.9 | 0.6 |
| Glass Wool + Light | 24 | Glass Wool | 2.0 | 0.6 |
| TiO2@GW Dark | 3 | Solution | 2.6 | 0.5 |
| TiO2@GW Dark | 3 | Glass Wool | 2.5 | 0.4 |
| TiO2@GW Dark | 24 | Solution | 2.9 | 0.6 |
| TiO2@GW Dark | 24 | Glass Wool | 2.4 | 0.6 |

| | | | | |
|---|---|---|---|---|
| TiO2@GW + Light | 3 | Solution | 2.3 | 0.3 |
| TiO2@GW + Light | 3 | Glass Wool | 2.5 | 0.4 |
| TiO2@GW + Light | 24 | Solution | 2.1 | 0.5 |
| TiO2@GW + Light | 24 | Glass Wool | 2.5 | 0.6 |

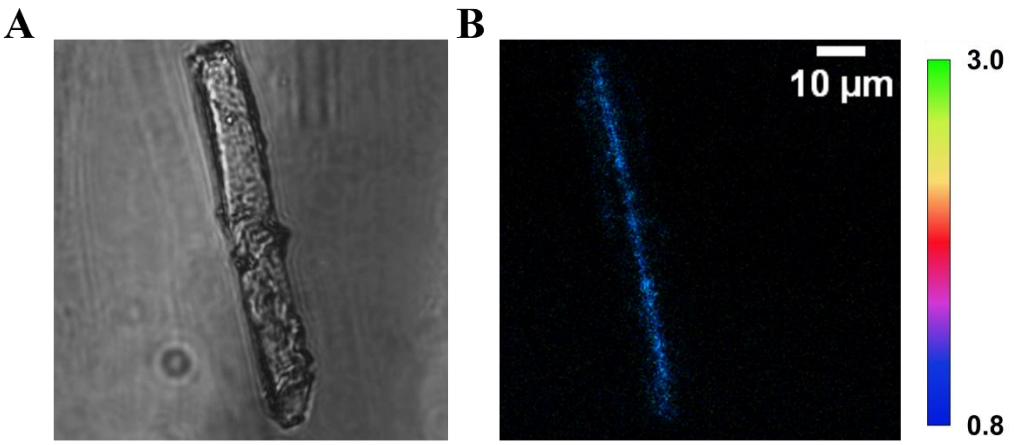


**Figure 4.3.7** Representative images of $TiO_2$@GW in 5% LB without SYTO9. (A) White light microscope and (B) Fluorescence lifetime image (ex: 485 nm). Different colours represent various lifetimes of the dye, excited at 485 nm. The colour bar scale ranges from 0.8 to 3 ns. The brightness of the images was enhanced by 20% to ensure all FLIM data is clearly visible.

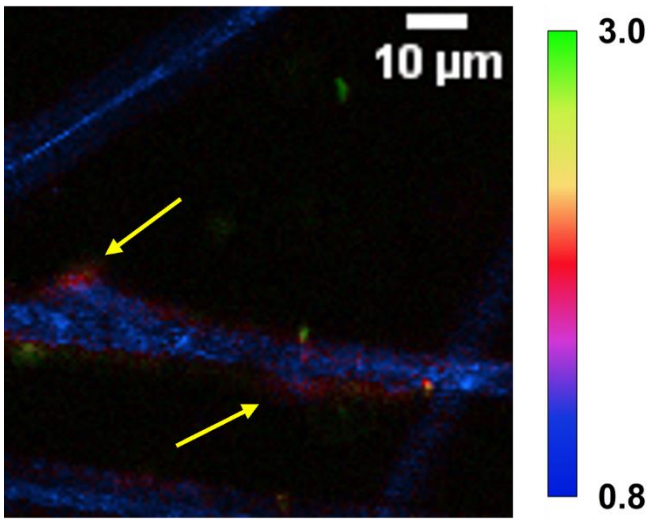


**Figure 4.3.8** Representative FLIM image of $TiO_2$@GW sample irradiated with UVA light for 24 hours. Yellow arrows show lifetimes shorter than the ones for live cells on the catalyst surface. Initial *E. coli* concentration was set at $10^6$ CFU/mL in 5% LB in PBS. Different colours represent various lifetimes of the dye, excited at 485 nm. The colour bar scale ranges from 0.8 to 3 ns. The brightness of the images was enhanced by 20% to ensure all FLIM data is clearly visible.

## 4.4 Accompanied Chapter 4

The discussion in this chapter began with disappointing results. However, through a closer examination of the system, we identified gaps in the testing of supported photocatalysts. Most of the published reports tend to focus on overall photocatalytic activity without thoroughly addressing the limitations of these systems or how to overcome them. We saw our preliminary results as an opportunity to contribute to the field by using our experiments to highlight and discuss these limitations.

Some of the parameters described here are now being tested and discussed within our research group to improve our developed photocatalysts. Key aspects include testing continuous flow systems for bacterial inactivation, increasing aeration in both batch and flow systems, and experimenting with different supporting materials besides glass to enhance the optical properties of our materials.

# 5. Magnetic catalyst for efficient One-Pot Synthesis of Schiff Bases from Benzyl Alcohol and Nitro Compounds under UV irradiation

This chapter is adapted from a final manuscript submitted to *Catalysts*. The final published version may have small differences.

## 5.1 Preamble to Chapter 5

The following chapter expands on the applicability of iron and titanium nanomaterials in the field of photocatalysis. In this chapter, a novel hybrid $Fe_3O_4$@$TiO_2$ nanomaterial was fabricated and tested for the synthesis of Schiff bases, which are crucial chemicals for the pharmaceutical and agricultural industries, forming the core of several important molecules. The current synthesis of Schiff bases involves coupling carbonyl groups with primary amines. To make the process more economical, it is desirable to use more readily available and affordable precursors. Therefore, we explored various catalysts for the synthesis of imines using benzyl alcohol and nitrobenzene as reagents. Comparing $TiO_2$-based catalysts, we found that the new magnetic $TiO_2$ was a highly effective alternative to expensive and at-risk metals such as palladium and ruthenium which are commonly used.

After individually investigating the properties and applications of titanium and iron-based nanomaterials, we decided to combine those two transition metals in a hybrid nanoparticle. Based on the knowledge previously developed from the synthesis of magnetic iron oxides and on the properties of $TiO_2$, we then developed a magnetic $TiO_2$ material, via a simple synthetic route, and that resulted in a material that combines the exceptional photo reactivity of $TiO_2$ with the magnetic properties of $Fe_3O_4$, creating a promising photocatalyst for organic synthesis. We tested the catalytic property of this material on the synthesis of Schiff bases, which are essential compounds from the synthesis of several commercial molecules. Traditionally, Schiff bases are formed from the condensation of aldehydes (or ketones) with primary amines. However, carbonyl and amino compounds are generally produced from the corresponding alcoholic and nitro compounds via

transition metal-based oxidants/catalysts, often relying on heavy metals. We believed that our developed catalyst could provide an affordable and sustainable alternative to synthesize Schiff bases directly from alcohol and nitro compounds in one pot, further reducing the number of required synthetic steps.

We began by testing several $TiO_2$-based catalysts to determine if they could selectively form the desired Schiff base. Using UVA irradiation (370 nm), we found that among the tested catalysts, $Fe_3O_4$@$TiO_2$ performed comparably to others, with the added advantage of being magnetic. Optimizing its catalytic performance demonstrated that, at longer irradiation times, the magnetic catalyst outperformed materials like P25. Within the first six hours of irradiation, we observed a high production rate of 6.8 mmol $h^{-1}$, significantly superior to those reported in the literature, and after 20 hours, Schiff base production yields exceeded 99%. Through a series of optimization reactions, we aimed to understand the catalytic mechanism. The catalytic process likely involves the photoexcitation of $TiO_2$ with UVA, generating hot electrons that are transferred to magnetite, enhancing the $Fe^{3+/}Fe^{2+}$ cycling. Upon $Fe^{3+}$ regeneration the released electron is accepted by the nitrobenzene accelerating the conversion to aniline conversion. The excess benzyl alcohol helped trapping the photogenerated hole which has enough energy to oxidase the alcohol precursors into the aldehyde product. Understanding the catalytic mechanism can help us optimize our catalytic conditions and further implement our new green catalysts.

### 5.2 Submitted Manuscript

This manuscript was submitted for publication

**ABSTRACT**

The versatility and significance of imines (Schiff bases) make them highly attractive for various industrial applications. Achieving high production rates using readily available and inexpensive reagents is crucial for optimizing production. This study investigates photocatalytic routes for the one-pot synthesis of Schiff bases using alcohol and an aromatic nitro compound as reagents. Utilizing photoirradiation at 370 nm with $TiO_2$ loaded with various metals, we demonstrate exceptional efficiency in the one-pot synthesis of Schiff bases under an inert

atmosphere. Notably, our newly developed $Fe_3O_4$@$TiO_2$ magnetic catalyst offers an excellent option for synthesizing the corresponding imine (N-benzylamine), achieving a remarkable production rate of 6.8 mmol $h^{-1}$ during the first 6 hours of irradiation, and reaching over 99% yield after 20 hours. This success is attributed to a series of catalytic reactions involving the photocatalytic oxidation of benzyl alcohol to benzaldehyde and the simultaneous *in situ* reduction of nitrobenzene to aniline. Subsequent catalytic condensation of these products, facilitated by the active sites at the $TiO_2$-metal interface, ultimately yields the desired imine. The magnetic catalytic system exhibits outstanding performance, representing a promising alternative for sustainable and efficient chemical transformations. Besides this, its magnetic properties confer an advantage in separation processes, enhancing efficiency, and substantially decreasing processing times.

## INTRODUCTION

Schiff bases are condensation products of primary amines with carbonyl compounds like aldehydes or ketones.[1] Its common structural feature is the azomethine (imine) group with a general formula of RN=CR' (R' ≠ H) where R and R' can be alkyl, aryl, or heterocyclic groups which can be substituted in various ways. The term Schiff base originates from Hugo Schiff, a German chemist, who in 1864 reported the first synthesis of imines and introduced a new class of organic compounds.[2,3]

These organic compounds are extensively used in different fields, and they serve multiple purposes such as dyes, catalysts, and intermediate species in organic synthesis. They can even work as polymer photostabilizers providing very good long-term stability for Polyvinyl Chloride (PVC) films through UV absorption or screening, peroxide decomposition, and radical scavenging mechanisms.[4] These compounds have also demonstrated diverse biological activities including antibacterial and antifungal activities, for example, Jarrahpour *et al*.[5] confirmed a moderate activity against tested gram-positive bacteria *Staphylococcus aureus* when using an azo Schiff base such as 2-hydroxy-3-methoxy-5 (4-methoxyphenylazo)benzaldehyde, while de Souza *et al*.,[6] proved effectiveness against *Mycobacterium tuberculosis* H37Rv, exhibiting a minimum inhibitory concentration (MIC) value of 8 μg/mL when using a Schiff base such as N-(salicylidene)-2-

hydroxyaniline. On the other hand, a wide range of Schiff bases have been evaluated as adaptable ligands capable of coordinating a range of metal ions across various coordination geometries and oxidation states and some metal complex derivatives of 2N-salicylidene-5-(p-nitrophenyl)-1,3,4-thiadiazole (HL) with Co(II), Pd(II), Rh (III) and Au (III) ions, respectively, showed moderate activity against *Staphylococcus aureus*, *Salmonella typhi*, and *Escherichia coli* strains and a slightly higher activity compared to the ligand HL *per se*.[7]

This versatility extends their applicability not only as effective antibacterial agents but also as catalysts in various homogeneous, heterogeneous reactions, Heck reaction, Henry reaction, carbonylation reaction epoxidation reactions,[8] among others. Therefore, it is clear that the discovery of Schiff bases opened up opportunities across a broad spectrum of scientific disciplines. Furthermore, in different scientific reports,[9,10] Schiff bases can be synthesized through simple and versatile methods, such as the condensation reaction between primary amines and carbonyl compounds, wherein specifically, there is a nucleophilic addition of the $NH_2$ group from the amine (B) compound to the C=O of the aldehyde or ketone (A), resulting in the creation of a hemiaminal[11] compound (C) under reflux conditions, while simultaneously eliminating water. Subsequently, dehydration occurs, leading to the production of an imine (compound D) as shown in Scheme 5.2.1:

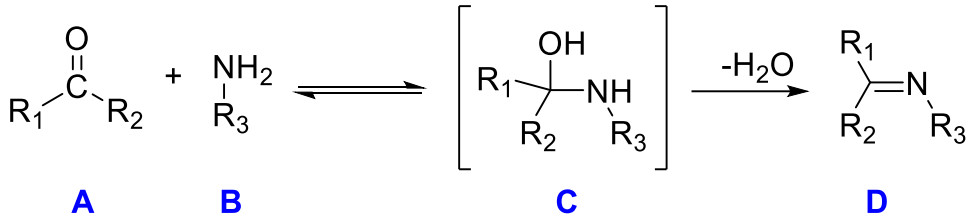


**Scheme 5.2.1.** Thermal Schiff Base synthesis

However, as widely acknowledged, many traditional organic transformations and syntheses involve high temperatures and sometimes, high pressures, resulting in considerable energy consumption and environmental harm. Consequently, it is essential to seek cleaner and more efficient organic synthesis methods as alternatives to conventional industrial practices. Photocatalysis has emerged as a promising technique, garnering widespread interest for its

potential contributions to clean energy generation and environmental remediation. Photocatalytic synthesis of imines has been explored using homogenous catalysts, for instance, Saranya *et al.*,[12] showed an efficient catalytic approach for the selective synthesis of imines (yields between 30-90%) in air at room temperature using diruthenium(II) complexes $[(\eta 6\text{-p-cymene})_2Ru_2Cl_2(\mu\text{-L})]$ as a catalyst, 4-methoxybenzyl alcohol and p-anisidine as starting materials. Using heterogenous $Pt@TiO_2$, Shiraishi *et al.*[13] observed yields of up to 84 % for N-benzylideneaniline using $Pt@TiO_2$ using benzyl alcohol and aniline as initial substances. As noticed from these reports, the initial reactants are primary amines and alcohols. Specifically, the utilization of anilines as substrates raises concerns due to their susceptibility to autooxidation.[14] Although this will depend on the chemical stability of the arylamine and other substitutions on the benzene ring. An alternative approach involves employing nitroarenes as reactants, culminating in a one-pot synthesis of imines via the oxidative coupling of an alcohol and a nitroarene. This method uses stable and cost-effective reactants while reducing the required synthetic steps.

This approach was previously reported by Selvam *et al.*[15] who observed the production of Schiff bases from the photoirradiation ($\lambda = 300$ nm) of $TiO_2$ loaded with Pd nanoparticles (2 wt%) in an aqueous solution of benzyl alcohol and nitrobenzene at room temperature for 4h. However, due to the strong hydrogenation ability of palladium, the products had higher selectivity towards secondary amines.[16] At this point, it is essential to recognize that even though Pd nanomaterials are widely used as efficient catalyst materials owing to their high specific surface area, abundant active sites, and superior catalytic activity, their continuous use raises concerns about their environmental impact.[17] Despite their valuable catalytic and optical properties, the increasing exposure of Pd nanomaterials to the ecological environment poses challenges.[17]

Similarly, Wu et *al.*,[18] reported a one-pot reaction utilizing $Cd_xZn_{1-x}S$ as a catalyst. Under visible light, the authors observed a maximum Schiff base yield of 55.2% after 4h. Nevertheless, these reactions were done under high $N_2$ pressure and with a large catalyst loading (6 mg/mL), which reduces the feasibility of scaling up Schiff base production. Despite this, unlike Pd, the utilization of Cadmium in such syntheses, while yielding decent results, raises concerns due to its inherent toxicity, posing substantial risks to both human health and the environment. Consequently, as highlighted by these scientific reports, the metals employed in these

investigations not only contribute to environmental degradation but also exacerbate the precarious status of certain metals, which are increasingly vulnerable to depletion. For example, Hayes *et al.*,[19] demonstrated in their study that elements such as C, Mg, Ca, Sc, Co, Ge, Sb, Cs, and Pd, among others, have a percentage critically higher than 60% and have a supply chain that is vulnerable to disruption. These elements serve an essential function in the manufacturing of different products, and thus their absence would have significant consequences. Thus, it becomes imperative to explore alternative materials.

To develop better environmentally friendly alternatives, we propose exploring the photocatalytic activity of four $TiO_2$-based heterogeneous catalysts for the synthesis of Schiff bases. We chose widely used photocatalysts such as P25 and Pd@$TiO_2$ and compared their activity with new alternatives involving first-row transition metals like Fe and Cu on $TiO_2$ ($Fe_3O_4$@$TiO_2$ and Cu@$TiO_2$). Aiming at practical industrial applications and greener alternatives, we tested our catalysts in a one-pot approach for the synthesis of imines, starting from nitrobenzene and benzyl alcohol. Our initial efforts showed that $Fe_3O_4$@$TiO_2$ exhibits similar activity to Pd@$TiO_2$ and $TiO_2$ catalysts. Considering the experimental results, along with concerns about element depletion and the environmental impact of certain chemicals, iron presents itself as a viable option. Additionally, $Fe_3O_4$ nanoparticles exhibit superparamagnetism, enabling magnetic separation in the presence of a magnetic field. The reactions were driven using UVA irradiation, the spectral region largely absorbed by $TiO_2$. We also measured the time profile evolution of the reaction, showing production rates of up to 6.8 mmol/h, which is more than ten times higher than previously reported. These findings suggest that the reaction conditions are ideal for scaling up.

## EXPERIMENTAL DETAILS

All chemicals were purchased from Sigma Aldrich and used as received unless otherwise stated. $TiO_2$ P25 was purchased from Univar Canada.

## Catalyst Synthesis

**$Fe_3O_4$@$TiO_2$:** Magnetic $TiO_2$ NPs were synthesized by in situ precipitation of $Fe_3O_4$ on $TiO_2$ NPs. In brief, a 0.32 mg/mL aqueous solution of commercial P25 was added to a 3-neck round bottom flask. To this solution, 0.056 g of $Fe(NO_3)_3 \cdot 9H_2O$ and 0.032 g of $Fe(SO_4) \cdot 7H_2O$ were added, to obtain a proportion of 2:1 of Fe (III) to Fe(II). The solution was purged for 10 min and then heated at 85°C and kept at this temperature for 10 min under $N_2$ flow, to equilibrate the temperature. To this solution, 360 µL of $NH_4^+$ was added dropwise and the resulting dark solution was kept under $N_2$ for another 10 min. The resulting material was separated using an external magnet washed five times with Milli-Q water and dried under vacuum.

**Pd@$TiO_2$:** Based on a reported synthesis.[20] Approximately 15 mg of metal precursor salt ($PdCl_2$) was mixed with $TiO_2$ (~500 mg) in 150 mL of Milli-Q water and sonicated for 20 min. The slurry was irradiated in a Luzchem photoreactor equipped with 14 UVA bulbs for 24 h with vigorous stirring in a crystallizing Pyrex® dish with a Pyrex® cover. The slurry was centrifuged and washed with Milli-Q water four times to remove unreacted metal precursor salt and dried overnight in a desiccator under vacuum. The obtained powder had a dark grey color.

**Cu@$TiO_2$:** Based on a reported synthesis.[20] A total of 55 mg of $CuCl_2 \cdot 2H_2O$ were mixed with $TiO_2$ (~300 mg) and 95 mg of the benzoin-type photoinitiator Irgacure-2959 in 130 mL of Milli-Q water and purged with argon for 15 min. After this, the slurry was irradiated in a Luzchem photoreactor equipped with 14 UVA bulbs for 24 h with vigorous stirring. The slurry was filtered and washed with Milli-Q water at least seven times to remove unreacted metal precursor salt and dried overnight in a desiccator under vacuum. The powder had an intense beige colour with green tones.

## Catalyst Characterization

Transmission electron microscopy (TEM) images were collected on a JEM2100F FETEM (JEOL) operating at 200 kV. Diffuse reflectance measurements were carried out using an Agilent Cary 7000 UV-Vis-NIR Universal Measurement Spectrophotometer coupled with an Agilent praying Mantis accessory. The metal composition of the materials was determined by Inductively Coupled Plasma Optical Emission Spectrometry (ICP-OES), using an Agilent Vista Pro ICP

Emission Spectrometer. Approximately 10 mg portions were accurately weighed in triplicate and digested with *aqua regia*. Solutions were further diluted and measured by ICP-OES. The following emission lines were used for quantification when applicable: Fe 238.20 nm, Pd 340.45 nm, and Cu 327.39 nm. Powder X-ray diffraction analysis was carried out at room temperature utilizing a Bruker D8 Endeavor Polycrystalline X-Ray Diffractometer (PXRD) in Bregg Brentano geometry, using Cu Kα radiation (λ = 1.5418 Å), powered at 40 kV and 25 mA (1kW). Diffractograms were collected by a LynxEye XE-T 1-D silicon strip detector with 192 channels, with 2θ range from 20° to 90°.

**Photocatalytic activity**

The photocatalytic performance of the synthetized catalysts was performed by adding 5 mL of fresh solution of nitrobenzene (0.1 M) in benzyl alcohol in a Pyrex glass tube, loaded with 10 mg of the catalyst. The solution was sonicated and purged for 10 min with $N_2$. Irradiation was done using a UVA LED (λ=370 nm) with an irradiance power of 13.5 $mW.cm^{-2}$ (Figure 5.3.1.). Samples were irradiated and stirred for up to 6 h. The catalysts were removed using a hydrophilic PTFE syringe filter, with 0.2 μm pore size. Quantification of products was performed by mass spectrometry in an Agilent 6890-N Gas Chromatograph with an Agilent 5973 mass selective detector, 3,5-Di-tert-butyltoluene (4 mM in Dichloromethane as the solvent) as an external standard. The timed events feature was used within the setpoint control of the local user interface (OFF at 6.20 min/ON at 8.70 min) to prevent an excessive concentration of Benzyl Alcohol from reaching the detector.

**RESULTS AND DISCUSSION**

**Catalyst Characterization**

In this work, we selected four $TiO_2$-based catalysts to evaluate possible photocatalytic routes for one-pot imine synthesis. Transmission electron microscopy (TEM) was used as a powerful tool to learn more about the nanoparticles, their morphology, and spatial distribution. Figure 5.2.1 shows the TEM images of the catalysts, unveiling the distinctive spherical morphology of the nanoparticles (NPs). Upon closer examination of Figure 5.2.1, it becomes evident that the NPs were deposited onto the catalyst surface. This deposition is particularly visible

in panel B, for Pd@$TiO_2$, where the TEM image distinctly shows the presence of diminutive particles decorating the $TiO_2$ surface. The same scenario is visible for panels C and D. Previous publications in our group,[20] have shown that the mean particle size of the metallic NPs is around 3.0 ± 0.2 nm. Since the distinction between two metal-oxide in TEM is challenging due to the similar electron densities, we could not measure the diameter of the $Fe_3O_4$ over P25. However previous publications from our group, using the same synthetic route, produced NPs with diameters around 12.5 ± 3 nm.[21]

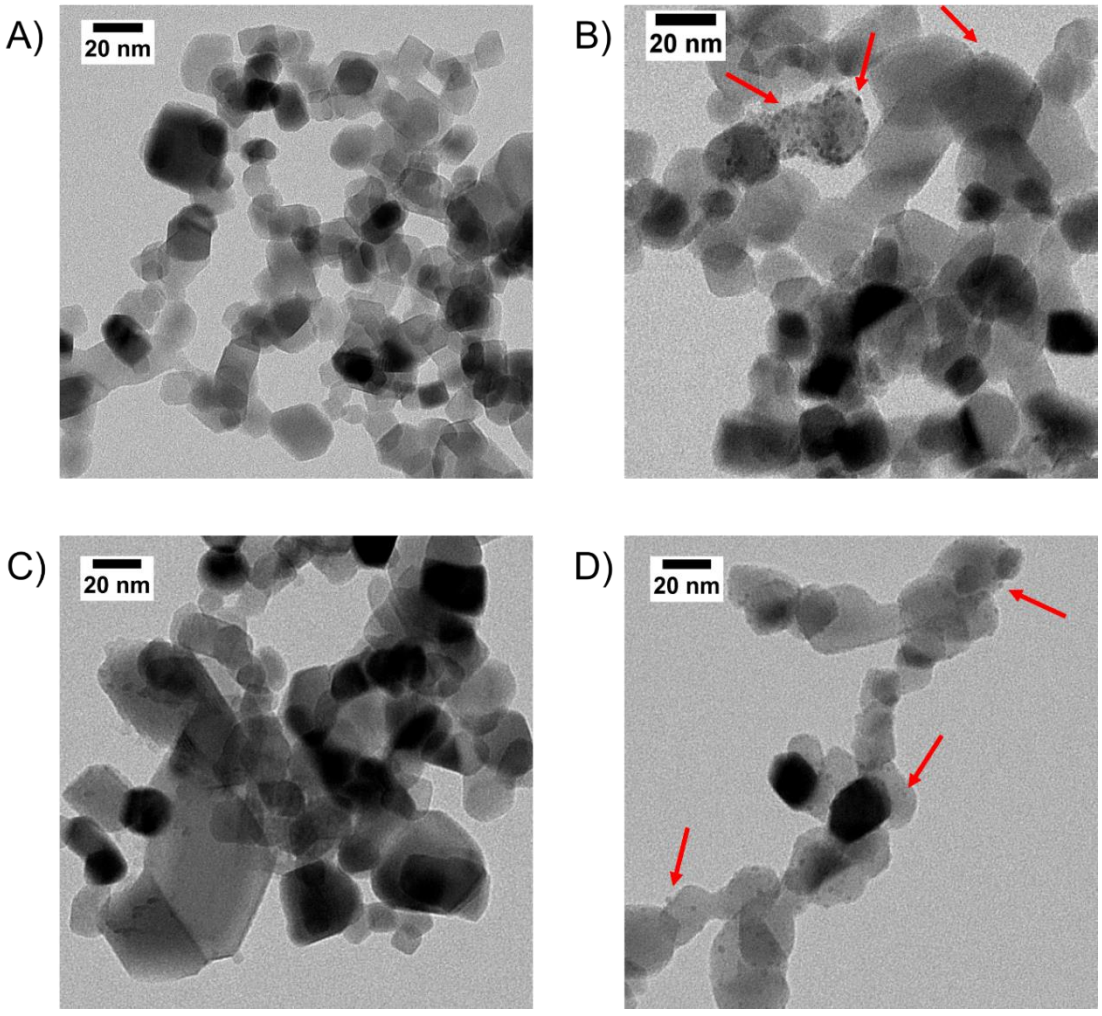


**Figure 5.2.1.** Representative TEM images of $TiO_2$ (A), Pd@TiO2 (B), $Fe_3O_4$@$TiO_2$ (C) and Cu@$TiO_2$ (D). Red arrows indicate representative Pd and Cu nanoparticles on P25. Scale bar: 20 nm.

For the bimetallic nanoparticles (NPs), metal loadings were determined using inductively coupled plasma optical emission spectroscopy (ICP-OES) analysis, as shown in Table 5.2.1. Synthesis via photo-deposition resulted in lower metal loadings of 2% and 3% for Pd and Cu, respectively. Iron oxide on $TiO_2$ was synthesized by co-precipitation on the semiconductor surface, yielding a 12% loading. The higher loading of iron oxide was intentional, aiming to explore magnetite's catalytic properties, and its magnetism, which facilitates catalyst removal. Indeed, after synthesis, $Fe_3O_4$@$TiO_2$ demonstrated a response to an external magnetic field, as shown in Figure 5.3.2.

**Table 5.2.1.** Metal loading of the three bimetallic catalysts evaluated in this work. Metal quantification was done using ICP-OES following Fe, Pd, and Cu emission lines.

| Material | Metal Loading (%) |
|---|---|
| $Fe_3O_4$@$TiO_2$ | 12 wt % (± 0.93) Fe |
| Pd@$TiO_2$ | 2.0 wt % (± 1.70) Pd |
| Cu@$TiO_2$ | 3.0 wt % (± 1.04) Cu |

Moreover, X-ray diffraction (XRD) helped us to provide insights into the crystalline structures of the synthesized materials. For our tests, P25 was the source of titanium dioxide. P25 is formed from $TiO_2$ nanoparticles, with a diameter between 10-50 nm (Figure 5.2.1A), composed of 80 % anatase and 20 % rutile phase.[22] The diffractogram of P25 (Figure 5.2.2) confirms its crystalline structure. Peaks assigned for anatase and rutile are identified as A and R, respectively, according to ICCD cards n° 01-083-5916 and 01-076-1940. In the diffractogram, for all the metal-loaded $TiO_2$ catalysts the same peaks assigned to $TiO_2$ (P25) can be identified (Figure 5.2.2). From the diffractogram of Cu@$TiO_2$, we could identify the structure of the Cuprite ($Cu_2O$) (ICCD: 96-900-7498), a cubic-shaped crystal formed from the oxidation of $Cu^0$. The diffractogram peaks assigned to $Cu_2O$ can be found at 2θ values 36.4°, 42.3°, and 61.4°, relative to the crystal planes (111), (020), and (022), respectively.

On the other hand, XRD of $Fe_3O_4$@$TiO_2$ reveals the formation of cubic magnetite ($Fe_3O_4$), according to ICCD card n° 04-009-8439, using the peaks corresponding to the planes (220), (311), (400) and (511), at 2θ values of, 29.9°, 35.3°, 43.0°, and 56.9° to detect the crystal form. As for Pd@$TiO_2$ we can observe the dominance of $TiO_2$ peaks, with the only identifiable peak for Pd being at 2θ of 40.01°, which corresponds to the (111) plane of cubic Pd (ICCD: 96-153-4922).

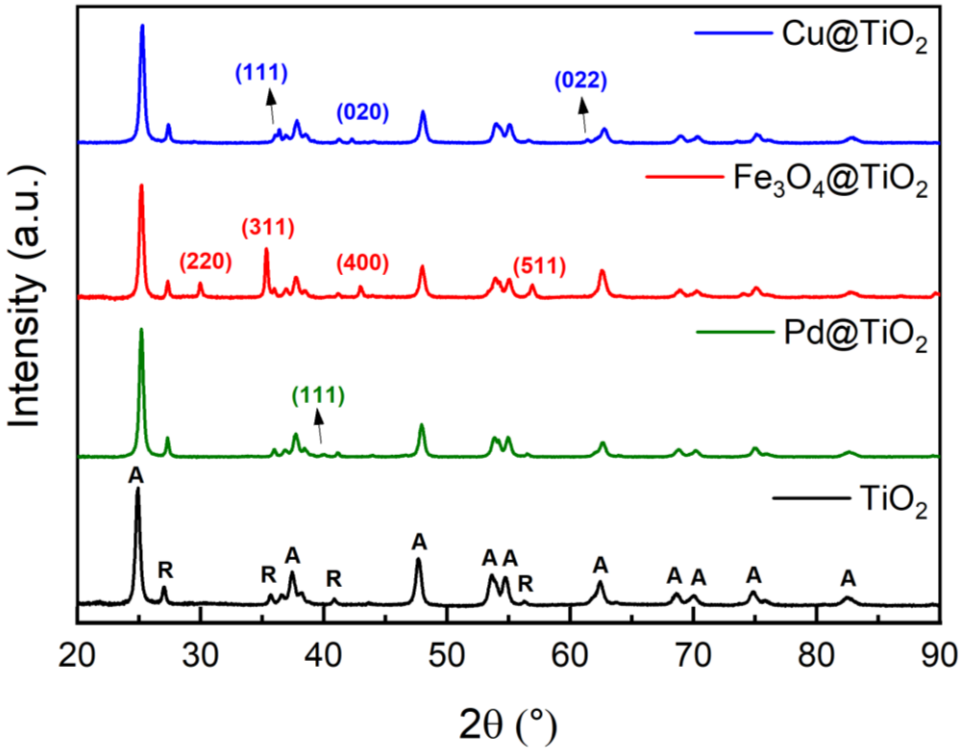


**Figure 5.2.2.** XRD patterns of the catalysts used: $TiO_2$ (P25) (black), Pd@$TiO_2$ (green), Fe@$TiO_2$ (red) and Cu@$TiO_2$ (blue). Numbers in parenthesis correspond to the characteristic (h k l) interplanar planes for each crystalline phase. A: anatase $TiO_2$ and R: rutile $TiO_2$

In addition, diffuse reflectance measurements were carried out for all the catalysts to study their optoelectronic properties. Measurements were recorded between 200 nm and 800 nm using the diffuse reflectance mode. The addition of the metal on P25 did shift the catalyst absorbance into the visible range (Figure 5.3.3), a change that is more pronounced on $Fe_3O_4$@$TiO_2$, due to the higher loading percentage.

**Selecting the Optimal Catalyst: Exploring variations for enhanced reaction performance**

At the beginning of our studies, we aimed to evaluate whether the system chosen yields imines using benzyl alcohol and nitrobenzene as reagents. Benzyl alcohol was chosen as an alkylation surrogate for aldehydes due to its cost-effectiveness. Previous research has demonstrated that an excess of benzyl alcohol enhances the reaction, thus we employed it as a solvent, facilitating potential solution reusability.[23,24]

Across all reactions, the primary products observed included benzaldehyde (BenzA), and N-Benzylideneaniline (Schiff-base). Additionally, the GCMS trace shows a few peaks at 12.21 min and 13.50 min that appeared to be contaminations as they are shown in the chromatogram before the reaction started. A representative chromatogram is depicted in Figure 5.2.3 when using $Fe_3O_4$@$TiO_2$ as the catalyst. The mass spectra of the products shown in Figure 5.2.3 can be seen in Figure 5.3.4. Specifically, a tandem process occurred wherein the nitroarene undergoes reduction to form an aromatic amine through interaction with the alcohol, concurrently oxidizing the alcohol to yield the aldehyde (BenzA). Following this process, the aldehyde (BenzA) and the amine (aniline) coupled to produce the corresponding imine (Schiff Base, N-Benzylideneaniline). The presence of BenzA demonstrates the successful oxidation of the Benzyl alcohol for all catalysts (Figure 5.3.5 - 5.3.7) and its high abundance is attributed to the chosen stoichiometry.

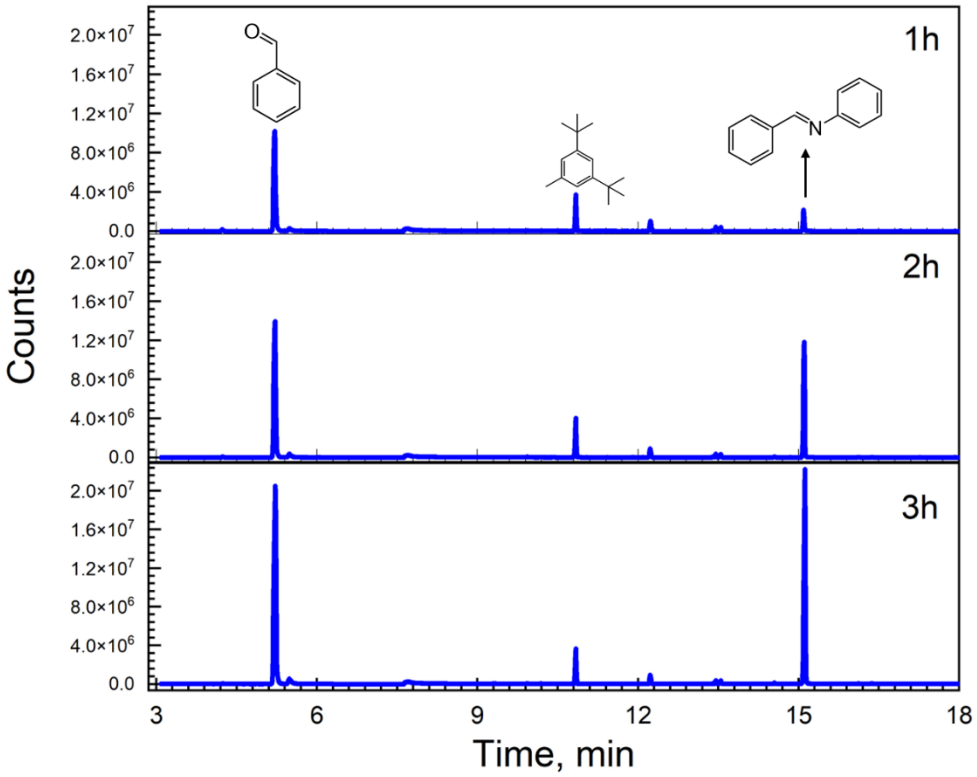


**Figure 5.2.3.** Chromatograms showing the peaks obtained after performing the reaction with nitrobenzene 0.1 M in benzyl alcohol and 10 mg of $Fe_3O_4$@$TiO_2$. 5 mL of solution was irradiated for 3h under UVA irradiation and continuous stirring. Samples were taken every hour and filtered using a PTFE syringe filter. 3,5-Di-tert-butyltoluene was used as an external standard (peak at 10.84 min) The products have the following retention times: BenzA (5.17 min), 3-Benzylaniline (3-BA) (12.21 min), Schiff Base (15.10 min). The timed events feature of the local user interface was used (Turned off at 6.20 minutes and activated at 8.70 minutes) to prevent the risk of a high concentration of Benzyl Alcohol reaching the detector.

Aniline is also one of the products, although is at low concentrations, indicating our catalysts' ability to successfully oxidize the Benzyl alcohol while reducing the nitrobenzene to aniline. In our study, gas chromatography analysis revealed a challenge in detecting the aniline peak due to its proximity to the retention time of the solvent (benzyl alcohol) when nitrobenzene was employed as the substrate. However, our subsequent experiment using 3-nitroanisole (3-NA) keeping benzyl alcohol as the solvent and $Fe_3O_4$@$TiO_2$ as the catalyst, yielded more distinct results as depicted in Figure 5.2.4. In this particular case, although *m*-anisidine was present in relatively low concentrations, was discernible in the chromatogram (retention time of 9.63 min), indicative

of our catalysts' proficiency in facilitating the oxidation of benzyl alcohol while concurrently reducing nitro compounds to amines. This observation underscores the importance of substrate selection and catalyst design in optimizing reaction outcomes, providing valuable insights for the development of efficient catalytic systems.

As evidence, Figure 5.2.4 demonstrates the continued success of this study, namely, the synthesis of the Schiff base. However, a comparison of the results depicted in Figures 5.2.3 and 5.2.4 reveals a notable distinction: following a 3-hour reaction period, the peak intensity observed when using nitrobenzene as the starting substrate is higher than that of 3-nitroanisole. This difference can be explained due to the electronic effects. In fact, when comparing the electron density contributions of the nitro group in molecules like nitrobenzene to that of the methoxy group on the aromatic ring, the electron-donating effect of the methoxy group is stronger.[25] This leads to a lower electron density around the nitro group in 3-anisole, which indicates that the electronic effect of substituents on the aromatic ring is also an important factor for reaction rates. Additionally, as stated by Hirao *et al*.,[26] analyzing the electronic structure and the distribution of electron density within the benzene ring is important to determine the reactivity of the ortho, meta, and para positions of the substituted benzene ring when being exposed to an electrophile. In this case, the presence of a methoxy group likely enhances electron density within the ring.

However, it is reasonable to think that this alteration in electron density might potentially modify the molecule's reactivity towards the electrophilic carbonyl of benzaldehyde, altering its susceptibility to form the Schiff base.

We then proceeded to compare the photocatalytic activity of four $TiO_2$-based catalysts. In our comparative analysis, we subjected the samples to irradiation for up to 3 hours and observed varying imine yields dependent on the catalysts employed. As evidenced in Figure 5.2.5, Pd@$TiO_2$ exhibited a maximum production of 26.9 mmol (27 %) after 3h of irradiation (Figure 5.2.5). Remarkably, Pd@$TiO_2$ was the only catalyst capable of yielding the fully reduced product, N-Benzylaniline. This observation is highlighted in Figure 5.3.6 where a distinct peak began to appear around 15.65 min at the 2-hour mark. This is a result of the strong hydrogenation ability of noble metals, which decreases the selectivity towards the desired imine.[15,16,27] $TiO_2$ had a similar Schiff base, producing 28.7 mmol (Figure 5.2.5). Prior publications had showcased the potential

of $TiO_2$ for the tandem imine formation from alcohols and nitroarenes.[28–30] In particular, P25 takes advantage of rutile's high photocatalytic reduction of nitrobenzene coupled with the higher concentration of Lewis acid sites on anatase which facilitates the condensation of BenzA and aniline.[28]

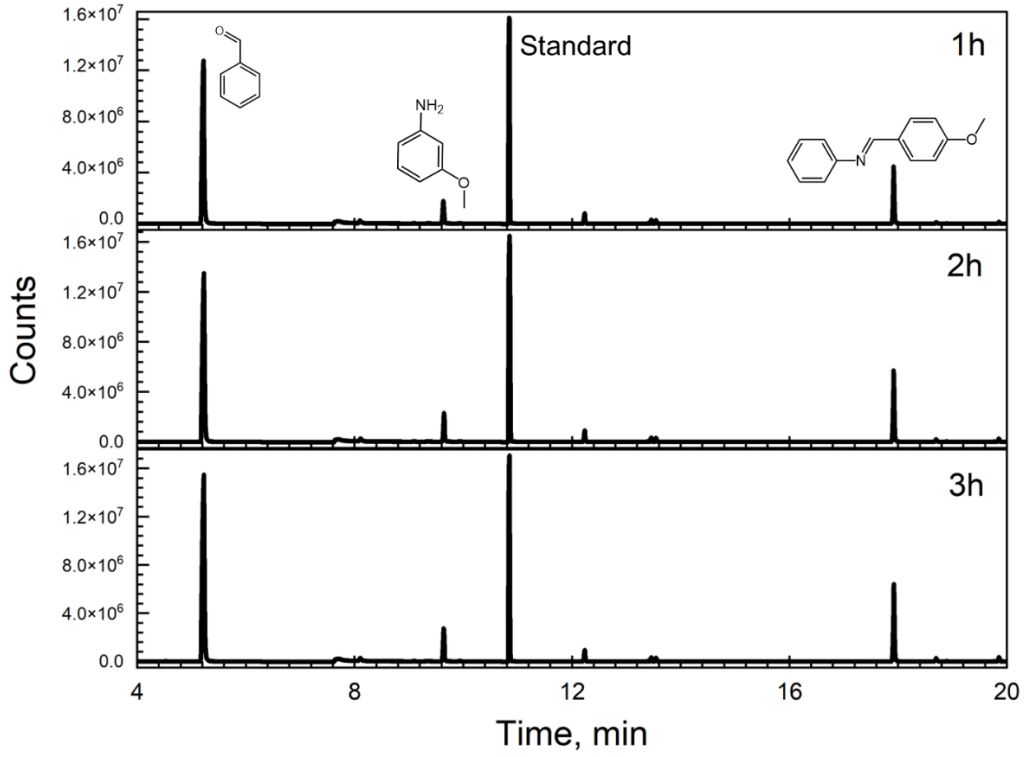


**Figure 5.2.4.** Chromatograms showing the peaks obtained after performing the reaction with 3-nitroanisole 0.1 M in benzyl alcohol and 10 mg of $Fe_3O_4$@$TiO_2$. 5 mL of solution was irradiated for 3h under UVA irradiation and continuous stirring. Samples were taken every hour and filtered using a PTFE syringe filter. 3,5-Di-tert-butyltoluene was used as an external standard (peak at 10.84 min) The products have the following retention times: BenzA (5.17 min), *m*-anisidine (9.63 min), Schiff Base N-(4-Methoxybenzylidene)aniline (17.94 min). The timed events feature of the local user interface was used (Turned off at 6.20 minutes and activated at 8.70 minutes) to prevent the risk of a high concentration of Benzyl Alcohol reaching the detector.

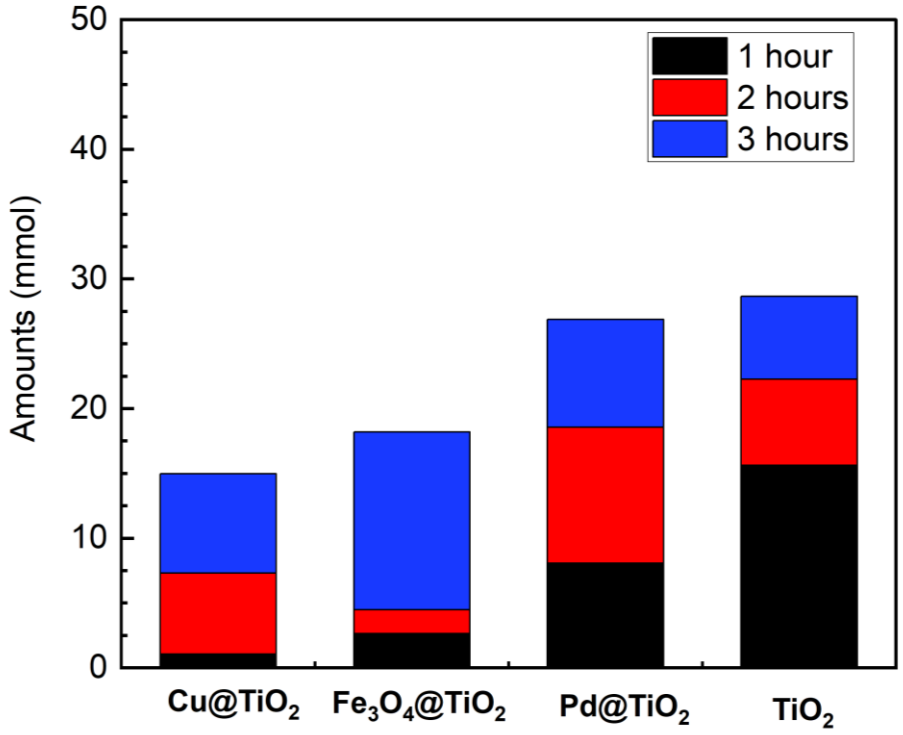


**Figure 5.2.5.** Photocatalytic performance for the selectively generated Schiff Base N-Benzylideneaniline in the coupled system of benzyl alcohol and nitrobenzene using different catalysts under UVA light irradiation for 1-3 h. Reaction conditions: benzyl alcohol (as the solvent, 5 mL), nitrobenzene (0.1 mmoles/L), M@$TiO_2$ (10 mg), under Argon, UVA light irradiation (λ= 370 nm). Schiff-base production was quantified using GC-MS.

Interestingly, the Fe and Cu-loaded catalysts exhibited a delayed onset in catalyzing conversion, evident from their low yields within the initial 2 hours, followed by a pronounced increase in yield from 2 to 3 hours. In our previous studies with Cu@$TiO_2$, we observed a similar slower catalytic rate compared to Pd-loaded $TiO_2$ in the hydrogenation of alkynes.[20] Just as with the alkynes, Cu exhibited superior control over the selectivity of the reaction, while Pd excelled in enhancing its rate. This difference highlights how various catalysts play a crucial role in controlling both the speed and specificity of chemical reactions.

Despite their slower kinetics relative to other catalysts, Cu@$TiO_2$ and $Fe_3O_4$@$TiO_2$ demonstrated substantial Schiff-base formation within a short timeframe, 15.3 and 18 mmol, respectively (Figure 5.2.5). This contrasts with previous reports utilizing Fe and Co-based

catalysts, where reaction completion often required days,[23,24] showing that the association with $TiO_2$ is beneficial to improve the yields for those catalysts. It is also noteworthy that we did not employ bases, in contrast with prior reports,[23,24,31,32] and yet achieved satisfactory yields in a short timeframe.

Based on the previous results, P25 exhibited higher yields in the synthesis of Schiff bases, however, its powdered form hinders separation processes, often requiring an extra centrifugation step. In contrast, $Fe_3O_4$@$TiO_2$ offers the distinct advantage of magnetic removal, facilitating the separation process while keeping good reaction yields. Therefore, recognizing this advantage, we have directed our efforts towards enhancing the yield of this magnetic catalyst, as its facile removal makes it an attractive candidate for scaling up applications in organic synthesis.

**Optimizing reaction conditions using $Fe_3O_4$@$TiO_2$ as a catalyst**

The first observation was that the reactions using $Fe_3O_4$@$TiO_2$ had a delayed start compared to pure $TiO_2$. Consequently, we first evaluated the Schiff base yield at longer irradiation times and compared it with $TiO_2$ alone. After running the reactions with both catalysts for 6 hours, P25 produced 36.6 mmol (Table 5.2.2, entry 2) of the Schiff base, while $Fe_3O_4$@$TiO_2$ produced 41.7 mmol base (Table 5.2.2, entry 1). This results in a Schiff base rate of 6.8 $mmol^{-1}$, which is over ten times higher than the values previously published, which has rates ranging from 4.6 μmol $h^{-1}$ to 0.34 mmol $h^{-1}$ reported[28,29,33–36] (Table 5.3.1). Noting that the magnetic catalyst performs better with extended irradiation we conducted it for 20 hours, achieving over 99% of the desired product. Thus, even with the longer irradiation time, we obtained a significantly high production rate of 4.95 mmol $h^{-1}$.

We also investigated whether the catalytic delay persisted during a second use of the catalyst. To test this, we conducted a reaction for 3 hours under UVA irradiation. After this period, 0.1 M of fresh nitrobenzene was added to the solution, which would avoid wasting the excess benzyl alcohol and the produced BenzA. The reaction was then irradiated for another three hours. Figure 5.3.10 compares the results from the first and second uses of the catalyst difference between the first use of the catalyst. During the first use, $Fe_3O_4$@$TiO_2$ produced 13.8 mmol of N-benzylamine

after three hours. However, during the second use, the catalyst yielded over 44.3 mmol of the desired Schiff base in the same time frame.

Afterwards, we proceed to evaluate changes in lighting conditions to enhance the Schiff base production yield. We compared the product yield at the 3-hour mark for all the optimization reactions. Since irradiance can alter the distribution of products,[37,38] we evaluated the resulting imine yields at lower irradiance. For our system, reducing the irradiance resulted in a lower Schiff base yield (Table 5.2.2, entry 4). Next, we evaluated the influence of wavelength by irradiating the reaction with a blue LED (450 nm), which excites the iron oxide but not $TiO_2$. This led to a substantial production of BenzA, while neither Schiff base nor amine was detected (Table 5.2.2, entry 3 and Figure 5.3.8). Likewise, the absence of irradiation resulted in no Shiff base formation (Table 5.2.2, entry 6 and Figure 5.3.9) and a significantly lower BenzA (5.17 min) production. These results suggest that $TiO_2$ excitation is required for the reaction to occur.

**Table 5.2.2.** Optimizing Schiff-base yield produced $Fe_3O_4@TiO_2$ as a catalyst.[a] Reusing the catalyst and the Benzyl alcohol solution after 3 hours irradiation.

| Entry | Catalyst | Light source | Irradiance ($mW.cm^{-2}$) | Time (h) | Yield Schiff base (%) | Production rate ($mmol\ h^{-1}$) |
|---|---|---|---|---|---|---|
| **1** | $Fe_3O_4@TiO_2$ | **370 nm** | **13.5** | **6** | **41.6** | **6.9** |
| **2** | $TiO_2$ | **370 nm** | **13.5** | **6** | **36.7** | **6.1** |
| **3** | $Fe_3O_4@TiO_2$ | **370 nm** | **13.5** | **20** | **> 99** | **4.95** |
| **4** | $Fe_3O_4@TiO_2$ | **370 nm** | **5.3** | **3** | **1.9** | **0.63** |
| **5** | $Fe_3O_4@TiO_2$ | **450 nm** | **13.0** | **3** | **ND** | **ND** |
| **6** | $Fe_3O_4@TiO_2$ | **None** | **NA** | **3** | **ND** | **ND** |
| **7** | $Fe_3O_4@TiO_2$ | **370 nm** | **13.5** | **3[a]** | **44.3** | **14.76** |

**Mechanistic Insights into the Synthesis of Schiff Bases from Nitrobenzene and Benzyl Alcohol**

Based on our previous findings, we propose a plausible mechanism to elucidate the synthesis of Schiff Bases from nitrobenzene and benzyl alcohol catalyzed by M@$TiO_2$. Initially, the photocatalytic reaction on M@$TiO_2$ is initiated by the photoexcitation of $TiO_2$, leading to the generation of electron ($e^-$) and hole ($h^+$) pairs. The moderate oxidation potential of the photogenerated holes allows the $h^+$ to oxidize benzyl alcohol, yielding BenzA and hydrogen ions ($H^+$). BenzA was identified as one of the main products in our experiments, which is crucial in this process. The $H^+$ ions formed are subsequently reduced on the surface of the metal to generate H-metal species. This is the case of Pd@$TiO_2$, in which it has been proposed that Pd-H species will likely form in materials like Pd-decorated $TiO_2$ (Pd@$TiO_2$) when exposed to light.[39] In fact, Paul Sabatier who won the Nobel Prize in 1912[30], worked with Nickel (Ni) and different molecules such as hydrocarbons, alcohols, and acids, mentioned that the hydrogen coming in contact with the metal of a catalyst forms very quickly on the surface of each grain. These species can serve as active sites for reducing agents on the surface of Pd, facilitating specific reactions like converting nitrobenzene into aniline. This affirmation is supported by our experiment using 3-nitroanisole, where *m*-anisidine, an aniline derivative, was identified. The catalytic condensation of BenzA with aniline on the Lewis acid sites of the $TiO_2$ surface leads to the formation of the Schiff base. Our experimental results, particularly, highlighted in Figure 5.2.5, demonstrate the efficiency of this reaction on the M@$TiO_2$ catalysts.

It should be noted that the reaction could vary depending on the metal used to decorate $TiO_2$. For instance, for $Fe_3O_4$@$TiO_2$, we propose that upon catalyst excitation, the holes generated on the catalyst surface may oxidize benzyl alcohol, as described for Pd@$TiO_2$. Additionally, iron species could facilitate electron transfer, enabling the reduction of nitrobenzene to aniline.[39] Indeed, Xu *et al.,*[40] found out that when $TiO_2$ interacts with $Fe^{+3}$, it affects how quickly $Fe^{+3}$ is reduced to $Fe^{+2}$. Particularly, in the presence of P25, $Fe^{2+}$ is formed much faster and accumulates in larger amounts at the beginning of the reaction. This is likely due to the positive energy difference between the conduction band (CB) of $TiO_2$, and the CB of $Fe_3O_4$.[41] This difference allows for easy transfer of the photogenerated $e^-$ to the magnetic catalyst, facilitating the $Fe^{3+}/Fe^{2+}$

cycling.[41,42] During the regeneration of $Fe^{3+}$, the electrons could potentially reduce nitrobenzene to aniline.

A plausible scenario for this is depicted in Figure 5.2.6. Another possible route involves photogenerated electrons helping in the reduction of nitrobenzene to form aniline in the presence of $H^+$ ions. H-Fe species may also be generated, assisting in the reduction of the nitro moiety, yielding an amine. This process could lead to the condensation between benzaldehyde and aniline.[31] However, it is important to highlight that as mentioned by Moniz *et. al*.,[39] who also worked with a nanocomposite of iron, the role of this metal in catalytic processes, particularly when it interacts with $TiO_2$, remains a subject of ongoing research, presenting intriguing possibilities. While some studies propose that its presence facilitates hole transfer, others suggest its involvement in electron transfer mechanisms.[43,44] Recent investigations have highlighted the electron transfer phenomena occurring between iron and $TiO_2$.[45]

It is crucial to note that light plays a significant role in the mechanism. Specifically, prolonged photoirradiation significantly enhances the production of the Schiff Base, as evidenced by the increase in yield from 19 % after 3 hours of irradiation to almost 99 % after 20 hours of UVA irradiation when using the novel metallic catalyst (Figure 5.2.5 and Table 5.2.2). Thus, extending the duration of photoirradiation results in a more efficient reaction given the greater number of photons available to interact with the reactants on the catalyst surface. This increased photon exposure allows more reactions to occur, leading to higher conversion of the reactants into the desired Schiff base product. The $M@TiO_2$ catalysts facilitate the reaction between the reactants under UVA irradiation, a fact that was confirmed when experimenting without light (Figure 5.3.9), and no Schiff base was identified. Thus, the metallic component likely acts as a co-catalyst, enhancing the efficiency of the overall reaction. In summary, our study elucidates the steps involved in the synthesis of Schiff bases, providing crucial insights into the catalytic activity and reaction kinetics of different $M@TiO_2$ catalysts. It is noteworthy that, to the best of our knowledge, $Fe_3O_4@TiO_2$ catalyst has exhibited remarkable efficiency in facilitating Shiff base synthesis. This finding highlights the promising potential of iron-based catalysts for this reaction, emphasizing their importance in catalysis research. Additionally, its abundance and cost-effectiveness, offer a more sustainable alternative. This not only addresses environmental concerns but also highlights

its efficacy, while simultaneously mitigating risks associated with resource depletion, particularly evident when working with Palladium.

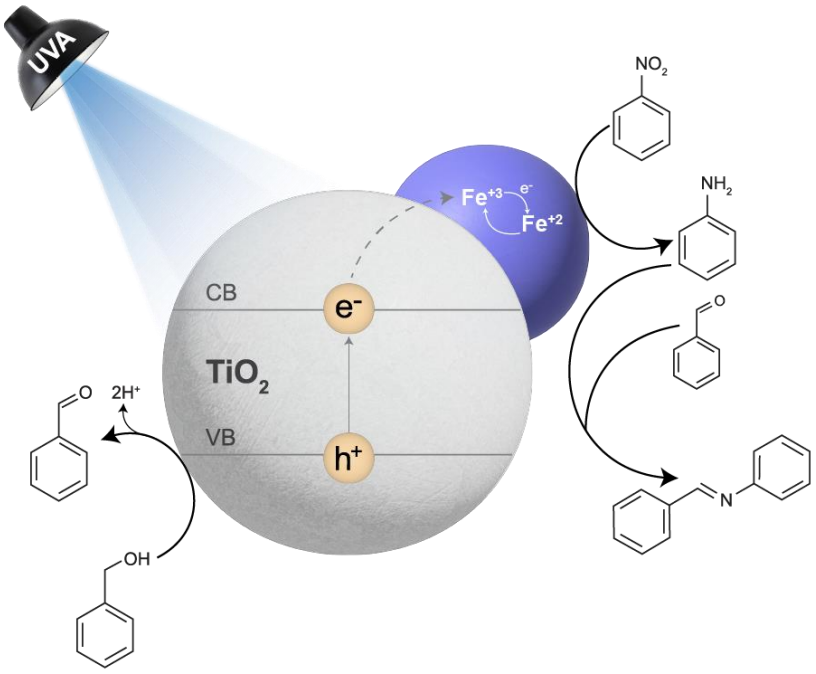


**Figure 5.2.6.** Plausible scenario to understand the activity shown by $Fe_3O_4$@$TiO_2$. Figure inspired by similar concepts in the literature.[15]

## CONCLUSIONS

To the best of our knowledge, the use of $Fe_3O_4$@ $TiO_2$ in organic synthesis, such as in the formation of Schiff Bases is not widespread. However, we want to underscore its potential for broader applications due to several features. Our study strongly indicates the potential efficacy of using $Fe_3O_4$@$TiO_2$ for synthesizing Schiff Bases. When irradiating the reaction comprising nitrobenzene and benzyl alcohol and the magnetic catalyst for 3 hours, we observed a Shiff base production of approximately 18 %. Impressively, extending the reaction duration to 20 hours resulted in nearly 99% production of the desired product. In contrast, analogous systems such as

$Pd@TiO_2$ and $Cu@TiO_2$ exhibited adequate production of the Schiff base; however, it is often accompanied by undesirable over-hydrogenation products, particularly notable in the case of Pd. By refining the experimental parameters, we have identified the optimal conditions for the magnetic catalyst. Our findings highlight the promising catalytic role of $Fe_3O_4@TiO_2$ in the field of catalysis research, given its ability to easily separate from the mixture reaction. This catalyst presents an alternative to address not only environmental concerns but also to mitigate the use of scarce resources such as Palladium.

**Supplementary materials:** Figures 5.3.1–5.3.10: GC-MS characterization, and MS spectra of the products. These results were obtained when performing the reactions with nitrobenzene and aniline under UVA irradiation, inert atmosphere, and $M@TiO_2$. Spectral irradiance of the light sources employed in the synthesis of the Schiff base is shown. Control experiments without light are depicted and a picture of $Fe_3O_4@TiO_2$ after its synthesis next to a magnet to demonstrate its response to an external magnetic field is provided. Additionally, the reusability of the magnetic catalyst is shown in Figure 5.3.10 and Table 5.3.1 shows a comparison illustrating the findings of this study alongside previous scientific publications.

**Funding:** This research was funded by the Natural Sciences and Engineering Research Council of Canada, the Canada Foundation for Innovation and the Canada Research Chairs Program.

**Data Availability Statement:** Original data are available from the corresponding author upon reasonable request.

**Conflicts of Interest:** The authors declare no conflict of interest.

## REFERENCES

(1) Louis F. Fieser; Mary Fieser. Advanced Organic Chemistry; Reinhold Publishing Corp: New York, 1961.

(2) Schiff, H. Sopra Una Nova Serie Di Basi Organiche [On a New Series of Organic Bases]. Giorn. Sci. Nat. Econ. Palermo (in Italian) 1866, 2, 201–257.

(3) Schiff, H. Eine Neue Reihe Organischer Diamine [A New Series of Organic Diamines]. Ann. Chem. Pharm. (in German) 1866, 3, 343–370.

(4) Yousif, E.; Al-Amiery, A. A.; Kadihum, A.; Kadhum, A. A. H.; Mohamad, A. B. Photostabilizing Efficiency of PVC in the Presence of Schiff Bases as Photostabilizers. Mol. 2015, 20 (11), 19886–19899.

(5) Jarrahpour, A. A.; Motamedifar, M.; Pakshir, K.; Hadi, N.; Zarei, M. Synthesis of Novel Azo Schiff Bases and Their Antibacterial and Antifungal Activities. Mol. 2004, 9 (10), 815–824.

(6) De Souza, A. O.; Galetti, F. C. S.; Silva, C. L.; Bicalho, B.; Parma, M. M.; Fonseca, S. F.; Marsaioli, A. J.; Trindade, A. C. L. B.; Gil, R. P. F.; Bezerra, F. S.; Andrade-Neto, M.; De Oliveira, M. C. F. Antimycobacterial and Cytotoxicity Activity of Synthetic and Natural Compounds. Quim. Nova 2007, 30 (7), 1563–1566.

(7) Yousif, E.; Majeed, A.; Al-Sammarrae, K.; Salih, N.; Salimon, J.; Abdullah, B. Metal Complexes of Schiff Base: Preparation, Characterization and Antibacterial Activity. Arab. J. Chem. 2017, 10, S1639–S1644.

(8) Juyal, V. K.; Pathak, A.; Panwar, M.; Thakuri, S. C.; Prakash, O.; Agrwal, A.; Nand, V. Schiff Base Metal Complexes as a Versatile Catalyst: A Review. J. Organomet. Chem. Elsevier B.V. October 15, 2023.

(9) Mahmood, K.; Maah, M. J.; Yusoff, I. Bin; Ashraf, M. A.; Wajid, A.; Yusoff, I. Synthesis, Characterization and Biological Activity of Schiff Bases; 2011, 10(1), 185

(10) Çınar, E.; Başaran, E.; Erdoğan, Ö.; Çakmak, R.; Boğa, M.; Çevik, Ö. Heterocyclic Schiff Base Derivatives Containing Pyrazolone Moiety: Synthesis, Characterization, and in Vitro Biological Studies. J. Chin. Chem. Soc. 2021, 68 (12), 2355–2367.

(11) Pharm, I. J.; Mahmood, A. A. Green Synthesis of Schiff Bases: A Review Study. Iraqi J. Pharm 2022, 18 (2), 180–193.

(12) Saranya, S.; Ramesh, R.; Grzegorz Małecki, J. One-Pot Catalytic Approach for the Selective Aerobic Synthesis of Imines from Alcohols and Amines Using Efficient Arene Diruthenium(II) Catalysts under Mild Conditions. Eur. J. Org. Chem. 2017, 2017 (45), 6726–6733.

(13) Shiraishi, Y.; Ikeda, M.; Tsukamoto, D.; Tanak, S.; Hirai, T. One-Pot Synthesis of Imines from Alcohols and Amines with $TiO_2$ Loading Pt Nanoparticles under UV Irradiation. Chem. Comm. 2011, 47 (16), 4811–4813.

(14) Siraki, A. G. Free Radical Metabolites in Arylamine Toxicity. In Advances in Molecular Toxicology; Elsevier B.V., 2013; Vol. 7, pp 39–82.

(15) Selvam, K.; Sakamoto, H.; Shiraishi, Y.; Hirai, T. One-Pot Synthesis of Secondary Amines from Alcohols and Nitroarenes on $TiO_2$ Loaded with Pd Nanoparticles under UV Irradiation. New J. Chem. 2015, 39 (4), 2467–2473.

(16) Geng, L.; Jian, W.; Jing, P.; Zhang, W.; Yan, W.; Bai, F. Q.; Liu, G. Crystal Phase Effect of Iron Oxides on the Aerobic Oxidative Coupling of Alcohols and Amines under Mild Conditions: A Combined Experimental and Theoretical Study. J. Catal. 2019, 377, 145–152.

(17) Luo, S.; Liu, Y.; Zhu, Y.; Niu, Q.; Cheng, M.; Ye, S.; Yi, H.; Shao, B.; Shen, M.; Wen, X.; Zeng, G.; Liu, Z. Perspectives on Palladium-Based Nanomaterials: Green Synthesis, Ecotoxicity, and Risk Assessment. Environ. Sci. Nano 2021, 8 (1), 20–36.

(18) Wu, Y.; Ye, X.; Zhang, S.; Meng, S.; Fu, X.; Wang, X.; Zhang, X.; Chen, S. Photocatalytic Synthesis of Schiff Base Compounds in the Coupled System of Aromatic Alcohols and Nitrobenzene Using $Cd_XZn1{-}XS$ Photocatalysts. J. Catal. 2018, 359, 151–160.

(19) Hayes, S. M.; McCullough, E. A. Critical Minerals: A Review of Elemental Trends in Comprehensive Criticality Studies. Resour. Policy 2018, 59, 192–199.

(20) Cely-Pinto, M.; Wang, B.; Scaiano, J. C. Photocatalytic Semi-Hydrogenation of Alkynes: A Game of Kinetics, Selectivity and Critical Timing. Nanomater. 2023, 13 (17), 1–15.

(21) da Silva, D. R. C.; Scaiano, J. C. Exploring the Antibacterial Properties of Lignin-coated Magnetic Nanoparticles Synthesized in a One-pot Process. Photochem Photobiol 2023, 99 (2), 706–715.

(22) Ohtani, B.; Prieto-Mahaney, O. O.; Li, D.; Abe, R. What Is Degussa (Evonik) P25? Crystalline Composition Analysis, Reconstruction from Isolated Pure Particles and Photocatalytic Activity Test. J. Photochem. Photobiol. A 2010, 216, 179–182.

(23) Cano, R.; Ramón, D. J.; Yus, M. Impregnated Ruthenium on Magnetite as a Recyclable Catalyst for the N-Alkylation of Amines, Sulfonamides, Sulfinamides, and Nitroarenes Using Alcohols as Electrophiles by a Hydrogen Autotransfer Process. J. Org. Chem. 2011, 76 (14), 5547–5557.

(24) Zanardi, A.; Mata, J. A.; Peris, E. One-Pot Preparation of Imines from Nitroarenes by a Tandem Process with an Ir–Pd Heterodimetallic Catalyst. Chem. Eur. J. 2010, 16 (34), 10502–10506.

(25) Zhang, Y.; Fulajtárová, K.; Kubů, M.; Mazur, M.; Hronec, M.; Čejka, J. Electronic/Steric Effects in Hydrogenation of Nitroarenes over the Heterogeneous Pd@BEA and Pd@MWW Catalysts. Catal Today 2020, 345, 39–47.

(26) Hirao, H.; Ohwada, T. Theoretical Study of Reactivities in Electrophilic Aromatic Substitution Reactions: Reactive Hybrid Orbital Analysis. J. Phys. Chem. A 2003, 107 (16), 2875–2881.

(27) Sabatier, P. How I Have Been Led to the Direct Hydrogenation Method by Metallic Catalysts 1. Ind Eng Chem 1926, 18 (10), 1005–1008.

(28) Hirakawa, H.; Katayama, M.; Shiraishi, Y.; Sakamoto, H.; Wang, K.; Ohtani, B.; Ichikawa, S.; Tanaka, S.; Hirai, T. One-Pot Synthesis of Imines from Nitroaromatics and Alcohols by Tandem Photocatalytic and Catalytic Reactions on Degussa (Evonik) P25 Titanium Dioxide. ACS Appl. Mater. Interfaces. 2015, 7 (6), 3797–3806.

(29) Tong, J.; Wang, J.; Shen, X.; Zhang, H.; Wang, Y.; Fang, Q.; Chen, L. One-Pot Synthesis of Schiff Bases by Defect-Induced $TiO_{2-x}$-Catalyzed Tandem Transformation from Alcohols and Nitro Compounds. Inorg. Chem. 2021, 60 (14), 10715–10721.

(30) Sabatier, P. How I Have Been Led to the Direct Hydrogenation Method by Metallic Catalysts. Ind. Eng. Chem. Res. 1926, 18 (10), 1005–1008.

(31) Wu, J.; Darcel, C. Iron-Catalyzed Hydrogen Transfer Reduction of Nitroarenes with Alcohols: Synthesis of Imines and AZA Heterocycles. J. Org. Chemistry 2020, 86 (1), 1023–1036.

(32) Pérez, J. M.; Cano, R.; Yus, M.; Ramón, D. J. Straightforward Synthesis of Aromatic Imines from Alcohols and Amines or Nitroarenes Using an Impregnated Copper Catalyst. Eur. J. Org. Chem. 2012, 24, 4548–4554.

(33) Zou, G.; Cao, R.; Cui, C.; Luo, Y.; Huang, C.; Cui, X.; Wang, Z.; Song, Y. Photocatalytic One-Pot Alkylation of Nitrobenzene with Benzyl Alcohol for the Precise Synthesis of N-

Benzylideneaniline over F-Doped $Bi_2MoO_6$ Nanosheets. Catal. Sci. Technol. 2023, 13 (13), 3916–3926.

(34) Higashimoto, S.; Nakai, Y.; Azuma, M.; Takahashi, M.; Sakata, Y. One-Pot Synthesis of Imine from Benzyl Alcohol and Nitrobenzene on Visible-Light Responsive CdS–$TiO_2$ Photocatalysts. RSC Adv. 2014, 4 (71), 37662–37668.

(35) Liu, D.; Yang, P.; Zhang, H.; Liu, M.; Zhang, W.; Xu, D.; Gao, J. Direct Reductive Coupling of Nitroarenes and Alcohols Catalysed by Co–N–C/CNT@AC. Green Chem. 2019, 21 (8), 2129–2137.

(36) Ye, X.; Chen, Y.; Wu, Y.; Zhang, X.; Wang, X.; Chen, S. Constructing a System for Effective Utilization of Photogenerated Electrons and Holes: Photocatalytic Selective Transformation of Aromatic Alcohols to Aromatic Aldehydes and Hydrogen Evolution over Zn3In2S6 Photocatalysts. Appl. Catal. B: Environ. 2019, 242, 302–311.

(37) Gawargy, T. A.; Costa, P.; Lanterna, A. E.; Scaiano, J. C. Photochemical Benzylic Radical Arylation Promoted by Supported Pd Nanostructures. Org. Biomol. Chem. 2020, 18 (31), 6047–6052.

(38) Zhan, C.; Wang, Q.-X.; Yi, J.; Chen, L.; Wu, D.-Y.; Wang, Y.; Xie, Z.-X.; Moskovits, M.; Tian, Z.-Q. Plasmonic Nanoreactors Regulating Selective Oxidation by Energetic Electrons and Nanoconfined Thermal Fields. Sci. Adv. 2021, 7 (10).

(39) Hainer, A. S.; Hodgins, J. S.; Sandre, V.; Vallieres, M.; Lanterna, A. E.; Scaiano, J. C. Photocatalytic Hydrogen Generation Using Metal-Decorated $TiO_2$ : Sacrificial Donors vs True Water Splitting. ACS Energy Lett 2018, 3 (3), 542–545.

(40) Moniz, S. J. A.; Shevlin, S. A.; An, X.; Guo, Z.; Tang, J. Fe2O3–TiO2 Nanocomposites for Enhanced Charge Separation and Photocatalytic Activity. Chem. Eur. J. 2014, 20 (47), 15571–15579.

(41) Xu, L.; Meng, L.; Zhang, X.; Mei, X.; Guo, X.; Li, W.; Wang, P.; Gan, L. Promoting $Fe^{3+/}Fe^{2+}$ Cycling under Visible Light by Synergistic Interactions between P25 and Small Amount of Fenton Reagents. J Hazard Mater 2019, 379, 120795.

(42) Aguinaco, A.; Mánuel, J. M.; Blanco, E.; Domínguez, M.; Litrán, R.; Delgado, J. J.; Ramírez-del-Solar, M. $Fe_3O_4$-$TiO_2$ Thin Films in Solar Photocatalytic Processes. Materials 2022, 15 (19), 6718.

(43) Xu, L.; Qi, L.; Han, Y.; Lu, W.; Han, J.; Qiao, W.; Mei, X.; Pan, Y.; Song, K.; Ling, C.; Gan, L. Improvement of Fe2+/Peroxymonosulfate Oxidation of Organic Pollutants by Promoting Fe2+ Regeneration with Visible Light Driven g-$C_3N_4$ Photocatalysis. Chemical Engineering Journal 2022, 430, 132828.

(44) Peng, L.; Xie, T.; Lu, Y.; Fan, H.; Wang, D. Synthesis, Photoelectric Properties and Photocatalytic Activity of the $Fe_2O_3$/$TiO_2$ Heterogeneous Photocatalysts. Phys. Chem. Chem. Phys. 2010, 12 (28), 8033.

(45) Bahnemann, D. W.; Hilgendorff, M.; Memming, R. Charge Carrier Dynamics at $TiO_2$ Particles: Reactivity of Free and Trapped Holes. J. Phys. Chem. B 1997, 101 (21), 4265–4275.

(46) Nolan, M. Electronic Coupling in Iron Oxide-Modified TiO2 Leads to a Reduced Band Gap and Charge Separation for Visible Light Active Photocatalysis. Phys. Chem. Chem. Phys. 2011, 13 (40), 18194.

(47) Ye, X.; Chen, Y.; Ling, C.; Ding, R.; Wang, X.; Zhang, X.; Chen, S. One-Pot Synthesis of Schiff Base Compounds via Photocatalytic Reaction in the Coupled System of Aromatic Alcohols and Nitrobenzene Using CdIn2S4 Photocatalyst. Dalton Trans. 2018, 47 (32), 10915–10924.

(48) Liu, D.; Yang, P.; Zhang, H.; Liu, M.; Zhang, W.; Xu, D.; Gao, J. Direct Reductive Coupling of Nitroarenes and Alcohols Catalysed by Co-N-C/CNT@AC. Green Chem. 2019, 21 (8), 2129–2137.

(49) Tong, J.; Wang, J.; Shen, X.; Zhang, H.; Wang, Y.; Fang, Q.; Chen, L. One-Pot Synthesis of Schiff Bases by Defect-Induced $TiO_{2-x}$ Catalyzed Tandem Transformation from Alcohols and Nitro Compounds. Inorg. Chem. 2021, 60 (14), 10715–10721.

## 5.3 Submitted Version of Supporting Information

# Supporting information

# Magnetic catalyst for efficient One-Pot Synthesis of Schiff Bases from Benzyl Alcohol and Nitro Compounds under UV irradiation

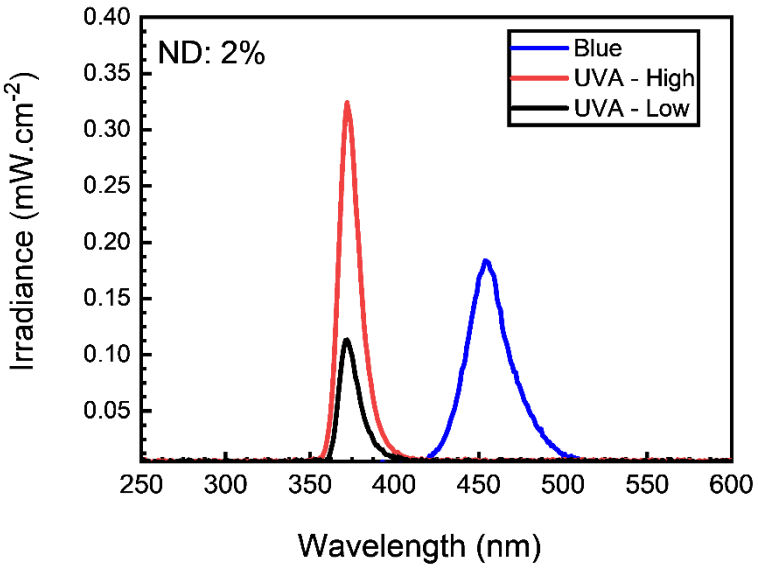


**Figure 5.3.1.** Emission spectra of light sources used in this work. In Blue 1x450 nm LED, in red 1x370 nm LED (UVA at higher intensity) and in black 1x370 nm LED (UVA at Lower intensity). ND: neutral density filter.

**Figure 5.3.2.** $Fe_3O_4@TiO_2$ after its synthesis next to a magnet to demonstrate its response to an external magnetic field.

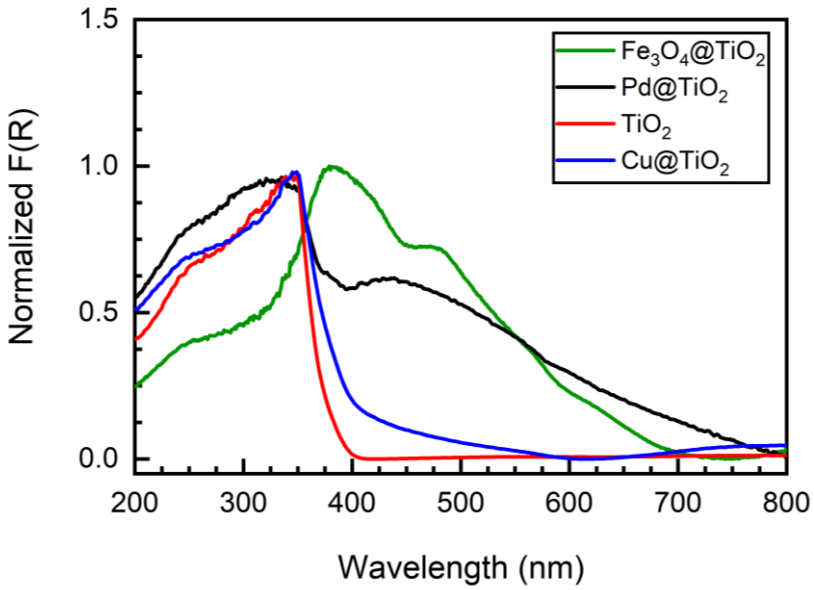


**Figure 5.3.3**. Diffuse Reflectance of the catalysts used in this study.

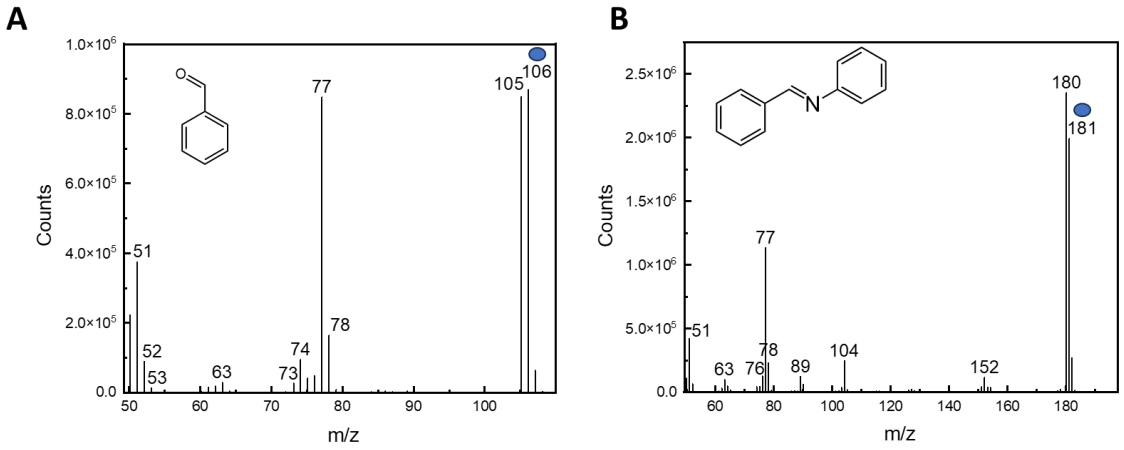


**Figure 5.3.4**. Mass spectra of the products. Each spectrum shows (●) the molecular ion of the molecules.

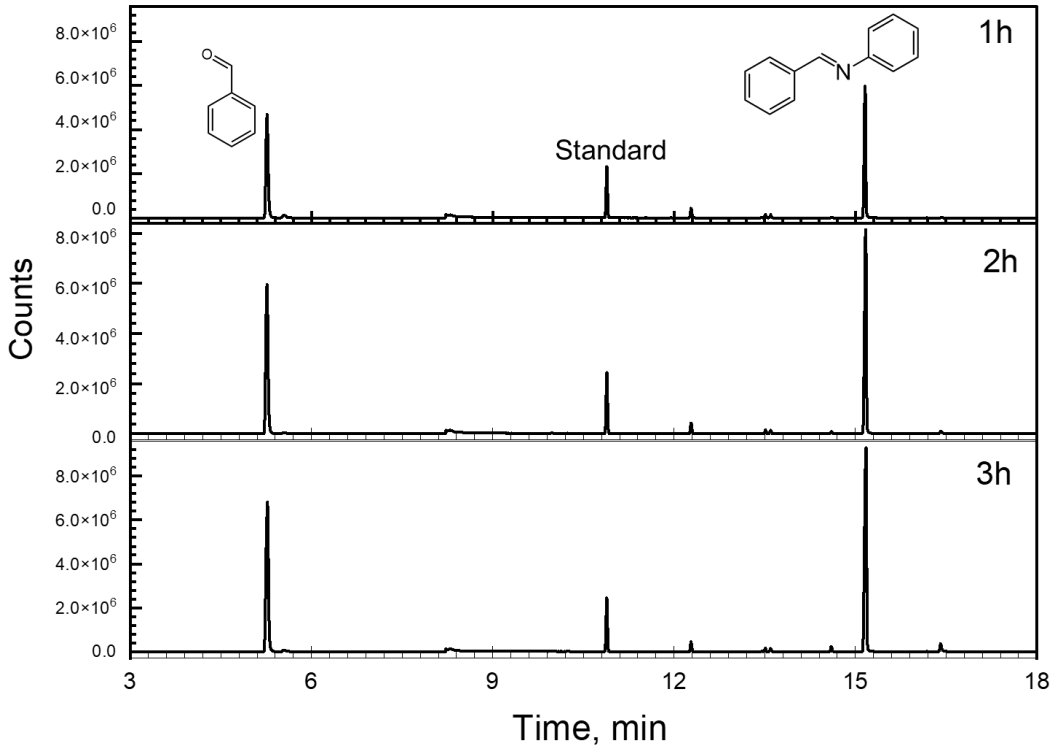


**Figure 5.3.5.** Chromatograms showing the peaks obtained after performing the reaction with nitrobenzene 0.1 M in benzyl alcohol and 10 mg of $TiO_2$. 3,5-Di-tert-butyltoluene was used as an external standard (peak at 10.84 min) The major products have the following retention times: BenzA (5.17 min), Schiff Base (15.10 min). The timed events feature of the local user interface was used (Turned off at 6.20 minutes and activated at 8.70 minutes) to prevent the risk of a high concentration of Benzyl Alcohol reaching the detector.

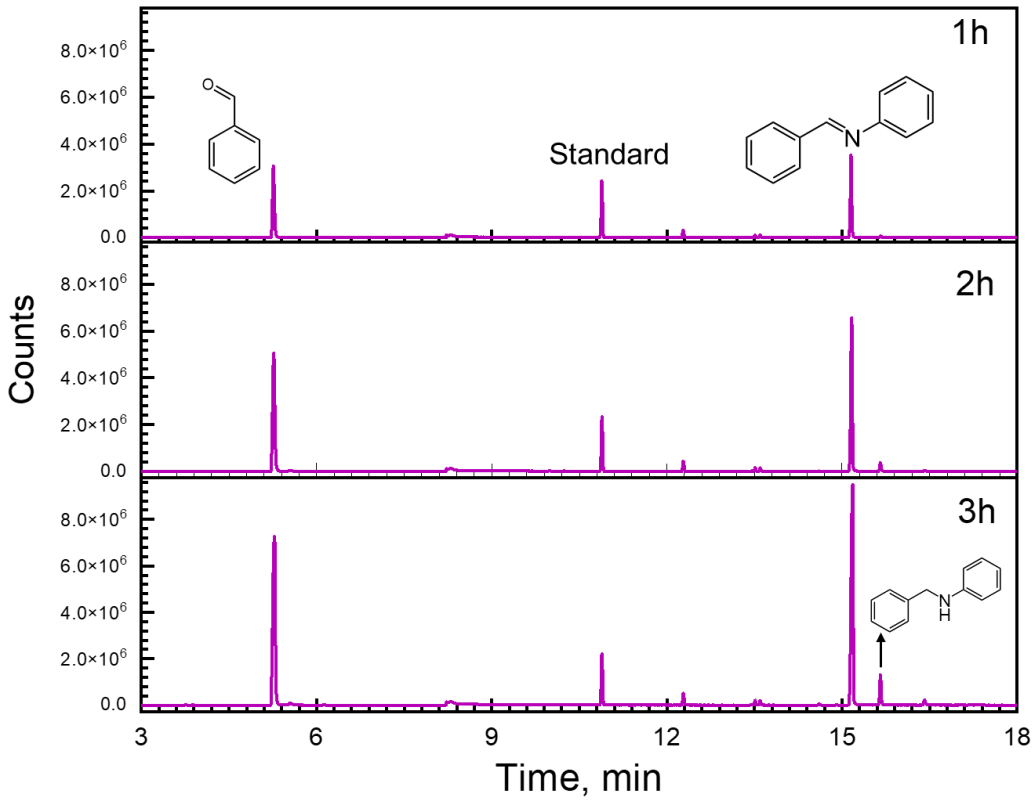


**Figure 5.3.6.** Chromatograms showing the peaks obtained after performing the reaction with nitrobenzene 0.1 M in benzyl alcohol and 10 mg of Pd@$TiO_2$. 3,5-Di-tert-butyltoluene was used as an external standard (peak at 10.84 min) The major products have the following retention times: BenzA (5.17 min), Schiff Base (15.10 min). The timed events feature of the local user interface was used (Turned off at 6.20 minutes and activated at 8.70 minutes) to prevent the risk of a high concentration of Benzyl Alcohol reaching the detector.

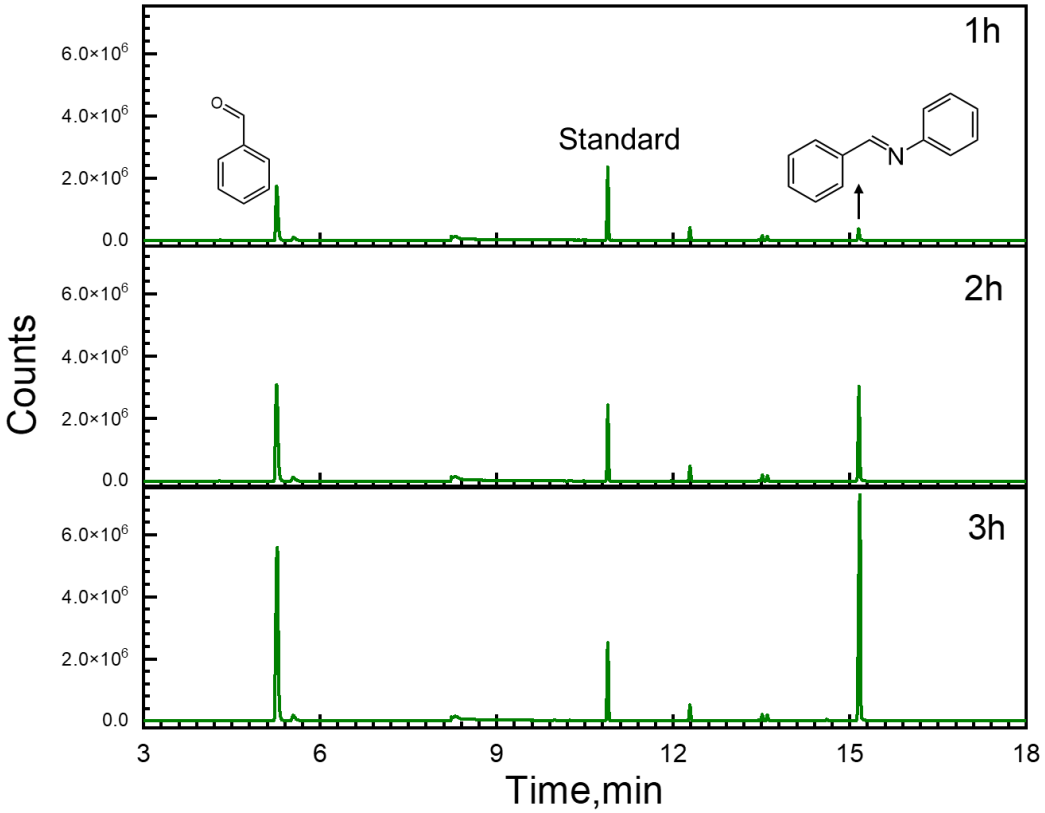


**Figure 5.3.7.** Chromatograms showing the peaks obtained after performing the reaction with nitrobenzene 0.1 M in benzyl alcohol and 10 mg of Cu@$TiO_2$. 3,5-Di-tert-butyltoluene was used as an external standard (peak at 10.84 min) The major products have the following retention times: BenzA (5.17 min), Schiff Base (15.10 min). The timed events feature of the local user interface was used (Turned off at 6.20 minutes and activated at 8.70 minutes) to prevent the risk of a high concentration of Benzyl Alcohol reaching the detector.

**Table 5.3.1.** Comparison table illustrating the findings of this study alongside previous research on the one-pot Schiff Base synthesis using nitrobenzene and benzyl alcohol as reagents. The table shows the production rates in mmol h-1 achieved with various catalytic materials under different conditions. Production rates were estimated using the highest published yields for each reference, multiplying the initial nitrobenzene concentration, divided by the reaction times.

| Catalyst | Time (Hours) | Atm | Light (nm) or Heat (°C) | Yield (%) | Schiff base production rate (mmol/H) | Ref. |
|---|---|---|---|---|---|---|
| **$Fe_3O_4$@$TiO_2$** | 6 | $N_2$ | >300 | 41.6 | 6.8 | This work |
| **$CdIn_2S_4$** | 8 | $N_2$ | >420 | 32 | 0.34 | [1] |
| **Co–N–C/CNT@AC** | 18 | $N_2$ | Heat 160 | 97 | 0.26 | [2] |
| **PC-$TiO_{2-x}$_590** | 18 | Ar | >300 | 100 | 0.02 | [3] |
| **P25** | 10 | $N_2$ | >300 | 93 | 0.005 | [4] |
| **$F_{0.04}$-BMO-NS** | 10 | $N_2$ | ≥ 400 | 95.5 | 0.0019 | [5] |
| **CdS (15 wt%)–$TiO_2$** | 10 | $N_2$ | 420 | - | 0.0018 | [6] |
| **$Cd_xZn_{1-x}S$** | 4 | Air | >420 | 55 | 0.0011 | [7] |

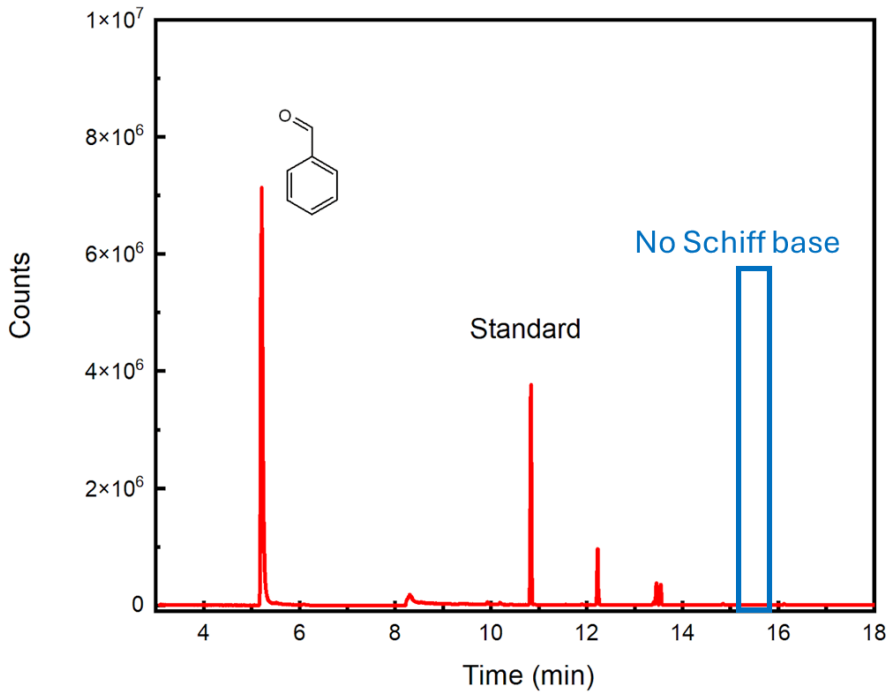


**Figure 5.3.8.** Chromatogram showing the peaks obtained after 3 hours at 450 nm light irradiation. No peak for the Schiff base (15.10 min) was obtained after reacting with nitrobenzene 0.1 M in benzyl alcohol and 10 mg of $Fe_3O_4$@$TiO_2$. 3,5-Di-tert-butyltoluene was used as an external standard (peak at 10.84 min). The timed events feature of the local user interface was used (Turned off at 6.20 minutes and activated at 8.70 minutes) to prevent the risk of a high concentration of Benzyl Alcohol reaching the detector.

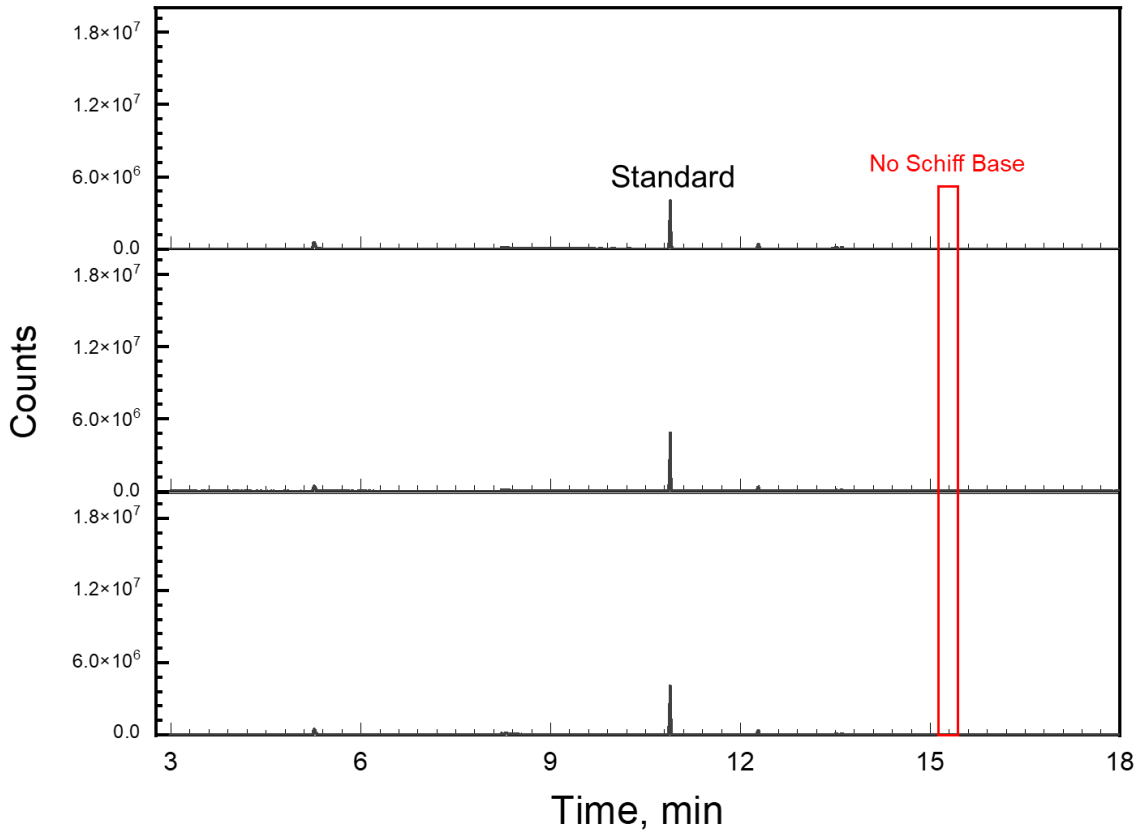


**Figure 5.3.9**. A control Experiment without light irradiation Chromatogram showing no peak for the Schiff base (15.10 min) was obtained after reacting with nitrobenzene 0.1 M in benzyl alcohol and 10 mg of $Fe_3O_4$@$TiO_2$. 3,5-Di-tert-butyltoluene was used as an external standard (peak at 10.84 min). The timed events feature of the local user interface was used (Turned off at 6.20 minutes and activated at 8.70 minutes) to prevent the risk of a high concentration of Benzyl Alcohol reaching the detector.

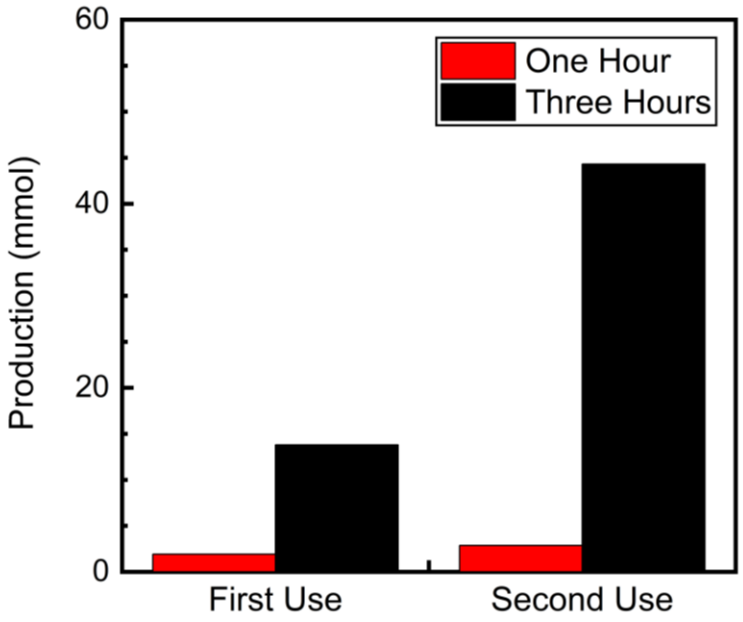


**Figure 5.3.10** N-benzylamine production using $Fe_3O_4$@$TiO_2$ as catalyst (10 mg) irradiated for up to 3 hours with UVA (λ= 370 nm) under $N_2$ atmosphere. After the first round of irradiation (first use), 0.1M of nitrobenzene was added to the solution and irradiated for another 3 hours (second use). Schiff-base production was quantified using GC-MS.

**References for the Supporting Information section**

(1) Ye, X.; Chen, Y.; Ling, C.; Ding, R.; Wang, X.; Zhang, X.; Chen, S. One-Pot Synthesis of Schiff Base Compounds via Photocatalytic Reaction in the Coupled System of Aromatic Alcohols and Nitrobenzene Using CdIn2S4 Photocatalyst. Dalton Trans. 2018, 47 (32), 10915–10924.

(2) Liu, D.; Yang, P.; Zhang, H.; Liu, M.; Zhang, W.; Xu, D.; Gao, J. Direct Reductive Coupling of Nitroarenes and Alcohols Catalysed by Co-N-C/CNT@AC. Green Chem. 2019, 21 (8), 2129–2137.

(3) Tong, J.; Wang, J.; Shen, X.; Zhang, H.; Wang, Y.; Fang, Q.; Chen, L. One-Pot Synthesis of Schiff Bases by Defect-Induced $TiO_{2-x}$ Catalyzed Tandem Transformation from Alcohols and Nitro Compounds. Inorg. Chem. 2021, 60 (14), 10715–10721.

(4) Hirakawa, H.; Katayama, M.; Shiraishi, Y.; Sakamoto, H.; Wang, K.; Ohtani, B.; Ichikawa, S.; Tanaka, S.; Hirai, T. One-Pot Synthesis of Imines from Nitroaromatics and Alcohols by Tandem Photocatalytic and Catalytic Reactions on Degussa (Evonik) P25 Titanium Dioxide. ACS Appl. Mater. Interfaces. 2015, 7 (6), 3797–3806.

(5) Zou, G.; Cao, R.; Cui, C.; Luo, Y.; Huang, C.; Cui, X.; Wang, Z.; Song, Y. Photocatalytic One-Pot Alkylation of Nitrobenzene with Benzyl Alcohol for the Precise Synthesis of N-Benzylideneaniline over F-Doped Bi2$MoO_6$ Nanosheets. Catal. Sci. Technol. 2023, 13 (13), 3916–3926.

(6) Higashimoto, S.; Nakai, Y.; Azuma, M.; Takahashi, M.; Sakata, Y. One-Pot Synthesis of Imine from Benzyl Alcohol and Nitrobenzene on Visible-Light Responsive CdS–$TiO_2$ Photocatalysts. RSC Adv. 2014, 4 (71), 37662–37668.

(7) Wu, Y.; Ye, X.; Zhang, S.; Meng, S.; Fu, X.; Wang, X.; Zhang, X.; Chen, S. Photocatalytic Synthesis of Schiff Base Compounds in the Coupled System of Aromatic Alcohols and Nitrobenzene Using CdXZn1−XS Photocatalysts. J. Catal. **2018**, 359, 151–160.

## 5.4 Accompanied Chapter 5

As one may have noticed, this chapter takes a different approach from the previous ones. Coming from a biological background, my initial focus was on the medical and environmental applications of titanium and iron-based catalysts, which were the subjects of earlier chapters. However, after spending several years working within a catalysis group, it was inevitable a growing interest in organic reactions. When we first developed the new magnetic titanium dioxide, we were curious to see how it would perform compared to the gold standards in photocatalysis, such as Pd@$TiO_2$ and P25, as well as other first-row transition metals like Cu@$TiO_2$, which is gaining attention as a greener catalyst alternative. In collaboration with Melissa Cely, who has expertise on some of those photocatalysts and had used them for several organic reactions, we tested the new $Fe_3O_4$@$TiO_2$ utilizing radical recombination reactions, which she was interested in at the time.

During the initial experimental phase, the project took an exciting turn when we observed the exceptional performance of the new magnetic material in the synthesis of Schiff bases. Recognizing the importance of these compounds for various commercial applications, we shifted our focus to optimizing their production. I was glad to venture into this different area, as it proved to be a valuable learning experience, as I gained deeper insights into organic synthetic processes. Moreover, we successfully developed a highly effective and sustainable catalytic alternative for the synthesis of these crucial compounds.

# 6. Conclusions and Future Directions

Throughout this dissertation, we discussed several synthetic approaches and applications of iron- and titanium-based nanoparticles. By exploring their chemical, physical, and optical properties, we demonstrated how these materials can serve as earth-abundant alternatives to at-risk metals in various applications, including medical, environmental, and catalytic fields. In the following chapter, we will present conclusions, further analyze some of the results, and offer perspectives on the future development of these projects.

## 6.1 Further analysis and Future directions

### 6.1.1 Magnetic Nanoparticles

In chapter two, we described the synthesis of four magnetic nanoparticles coated with lignin, a biocompatible coating alternative. The antibacterial properties of these nanoparticles were significantly enhanced by leveraging some of the unique properties of iron oxides. The first one is the exceptional photothermal conversion capability of iron oxides, which when irradiated with NIR light, generated sufficient heat to cause cell ablation, reaching values of six and eight log-unit reduction. The second property is the catalytic activity of iron (Fe) in Fenton and Fenton-like reactions. In the presence of $H_2O_2$, these reactions produced increased levels of hydroxyl radicals, which killed a significant number of cells within 30 minutes. Moreover, combining both treatments, photothermal therapy (PTT) and chemodynamic therapy (CDT), resulted in enhanced bactericidal effects. Notably, samples containing lignin@Fe/Ag showed complete bacterial disinfection after just 1 minute of treatment and samples containing lignin@Fe/Co reached 6 log units reduction in the same time frame. Comparing the antibacterial results with cellular toxicity revealed that lignin@Fe/Co nanoparticles provided a balance between bactericidal activity and cellular toxicity.

The colony formation inhibition capability of iron oxide nanoparticles in solution remains a subject of debate. In our study, we observed that iron oxide NPs alone did not exhibit significant bactericidal performance even after 16 hours of incubation compared to hybrid materials. This contrasts with other reports that have demonstrated antibacterial activity for these nanoparticles in

solution.[1] Recently, Egorova and collaborators[2] reported that iron nanoparticles (FeNPs) in solution displayed minimal bactericidal activity, consistent with our findings. However, they found that when these NPs were used as a coating on reverse osmosis membranes, they were effective in inhibiting biofilm growth. This discovery highlights the potential of iron-based materials to prevent and combat biofilm formation on surfaces. Such applications are particularly important in medical devices, where biofilm formation poses a persistent challenge.

In this context, using iron oxide to impact biofilm formation on implants, such as knee and hip replacements, represents a promising strategy. Furthermore, coating these NPs with antibiotics combines their antibiofilm properties with enhanced antibiotic delivery. Using the same synthetic procedure used for the lignin-coated magnetic nanoparticles, we are moving into utilizing ciprofloxacin as a capping agent. Ciprofloxacin is a broad-spectrum antibiotic commonly used to treat implant infections. Our preliminary results show successful coating with the antibiotic, as we maintained the nanoparticle's magnetic behaviour. Some of the near-future tests of this new strategy include determining the correct antibiotic loading and ensuring that the antibiotic properties are not altered during the coating process.

Looking ahead, combining the photothermal effect observed in our studies can sensitize bacterial cell walls, facilitating the penetration and efficacy of treatment agents, including the nanoparticles themselves and the coating antibiotic. Additionally, the magnetic properties of these nanoparticles can be further exploited, as it was not fully utilized during the tests in Chapter 2 to improve antibacterial activity. For instance, with the assistance of an external magnetic field nanoparticles can achieve deeper biofilm penetration and enable on-demand antibiotic release.[3] This approach could enhance effective antibiotic delivery to the interior of biofilms and potentially be combined with the radical generation capabilities of iron-based materials.

When dealing with close contact with human bodies, an in-depth study of cellular and whole-body toxicity is crucial for the safe implementation of these techniques. While we did not find significant cellular toxicity of iron oxide alone, some studies suggest those nanoparticles may induce liver injuries.[4,5] However, the exact extent of this cytotoxicity is still not fully understood, with scientific results showing discrepancies. Therefore, it is important to evaluate the toxicity of

our specific materials, necessitating further research to elucidate their potentially harmful effects at the cellular and tissue levels, as well as their overall impact on the body.

### 6.1.2 Fibrous $TiO_2$

In Chapter 3 the utilization of $TiO_2$ in fibrous materials was discussed as a means to facilitate removal from solutions post-reaction. We explored this material's potential as an alternative for water remediation. Using crocin as a surrogate for organic contaminants, we observed the efficacy of the proposed catalysts: $TiO_2$ nanofibres (TNF), $TiO_2$ on glass wool (TGW), and $TiO_2$ in glass fibres filters (TGF). All catalysts demonstrated excellent performance in fixed-bed reactors, degrading over 80% of the dye in batch processes. In flow systems, irradiation times were significantly shorter than batch systems, with some samples being irradiated for less than 1 or 2 minutes, achieving bleaching values of 90%, 40%, and 30% for TGW, TGF, and TNF, respectively. Although degradation discrepancies were less pronounced in batch systems, the physical properties of these materials significantly influenced catalytic rates under flow conditions. These findings prompted a discussion on the key aspects that define effective catalysts for continuous flow systems, considering catalytic performance, physical characteristics, and synthetic features. From these results, we concluded that $TiO_2$@GW is a promising candidate for further investigations.

During this dissertation, we focused our discussions on alternatives for suspended $TiO_2$ particles to facilitate environmental applications. However, employing $TiO_2$ for commercial-scale water treatment also faces a challenge regarding $TiO_2$'s large band gap at ~3.1 eV, which requires wavelengths below 400 nm for photoexcitation. This limitation reduces its effectiveness under visible light, and consequently, the full use of solar irradiation which contains about ten times more visible light than ultraviolet.[6] Common strategies to optimize titanium dioxide include decorating or doping the nanoparticles with metals or metal oxides. Noble metals not only cause a red shift in the absorbance spectrum but also act as electron acceptors for the generated hot electrons, thereby decreasing charge recombination rates. However, these strategies introduce concerns related to the cost of these materials and the potential health and environmental risks associated with some of those metals.

Recently, our group has focused on self-doping titanium dioxide with Ti (III) species. These species, typically located on the material's surface, can be generated by calcining the catalyst under a reductive environment. The successful reduction of some Ti (IV) sites to Ti (III) is indicated by a colour change from white to black, hence the name black-$TiO_2$, illustrated in Figure 6.1.1. The colour change results from the creation of multiple defect sites, which produce intermediate gap states that lower the energy required to achieve an excited state.[7] Additionally, these defect sites serve as trapping sites for photogenerated carriers, thereby preventing rapid recombination without the need for adding a different metal.

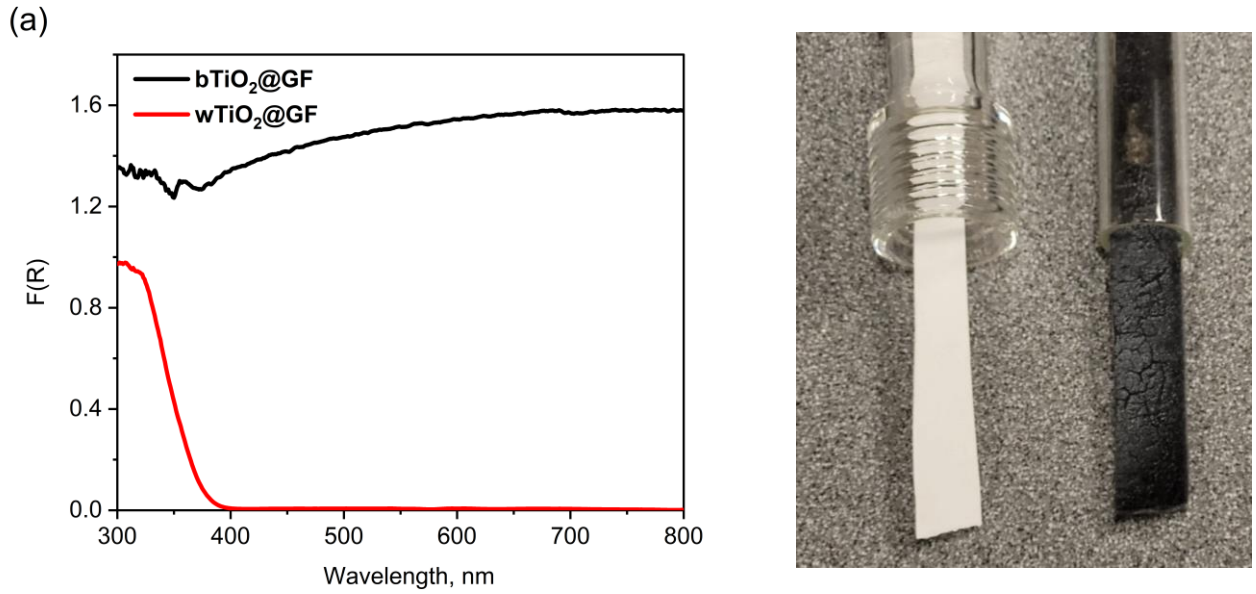


**Figure 6.1.1** Diffuse reflectance comparing the optical properties of white $TiO_2$ on glass filter ($wTiO_2$@GF) (red line) and black $TiO_2$ on glass filter ($bTiO_2$@GF) (black line) (A). Photographs illustrating the visual difference between white and black Titanium dioxide (B).

Building on our knowledge of supported fibrous $TiO_2$, we developed a blackened version of the $TiO_2$@glass filter (b-$TiO_2$@GF). When used in a continuous flow system and irradiated with visible light, this catalyst effectively degraded organic molecules, including organic dyes and endocrine disruptors. The method for producing blackened titanium dioxide is simple and can be extended to create blackened $TiO_2$@GW. This allows for scaled-up applications without the risk of leaching toxic metals into the water.

Another aspect investigated in Chapter 3 is the utilization of these catalysts in continuous flow systems. Using a bench-scale system, we observed that $TiO_2$ performed better than the other materials. This superior performance is primarily due to the better dispersion of the photocatalyst on the glass support, which allows for greater contact between the catalyst and the target molecule. Additionally, filling the tube with glass wool induces turbulent flow, enhancing collisions which may improve degradation rates compared to cardboard-like supported catalysts that tend to create laminar flow away from the catalyst. A simulation by Rasul and collegues[8] demonstrated that under a turbulent flow, there is a 37% increase in the mass transfer of the pollutant, which culminates in higher degradation values. For future implementation, TGW photocatalytic performances must be validated on a larger-scale flow system. As the system's scale increases, factors such as light penetration, volume, and flow dynamics will change significantly, necessitating further optimizations.

We also discussed the need to test the catalyst with realistic contaminants, including microorganisms. In Chapter 4, we examined the use of TGW against a bacterial contaminant, *E. coli*. Our tests revealed that the catalyst showed surprisingly lower photocatalytic efficiency, with log reduction values similar to those of light treatment alone. Given that TGW was an excellent catalyst for degrading organic dyes, we investigated the factors contributing to its reduced performance in these tests. We found that under realistic conditions, which may contain other organic contaminants or organic matter, the catalyst's performance was suppressed due to competition for the produced radicals. Additionally, while glass wool is effective for generating turbulent flow, its properties limit light penetration due to high scattering from the catalyst, thereby reducing its optical efficiency. Furthermore, the fixed bed catalyst provided a surface for bacterial attachment, which further hindered catalytic activity. Based on the observed results, we then

proposed several improvements for enhancing catalytic activity. Knowing that one of the main causes is the low optical properties and observing how well TGW performed in the continuous flow system from the data in Chapter 3, we believe that this would be the next step for the improvement of the catalytic activity.

We conducted preliminary experiments using a continuous flow system with a total volume of 25 mL and an irradiation time of 13 minutes. Comparing the data from the batch system to the flow results, we observed a significant reduction in the time required to achieve a one-log unit reduction, decreasing from three hours in batch to 13 minutes in flow. Moreover, under the same conditions, UVA irradiation alone did not exhibit any bactericidal effect, as the bacterial count remained constant. Figure 6.1.2 summarizes the results of using TGW in a continuous flow system. Each time point has a 20-minute difference, corresponding to the total residence time in the system. Initially, there was a decrease in bacterial count in the dark, stabilizing at about 0.4 log units after

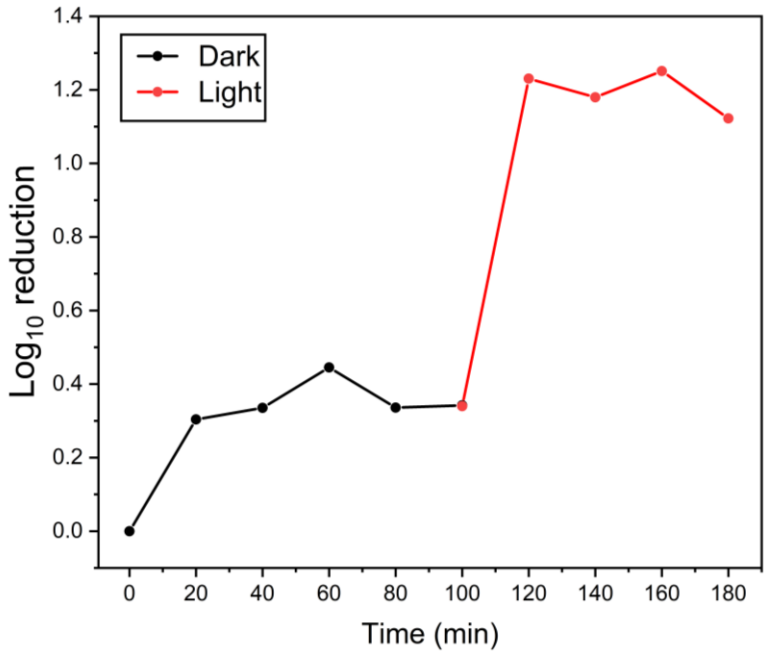


**Figure 6.1.2** Log reduction units for a bacterial solution ($10^6$ CFU/mL) treated in a continuous flow system containing 3.37 g of $TiO_2$@Glasswool (TGW). The total system volume was 36.7 mL, with a residence time of 20 minutes, including a irradiation time of 13 minutes. Each time point represents the time necessary for a solution to passthrough the entire system (residence time), in the dark (black line) and irradiated with a UVA light (red line).

one hour, which could be attributed to the bacterial attachment to the supported catalyst. When the light was turned on, represented by the red line, there was an increase in the log reduction, which remained consistent for treatment of four times the bed volume, meaning approximately 146 mL of solution. This demonstrates that improving the optical properties of our system significantly enhances its catalytic properties against microorganism contaminants. With further optimizations, such as adjusting irradiation times, flow rates, glass wool loading, and solution conditions, the catalyst may achieve even higher disinfection values.

The discussions raised in Chapter 4 are also being employed in our group's current tests, particularly in methodologies to optimize the optical properties of supported catalysts and to enhance the aeration of batch and continuous flow systems. In the context of water treatment future strategies may also include considering the conditions of the water sources, such as pH and the quantity of organic matter, with the use of natural water sources being a good starting point. Additionally, the bacterial attachment to catalysts has highlighted the limitations of plate counting techniques, which do not differentiate between bacterial viability and bacterial removal from the solution due to attachment to the catalyst. In this context, Sara Currie, a current master's student in our group, is exploring alternative cellular viability experiments, such as the use of fluorescence probes, as additional tests to improve sample testing reliability. Lastly, future developments should include mechanistic studies to better understand and enhance our catalysts, one example is the quantification and localization of generated reactive oxygen species.

### 6.1.3 Magnetic $TiO_2$

The combination of iron and titanium led to the fabrication of a hybrid magnetic $TiO_2$, employed in a one-pot synthesis of Schiff bases using nitrobenzene and benzyl alcohol as starting materials. The catalyst demonstrated impressive production rates, achieving a 99% yield of Schiff base after 24 hours of irradiation. This synthetic route allows for producing large amounts of Schiff base under mild conditions, avoiding strong oxidants, high $H_2$ pressure, and elevated temperatures. Notably, benzyl alcohol was used as both the solvent and reactant, with the excess aromatic alcohol favouring Schiff base formation and eliminating the need for an additional separation step. Our work also showed that the remaining reactant can be reused along with the catalyst for additional

reaction cycles. In our proposed mechanism, we observed that our dual catalysts work cooperatively to enhance product formation, allowing the three required reaction steps to occur in one pot: (i) oxidation of benzyl alcohol, (ii) reduction of nitrobenzene, and (iii) condensation of the carbonyl and amino products.

Through our mechanistic studies, we became interested in exploring the different optical properties of the used semiconductors. While $TiO_2$ only absorbs UVA light, iron with its smaller band gap is photoexcited by visible light. Using the monochromatic reaction system, we observed that the reaction requires the photoexcitation of $TiO_2$, as no Schiff base was formed under blue irradiation. However, upon further examination, we noted that blue light irradiation improves benzaldehyde production, an important intermediate for the formation of the Schiff base. Thus, our recent efforts shifted to test the concomitant use of both wavelengths, 370 and 450 nm. Preliminary results show that dual irradiation is beneficial for Schiff base production, enhancing the production rate by more than fivefold. This system is currently under examination, with plausible mechanisms being investigated. Future directions include not only clarifying the mechanisms but also expanding the molecule scope, optimizing yields, and extending the reusability of the catalyst.

We were pleased with these results, as they not only indicate a facile and sustainable route for synthesizing important compounds but also advocate for expanding the applicability of earth-abundant catalysts. Specifically, hybrids containing iron oxide and $TiO_2$ are mostly reported in tests using advanced oxidation processes for environmental remediation. Although they are great candidates for molecule degradation and microorganism disinfection, this work has proven that their applications can also be broadened to organic synthesis, opening doors for further exploration in different systems.

## 6.2 Conclusions

As a result of technological advancements, the overexploitation and utilization of natural resources have raised concerns about the long-term availability of several critical resources. Specifically, many elements are extensively used in various aspects of our lives, posing risks to their availability, environmental sustainability, and social impacts. In this dissertation, we

proposed several fabrication methodologies and applications of materials containing two earth-abundant elements, iron and titanium.

By employing a one-pot synthesis, we demonstrated that iron-based metal oxides are excellent alternatives for bacterial treatments. The properties of iron oxides suggest they are viable candidates for investigating bacterial infections, offering fewer health risks compared to other commonly used materials. Notably, the use of lignin as a biocompatible capping agent proved to be an excellent choice, facilitating nanoparticle stabilization while reducing toxicity toward human cells. This makes lignin a more sustainable and safer alternative to other commonly utilized capping materials.

As for titanium, its most known form is the use of titanium dioxide ($TiO_2$) which is recognized for its efficient photocatalytic performance, yet its commercial application remains limited. In Chapter 3, we investigated and compared fibrous alternatives to facilitate the implementation of this semiconductor for $TiO_2$ in water treatment. The three proposed materials were excellent catalysts for organic material degradation. Comparing their different degradation rates in batch and flow catalytic underscored the importance of selecting appropriate methods based on the desired system. By comparing their physical and catalytical aspects, we identified $TiO_2$@GW as a promising candidate for further studies due to its excellent catalytic performance and ideal physical properties for flow systems.

Based on these results, we further explored $TiO_2$@GW in Chapter 4. Our investigations highlighted important aspects to consider when developing and optimizing supported catalysts for water disinfection. Insufficient ROS production, limited $O_2$ availability, and poor optical properties, combined with bacterial adhesion on supported catalysts may contribute to suboptimal bactericidal activity. Based on our findings and discussions, higher bacterial disinfection could be achieved by improving light penetration, ensuring adequate aeration and enhancing mass transport.

The combination of iron and titanium resulted in the synthesis of a novel magnetic $TiO_2$, fabricated using a simple one-pot system. Their catalytic properties were validated through a tandem reaction to produce Schiff bases from benzyl alcohol and aldehydes, achieving high production rates of the desired compound. This work expanded the scope of applications for $Fe_3O_4$

and $TiO_2$ hybrid materials in catalysis research where they can stand out due to their excellent catalytic performance, magnetic properties, and sustainability.

Overall, this dissertation proposed several fabrication methodologies and applications for materials containing iron and titanium. By demonstrating their effectiveness as antibacterial agents, in water remediation, and as photocatalysts for organic synthesis, this work highlights the versatility and potential of Fe and Ti-based nanomaterials. This work contributes to advancements in research areas interested in developing sustainable alternatives to at-risk elements.

## 6.3 References

(1) Vinothini, P.; Malaikozhundan, B.; Krishnamoorthi, R.; Dayana Senthamarai, M.; Shanthi, D. Potential Inhibition of Biofilm Forming Bacteria and Fungi and DPPH Free Radicals Using Tamarindus Indica Fruit Extract Assisted Iron Oxide Nanoparticle. *Inorg. Chem. Commun.* **2023**, *156*, 111206.

(2) Egorova, A.; Xia, B.; Vyas, H. K. N.; Armendáriz-Ontiveros, M. M.; Lin, Y.-C.; Garcia-Garcia, A.; Wang, D. K.; Cullen, P. J.; Fimbres Weihs, G.; Mai-Prochnow, A. Iron Nanoparticle Coating and Plasma-Activated Water Cleaning as a Biofouling Removal Method for Reverse Osmosis Membranes Suitable for Desalination. *J. Water Proc. engineering* **2024**, *59*, 105043.

(3) Huang, Z.; Li, Y.; Yin, W.; Raby, R. B. N.; Liang, H.; Yu, B. A Magnetic-Guided Nano-Antibacterial Platform for Alternating Magnetic Field Controlled Vancomycin Release in Staphylococcus Aureus Biofilm Eradication. *Drug Deliv. and Transl. Res.* **2024**.

(4) Paunovic, J.; Vucevic, D.; Radosavljevic, T.; Vukomanovic Djurdjevic, B.; Stankovic, S.; Pantic, I. Effects of Iron Oxide Nanoparticles on Structural Organization of Hepatocyte Chromatin: Gray Level Co-Occurrence Matrix Analysis. *Microsc. Microanal.* **2021**, *27* (4), 889–896.

(5) Wadhawan, S.; Wadhawan, D.; Jain, A.; Mehta, S. K. Toxic Implication of Nanoparticles: A Review of Factors, Mechanism, Exposure and Control Strategies. *Int. J. Environ. Sci. Technol.* **2024**.

(6) Scaiano, J. *Photochemistry Essentials*; American Chemical Society: Washington, DC, USA, 2022.

(7) Chen, X.; Liu, L.; Yu, P. Y.; Mao, S. S. Increasing Solar Absorption for Photocatalysis with Black Hydrogenated Titanium Dioxide Nanocrystals. *Science (1979)* **2011**, *331* (6018), 746–750.

(8) Rasul, M. G.; Ahmed, S.; Sattar, M. A.; Jahirul, M. I. Hydrodynamic Performance Assessment of Photocatalytic Reactor with Baffles and Roughness in the Flow Path: A Modelling Approach with Experimental Validation. *Heliyon* **2023**, *9* (9), e19623.

# A: Appendix

## A.1 -Statistical Analysis of data presented in Chapter 2

Statistical analysis for Chapter 2 was performed using R studio (version 1.4.1717). We first determined whether there was a difference between the means of the treatment groups. For this, we employed the One-way Analysis of Variance (ANOVA). For experiments evaluating the antibacterial performance of the catalysts, we compared the average $\log_{10}$ reductions. In the analysis of the cellular toxicity, we used the mean percentage viability for each treatment The ANOVA results led us to reject the null hypothesis ($p<0.05$), in all treatments, indicating the means of the treatment groups were not the same. To identify which groups differed from each other, we conducted a *post-hoc* test using Tukey's Honest Significant Difference (HSD). Due to the extensive list of pairwise comparisons produced, we presented the results using a compact letter display (CLD). This method labels treatment groups with letters: groups sharing the same letter are statistically similar, while groups with different letters are statistically distinct. This approach allowed us to clearly identify which treatments were statistically different from one another.

Antibacterial results and $\log_{10}$ averages can be found in figures 2.2.4, 2.2.6 and 2.2.7 (A and B). Cell toxicity results expressed, and percentage viability can be found in Figure 2.2.8.

### A.1.1 Statistical results for the Minimal Inhibitory Concentration tests for *E. coli*

**Table A.1.1.1** Output of the ANOVA test. Tests were done using the $Log_{10}$ reduction for each sample, done in triplicates. Degrees of freedom were calculated by the subtraction of the sample size number (24), by the number of parameters (1). Sum Sq was calculated from the squared $Log_{10}$ values. Mean Sq by dividing the Sum Sq by the degree of freedom. F value is the ratio between the variance between the groups (how much the means of different groups vary from each other) over the variance within a group (how much the individual data points within each group vary from their group mean). Pr > F is the p-value associated with the F value calculated. 0 '***', 0.001 '**', 0.01 '*' , 0.05 '.', 0.1 ''

| | Degrees of freedom | Sum Sq | Mean Sq | F value | Pr (>F) |
|---|---|---|---|---|---|
| **Results** | 23 | 199.45 | 8.672 | 281.8 | <2e-16*** |
| **Residuals** | 48 | 1.48 | 0.031 | - | - |

The mean Sq value obtained represents the average variability or dispersion of the data points within the treatment groups. A high mean Sq value indicates substantial variability within these groups. The F-value measures the likelihood of significant differences between at least some of the group means. This value is compared to a critical F-value from the F-distribution table, which is determined based on the degrees of freedom.[1] If the calculated F-value exceeds the critical F-value, the null hypothesis (that the group means are equal) is rejected, indicating statistical differences between some of the group means. The p-value (Pr(>F)) reflects the probability that the calculated F-value would occur if the null hypothesis were true.[1] A small p-value indicates a low probability that the results happened by chance. In this experiment, the p-value was close to zero (<2e-16), suggesting a strong likelihood that the differences did not occur by chance and are statistically significant.

Those analysis were done for all ANOVA tests presented in appendices A.1 and A.2.

**Table A.1.1.2** Compact Letter Display (CDL) from the Tukey HSD test performed on the data from the MIC assay against E.coli. From ANOVA results we concluded that the average between groups is statistically different assuming $p<0.05$. To learn where the differences are, we performed a post hoc test, Tukey, which did a multiple comparison between the log10 reduction values. To facilitate visualization, we employed CLD analysis which groups similar treatments in letter groups. Lignin@Fe (LFe), Lignin@FeAg (LFeAg), Lignin@Co (LCo) and Lignin@FeCo (LFeCo). MNPs in solution are expressed in mg/L.

| LFe (mg/L) | CLD | LFeAg (mg/L) | CLD | LFeCo. (mg/L) | CLD | LCo (mg/L) | CLD |
|---|---|---|---|---|---|---|---|
| 1000 | ef | 1000 | f | 1000 | d | 1000 | a |
| 500 | ef | 500 | f | 500 | d | 500 | a |
| 250 | f | 250 | f | 250 | d | 250 | a |
| 125 | f | 125 | ef | 125 | ef | 125 | b |
| 62.5 | f | 62.5 | ef | 62.5 | de | 62.5 | c |
| 31.25 | ef | 31.25 | f | 31.25 | f | 31.25 | c |

### A.1.2 Statistical results for the Photodynamic therapy (PTT) and Chemodynamic therapy tests (CDT) for *E.coli*

**Table A.1.2.1** Output of the ANOVA test. Tests were done using the $Log_{10}$ reduction for each sample, done in triplicates. Degrees of freedom were calculated by the subtraction of the sample size number (40), by the number of parameters (1). Sum Sq was calculated from the squared $Log_{10}$ values. Mean Sq by dividing the Sum Sq by the degree of freedom. F value is the ratio between the variance between the groups (how much the means of different groups vary from each other) over the variance within a group (how much the individual data points within each group vary from their group mean). Pr > F is the p-value associated with the F value calculated. 0 '***', 0.001 '**', 0.01 '*' , 0.05 '.', 0.1 ''

| | Degrees of freedom | Sum Sq | Mean Sq | F value | Pr (>F) |
|---|---|---|---|---|---|
| | | **Photodynamic therapy** | | | |
| **Results** | 39 | 550.9 | 14.13 | 467.5 | <2e-16*** |
| **Residuals** | 80 | 2.4 | 0.03 | - | - |
| | | **Chemodynamic therapy** | | | |
| **Results** | 39 | 1039.5 | 26.654 | 1563 | <2e-16*** |
| **Residuals** | 80 | 1.4 | 0.017 | - | - |

**Table A.1.2.2** Compact Letter Display (CDL) from the Tukey HSD test performed on the data from the Photodynamic therapy test against *E.coli*. From the ANOVA results we concluded that the average between groups is statistically different assuming $p<0.05$. To learn where are the differences, we performed a post-hoc test, Tukey, which did a multiple comparison between the $\log_{10}$ reduction values. To facilitate visualization, we employed CLD analysis which groups similar treatments in letter groups. Lignin@Fe (LFe), Lignin@FeAg (LFeAg), Lignin@Co (LCo) and Lignin@FeCo (LFeCo). Controls dark and light were the NPs incubated in 50% LB only.

| Sample | 1 min | 5 min | 15 min | 30 min |
|---|---|---|---|---|
| **Control Dark** | p | ijkl | jklmn | ijkl |
| **Control Light** | g | op | nop | mnop |
| **LFe Dark** | ijklm | lmn | jklmn | klmn |
| **LFe Light** | jklmn | lmn | klmn | hi |
| **LFeAg Dark** | lmno | ijkl | ijkl | lmn |
| **LFeAg Light** | hi | gh | gh | hi |
| **LFeCo Dark** | bcd | cd | e | f |
| **LFeCo Light** | lmno | bc | b | a |
| **LCo Dark** | hijk | f | hij | hij |
| **LCo Light** | lmn | g | d | cd |

**Table A.1.2.3** Compact Letter Display (CDL) from the Tukey HSD test performed on the data from the chemodynamic therapy assay against *E.coli*. From the ANOVA results we concluded that the average between groups is statistically different assuming $p<0.05$. To learn where are the differences, we performed a post-hoc test, Tukey, which did a multiple comparison between the $\log_{10}$ reduction values. To facilitate visualization, we employed CLD analysis which groups similar treatments into letter groups. Lignin@Fe (LFe), Lignin@FeAg (LFeAg), Lignin@Co (LCo) and Lignin@FeCo (LFeCo). Controls dark and light were the NPs incubated in 50% LB only.

| Sample | 1 min | 5 min | 15 min | 30 min |
|---|---|---|---|---|
| **Control Dark** | q | mnopq | nopq | opq |
| **Control Light** | pq | nopq | pq | pq |
| **LFe Dark** | lm | kl | lmn | ij |
| **LFe Light** | kl | j | ij | h |
| **LFeAg Dark** | q | ij | g | hi |
| **LFeAg Light** | a | a | a | a |
| **LFeCo Dark** | lmno | lmnop | k | f |
| **LFeCo Light** | c | bc | bc | b |
| **LCo Dark** | fg | fg | fg | fg |
| **LCo Light** | e | e | d | d |

### A.1.3 Statistical results for the Minimal Inhibitory Concentration tests for *S. aureus*

**Table A.1.3.1** Output of the ANOVA test. Tests were done using the $Log_{10}$ reduction for each sample, done in triplicates. Degrees of freedom were calculated by the subtraction of the sample size number (24), by the number of parameters (1). Sum Sq was calculated from the squared $Log_{10}$ values Mean Sq by dividing the Sum Sq by the degree of freedom. F value is the ratio between the variance between the groups (how much the means of different groups vary from each other) over the variance within a group (how much the individual data points within each group vary from their group mean). Pr > F is the p-value associated with the F value calculated. 0 '***', 0.001 '**', 0.01 '*' , 0.05 '.', 0.1 ''

| | Degrees of freedom | Sum Sq | Mean Sq | F value | Pr (>F) |
|---|---|---|---|---|---|
| **Results** | 23 | 458.0 | 20.817 | 332.1 | <2e-16*** |
| **Residuals** | 46 | 2.9 | 0.063 | - | - |

**Table A.1.3.2** Compact Letter Display (CDL) from the Tukey HSD test performed on the data from the MIC assay performed against *S. aureus*. From the ANOVA results, we concluded that the average between groups is statistically different assuming $p<0.05$. To learn where the differences are, we performed a ***post-hoc*** test, Tukey, which did a multiple comparisons between the $log_{10}$ reduction values. To facilitate visualization, we employed CLD analysis which group similar treatments into letter groups. Lignin@Fe (LFe), Lignin@FeAg (LFeAg), Lignin@Co (LCo) and Lignin@FeCo (LFeCo). MNPs in solution are expressed in mg/L

| LFe (mg/L) | CLD | LFeAg (mg/L) | CLD | LFeCo. (mg/L) | CLD | LCo (mg/L) | CLD |
|---|---|---|---|---|---|---|---|
| 1000 | gh | 1000 | h | 1000 | cd | 1000 | a |
| 500 | gh | 500 | gh | 500 | de | 500 | b |
| 250 | h | 250 | h | 250 | ef | 250 | b |
| 125 | gh | 125 | gh | 125 | e | 125 | b |
| 62.5 | h | 62.5 | gh | 62.5 | ef | 62.5 | c |
| 31.25 | gh | 31.25 | g | 31.25 | f | 31.25 | c |

### A.1.4 Statistical results for the Photodynamic therapy (PTT) and Chemodynamic therapy tests (CDT) for *S. aureus*

**Table A.1.4.1** Output of the ANOVA test. Tests were done using the $Log_{10}$ reduction for each sample, done in triplicates. Degrees of freedom were calculated by the subtraction of the sample size number (40), by the number of parameters (1). Sum Sq was calculated from the squared $Log_{10}$ values. Mean Sq by dividing the Sum Sq by the degree of freedom. F value is the ratio between the variance between the groups (how much the means of different groups vary from each other) over the variance within a group (how much the individual data points within each group vary from their group mean). Pr > F is the p-value associated with the F value calculated. 0 '***', 0.001 '**', 0.01 '*' , 0.05 '.', 0.1 ''

| | Degrees of freedom | Sum Sq | Mean Sq | F value | Pr (>F) |
|---|---|---|---|---|---|
| | | **Photodynamic therapy** | | | |
| **Results** | 39 | 165.13 | 4.234 | 98.62 | <2e-16*** |
| **Residuals** | 80 | 3.43 | 0.043 | - | - |
| | | **Chemodynamic therapy** | | | |
| **Results** | 39 | 154.92 | 3.972 | 81.78 | <2e-16*** |
| **Residuals** | 80 | 3.89 | 0.049 | - | - |

**Table A.1.4.2** Compact Letter Display (CDL) from the Tukey HSD test performed on the data from the Photodynamic therapy test against *S. aureus*. From the ANOVA results we concluded that the average between groups is statistically different assuming $p<0.05$. To learn where are the differences, we performed a post-hoc test, Tukey, which did a multiple comparison between the $\log_{10}$ reduction. To facilitate visualization, we employed CLD analysis which groups similar treatments into letter groups. Lignin@Fe (LFe), Lignin@FeAg (LFeAg), Lignin@Co (LCo) and Lignin@FeCo (LFeCo). Controls dark and light were the NPs incubated in 50% LB only.

| Sample | 1 min | 5 min | 15 min | 30 min |
|---|---|---|---|---|
| **Control Dark** | jklmn | klmn | klmn | jklmn |
| **Control Light** | n | mn | klmn | klmn |
| **LFe Dark** | lmn | hijklm | klmn | klmn |
| **LFe Light** | klmn | fghij | fgh | efg |
| **LFeAg Dark** | cd | cd | c | c |
| **LFeAg Light** | cd | b | b | a |
| **LFeCo Dark** | fgh | hijklmn | ghijkl | ijklmn |
| **LFeCo Light** | fgh | ghijk | ghijklm | efg |
| **LCo Dark** | cde | cde | def | fghi |
| **LCo Light** | cde | cde | c | b |

**Table A.1.4.3** Compact Letter Display (CDL) from the Tukey HSD test performed on the data from the Chemodynamic therapy test against S. aureus. From the ANOVA results we concluded that the average between groups is statistically different assuming $p<0.05$. To learn where are the differences, we performed a post hoc test, Tukey, which did a multiple comparison between the $\log_{10}$ reduction. To facilitate visualization, we employed CLD analysis which groups similar treatments in letter groups. Lignin@Fe (LFe), Lignin@FeAg (LFeAg), Lignin@Co (LCo) and Lignin@FeCo (LFeCo). Controls dark and light were the NPs incubated in 50% LB only.

| Sample | 1 min | 5 min | 15 min | 30 min |
|---|---|---|---|---|
| **Control Dark** | defg | defgh | defg | de |
| **Control Light** | defg | def | def | de |
| **LFe Dark** | ij | fghij | ij | j |
| **LFe Light** | j | j | ghij | def |
| **LFeAg Dark** | d | def | def | def |
| **LFeAg Light** | def | c | b | b |
| **LFeCo Dark** | def | def | defg | def |
| **LFeCo Light** | d | def | hij | de |
| **LCo Dark** | def | defgh | defg | de |
| **LCo Light** | defg | defg | de | a |

### A.1.5 Statistical Results for Cell Toxicity Assay

**Table A.1.5.1** Output of the ANOVA test. Tests were done using the percentage viability for each sample, done in triplicates. Degrees of freedom were calculated by the subtraction of the sample size number (10), by the number of parameters (1). Sum Sq was calculated from the squared % viability values. Mean Sq by dividing the Sum Sq by the degree of freedom. F value is the ratio between the variance between the groups (how much the means of different groups vary from each other) over the variance within a group (how much the individual data points within each group vary from their group mean). Pr > F is the p-value associated with the F value calculated. 0 '***', 0.001 '**', 0.01 '*' , 0.05 '.', 0.1 ''

| | Degrees of freedom | Sum Sq | Mean Sq | F value | Pr (>F) |
|---|---|---|---|---|---|
| **Results** | 9 | 46509 | 5168 | 38.8 | <2e-16*** |
| **Residuals** | 90 | 11988 | 133 | - | - |

**Table A.1.5.2** Compact Letter Display (CDL) from the Tukey HSD test performed on the data from the MTT assay test on HT1080 cells. From the ANOVA results we concluded that the average between groups is statistically different assuming $p<0.05$. To learn where are the differences, we performed a post hoc test, Tukey, which did a multiple comparison between the % viability values. To facilitate visualization, we employed CLD analysis which groups similar treatments into letter groups. Lignin@Fe (LFe), Lignin@FeAg (LFeAg), Lignin@Co (LCo) and Lignin@FeCo (LFeCo). Controls dark and light were the NPs incubated in DMEM in absence of NPs.

| Sample | Dark | Light |
|---|---|---|
| **Control** | ab | a |
| **LFe** | ab | bc |
| **LFeAg** | f | f |
| **LFeCo** | cd | cde |
| **LCo** | ef | de |

## A.2 -Statistical Analysis of data presented in Chapter 4

Statistical analysis for Chapter 4 was performed using R studio (version 1.4.2). We first determined whether there was a difference between the means of the treatment groups. For this, we employed the One-way Analysis of Variance (ANOVA). For experiments evaluating the antibacterial performance of the catalysts, we compared the average $\log_{10}$ reductions. Log reduction was calculated by comparing the bacterial growth in the treated samples against the bacterial count on a control sample incubated in 5 % LB without light irradiation. The ANOVA results led us to reject the null hypothesis ($p<0.05$), indicating the means of the treatment groups were not the same. To identify which groups differed from each other, we conducted a *post-hoc* test using Tukey's Honest Significant Difference (HSD). Due to the extensive list of pairwise comparisons produced, we presented the results using a compact letter display (CLD). This method labels treatment groups with letters: groups sharing the same letter are statistically similar, while groups with different letters are statistically distinct. Note that some treatments are labelled with more than one letter, which means that those groups are statistically similar to other treatments with similar letters. This approach allowed us to clearly identify which treatments were statistically different from one another.

Antibacterial results and $\log_{10}$ averages can be found in Figure 4.2.1

### A.2.1 Statistical results for the antibacterial experiments

**Table A.2.1** Output of the ANOVA test. Tests were done using the $Log_{10}$ reduction for each sample, done in triplicates. Degrees of freedom were calculated by the subtraction of the sample size number (40), by the number of parameters (1). Sum Sq was calculated from the squared $Log_{10}$ values Mean Sq by dividing the Sum Sq by the degree of freedom. F value is the ratio between the variance between the groups (how much the means of different groups vary from each other) over the variance within a group (how much the individual data points within each group vary from their group mean). Pr > F is the p-value associated with the F value calculated. 0 '***', 0.001 '**', 0.01 '*' , 0.05 '.', 0.1 ''

| | Degrees of freedom | Sum Sq | Mean Sq | F value | Pr (>F) |
|---|---|---|---|---|---|
| **Results** | 39 | 178.8 | 4.585 | 27.78 | <2e-16*** |
| **Residuals** | 80 | 13.2 | 0.165 | - | - |

**Table A.2.2** Compact Letter Display (CDL) from the Tukey HSD test performed on the data from the antibacterial tests. From the ANOVA results, we concluded that the average between groups is statistically different assuming $p<0.05$. To learn where are the differences, we performed a post-hoc test, Tukey, which did a multiple comparisons between the $\log_{10}$ reduction values. To facilitate visualization, we employed CLD analysis which groups similar treatments into letter groups. Controls light were the NPs incubated in 5 % LB only and exposed to the light.

| Sample | 1 Hour | 2 Hours | 3 Hours | 6 Hours | 24 Hours |
|---|---|---|---|---|---|
| **Control Light** | ghijkl | cdefghij | cdefg | b | a |
| **Glass wool Light** | defghijk | efghijkl | cdefgh | efghijkl | bcdef |
| **Glass wool Dark** | efghijkl | fghijkl | mn | n | defghijk |
| **$TiO_2$@GW Light** | ijklm | jklm | cde | bc | bcde |
| **$TiO_2$@GW Dark** | klm | ghijklm | lmn | fghijkl | hijklm |

## A.2.2 References

(1) Herzog, Michael H., Gregory Francis, and Aaron Clarke. *Understanding statistics and experimental design: how to not lie with statistics*. Springer Nature, 2019.

## A.3 -Journal Permissions

This dissertation contains altered manuscripts and images that are republished under the permissions granted by the publishing journals.

Permission to reproduce Figure 1.5.4:

This Agreement between Daliane Regis Correa da Silva ("You") and Elsevier ("Elsevier") consists of your license details and the terms and conditions provided by Elsevier and Copyright Clearance Center.

| | |
|---|---|
| License Number | 5854480318630 |
| License date | Aug 22, 2024 |
| Licensed Content Publisher | Elsevier |
| Licensed Content Publication | Journal of Molecular Catalysis A: Chemical |
| Licensed Content Title | Photocatalytic degradation of organic dyes in the presence of nanostructured titanium dioxide: Influence of the chemical structure of dyes |
| Licensed Content Author | A.R. Khataee,M.B. Kasiri |
| Licensed Content Date | Aug 3, 2010 |
| Licensed Content Volume | 328 |
| Licensed Content Issue | 1-2 |
| Licensed Content Pages | 19 |
| Start Page | 8 |
| End Page | 26 |
| Type of Use | reuse in a thesis/dissertation |
| Portion | figures/tables/illustrations |
| Number of figures/tables/illustrations | 2 |
| Format | electronic |
| Are you the author of this Elsevier article? | No |
| Will you be translating? | No |
| Title of new work | Unveiling The Versatility of Titanium and Iron Nanostructures: Applications Across Medicine, Environmental Remediation and Organic Reactions |
| Institution name | University of Ottawa |
| Expected presentation date | Oct 2024 |
| Portions | Table 1, Figure 1 |
| The Requesting Person / Organization to Appear on the License | Daliane Regis Correa da Silva |